The

Computational Analysis of the Slipstream Characteristics of High-Speed Trains

by

Shibo Wang

A Thesis submitted to Monash University
for the degree of
Doctor of Philosophy

September 2017
Department of Mechanical & Aerospace Engineering
Monash University

To my parents.

Statement of Originality

This thesis contains no material that has been accepted for the award of a degree or diploma in this or any other university. To the best of the candidate's knowledge and belief, this thesis contains no material previously published or written by another person except where due reference is made in the text of this thesis.

Candidate: Shibo Wang

<September 2017>

Notice

The sinister spirit sneered:

  ‘ It had to be! ’

And again the spirit of pity whispered,

  ‘ Why? ’

Thomas Hardy, 1918.

Abstract

High-speed trains have proven to be a viable intercity transportation method, due to their high transportation efficiency both in time and energy. Because of this, many countries have built comprehensive high-speed rail networks, such as Germany, Japan, France and China. Historically, when high-speed train development began much of the research focus was on improvements in electric motor technology and reduction of frame weight, rather than developing an improved understanding the train aerodynamics. Progress in the former two areas resulted in a remarkable speed-up of high-speed trains over the past few decades. Because improvements in these areas are now likely to be more incremental, understanding the aerodynamic aspects is becoming increasingly critical, as the aerodynamic drag increases with the square of the train speed and bad aerodynamic performance leads to significant energy loss. Additionally, many problems that can be neglected when trains travel at lower speeds are being raised, and become the main limiting factors to further speed-up. An associated problem is the induced flow caused by a train passing, which is also known as *slipstream*. The main practical concern of slipstream is its potential safety hazard to the commuters waiting on a platform and to trackside workers. The essence of understanding slipstream is through investigations of the flow characteristics around high-speed trains.

Compared with the conventional aircraft and ground vehicles, high-speed trains have the following distinct features: significant larger length to height ratio, and proximity to ground with a much higher cruising speed than most ground vehicles. These features bring challenges for both experimental investigations and numerical simulations. Current common practice in high-speed train slipstream research is based on three approaches: full-scale tests, reduced-scale experiments and numerical simulations. The research undertaken in this PhD program first reviewed the state-of-the-art of Computational Fluid Dynamics (CFD) modelling techniques, and then utilised the strength of CFD to study high-speed train slipstream characteristics in greater detail than generally possible through experiments. In this research program, the effects of three geometric features on high-speed train slipstream characteristics are thoroughly investigated, including the variation of ground boundary conditions, the inclusion of bogies and the presence of rails, as well as examining the fidelity of different turbulence modelling techniques. Some care was taken to validate the computer modelling against experimental results where available.

These investigations revealed the strong effects of these geometric features on wake slipstream development, for instance, the inclusion of rails in the computational model had a strong influence on outward movement of the time-mean trailing streamwise vortex structures, which are the main identifiable large-scale wake structures. In turn this led to a significant delay in the time after the train passed at which maximum induced velocity occurred, in addition to changing the magnitude of the slipstream reading. This has potential implications for the testing required to satisfy the slipstream regulations, especially since the European regulations have recently been modified to remove the requirement for rails in validation testing. The work on bogies led to the surprising result that the spanwise wake oscillation, which previously had been speculated to be due to vortex shedding from the bogies, was more likely due to an intrinsic wake instability associated with the streamwise wake vortices. Finally, the research on the accuracy of different turbulence models for predicting different aspects of slipstream, should enable practitioners to choose the most appropriate model for the predicting a particular aspect of flow behaviour.

Acknowledgments

Undertaking a PhD study is one of the best decisions I have made so far, and I am sure that the past three-and-a-half year's journey is one of the most precious memory in my life. The destination is always important, but I believe those people who walk with me throughout the journey are more memorable. Here, I would like to take this opportunity to acknowledge them.

The most important people I would like to thank are my supervisors: Prof. Mark Thompson, Prof. John Sheridan, Mr. David Burton and Dr. Astrid Herbst. I feel very lucky to have such an 'All-star' supervisor squad. Mark always encourages me to try different things, and supports me with his expertise. He never laughs at my silly ideas, and is always patient and supportive. John always patiently explains to me when there is something I do not understand, and his passion on research really motivates me. David generously provides me a lot of advice from a more practical perspective; and as the wind tunnel manager, he also offers me the opportunities to work casually at the tunnel when I face financial difficulties. Astrid, as an expert from a leading train manufacturer Bombardier, kindly shares a lot of her real-life experience with me. If we say PhD research is exploring in the darkness, their supervision is the light house that makes me feel secure, and guides me through the darkness.

I am also proud to be part of the Fluids Laboratory for Aeronautical and Industrial Research (FLAIR) and the Wind Tunnel Platform, where I broaden my horizons and meet many great people. I also would like to acknowledge the support of the Department of Mechanical and Aerospace Engineering, as well as the Faculty of Engineering, who offered me a scholarship. Additionally, I would like to thank the Graduate Research Academic Support Team; especially Lilian Khaw, who has helped me a lot with my paper and report writing. I deeply know that how important a strong technical support is for a numerical-based project. Here, I would like to thank Australia National Computational Infrastructure (NCI) for the computational hours allocated to this project, and visualisation aid from the Multi-modal Australian ScienceS Imaging and Visualisation Environment (MASSIVE) platform. Additionally, every research student understands and appreciates the importance of friendship; here, I would like to thank my fellow Monash colleagues: James Bell, Chaoran Li, Farah Houdroge, Matthew Corallo, Terence Avadiar, Daniel Tudball-Smith, Damien McArthur, Timothy Crouch, Jisheng Zhao, Shian Chi, Jordan Dunlop, Siavash Maleki, Daniah Aljubaili, Jiachun

Huang, Thomas McQueen.

I am eternally grateful to my parents, Zhiqi Wang and Xuejing Wan, for their limitless and unconditional love. They are keen to discuss the progress of my research with me, although I am quite sure most of the time they do not exactly know what I am doing. They feel happy for me, even there is only a tiny progress I have made; and for those down times, they always comfort me and tell me not to worry. Even though they are thousands miles away, I feel that their support and encouragement are always around me. I also would like to dedicate this thesis to my grandpa, Wenzhong Wan, who was an engineering professor. I can not imagine how happy he would be to see my achievement today; and I will always remember what he told me “quality is the foundation of research”. Additionally, a big ‘thank you’ to all my relatives who support me.

Many people say that knowledge is boundless; we cannot see the shore even we exhaust our whole life. But I believe that even though knowledge is boundless, every small step of advancement has its own joy. Here, I would like to express my sincere appreciation again to those people who make my PhD journey joyful.

I know it is not the end; it is not even the beginning of the end; but, it is the end of the beginning. I do not know what the future will hold for me, but what I do know is that the future starts from this moment.

List of Publications

Journal Articles

Wang, S., Bell, J. R., Burton, D., Herbst, A. H., Sheridan, J. & Thompson, M. C. 2017 The Performance of Different Turbulence Models (URANS, SAS and DES) for Predicting High-Speed Train Slipstream, *Journal of Wind Engineering and Industrial Aerodynamics* 165, 46–57. (provided in Appendix B)

Wang, S., Burton, D., Herbst, A. H., Sheridan, J. & Thompson, M. C. 2017 The Effect of the Ground Boundary Condition on High-Speed Train Slipstream, *Journal of Wind Engineering and Industrial Aerodynamics.* (submitted)

Wang, S., Burton, D., Herbst, A. H., Sheridan, J. & Thompson, M. C. 2017 The Effect of Bogies on the Slipstream Characteristics of a Generic High-Speed Train, *Journal of Fluids and Structures.* (under review)

Wang, S., Burton, D., Herbst, A. H., Sheridan, J. & Thompson, M. C. 2017 The Impact of Rails on the Slipstream Characteristics of a Generic High-Speed Train, *Journal of Wind Engineering and Industrial Aerodynamics.* (in draft)

Wang, S., Burton, D., Herbst, A. H., Sheridan, J. & Thompson, M. C. 2017 An Improved Numerical Method for High-Speed Train Gust Analysis, *Journal of Rail and Rapid Transit.* (in draft)

Conference Papers

Wang, S., Burton, D., Sheridan, J. & Thompson, M. C. 2014 Characteristics of Flow over a Double Backward-Facing Step, *19th Australasian Fluid Mechanics Conference,* Melbourne, Australia, 8-11 December.

Wang, S., Bell, J. R., Burton, D., Herbst, A. H., Sheridan, J. & Thompson, M. C. 2016 The Accuracy of Different Turbulence Models (URANS, SAS and DES) for Predicting High-Speed Train Slipstream, *2nd International Conference in Numerical and Experimental Aerodynamics of Road Vehicles and Trains,* Gothenburg, Sweden, 21-23 June.

Wang, S., Bell, J. R., Burton, D., Herbst, A. H., Sheridan, J. & Thompson, M. C. 2016 On the Suitability of Scale-Adaptive Simulation to Predict High-Speed Train Slipstream, *8th European Postgraduate Fluid Dynamics Conference,* Warsaw, Poland, 6-9 July.

Nomenclature

Roman symbol	**Description**
A	POD mode coefficient
C_D	Train drag coefficient
C_{DES}	DES coefficient, a empirical constant of 0.65
d	The distance to the wall
d_{DES}	The length scale for DES ($d_{DES} = min(d, C_{DES}\Delta_{max})$)
d_{DDES}	The improved length scale for DDES ($d_{DDES} = d - f_d\ max(0, d - C_{DES}\Delta)$)
D	Fluid domain
D_ω	The cross-diffusion term in $SST - k\omega$ model
E_c	The energy percentage of a POD mode
f	Body force
f_d	The shield function for DDES
G	LES cut-off filter function
$\widetilde{G_k}$	The generation of turbulence kinetic energy due to mean velocity gradients
G_ω	The generation of ω
H	Height of the train
i, j, m, n	Arbitrary numbers for indexing
k	Turbulent kinetic energy per unit mass
L_{vK}	SAS length scale ($L_{vK} = \kappa \left\| \frac{\bar{U}'}{\bar{U}''} \right\|$)
$M_i(x)$	Normalised spatial distribution of mode i ($M_i(x) = \frac{\sigma_i(x)}{\\|\sigma_i(x)\\|}$)
$\mathcal{R}$	Right singular matrix in POD decomposition

Continued on the next page.

Continued from previous page.

Roman symbol	**Description**
S	POD basis
S_{ij}	Strain rate tensor
S_k, S_ω	The user-defined source terms in $SST - k\omega$ model
St_W	Strouhal number based on the train width
t	Time
T	POD temporal domain
T_{ref}	Reference time (H/U_∞)
U_{GF}, V_{GF}, W_{GF}	Ground-fixed velocity component in the x, y, z directions
u_{ij}	Velocity gradient
U_{max}	Maximum train peak slipstream velocity, also known as the TSI value ($U_{max} = \overline{U}_{peak} + 2\sigma_{peak}$)
U_{peak}	Train peak slipstream velocity per individual measurement
$\overline{U}_{peak}$	Time-averaged train peak slipstream velocity
$U_{slipstream}$	Slipstream velocity
U_{TF}, V_{TF}, W_{TF}	Train-fixed velocity component in the x, y, z directions
U_∞	Freestream velocity
v	Velocity component
$\mathcal{V}$	Volume of a computational cell
W	Width of the train
x, y, z	Spatial displacement in longitudinal, transverse and vertical direction
Y_k, Y_ω	The dissipation of k and ω due to turbulence

Greek symbol	**Description**
Δt	The solver timestep
Δ_{max}	The max local cell dimension
Γ_k, Γ_ω	The effective diffusivity of k and ω
ϵ	Turbulent dissipation
ϵ_{orth}	The orthogonality factor between two POD modes
κ	von Karman constant, a coefficient of 0.41
Λ	The diagonal matrix in POD formulation, contains the energy proportion of individual modes

Continued on the next page.

Continued from previous page.

Greek symbol	**Description**
ν	Molecular viscosity
ρ	Density of the fluid
$\sigma_i(x)$	Spatial distribution of mode i
σ_{peak}	The standard deviation of train peak slipstream velocity as specified in gust analysis
σ_x	The standard deviation of variable x
τ_{ij}	Stress tensor: RANS formulation (Reynolds stress tensor, $\tau_{ij} = \overline{u_i^{'}u_j^{'}}$) or LES formulation (sub-grid stress tensor, $\tau_{ij} = \widetilde{u_i u_j} - \widetilde{u}_i\widetilde{u}_j$)
Φ, ϕ	Arbitrary flow dataset depending on different scenarios
ω	Specific dissipation rate
Ω	Two dimensional spatial POD mode distribution

Other symbol	**Description**
$\int$	Integration
Σ	Summation
$'$	First derivative
$''$	Second derivative
X^T	Transpose of matrix X
$\|X\|$	Norm of matrix X
$\bigtriangledown$	Gradient
$\overline{X}$	Time-averaged value of X
$\widetilde{X}$	Filtering value of X

Abbreviation	**Description**
$1s\ MA$	1 Second Moving-Average
CAD	Computer-Aided Design
CEN	European Committee for Standardisation
CFD	Computational Fluid Dynamics
DES	Detached Eddy Simulation
$DDES$	Delayed Detached Eddy Simulation
DNS	Direct Numerical Simulation
$ELES$	Embedded Large Eddy Simulation

Continued on the next page.

Continued from previous page.

Abbreviation	**Description**
FFT	Fast Fourier Transform
HST	High-Speed Train
$ICE3$	Inter-City-Express 3
$IDDES$	Improved Delayed Detached Eddy Simulation
LES	Large Eddy Simulation
$M1WR$	Model 1 With Rails
$M2NR$	Model 2 No Rails
$M2WR$	Model 2 With Rails
$MGRW$	Moving Ground with Rotating Wheels
$MGSW$	Moving Ground with Stationary Wheels
POD	Proper Orthogonal Decomposition
$RANS$	Reynolds-Averaging Navier-Stokes equations
SAS	Scale-Adaptive Simulation
$SGSW$	Stationary Ground with Stationary Wheels
SRS	Scale Resolve Simulation
SST	Shear-Stress Transport
SVD	Singular Value Decomposition
TOR	Top of the Rails
TSI	Technical Specifications for Interoperability
$URANS$	Unsteady Reynolds-Averaging Navier-Stokes equations
$WMLES$	Wall-Modelled Large Eddy Simulation

Contents

List of Figures

Introduction

High-Speed Trains (HSTs) are an important transportation method, especially for intercity bulk volume transport. For this type of transportation between 100 and 1000 km, HST shows significant strength compared with travelling by air and driving in terms of energy and time efficiency (Raghunathan *et al.* 2002). Because at these travel distances, HST can deliver passengers closer to the city centres compared with travelling by air in a competitive time. For example, the distance between Tokyo and Osaka is 552.6 km, and the travel time for HSTs and aeroplanes are about 2 hours 25 minutes and 1 hour 5 minutes respectively. However if we add the travel time between the airports and city centres, the total time for travelling by air is 2 hours and 40 minutes, which is longer than travelling by HST. That is why, based on an average of 120,000 passengers per day on this route, 84% of the passengers choose to take the HST, while only 16% choose to travel by air (Japan Railway Company 2017). Additionally, HST is more environmental friendly. Using the same route between Tokyo and Osaka as an example, the carbon dioxide emission per seat for the HST (Series N700) is 4.2 kg, while for the aeroplane (B777-200) is 50 kg, which is approximately twelve times higher (Japan Railway Company 2017). Many urbanised countries have well established HST railway systems, for example, the German Inter City Express (ICE), Japanese Shinkansen, French Train *à* Grande Vitesse (TGV), Chinese China Rail High-speed (CRH). European countries have an existing high-speed rail network of 7,343 km and a total length of 2,493 km high-speed lines are currently under construction (European Commission 2014). China has a high-speed rail grid with four horizontal and four vertical lines that constitute a total length of 12,958 km (Morgan Stanley 2011). As an important component of the transportation system, high-speed rail supports a substantial passenger demand. For instance, Japan operates 323 regular Shinkansen HSTs travelling at a speed of 270 km/h between Tokyo and Shin Osaka per day, which in total conveys approximately 143 million passengers annually (Japan Railway Company 2017).

Australia is an ideal candidate for the modern high-speed rail system, especially at the Brisbane-Sydney-Canberra-Melbourne route, as shown in Fig. I (a). The Australian government has done two feasibility studies on the implementation of high-speed rail for this route: phase 1 (Phase 1 2011) and phase 2 (Phase 2 2013). Additionally, the plan proposed attempts to build the corridor next to the existing infrastructure (i.e. highways), as shown in Fig. I (b). This makes the study of train-induced wind to the surrounding environment crucial. The total length of the proposed high-speed rail network is approximately 1,748 kilometres, and estimated investment is around 114 billion Australian dollars (in 2012 dollars). With the new high-speed rail network, the travel time between Brisbane-Sydney and Sydney-Melbourne would be shortened from the current 10 hours 30 minutes and 13 hours 35 minutes to 2 hours 37 minutes and 2 hours 44 minutes. The forecast annual passenger trips from Brisbane-Sydney and Sydney-Melbourne are 10.86 and 18.76 million, respectively (Phase 1 2011) (Phase 2 2013).

Understanding the aerodynamics of high-speed trains is essential, especially with the rapid technology development leading to trains become faster and lighter. Many problems that are negligible at lower speeds then become crucial, such as the safety concerns caused by slipstream, aerodynamic noise and vibration, impulse forces when two trains pass each other and interaction between the trains and tunnel system. Compared with conventional road vehicles and aeroplanes, high-speed trains typically have a very large length to height ratio, and they travel close to adjacent structures and interact with one another. Due to the distinct characteristics, high-speed train aerodynamics cannot be understood using the aerodynamics applied to aeroplanes and ground vehicles. Current research areas relating to the train aerodynamics are: aerodynamic drag, pressure variation inside trains, train-induced flow, crosswind effect, ground effect, pressure waves inside tunnels, impulse waves at the exits of tunnels, noise and vibration, etc (Raghunathan *et al.* 2002).

Slipstream is defined as the induced airflow caused by the train movement, from the perspective of a fixed ground position next to the track. The slipstream is a combined effect of multiple flow features: the head pressure pulse, boundary layer development along the train body, flow under the bogies and the wake behind the train. The intensity of the slipstream is associated with the cross-sectional area of the train body, the shape of the head and tail, surface roughness and train length (Raghunathan *et al.* 2002). The

Figure I: The plan of the high-speed rail in Australia: (a) proposed high-speed rail line on the east coast, (b) schematic of a potential corridor with shared infrastructure (Infrastructure Partnerships Australia 2016).

slipstream causes safety hazards to trackside workers and commuters on platforms, and damage to trackside infrastructure. In European countries, the Technical Specification for Interoperability (TSI) relating to the rolling stock subsystem sets up limiting values for the slipstream intensity and specifies the measurement procedure (TSI 2014). Thus, an accurate prediction of slipstream behaviour has practical significance in the train industry, especially at an early design stage. Additionally, the prediction of slipstream intensity relies heavily on an in-depth understanding of the flow features around high-speed trains. Many techniques are applied to study the flow field around a high-speed train, the main ones include full-scale tests, wind-tunnel experiments, moving model rig tests and numerical simulations.

Overview of the Project

The research undertaken in this PhD program aims to strengthen the understanding of slipstream characteristics by utilising cutting-edge Computational Fluid Dynamics (CFD) techniques to predict the flow field around a HST with different geometry configurations. This research is part of an ongoing collaboration with Bombardier transportation, a world leading HST manufacturer. Attention is restricted to trains in an open-air environment with no crosswinds (i.e. tunnel flows will not be considered). The research undertaken in this PhD program aims to review the state-of-the-art of Computational Fluid Dynamics (CFD) techniques as applied to this problem, and utilise the strengths of CFD to study HST slipstream characteristics with geometric variations in greater detail than possible through experiments. To fulfil the aim, this PhD project is further divided into four individual but related studies. The first study reviews the current computational approaches for studying HST slipstream, and evaluates the performance of three widely-used turbulence models. The optimal numerical settings derived from the first study are then applied to studying the effects of three important geometric variations on HST slipstream characteristics. These aspects are the variation of ground boundary conditions, the inclusion of bogies and the presence of rails.

Thesis Structure

The thesis will provide a detailed description of numerical procedures and the analysis undertaken, and a schematic illustrating the structure of this thesis report is presented in Fig. II. An introduction to HST aerodynamics with a detailed literature review for each of the individual studies is presented in *Chapter 1*. *Chapter 2* introduces the numerical methodology, and the post-processing techniques employed in this project are presented in *Chapter 3*. *Chapter 4* evaluates the performance of three state-of-art turbulence models for predicting HST slipstream. The three geometric studies: (1) the variation of ground boundary condition, (2) the inclusion of bogies and (3) the presence of rails, are presented in *Chapter 5*, *6* and *7*, respectively. Conclusions on the findings and contributions of this PhD research program are presented in *Chapter 7*; the related regulations and manuscripts of the associated publications are attached as *Appendices*. An outline of each chapter is presented below.

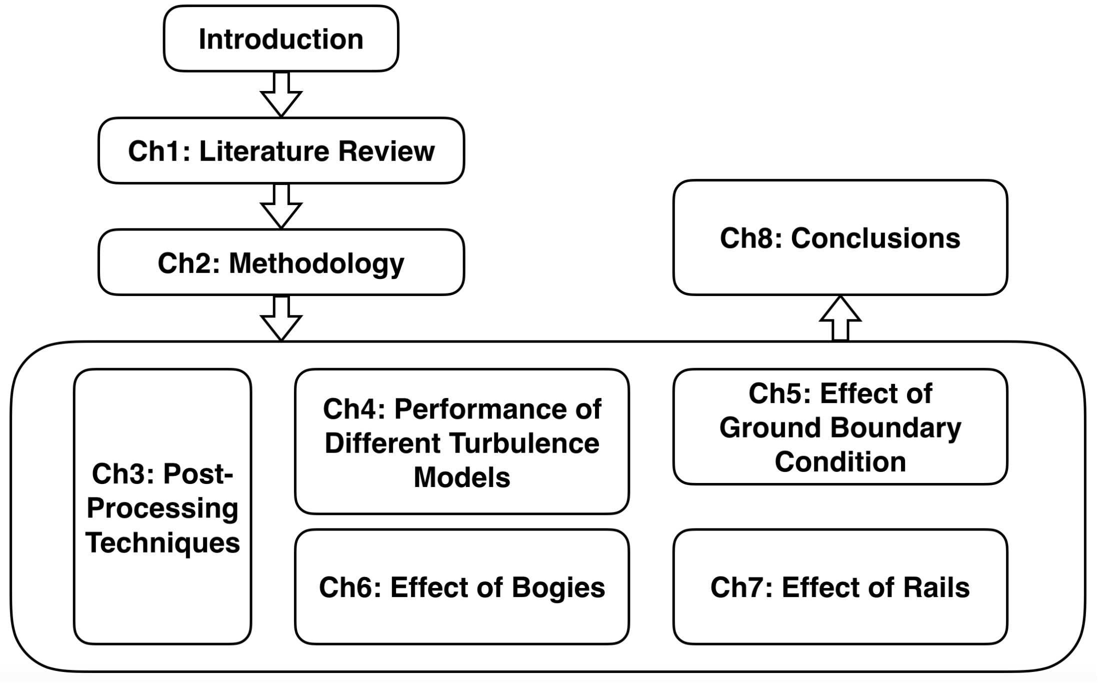

Figure II: The schematic of the structure of this thesis report.

Chapter 1: Literature Review Starts with an overview of the current HST industry and its development, and the problems and issues associated with the development of HST aerodynamics research are highlighted. A comprehensive literature review summaries the efforts that have been channelled into understanding HST aerodynamics and the progress made on improving the aerodynamic performance of HSTs. From reviewing the previous studies, the research gaps are identified, and the scope of current project is specified.

Chapter 2: Methodology Details the numerical simulation methodology for the individual studies, including: the geometry, computational domain, boundary conditions, grid description, solver settings and turbulence models. A mesh independence test and timestep sensitivity test are undertaken by comparing with the wind-tunnel experimental data, for examining the validity of the numerical method. Additionally, an uncertainty analysis is presented to identify the potential sources of error.

Chapter 3: Post-Processing Techniques Introduces the common post-processing techniques for this project, including gust analysis, conditional phase-averaging and cross-correlation, and proper orthogonal decomposition. Gust analysis is used to artificially replicate the field measurements of full-scale testing to obtain an ensemble average of the temporal slipstream data under the TSI specifications (TSI 2014). Conditional phase-averaging is always integrated with cross-correlation for identifying the spanwise oscillation of the wake structure. Proper Orthogonal Decomposition (POD) is utilised to extract the dominant dynamic flow structures from a turbulence flow field. The detailed procedures underlying the techniques and the corresponding algorithms are presented in this chapter.

Chapter 4: Performance of Different Turbulence Models Evaluates the performance of three widely-used turbulence models: URANS, SAS and DES, to predict slipstream of a full-featured generic train model, and the results are compared with wind-tunnel experiments to determine the fidelity of the models. Specifically, this study aims to determine the suitability of different turbulence modelling approaches, involving significantly different computational resources, for modelling different aspects of slipstream.

Chapter 5: Effect of the Ground Boundary Condition Investigates the effect of relative ground motion on a HST slipstream based on three ground/wheel configurations: a stationary ground with stationary wheels, a moving ground with stationary wheels, and a moving ground with rotating wheels. These configurations are relative to the train frame-of-reference. The effects of ground-motion on slipstream assessment are determined based on unsteady statistics and gust analysis. Additionally, the mechanism of how the ground motion influences slipstream is revealed by analysing the interaction between train induced flow structure and the ground boundary layer. The ground-motion effect on the time-averaged flow structure and wake dynamics is determined and analysed. Specifically, this study identifies two ways that the ground boundary layer interferes with the slipstream measurement: direct introduction of the high slipstream velocity region due to ground boundary layer development, and indirect widening of the wake structure by deformation of the trailing vortices. The altered aerodynamic loading on a HST due to ground motion is visualised through the train surface-pressure distribution, and the resultant impact on drag and lift forces is determined. For wheel rotation it is concluded as that its effect is mainly restricted to be within the bogie regions, with no significant influence on the wake structure.

Chapter 6: Effect of Bogies Studies the effect of bogies on HST slipstream characteristics based on two generic train configurations: a *Simplified Train Model* with the bogies covered by a flat surface, and a *Full-featured Train Model* with simplified bogie-sets. A thorough investigation of the bogie effects on HST slipstream characteristics is achieved by systematically comparing the flow structures, slipstream assessments and aerodynamics between the two configurations. Remarkably, this study discovers that the generation and stability of the spanwise oscillation of the wake is correlated to the formation of the pair of counter-rotating vortices behind the tail, instead of the presence of bogies. Specifically, the wake's spanwise motion is representative of an inherent instability of a trailing vortex pair, and the bogies may only influence this flow feature through altering the near-wake turbulence level and the strength of the trailing vortices. Apart from that, how the alteration to the flow structures further affects slipstream is again studied according to statistical and gust analyses, and the influences on the aerodynamic loading are determined by comparing the train surface-pressure distributions between the two models.

Chapter 7: Effect of Rails Analyses the effect of rails on the HST slipstream characteristics by systematically comparing the flow features of two geometric configurations: *No Rails* and *With Rails.* The train model is identical in both configurations, with the only difference is whether rails are included. This is particularly relevant, given experimental testing often omits the rails. The aim of this study is to understand the potential effects of the rails on HST slipstream characteristics, and discover the underlying mechanism of how the rails interfere with the flow structures. Furthermore, how the altered flow further affects slipstream is another main interest of this study.

Chapter 8: Conclusions Summarises the key results and contributions of this program, and suggests possibilities for further research beyond its scope.

Appendices Includes the relevant regulations (Appendix A) and manuscripts published during the PhD candidature (Appendix B).

Chapter 1

Literature Review

1.1 Slipstream and General Flow Structures

Slipstream, i.e., the air movement induced by a high-speed train (HST) as it passes, is a safety hazard to commuters and trackside workers, and can even cause damage to infrastructure along track lines. The slipstream is a combined effect of multiple flow features: the head pressure pulse, boundary layer development along the train body, flow under the bogies and the wake behind the train. The strength of slipstream is quantified by the *slipstream velocity* ($U_{slipstream}$) according to the European Guidelines (CEN 2013). In full-scale testings, slipstream velocity is measured in a ground-fixed (GF) stationary reference frame, while CFD simulations are based on the train-fixed (TF) reference frame, hence a change of frame is required. The *slipstream velocity* ($U_{slipstream}$) is defined by

$$U_{slipstream} = \sqrt{\left(U_{GF}^2 + V_{GF}^2\right)}, \tag{1.1}$$

where

$$U_{GF} = U_{\infty} - U_{TF}, V_{GF} = V_{TF}. \tag{1.2}$$

In Equations 1.1 and 1.2, the subscripts *GF* and *TF* indicate *ground-fixed* and *train-fixed* reference frames, respectively. Velocities, including slipstream velocities, quoted in this project are typically normalised by the freestream velocity (U_{∞}). Also note that slipstream is only based on the downstream (U) and transverse (V) components of the velocity. The vertical velocity component is ignored. According to the TSI specifications (TSI 2014), $U_{slipstream}$ is measured at 3 m away from the centreplane and at two different heights (trackside height and platform height) above the top of the rails (TOR). The trackside and platform heights are 0.2 m ($z = 0.05H$) and 1.4 m ($z = 0.35H$) above the TOR, respectively.

Slipstream is a function of train cross-sectional area, total length, nose/tail shape, surface roughness, speed and environmental conditions (Raghunathan *et al.* 2002). The primary concern of slipstream is in regard to safety hazards to passengers waiting on platforms and trackside workers, while as a secondary concern, it may also lead to damage of the surrounding infrastructure around the railway lines. Slipstream causes a sudden change in wind speed close to the train, possibly destabilising people next to it. The force exerted on a body depends on its orientation and cross-sectional area, while if we take the human response into consideration, this destabilisation may vary with age and gender (Jordan *et al.* 2008) (Jordan *et al.* 2009) (Penwarden *et al.* 1978). Due to the safety hazards associated with slipstream, related regulations are enforced worldwide.

This project employs the European regulations which are promulgated by the European Committee for Standardisation (CEN). CEN provides guidelines on how the slipstream velocity should be measured and limitations of maximum allowable slipstream velocity, which the train manufacturers have to comply. The *Technical Specifications for Interoperability* (TSI) interprets the regulations specified in CEN, and provides specified annotations and requirements that HSTs have to meet to operate in the European Union. The relevant clauses to this project are presented in Appendix A.

The key to analysing slipstream is to understand the flow structures around HSTs. However, compared with conventional aircrafts and ground vehicles, high-speed trains have the following distinct features: significantly larger length-to-height ratios, and proximity to the ground with a much higher cruising speed. Because of these, the existing knowledge of neither vehicle aerodynamics nor aircraft aerodynamics can be directly applied to understand the train aerodynamics. The distinct features bring challenges for both experimental investigations and numerical simulations. The interrelation between the flow structures and the slipstream velocity at the TSI specified measurement (TSI 2014) lines is visualised in Fig. 1.1.

According to a previous study (Baker 2010), the flow around a high-speed train can be divided into three regions: the nose region around the front of the train, the boundary layer region along the length of the train, and the wake region behind the train. A brief description of the flow features within each region is presented below, followed by a more detailed review of the literature related to the individual studies.

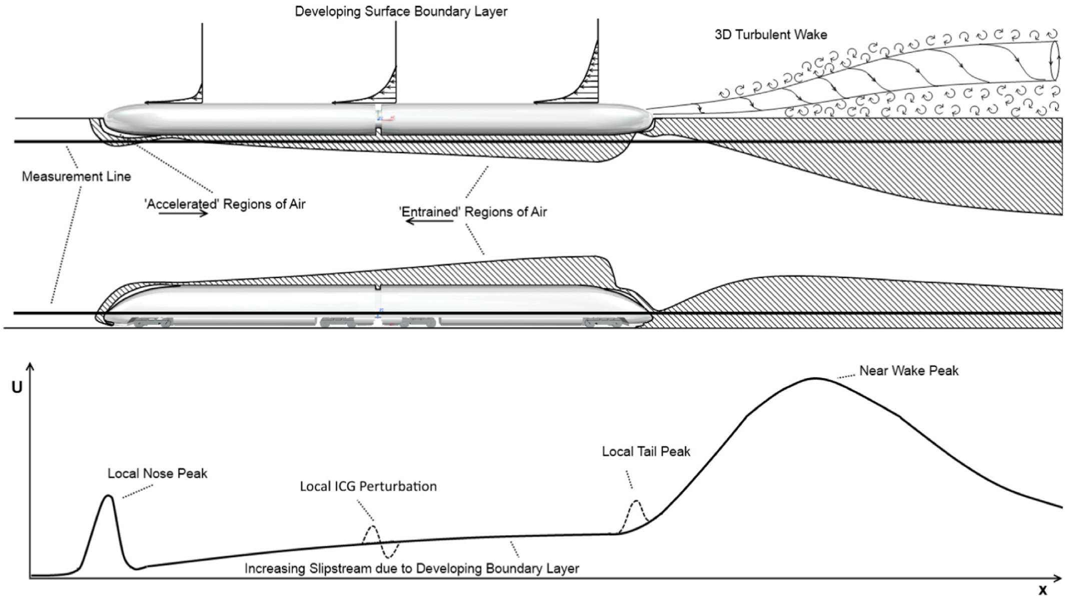

FIGURE 1.1: The inter-relation between the slipstream profile and the flow structure around a high-speed train (Bell *et al.* 2014b).

1.1.1 Nose Region

As shown in Fig. 1.1, there is a local peak in the slipstream velocity near the head of the train as it passes. This peak slipstream velocity is generated due to flow acceleration around the head. Specifically, according to the experimental measurements based on various train models, Europe-sponsored *AeroTRAIN project* concluded that the nose peak is primarily caused by lateral flow variations, with the longitudinal flows exhibiting reverse flows (Baker *et al.* 2014a). Generally, the magnitude of slipstream velocity is dominated by the longitudinal velocity components. However, within this region the flow acceleration in the lateral direction is significant, and it extensively contributes to the overall slipstream velocity. This phenomenon has been captured in the full-scale tests on various train models (Baker *et al.* 2014a), and can be clearly identified from the statistical slipstream profiles which are presented later in § 5 $\sim$ 7. Additionally, the longitudinal reverse flow was difficult to distinguish in physical experiments in the past, due to the limitation of conventional instruments, such as hot wires and 4-hole cobra probes (Hemida *et al.* 2014). Recently, by adopting ultra-sonic anemometers, *AeroTRAIN* (Baker *et al.* 2014a) successfully captured this reverse flow. This head pressure pulse is important in terms of the aerodynamic loading on trackside infrastructure.

1.1.2 Boundary Layer Region

The long boundary layer region, due to the large length-to-height ratio (L/H), is a significant feature distinguishing train aerodynamics from road vehicle aerodynamics. Simulating the long boundary-layer region and studying the length effect on the wake structure is one of the difficulties in computationally modelling a real train. Experimentally, a facility imposes strict limitations on the size of the model. Numerically, solving a full length-scale train requires an extremely large domain, which makes it very computationally demanding, especially for transient simulations. For a typical high-speed train, the L/H ratio is about 50 to 100. In previous length-effect studies, the L/H ratio of the model trains were all well below this range. For example, Bell *et al.* (2014a) studied L/H ratio up to 14 based on wind-tunnel experiments, and Muld *et al.* (2014) pushed the L/H ratio to about 28 using a numerical simulation of a train with 4 carriages. Muld *et al.* (2014) showed that different length configurations have little effect on the overall wake structure, but they influence wake frequencies and length scales significantly. Efforts have been made to study train aerodynamics with a more realistic L/H ratio. Pii *et al.* (2014) firstly solved the full length-scale train at full speed based on the transient Lattice Boltzmann technique. Results showing boundary layer development on the side of the train are presented in Fig. 1.2. The results agree well with measurements from the moving model rig experiment of Baker *et al.* (2001) and wind tunnel test of Paradot *et al.* (2002) that shows the boundary layer reaches semi-equilibrium along the first carriage, and then grows gradually along the rest of the train.

The main source of aerodynamic drag for a road vehicle is the pressure difference between the head and rear, while for a high-speed train, the main drag comes from the friction drag along the train body. Using the Japanese Shinkansen high-speed train (0 series) of 16 carriages as an example, about 90% of the aerodynamic drag comes from the friction drag on the middle part of the train (Raghunathan *et al.* 2002). The effect of the structures along the body, such as bogies (Mancini *et al.* 2001), pantographs (Ambrósio *et al.* 2012) and inter-carriage gaps (Mizushima *et al.* 2007), on the train aerodynamics has been extensively studied, especially with the respect to shape optimisation and drag reduction. Additionally, the train underbody flow within this region is another important flow feature, and it has been extensively studied from the perspectives of drag reduction and ballast flight. This flow feature is strongly correlated to the train

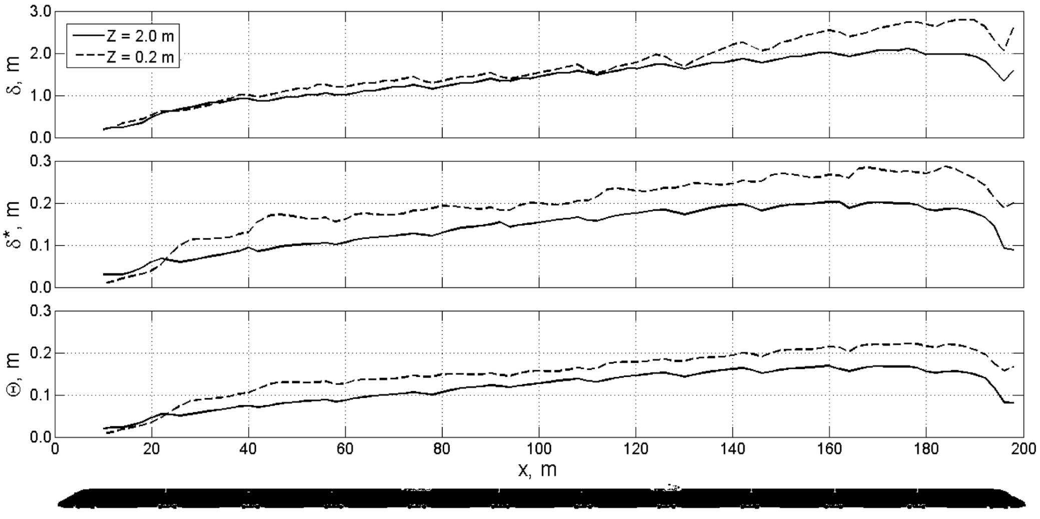

FIGURE 1.2: Boundary layer thickness, displacement thickness and momentum thickness along the side of the train at 0.2 and 2 m (Pii *et al.* 2014).

bogies, and more details regarding this is presented in § 1.4.

1.1.3 Wake Region

The wake region is the most important region for slipstream assessment, as the peak slipstream velocity occurs within it. This is the situation for HSTs such as the ICE3, but it is not always true for all train types such as freight trains. For example, Baker *et al.* (2014b) found that the maximum gusts around a freight train are typically measured at the front of the locomotive or in the vicinity of the inter-carriage gaps, based on the field measurements of a wide range of train models. The defining flow feature of a train wake is that the entire wake region is feed by the thick boundary layer developed over the train body. As a result, high-speed trains have much thicker separating shear layers (Baker 2010). Baker (2010) indicated that the train wake structure is a combination of shear layer separations, longitudinal helical flows, vortex streets and a separation cavity. The wake topology was resolved by Bell *et al.* (2016b) by showing that the dominant wake structure is a pair of counter-rotating vortices peeling from the train pillars, and it demonstrates a periodic oscillation in both the vertical and transverse direction, as shown in Fig. 1.3.

This longitudinal vortex pair is also identified in other analogous flows, for example, ground vehicles (Vino *et al.* 2005) and delta-wings (Délery 2001), as shown in Fig. 1.4. However the underlying mechanism of the unsteady characteristics is distinct for differ-

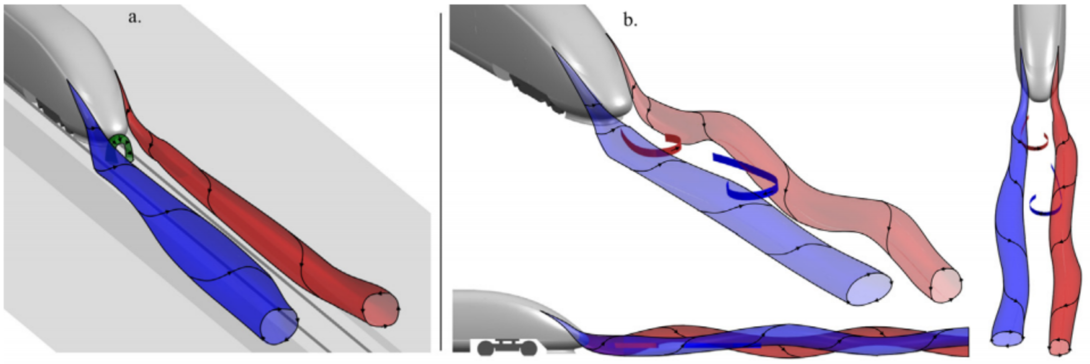

FIGURE 1.3: Schematics of the unsteady vortical structure behind the tail (Bell *et al.* 2016a).

ent flows. For vehicle aerodynamics, a much stronger separation region is determined behind the body, and the wake is predominantly energised by the alternating vortex shedding from the shear-layer roll up, which is commonly known as von Karman shedding (Vino *et al.* 2005). The trailing vortices generated by a Delta wing at a high angle of attack exhibit the *Crow instability* which is caused by the amplification of a particular wavelength perturbation through self and mutual induction, under the influence of vertical von Karman shedding (Bell 2015).

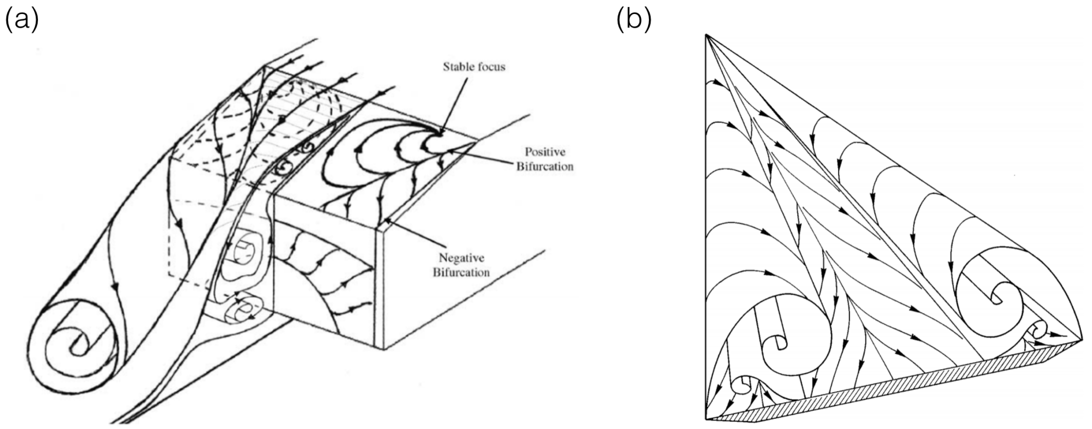

FIGURE 1.4: Schematics of longitudinal vortices identified in: (a) Ahmed body (Vino *et al.* 2005), (b) delta-wing at a large angle of attack (Délery 2001).

For HSTs, the trailing vortices formed at the tail pillars are the coherent wake structure, as illustrated by the total pressure iso-surface and velocity slices in Fig. 1.5. Dynamically, the spanwise oscillation of the wake structure was indicated in many studies through different techniques, including numerical simulations (Schulte-Werning *et al.* 2003) (Muld *et al.* 2012a) and physical experiments (Bell *et al.* 2016a) (Bell *et al.* 2016b). This oscillation can be visualised by the skin friction patterns, as shown in

Fig. 1.6; and typical Strouhal number of this oscillation is about 0.11 to 0.14 (Schulte-Werning *et al.* 2003). Additionally, this major wake oscillation (Karman vortices) causes a lateral vibration on the train, especially on the rear carriage (Raghunathan *et al.* 2002). This effect is known as *Last Car Oscillation*, and it causes discomfort to the passengers in the rear coach (Schulte-Werning *et al.* 2003).

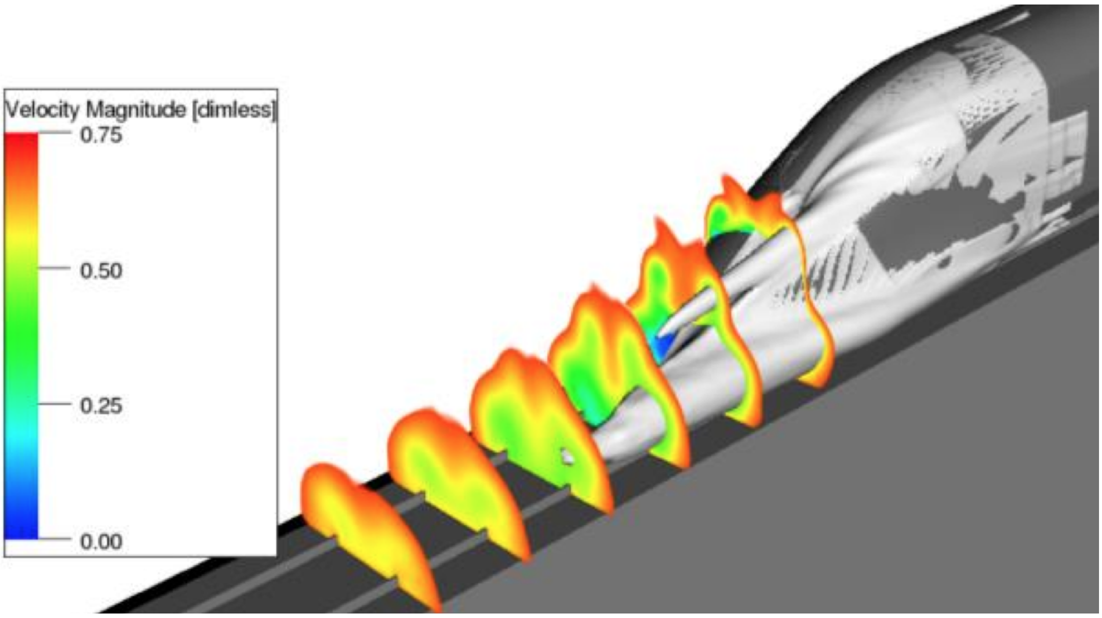

FIGURE 1.5: Typical time-averaged train wake structure, visualised by the isosurface of total pressure coefficient of 0.25 and velocity magnitude slices (Pii *et al.* 2014).

However the mechanism triggering this oscillation remains indefinite with two available hypotheses. Pii *et al.* (2014) proposed that the spanwise oscillation of the wake structure is caused by perturbation from the bogies, while Bell *et al.* (2016a) suggested that the periodic vortex shedding from the tail might be another possibility.

The flow characteristics of the wake region depend on two parameters: the upstream flow conditions and the shape of the tail. The upstream flow condition is determined by the flow development along the train body, including the thick boundary layer developed over the train body and the strong turbulent perturbations introduced by the bogies. A study on the shape of the tail found that the geometry of tail has little effect on the drag, but it significantly affects the slipstream characteristics (Schetz 2001). Bell *et al.* (2017) further studied the effects of the tail geometry on slipstream characteristics by varying the tail roof angles, and the results showed that an increasing tail roof angle leads to a transition from an unsteady wake with a pair of streamwise vortices to a large-scale separation dominated flow structure.

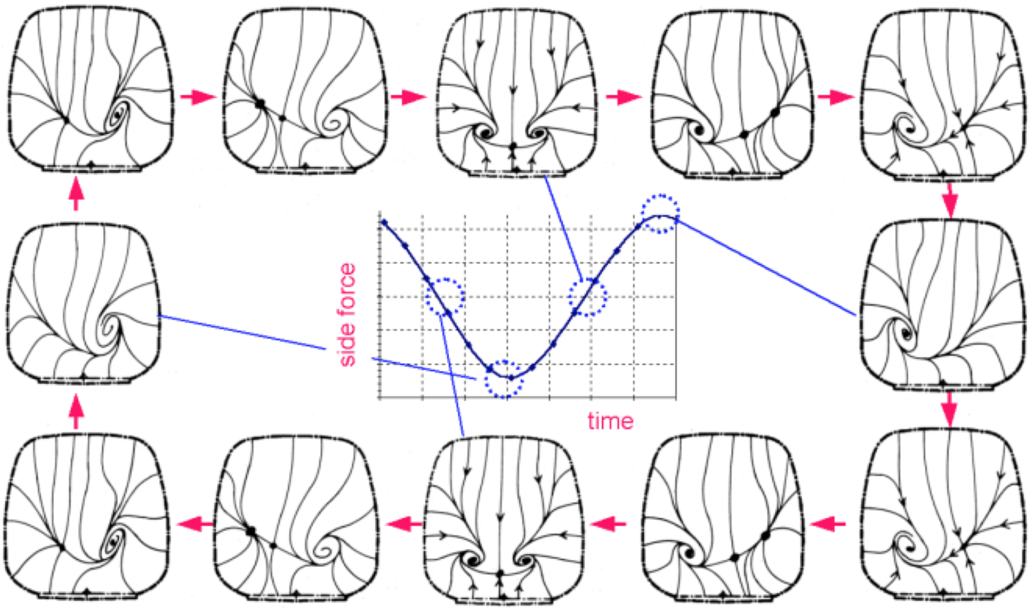

FIGURE 1.6: The oscillation of the wake structure visualised by the skin friction pattern (Schulte-Werning *et al.* 2003).

1.2 Research Methods

1.2.1 Full-scale Tests

Full-scale tests represent the most realistic operational conditions, without any scaling or simplifications; however, the testing is subject to the surrounding environment condition. A typical set-up of a full-scale test is shown in the Fig. 1.7 below. In order to accurately obtain the field data, the TSI enforces strict requirements for taking the measurements, for example, limits on allowable ambient wind speed, minimum number of valid runs and the instrument requirements (TSI 2014). Full-scale tests are generally very expensive and time consuming. Additionally, it is difficult to conduct a precise investigation based on full-scale tests, as variability of environmental conditions can cause substantial noise in the measurements. For example, obtaining a detailed wake topology from the full-scale testing based on the current available measurement instruments is nearly impossible.

1.2.2 Reduced-scale Experiments

Compared with the full-scale tests, reduced-scale tests are preformed earlier in the train design process helping to analyse aerodynamic performance at a much earlier stage. The two common reduced-scale tests are moving-model rig tests and wind-tunnel experiments, and the typical set-up for these two techniques are presented in

Figure 1.7: An example of full-scale set-up to measure the slipstream velocity at trackside (left) and on a platform (right) (Sterling *et al.* 2008).

Fig. 1.8.

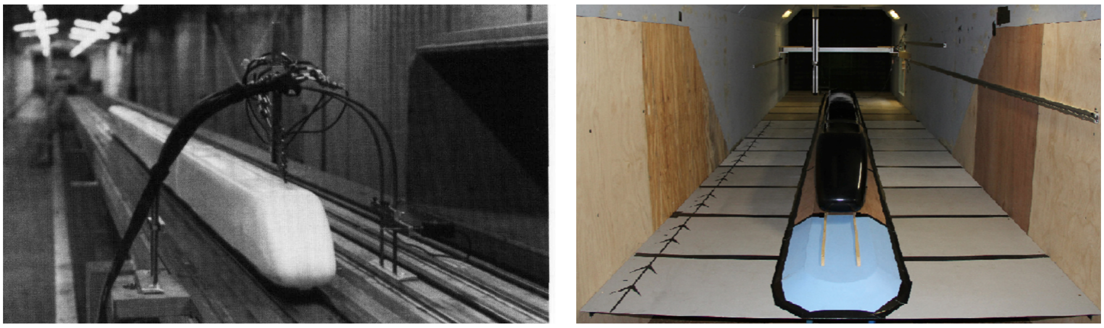

Figure 1.8: Typical set-up for moving model rig test (left) (Baker *et al.* 2001) and wind tunnel experiment (right) (Bell *et al.* 2014b).

Moving model tests use a similar measurement technique to full-scale tests. They measure the slipstream velocity next to the track based on a fixed frame-of-reference. Compared with wind-tunnel experiments, moving-model rig tests can easily obtain a realistic ground configuration. However moving model testing is also very expensive based on the specialised facility cost, and it is also very time consuming. Gil *et al.* (2010) showed a typical testing frequency is about 8-10 runs per day. In order to improve the efficiency, the concept of a rotating rail rig was proposed, which can provide approximately 80 laps per 1 min (Gil *et al.* 2010). The set-up of the rotating rig is presented in Fig. 1.9. However, this approach was later proven to be inaccurate as the tight rotation introduced a significant asymmetrical effect on the slipstream (Hemida *et al.* 2010).

In wind-tunnel experiments, the train is fixed and the air is moving; as a result, the reference frame of the train is used instead. With this approach, wind-tunnel experiments can easily obtain a time-averaged flow result, which is almost impossible

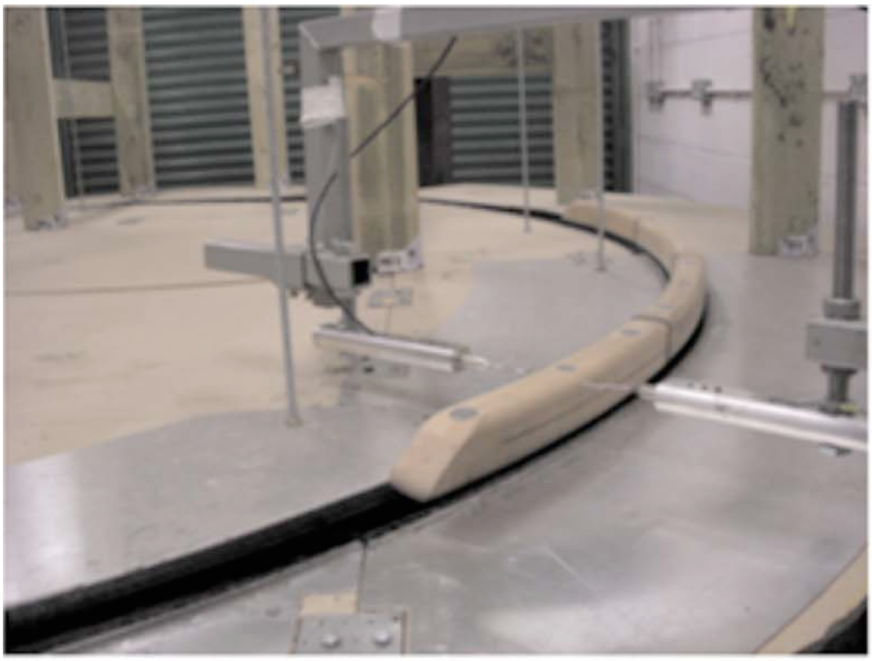

Figure 1.9: The set-up of rotating rail rig test for slipstream measurements (Gil *et al.* 2010).

for full-scale and difficult for moving-model rig tests. One of the main challenges for wind-tunnel experiments is the incorrect treatment of the ground, as the propagation of the counter-rotating vortices behind a train may be affected by whether the ground is fixed or moving relative to the train. In wind-tunnel experiments, without a moving belt, the unrealistic relative motion between the moving air and stationary ground generates an extra shear stress that affects flow structure development. Thus, the artificial boundary layer at the ground of the wind tunnel affects the direct applicability of the measurements. Similar effects have been studied for road vehicles (*Ahmed Body*), and the results show the wake structure is relatively insensitive to floor movement, but transient properties, such as shedding frequency, are found to be dependent on whether the floor is moving (Krajnović & Davidson 2005). However, the findings from the vehicles cannot be directly applied to the train aerodynamics, because trains and road vehicles have distinct wake structures. Therefore, the effect of the different ground representations on train slipstream characteristics still remains largely unexplored, and more discussion on this is presented in § 1.3.

1.2.3 Numerical Simulations

Applying numerical methods to resolve and analyse the aerodynamic characteristics of a HST can be dated back to decades ago, and it has witnessed remarkably advancement more recently due to the development of, and accessed to increased computing power and improvements to turbulence modelling.

Prior to 1990s, the numerical predictions around high-speed trains were conducted based on the panel method, which assumes that the flow is inviscid. Without taking any viscosity effects into account, Copley (1987) applied a 3-dimensional panel method for predicting the pressure distribution on a simplified train body with cross-wind at an incident angle of 25 degrees. The comparisons of circumferential pressure coefficient between the panel method and wind tunnel experiment at 0.75 and 9.5 body diameters from the nose are presented in Fig. 1.10 (a) and (b) respectively. The results showed that the panel method achieves a good agreement with the experimental data near the train nose when the flow is attached, and loses validity downstream due to its incapability of capturing the wake vortices (Copley 1987).

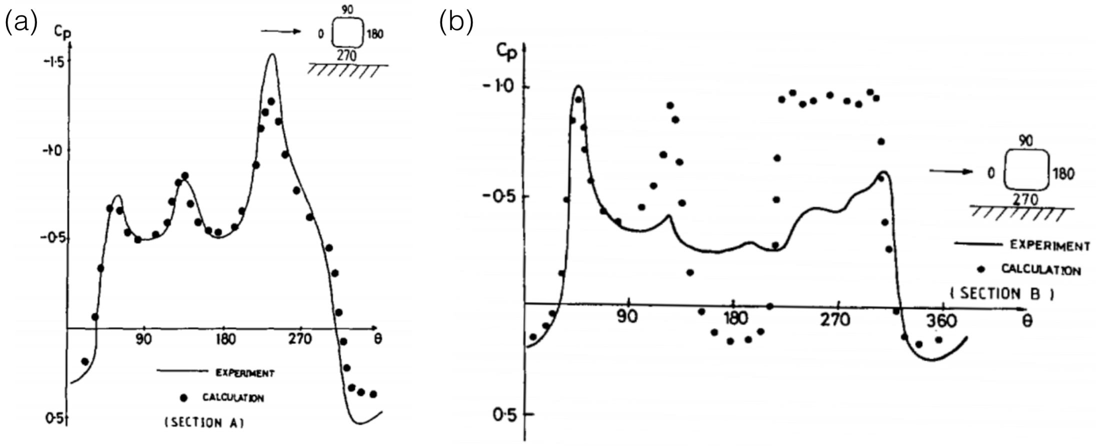

FIGURE 1.10: The comparison of circumferential pressure coefficient between the panel method and wind tunnel experiment at (a) 0.75 and (b) 9.5 body diameters from the nose (Copley 1987).

In 1992, Aita *et al.* (1992) applied the Reynolds-averaged Navier-Stokes equations on a French train model, and achieved a reasonably accurate time-averaged surface pressure prediction at the middle section, as shown in Fig. 1.11. This was a very first work of applying numerical simulation on a realistic train model, and the time-averaged flow field around the train was predicted by using only about 50,000 cell elements. Important flow features such as the flow separation at the tail were identified; and by comparing the velocity profiles at multiple locations around the tail, a good agreement was established with the wind tunnel results.

With further development in both numerical method and computing performance,

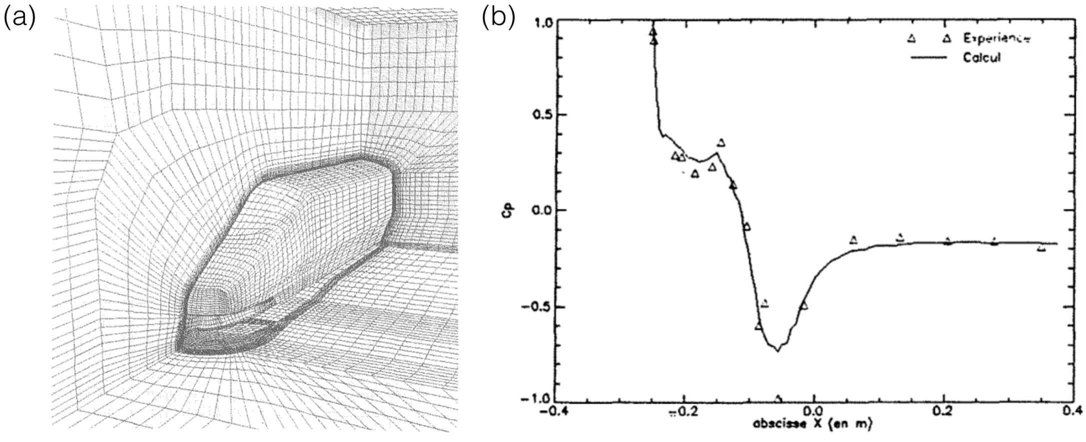

FIGURE 1.11: An early work of resolving the flow field around a realistic HST model with RANS approach: (a) mesh; (b) comparison of pressure coefficient at the middle section (Aita *et al.* 1992).

current CFD techniques have the capability in revealing rich flow physics, for instance, flow separation and reattachment, flow recirculation and time-dependent flow structures. RANS approach is still the most widely-used method for studying different flow structures, especially for industrial flows. RANS decomposes the Navier-Stokes equations by splitting the flow velocity into mean and fluctuating components, focusing on solving for the time- or ensemble-mean flow. Much effort has been channelled to optimise the RANS model, for example through the improvement of wall functions and development of more sophisticated turbulence models. For example, Schulte-Werning *et al.* (2001) utilised a standard $k - \epsilon$ turbulence model to predict the flow features around a modern HST. By comparing the flow pattern on the tail surface with the wind tunnel experiment, the RANS model showed that it was capable of accurately predicting dominant time-mean flow features such as the flow separation lines, as shown in Fig. 1.12.

Paradot *et al.* (2002) showed that RANS can achieve a good agreement with wind-tunnel experiments on time-averaged flow topology prediction and drag estimation, while in order to achieve a quantitatively accurate prediction in the complex areas, unsteady calculations are essential. By retaining the time-dependent terms, (U)RANS can be used to predict the large-scale dynamics for absolutely unstable flows. For example, Schulte-Werning *et al.* (2003) utilised URANS to predict the spanwise periodic vortex shedding from the tail of a train, as illustrated in Fig. 1.6.

With recent improvements in computing power, intermediate-scale flow turbulence

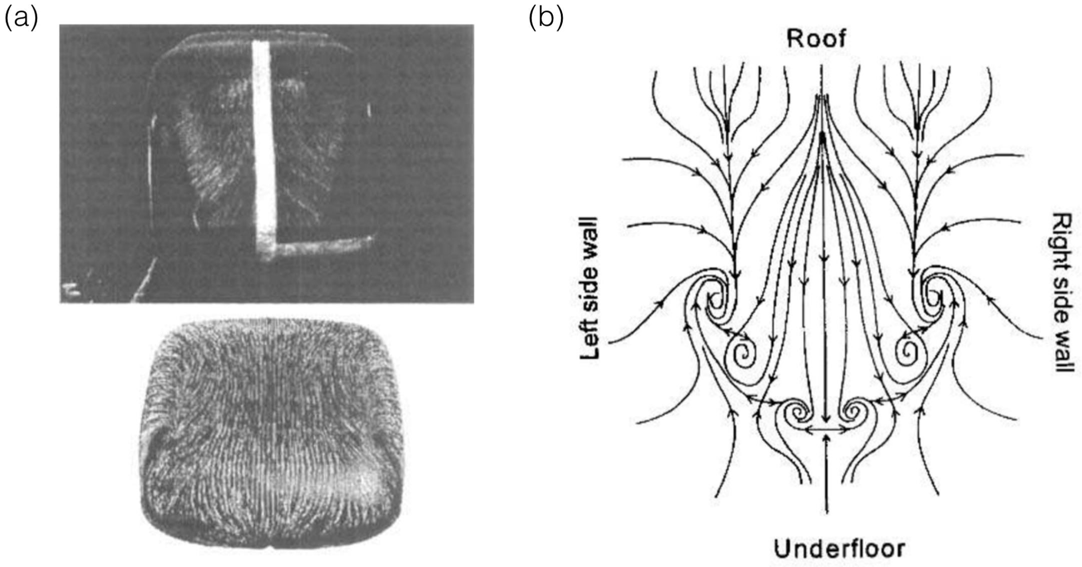

FIGURE 1.12: The comparison of the flow pattern on the tail between: (a) wind tunnel experiment; (b) RANS simulation (Schulte-Werning *et al.* 2001).

can be partially resolved, instead of the entirely modelled as in (U)RANS; and this numerical approach is known as *Scale-Resolving Simulation* (SRS). Common SRS approaches include *Large Eddy Simulation* (LES), *Detached Eddy Simulation* (DES) and *Scale Adaptive Simulation* (SAS).

Due to the high computational cost of *pure* LES at high Reynolds numbers, at this stage utilising LES to study HST aerodynamics is still prohibitive (Hemida *et al.* 2014). SAS modifies the classic URANS approach by incorporating the von Karman length scale. Interestingly, the modified model can capture the large temporal and spatial scales of the plain URANS approach, but by effectively automatically adjusting the turbulent length and time scales according to the selected spatial and temporal resolution, it can capture increasingly finer scales (Menter & Egorov 2010) (Egorov *et al.* 2010). It has been used as an alternative method to study complex industrial flows due to its balance between accuracy and cost. The fidelity of the SAS model has been verified on various engineering cases, such as bluff body aerodynamics (Egorov *et al.* 2010), aero-acoustics (Yang *et al.* 2014) and turbine machinery (Fossi *et al.* 2015). However, to the author's knowledge, SAS has not yet been applied to train aerodynamics. DES blends the LES and RANS approaches, utilising RANS to approximate the mean boundary layer behaviour and applying LES to capture the time-dependent flow away from wall boundaries. Therefore, the large to intermediate length-scale turbulence spectrum away from boundaries can be adequately resolved. DES has been widely used to study different aspects of train aerodynamics, such as wake instability (Muld *et al.* 2012a), slipstream assessment (Huang *et al.* 2016) and underbody flows (Zhang *et al.* 2016). Morden *et al.* (2015) compared RANS and DES predictions with wind tunnel measurement for predicting surface pressures upon a Class 43 High-Speed Train, and concluded that DES is superior in replicating the experimental results.

In overview, a model that captures more of the full range of flow structures is more computationally demanding. A detailed description of the turbulence models used in this project is presented in § 2.2, and the performance of each model in predicting the HST slipstream characteristics is included in § 4. Numerical simulation can predict a good approximation to aerodynamic performance at the very early development stage, which is valuable in design optimisation. Good practice is to conduct CFD simulations together with physical experiments. Specifically, CFD simulations can enhance an understanding of the flow field by providing a more detailed flow result, with physical experiments providing validation.

1.3 Effect of Ground Boundary Condition

Similar to vehicle aerodynamics, accurate modelling of the ground motion relative to a train is an important consideration. Currently, the most widely-used methods for studying HST aerodynamics are full-scale testing, moving-model testing, wind-tunnel experiments and numerical simulation. For physical experiments, full-scale and moving-model testing inherently employ a realistic ground boundary treatment, whilst in order to obtain an effective ground representation in a wind tunnel, some ground treatments are necessary to remove the unrealistic ground boundary layer growth. The commonly used ground simulation techniques in a wind tunnel are the image method, suction/blowing, lifted model and moving belt, as illustrated in Fig. 1.13.

Even though full-scale and moving-model testing utilise a more realistic stationary reference frame, the measurements are sensitive to environmental conditions, e.g., the ambient wind. Additionally, it is very difficult to undertake detailed measurements of the flow field around a moving model and to conduct unsteady statistical analyses, such as flow mapping of the mean or phase-averaged wake.

In contrast, wind-tunnel experiments adopt the vehicle reference frame, making it much easier to undertake measurements of the flow structure around the train model and in the wake. In general, it is both difficult and expensive to equip a wind tunnel

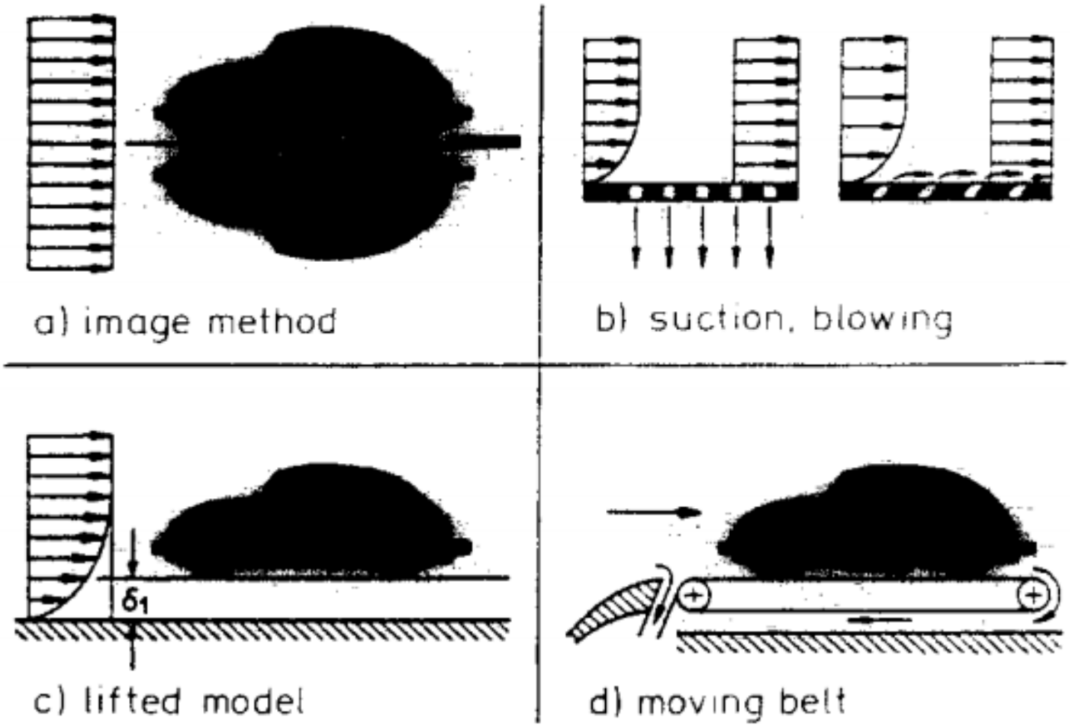

FIGURE 1.13: The commonly used ground simulation techniques in a wind tunnel: (a) image method, (b) suction/blowing, (c) lifted model and (d) moving belt (Fago *et al.* 1991).

with a moving floor for train aerodynamics research. Compared with conventional road vehicles, HSTs typically have a much larger length-to-height ratio, typically around 50 $\sim$ 100. Additionally, HSTs appear to have a longer coherent wake structure than road vehicles. For example, the region of interest for road vehicles is typically within 3 vehicle heights since drag is the primary consideration, while the region of interest for HST slipstream assessment can be up to 5 $\sim$ 10 train heights behind the tail because sideways wake movement/oscillation can have a strong effect on slipstream. As a consequence, even if a moving floor is implemented, a significantly longer moving-belt is required to represent the relative motion, not only along the long train but also in the extended wake region. Additionally, according to the CEN guidelines (CEN 2013), the aerodynamic performance of a HST needs to be studied not only on a flat ground configuration, but also on a ballast. The introduction of a moving ballast makes employing a moving-belt technique almost impossible for wind-tunnel experiments. A typical set-up for a wind tunnel experiment with the train located on a stationary ballast is illustrated in Fig. 1.8 (b). Therefore, understanding the potential differences that can be introduced by a stationary floor is essential.

Relative to HSTs, the effect of incorrect relative ground motion has been extensively studied for road vehicles. Because underbody flows contribute significantly to the aerodynamic drag of a modern car, and noting that ground motion can significantly alter the underbody flow; it is clear that correctly accounting for motion relative to the ground is critical for vehicle industries for drag estimation (Cogotti 1998). The influence of ground motion on the flow field is that, with a moving ground, the mass flux underneath the vehicle is increased in the streamwise direction and decreased in the spanwise direction, and this alters the aerodynamic loading on the underbody structure (Krajnović & Davidson 2005). However, the alteration to underbody dynamics does not provide a consistent trend on the aerodynamic loading. For example, Krajnović & Davidson (2005) reported that floor motion reduced drag by 8% and lift by 16% on a simplified car with a typical fastback geometry, while Burgin *et al.* (1986) found an increase in drag for flow past a bluff body with a moving ground. Both the consistency of the force difference and the effect on flow structures appears to vary from case to case. For instance, Sardou (1986) determined a significant alteration to the rear wake with/without ground motion, while Krajnović & Davidson (2005) found that the wake flow was relatively insensitive. The above differences, along with many other studies, indicate that although the general mechanism of ground motion is identical, the outcomes can be significantly altered by variation of the vehicle's geometry. Additionally, ground clearance (Fago *et al.* 1991) and Reynolds number (Sardou 1986) influence the effect of ground motion. The addition of rotating wheels has also been studied with ground motion, with Cogotti (1998) concluding that the best combination was for a moving ground with rotating wheels, and the second best choice was for a fixed ground with stationary wheels. This was because the effects of wheel rotation and a moving ground partly compensated each other, although not necessarily in a predictable way.

For future development of HSTs, a fuller understanding of the flow structure is becoming more important, and to achieve that an accurate ground boundary condition would seem important. If this is not possible, an understanding of the effects that can be caused by different ground motion configurations is essential. Some previous research has been channelled to investigate the effect of ground motion. Kwon *et al.* (2001) studied the performance of two ground simulation techniques: a moving-belt system and a tangential blowing system, based on a Korean HST. The results showed that a moving floor could increase the aerodynamic drag by approximate 15%, and this was explained to be the result of the increase of both friction and pressure drag.

Specifically, the alteration of the boundary-layer profile beneath the train increased the friction drag on the train underbody, and the pressure drag was increased due to the stronger vortical wake structures. Xia *et al.* (2017) compared the effect of a stationary and moving ground on the flow structure and aerodynamic loading on a Chinese HST (CRH3) on a flat ground configuration. An identical dominant wake structure was determined for both cases, while the moving ground case showed a narrower wake with slower vortex shedding, as compared to the one with a stationary ground. The effect of the ground boundary layer on the time-averaged wake structure is visualised by the slipstream velocity on multiple planes behind the tail, as shown in Fig. 1.14. Additionally, a significant variation to underbody pressure was identified due to the ground motion, which resulted in a large deviation for drag and lift prediction, and raising the train model could not effectively eliminate this variation.

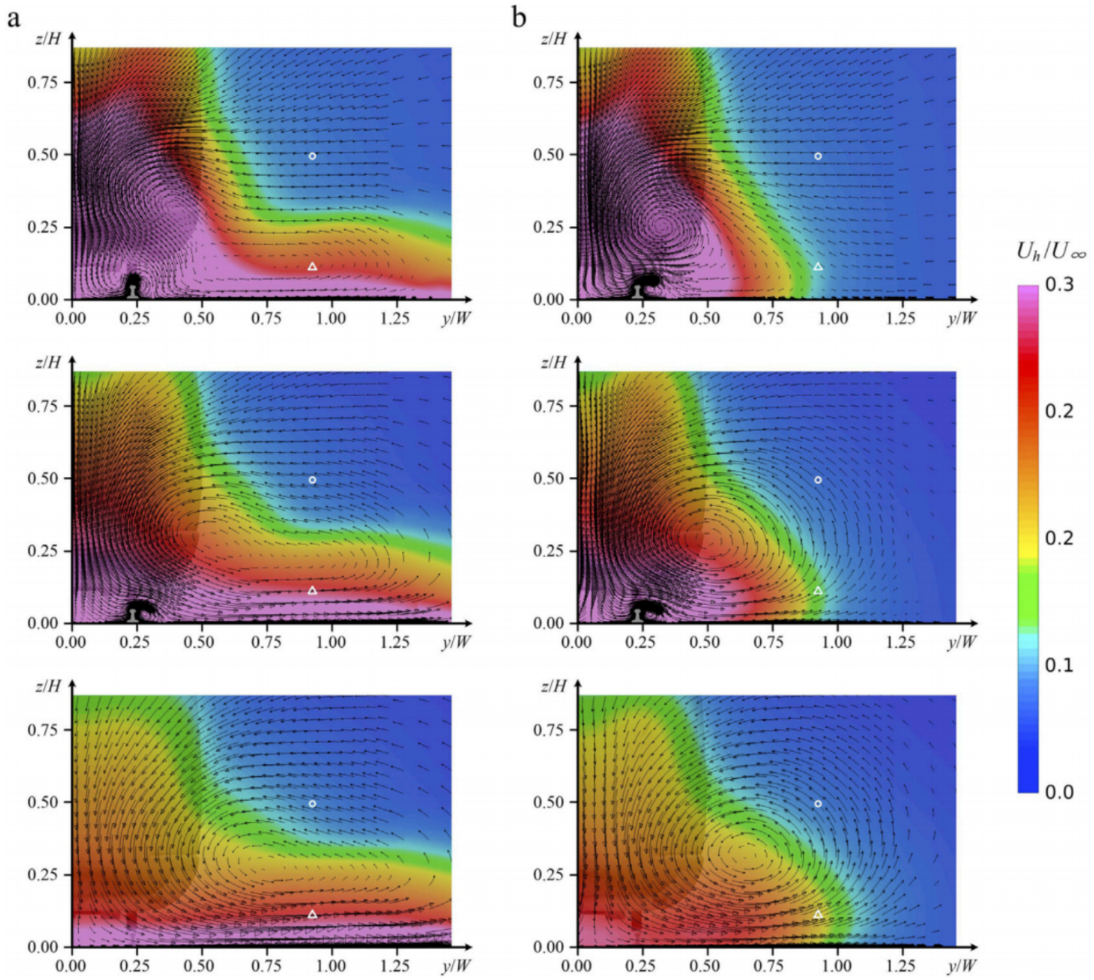

FIGURE 1.14: The comparison of the time-averaged train wake structure based on the slipstream velocity at 1, 3 and 5 train widths behind the tail (from top to bottom): (a) stationary ground, (b) moving ground (Xia *et al.* 2017).

Zhang *et al.* (2016) further examined the combination effect of the ground motion and wheel rotation on the underbody flow and aerodynamic loading. They found that the moving ground case showed a higher total drag on the train compared with a stationary ground; however, the application of rotating wheels did not show an identifiable further increase in drag. Additionally, the impact of rotating wheels was only exerted on the local pressure distribution within the bogie region, and showed an increase of the wheels' drag. Using a moving ground with rotating wheels was concluded as necessary, especially for studying the underbody flow of a HST.

1.4 Effect of Bogies

Research into investigating the aerodynamic characteristics of bogies has mainly been initiated for the following two reasons. Firstly, the bogies are a significant source of aerodynamic drag; thus, improving their aerodynamic performance is beneficial to energy efficiency. For example, for a streamlined HST travelling at cruising speed, aerodynamic resistance contributes to $75 \sim 80$ % of the total resistance, and $38 \sim 47$ % of that is caused by the bogies and associated interference drag (Raghunathan *et al.* 2002). Therefore, measures have been applied to optimise bogies for drag reduction. Mancini *et al.* (2001) showed that installing fairings on the existing bogies of an ETR 500 HST could reduce the drag by approximately 10%, and further reduction was expected by retrofitting the bogies. Secondly, the bogies can significantly alter the underbody flow, which is strongly correlated with the *ballast flight* phenomenon. The underbody flow can be characterised as a turbulent *Couette flow*, and García *et al.* (2011) have proposed an analytical solution for a simplified case. By studying a more realistic train model, Kaltenbach *et al.* (2008) reported that the ideal *Couette flow* could be regularly interrupted by the passing bogies and inter-carriage gaps. For example, the "funneling" of the flow into the rear of the first bogie cavity can introduce a strong secondary flow structure and further affect the downstream flow. As discovered by Kaltenbach *et al.* (2008), the underbody flow is strongly dependent on the geometry of the bogies; Jönsson *et al.* (2014) explicitly studied the bogie effect by comparing the underbody flow with and without bogies. The comparison concluded that the bogies significantly increased the velocity, velocity gradient and turbulence intensity of the underbody flow (Jönsson *et al.* 2014), as shown in Fig. 1.15.

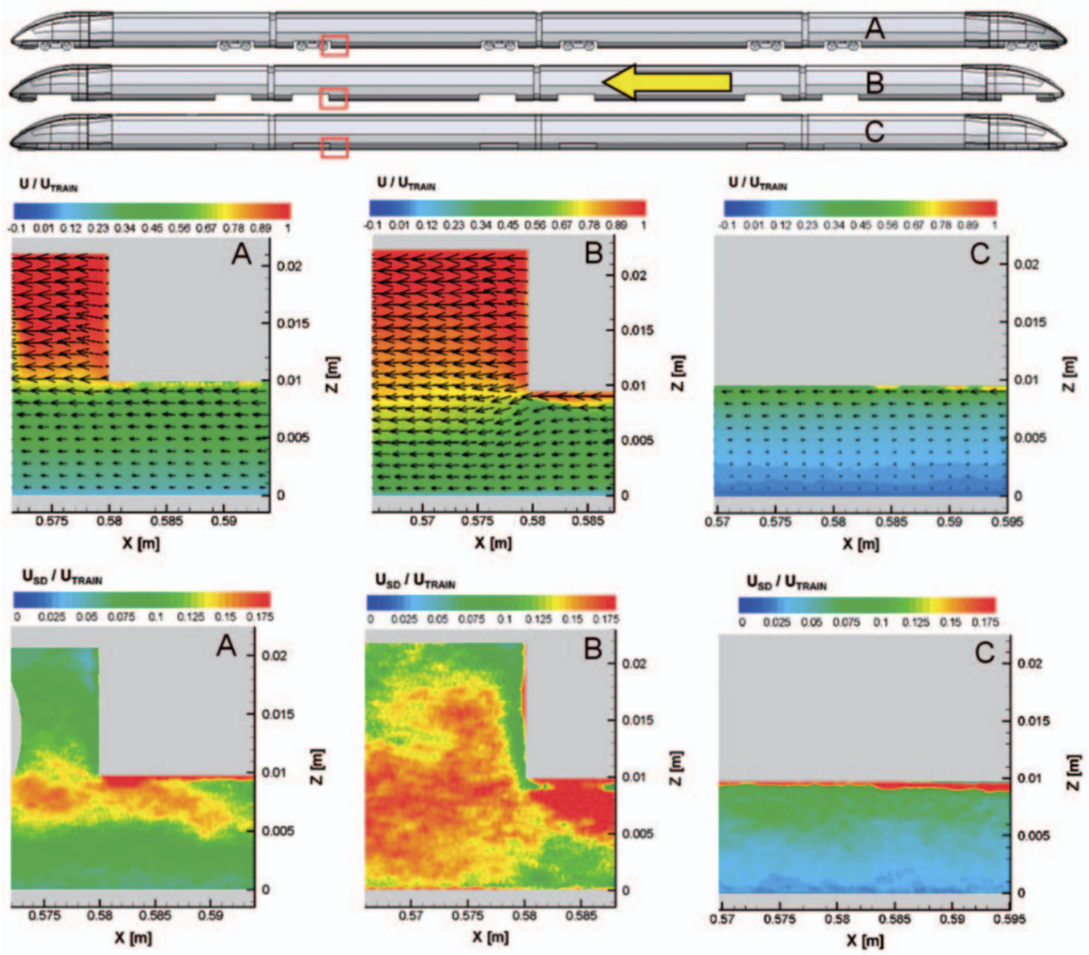

FIGURE 1.15: Comparison of the underbody flow conditions (upper row: time-averaged; lower row: standard derivation) between a (A) reference train,(B) rough train and (C) smooth train (Jönsson *et al.* 2014).

Ballast flight, where ballast particles become airborne during the passage of a train, was characterised as a combined effect of mechanical and aerodynamic loadings (Quinn *et al.* 2010). Therefore, fluid acceleration caused by the bogies could worsen the ballast flight phenomenon (Quinn *et al.* 2010). Additionally, the alteration to the underbody flow is also profound under crosswind conditions. Cooper (1981) determined that under cross-wind conditions, the bogies partially blocked the underbody flow and introduced a strong local pressure field, which resulted in a significant increase in the forces and moments. Copley (1987) further investigated the mechanisms affecting the aerodynamic loadings, and discovered that without the bogies, the vortical wake was like a three-dimensional *Karman Vortex Street*, with vortices being shed from successive points on both the roof and the under side of the train. However, when wheels were simulated, the vortices shed from the underside of the train were disrupted and reduced in strength, which increased the overall force components on the train (Copley 1987).

As can be seen from these two perspectives, the bogie effect has been investigated either for the aerodynamic loading exerted on the train surface for the purpose of drag reduction, or for the alteration to the local underbody flow field for the purpose of ballast flight analysis. In comparison, limited discussion has occurred on the bogie effects on a HST slipstream, and especially the wake structures. By studying the slipstream of a full-scale HST, Pii *et al.* (2014) identified the development of left-to-right pressure fluctuations along the train (shown in Fig. 1.16 (a)), which were caused by the presence of the bogies, and further inferred that the bogie-induced fluctuations trigger the wake's spanwise motion (shown in Fig. 1.16 (b)). From the correlation between the pressure fluctuation at the side surface of the tail and the wake's spanwise motion, Bell *et al.* (2016b) proposed that the origin of the spanwise motion can also be vortex shedding from the tail but the bogie-generated hypothesis cannot be ruled out.

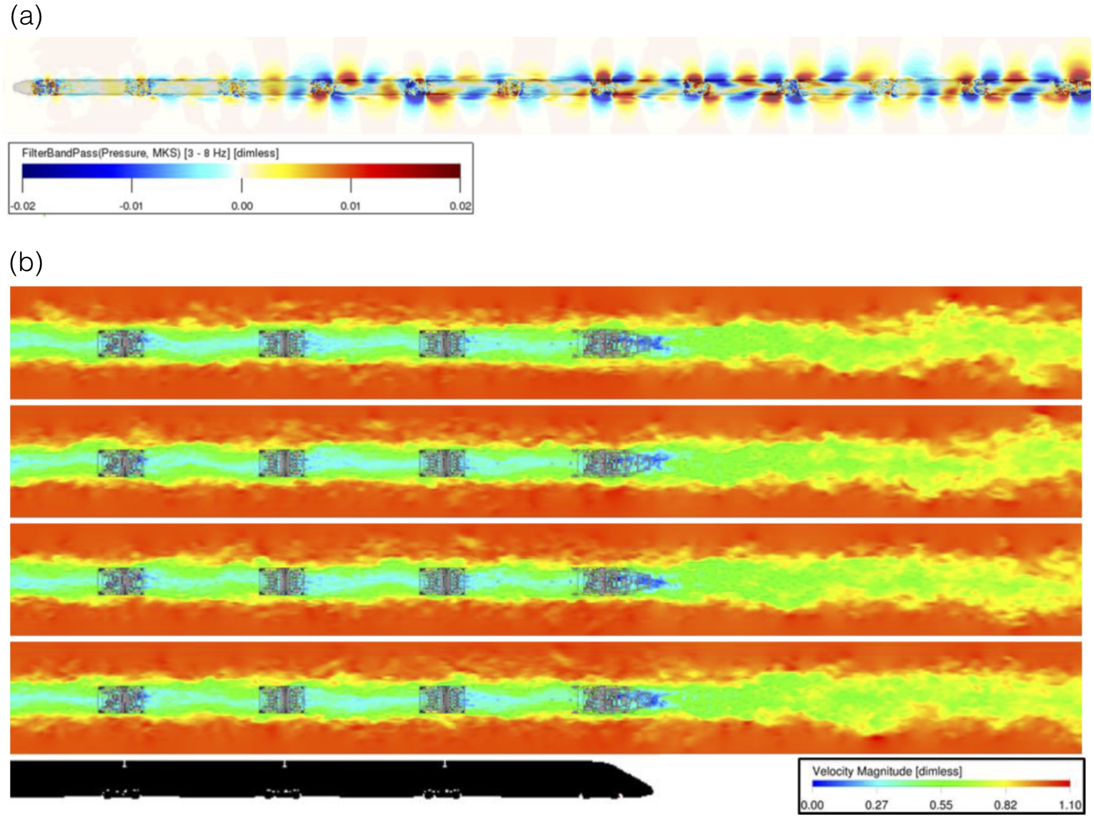

Figure 1.16: (a) The instantaneous pressure distribution around the bogies on the horizontal plane 0.2 m above the top of rail. (b) Wake oscillation visualised by velocity magnitude at four consecutive time instances: 0s, 0.125s, 0.025s, 0.0375s (from top to down) (Pii *et al.* 2014).

The spanwise oscillation of a HST wake has been identified as a typical HST slipstream characteristic, but its initiation is still not fully understood. Additionally, reviewing the methodologies for studying HST slipstream through computational analysis indicates that numerical set-ups, both with bogies (Muld *et al.* 2012a) (Yao *et al.* 2013) and without bogies (Östh *et al.* 2015) (Pereira & André 2013), have been adopted. Therefore, a study of the potential effects on the slipstream characteristics can be introduced by the bogies is critical to bridge the gap between the mentioned two numerical approaches.

1.5 Effect of Rails

Some research has been done to evaluate the HST aerodynamic performance with different ground configurations, for example, a viaduct and embankment (Cheli *et al.* 2010), flat ground and single track ballast (Bell *et al.* 2014b) and ground roughness (Jönsson *et al.* 2014). However, according to the author's knowledge, there is no explicit study on the effect of rails on the HST slipstream characteristics, or even from the general aerodynamic aspects. A potential reason is that rails are a permanent feature of the ground configuration, and not much in the way of modification can be done on this for improving HST aerodynamic performance. Therefore, little effort so far has been channeled to studying this phenomenon. According to the previous research, the pair of trailing vortices peeling from the tail pillars is the dominant flow structure within the wake, and the downwash from the tail pushes this flow structure towards the ground at the location where the rails are. Because of this interaction, the rails have a strong impact on the wake formation, even though its dimension is minor compared with the scale of the train. Modelling the rails can be difficult and expensive in both reduced-scale tests and numerical simulations. Additionally, by reviewing the previous studies on HST aerodynamics, both "with rail" and "without rail" approaches are indicated. However, the potential effects of the rails on the flow is not fully understood.

Additionally, the European Regulations on the inclusion of the rails were changed in the last few years. Comparing the CEN guidelines between 2011 (CEN 2011) and 2013 (CEN 2013), the requirement on the inclusion of rails has been changed. Specifically, CEN (2011) specifies a rail-included ground configuration, while in the 2013 specifications (CEN 2011), the rails were removed, as shown in Fig. 1.17. Please note that the two ballast configurations are designated for investigating the head pressure pulse, and no agreement has been achieved for numerically predicting HST slipstream in the CEN

Guidelines. Therefore, removal of the rails is not expected to significantly alter the head pressure pulse prediction; however, its impact on the slipstream remains undetermined.

In the following chapters these aspects will be explored using numerical modelling supported by and validated against experimental tests.

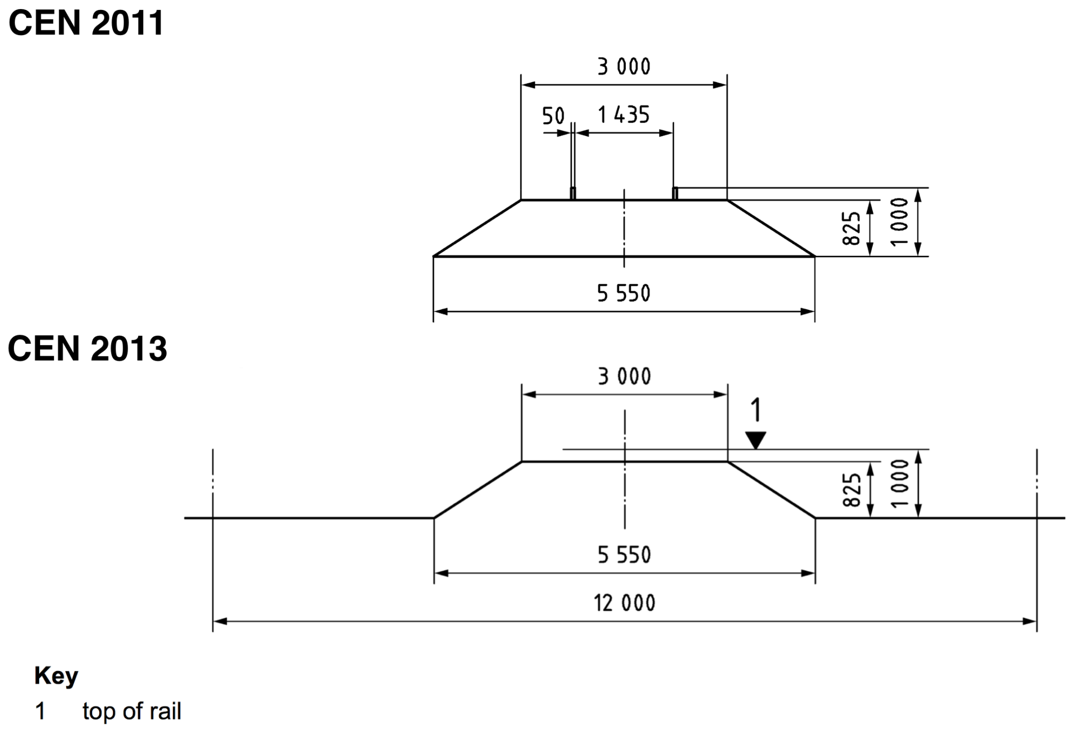
CEN 2011

CEN 2013

Figure 1.17: Illustration of the rule change on the inclusion of rails, based on the comparison of the ballast configurations specified in CEN (2011) and CEN (2013).

Chapter 2

Methodology

2.1 Geometry

The numerical train model utilised in this study is based on the 1/10 scale *Deutsche Bahn Inter-City-Express 3* (ICE3) high-speed train model, which is a widely operated train model in European and Asian countries. Examples of ICE3 HST in operation are presented in Fig. 2.1. ICE3 has a representative HST external shape, and its Computer-Aided Design (CAD) model is freely available from the DIN Standards Railway Committee (CAD 2014). Despite some specific features like a non-articulated architecture (e.g., more distributed motorised bogies), the generic external geometry makes ICE3 an ideal HST model for train slipstream investigation.

FIGURE 2.1: Full-scale operational ICE3 train (photo provided courtesy of Bombardier Transportation).

The ground modelling adapts the single track ballast configuration, which is specified in the CEN guidelines (CEN 2011) (CEN 2013). To achieve the primary aim of studying geometric effects on HST slipstream characteristics (i.e. the effects of bogies and rails), three train-ballast configurations are constructed:

- Configuration 1: flat-underbody train model (M1) & single track ballast with rails (WR)
- Configuration 2: full-featured train model (M2) & single track ballast without rails (NR)
- Configuration 3: full-featured train model (M2) & single track ballast with rails (WR)

In this study, these three geometric configurations are referred to as *Model 1 With Rails* (M1WR), *Model 2 No Rails* (M2NR) and *Model 2 With Rails* (M2WR) respectively, and the corresponding schematics are illustrated in Fig. 2.2. M2 is the reference numerical train geometry used in this project.

Compared with the full-scale train model (as shown in Fig. 2.1), the numerical train model (M2) is slightly geometrically simplified. Compared with the aspect ratio (length-to-height) of a realistic train, which is typically between 50 to 100, the length-width-height ratio of the CAD model is significantly reduced to 50:3:4. This is a typical limitation for studying train aerodynamics both numerically and experimentally. As introduced in § 1.1, the reduction of aspect ratio can alter the boundary layer development along the train, and further influence wake frequencies.

Although the model is simplified, omitting details such as the gaps between carriages and the air-conditioning units, it still includes key geometrical features that have a strong influence on the wake, and in particular, the bogies and snowploughs.

The flat-underbody train model (M1) is explicitly constructed to investigate the effect of bogies on train slipstream characteristics for Study 3 (presented in § 6). The ground clearance for all configurations is approximately 38 mm (in 1/10 scale), which is identical to the wind-tunnel model. The only difference between the flat-underbody model (M1) and full-featured train model (M2) is that the latter covers the bogie-sets with a flat surface, and all the other geometric features (i.e. the train overall dimension, inclusion of the snowplough and ground clearance) remain identical. The comparison of the underbody set up between the M1 and M2 models is illustrated in Fig. 2.3.

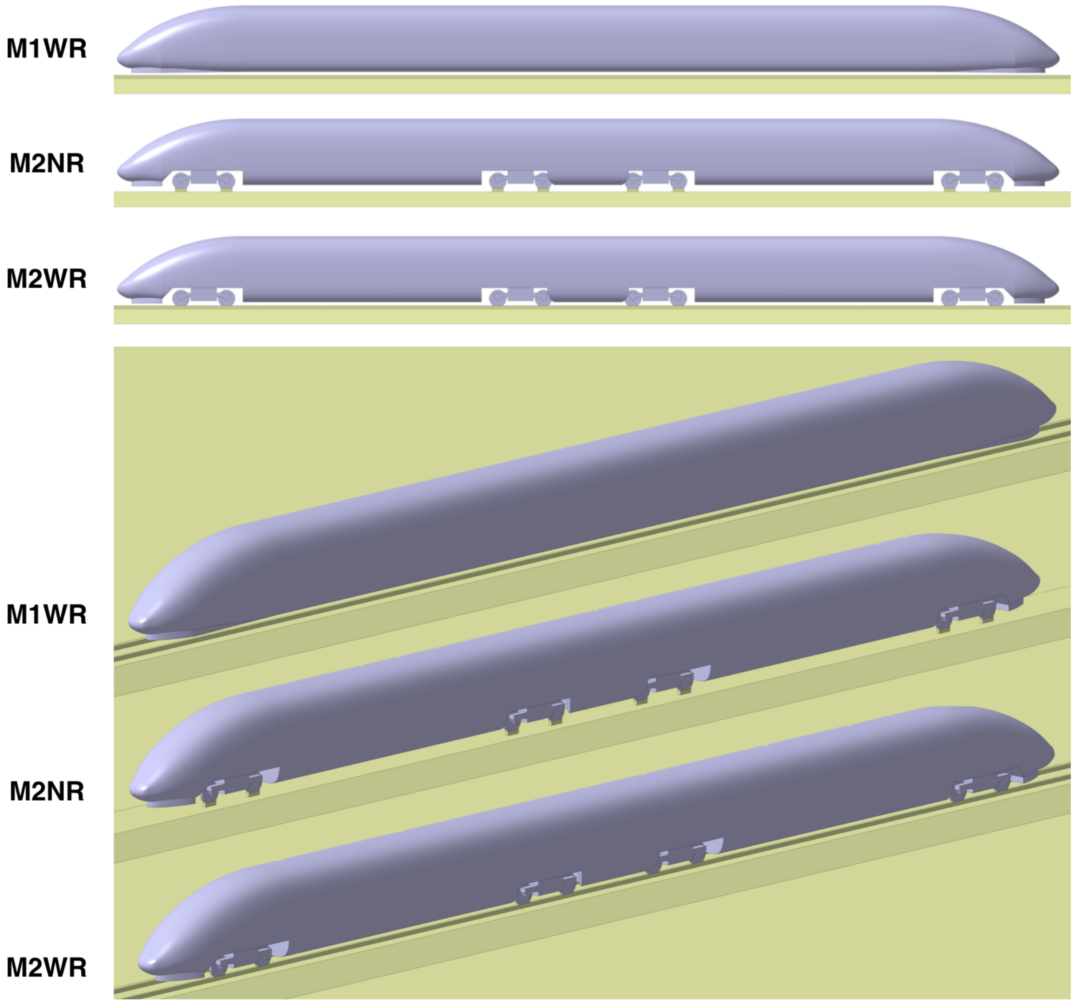

FIGURE 2.2: The side and isometric views of the three train/ground geometric configurations: M1WR, M2NR and M2WR.

Two ground configurations, single track ballast *with* and *without* rails (referred as WR and NR respectively), are modelled in this study. Initially, the aim of comparing the two ground configurations was to reveal the impacts of rails on HST slipstream development. The dimensions of the WR ground configuration are based on the 2011 CEN specifications (CEN 2011). Compared with the dimensions specified in CEN (2011), the thickness of the rails is extended from 5 mm to the wheel width of 13.5 mm in order to represent a realistic contact between the rails and wheels. The only difference between the WR and NR ground configuration is the existence of rails, all other dimensions remain identical, for example, the dimensions of the ballast and ground clearance. In the NR set up, the gap between the wheels and ballast is filled by extruding the (small) rectangular-shape wheel contact patch to the ballast surface. Please note that the wheel contact patches are a standard treatment for collapsed angles (i.e. singular

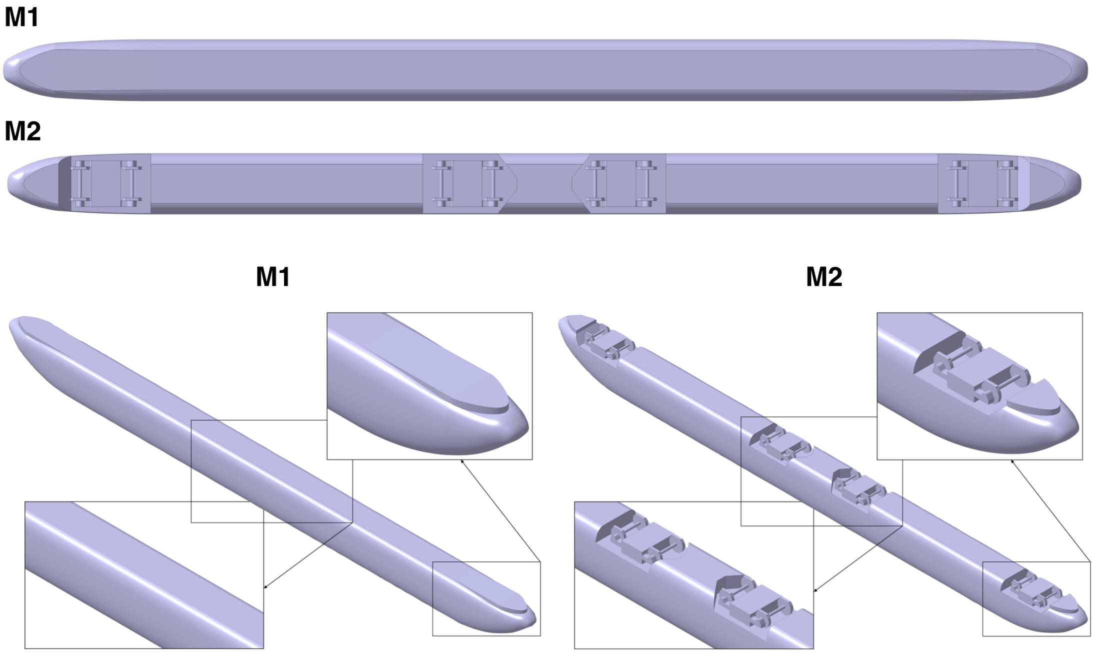

Figure 2.3: The comparison between the underbody structure between the flat-underbody (M1) and full-featured (M2) train model.

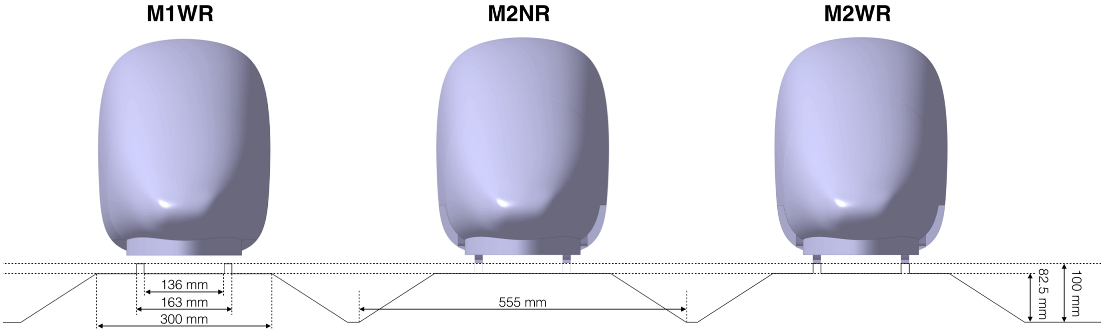

Figure 2.4: The schematics of different ground configurations.

cells due to the tangential contact) in numerical simulations. This is different from the common practice in wind-tunnel experiment with a moving belt, in which a gap is reserved to avoid direct contact between the wheels and moving ground. The layout and specifications of the ground configurations for the three geometric variations are illustrated in the Fig. 2.4.

Interestingly, compared with the original CEN specifications (CEN 2011), the latest regulation (CEN 2013) removes the requirement of modelling the rails on the ballast, but the reason for this modification is not addressed. Therefore, insight into understanding how the presence of rails may alter the train slipstream is essential for proper regulation development. In conclusion, the geometries used for each study and the corresponding

Table 2.1: The list of geometric configurations used in each study.

Topics	Chapter	Geometric configuration
Performance of different turbulence models	Chapter 4	M2WR
Effect of ground motion	Chapter 5	M2WR
Effect of bogies	Chapter 6	M1WR & M2WR
Effect of rails	Chapter 7	M2NR & M2WR

chapters are presented in Table. 2.1.

2.1.1 Computational Domain and Boundary Conditions

The construction of computational domain is identical for all the numerical simulations in this project. The train is positioned on a single ballast track in a computational domain consisting of hexahedral elements. The ballast is extended through the entire domain, i.e., from the inlet to outlet. To help visualise the layout of computational domain a schematic of M2WR configuration is presented in Fig. 2.5.

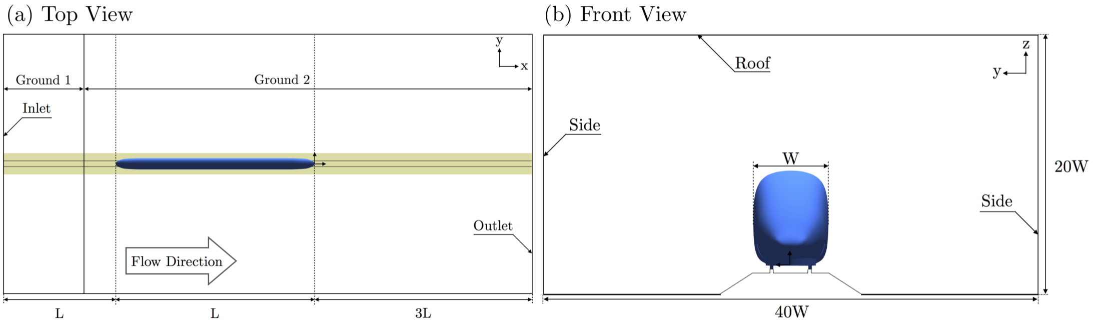

Figure 2.5: Schematics of the computational domain: (a) top-view; (b): front-view (Not to scale).

For the discussion for each study, dimensions are generally normalised by the train width (W) in the spanwise direction (y-direction), or by the length (L) of the train in the streamwise direction (x-direction). The origin of the coordinate system is positioned in the spanwise mid-plane, at the height of the top surface of the rails, with $x = 0$ corresponding to the tail tip.

Except for the ground and wheels, the boundary conditions for all other boundaries are identical between the different models. A uniform velocity boundary condition with a turbulence intensity of 1% is applied at the inlet to simulate the low-turbulence horizontal-flow freestream condition in the wind tunnel. The Reynolds number (based on W) is 7.2×10^5. These values are chosen for consistency to allow a direct comparison with wind-tunnel experiments, but noting that they are not representative of full-scale train operation which is typically approximately 20×10^6. A zero static pressure condition is applied at the outlet boundary. A no-slip wall boundary condition is applied to all train surfaces, except for the wheels, which may vary between different cases. Symmetry boundary conditions are applied at the top and sides of the computational domain. Note that for a clearer visualisation of the computational setup and domain dimensions, Fig. 2.5 is not drawn to scale. The corresponding case-dependent boundary conditions for the ground and wheels are introduced as follows.

Study 1: Performance of Different Turbulence Models (Chapter 4)

As the evaluation of the performance of different turbulence models is conducted based on validation against results from a parallel wind-tunnel experiment (undertaken by a past PhD student), a wind-tunnel equivalent ground boundary condition is applied in § 4. In order to replicate the elevated ground plane introduced in the wind-tunnel work to remove the floor boundary layer, the lower boundary of the computational domain is split into two parts, named *Ground 1* and *Ground 2*. *Ground 1* is $0.7L$ long and it employs a zero-shear wall condition to prevent boundary later development prior to where the equivalent of the leading edge of the elevated experimental ground plane was positioned. *Ground 2* is $4.3L$ long with a no-slip wall condition, as well as the train surface including the wheel-sets.

Study 2: Effect of Ground Motion (Chapter 5)

To explicitly investigate the effect of relative ground motion between the train and the lower boundary, three different ground & wheel boundary conditions are studied and compared: *Stationary Ground with Stationary Wheels* (SGSW), *Moving Ground with Stationary Wheels* (MGSW) and *Moving Ground with Rotating Wheels* (MGRW), and the corresponding boundary conditions are listed in Table. 2.2. To study the potential difference that may be introduced by a stationary ground configuration in a wind-tunnel experiment, SGSW applied the same boundary conditions as utilised in Study 1. When the no-slip moving wall condition is applied to the ground surface, both ground 1 and ground 2 move horizontally at the freestream velocity of U_∞. This is to simulate the realistic condition of a moving train travelling through still air where there is no relative motion between the air and ground. For the rotating wheel sets, the axes of rotation are along the centrelines of the axles. The wheel sets rotate at a constant angular velocity, with the speed at the rim equal to the speed of the moving ground. SGSW represents a typical wind tunnel experimental condition without a moving-belt, while MGRW is

Table 2.2: Boundary conditions of the grounds and wheel-sets for the Study 2.

Boundary conditions	SGSW
Ground 1	Zero-shear stationary wall
Ground 2	No-slip stationary wall
Wheel-sets	No-slip Stationary wall
Boundary conditions	MGSW
Ground 1	No-slip moving wall
Ground 2	No-slip moving wall
Wheel-sets	No-slip stationary wall
Boundary conditions	MGRW
Ground 1	No-slip moving wall
Ground 2	No-slip moving wall
Wheel-sets	No-slip rotational wall

more realistic for full-scale and moving-model tests. To have a more complete study of ground motion effect, an additional case, MGSW, is studied to isolate the effect of wheel rotation.

Study 3 & 4: Effect of Bogies and Rails (Chapter 6 & 7)
The realistic ground/wheel boundary condition is utilised in Study 3 & 4, specifically, moving ground and rotating wheels (MGRW). The ground moves at the speed of U_∞ for a representation of the relative motion between the train and ground. For the models that are equipped with bogies, the wheel-sets rotate at a specified speed which gives the speed at the rim equals to U_∞.

The boundary layer of incoming flow before approaching the train nose are depicted by U_{TF} profiles at $0.5H$ in front of the train nose at the centre-plane, as illustrated in Fig. 2.6. Loss of momentum caused by the train nose is indicated in all three cases, and the discrepancies introduced by the ground condition are limited below the TOR. There is no experimental data for a direct comparison at the same location. The boundary layer measurement, taken at $0.625H$ from the leading edge of the ballast in a empty tunnel, is plotted in Fig. 2.6. The local acceleration is introduced by the ramp of the ballast, which is expected to reduce the boundary layer thickness (Bell 2015).

2.2 Turbulence Modelling

One of the aims of this project is to develop a numerical approach for predicting HST slipstream. For this reason one primary task is to evaluate the up-to-date turbulence models applied to study the train aerodynamics. This project evaluates the performance

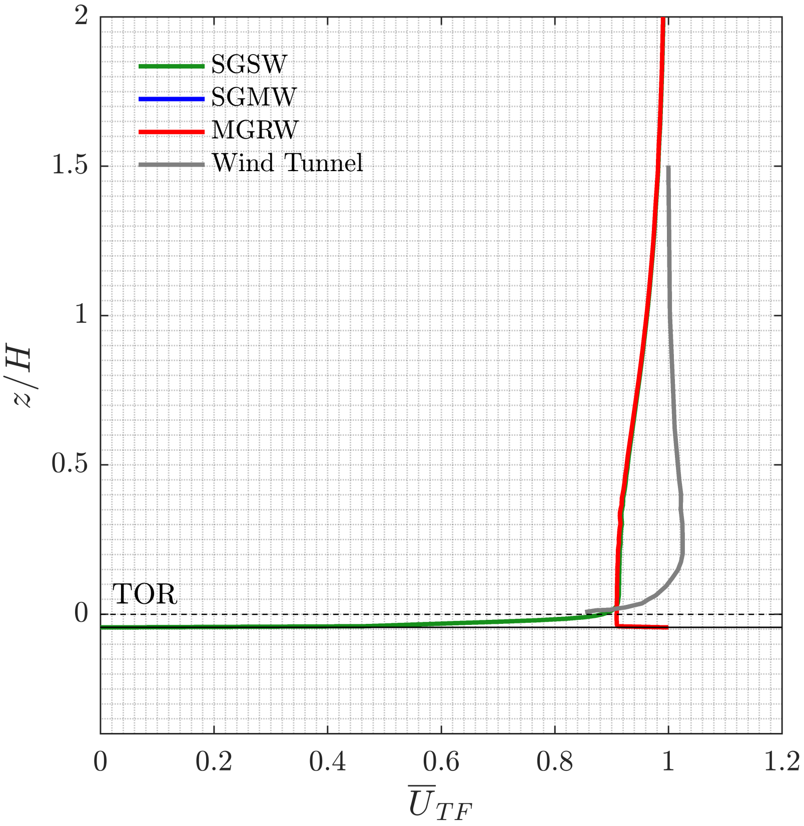

FIGURE 2.6: The comparison of ground boundary layers between SGSW, MGSW and MGRW at $0.5H$ in front of the train nose. The wind-tunnel measurement (without the presence of the train) at $0.625H$ behind the leading edge of splitter plate is plotted as a reference, results adapted from (Bell 2015).

of three different turbulence models (URANS, SAS and DES) in resolving the flow structures around a HST, and the results are presented in § 4. A brief introduction of the turbulence models involved in this project is presented here, which includes corresponding formulations, strengths and limitations.

The flow motion can be described by the Navier-Stokes equations:

$$\nabla \cdot \vec{v} = 0, \tag{2.1}$$

$$\rho(\frac{\partial \vec{v}}{\partial t} + \vec{v} \cdot \nabla \vec{v}) = -\nabla p + \mu \nabla^2 \vec{v} + f. \tag{2.2}$$

Eqn. 2.1 is the continuity equation, which represents conservation of mass, and Eqn. 2.2 describes conservation of momentum within the fluid. Here, $\vec{v} = (u, v, w)$ or (u_1, u_2, u_3), p, ρ and μ are the velocity vector, pressure, density and dynamic viscosity, respectively.

For an incompressible flow, conservation of the mass reduces to the condition that the velocity is divergence-free (as described by Eqn. 2.1). Meanwhile, Eqn. 2.2 represents that (the mass per unit volume times) the acceleration of a fluid parcel (left-hand side) equals the sum of external forces per unit volume (right-hand side). The forces consist of the divergence of the stress tensor ($\nabla \cdot (-p\vec{\vec{I}} + \mu(\nabla\vec{v} + (\nabla\vec{v})^T) \rightarrow -\nabla p + \mu\nabla^2\vec{v})$, where $-\nabla p$ and $\mu\nabla^2\vec{v}$ are the pressure and shear components respectively, and the body force is f (typically gravity, but this can be absorbed into the pressure term for single phase flows without free-surfaces).

Theoretically, the Navier-Stokes equations can accurately predict all Newtonian flows where the continuum approximation holds, while practically, the advective term $\vec{v} \cdot \nabla\vec{v}$ makes it difficult to solve, especially at high Reynolds numbers, because of nonlinearity and because this term causes energy to cascade from large to small scales. Consequently, for industrial flows, which are usually associated with high Reynolds numbers, some level of turbulence modelling is required. The range of length and time-scales that need to be captured increases approximately with Reynolds number to the power of $\frac{3}{4}$ (Ferziger & Perić 2002). Since increased resolution is required in each direction and the timestep also needs to be reduced similarly, capturing all relevant scales of high Reynolds number flows is well beyond current computational resources.

Some widely-used turbulence models relevant to this project are introduced here.

2.2.1 RANS Approach

Reynolds-averaging proceeds by first splitting the flow variables into time or ensemble mean, and fluctuating components (e.g., $u_i = \overline{u}_i + u_i'$). Putting this decomposition into the Navier-Stokes equations and averaging gives the *Reynolds-Averaged Navier-Stokes* (RANS) equations. Keeping the time derivative of the mean velocity, which implies that the averaging procedure can be thought of as averaging over an ensemble of turbulent flow states, gives the *Unsteady* RANS (URANS) model. The equations for the mean velocity components $\overline{u}_i$ and pressure ($\overline{p}$) are summarised as

$$\frac{\partial \overline{u}_i}{\partial x_i} = 0 \ , \tag{2.3}$$

$$\frac{\partial \overline{u}_i}{\partial t} + \overline{u}_j \frac{\partial \overline{u}_i}{\partial x_j} = -\frac{1}{\rho}\frac{\partial \overline{p}}{\partial x_i} + \frac{\partial}{\partial x_j}(\nu \frac{\partial \overline{u}_i}{\partial x_j}) + \frac{1}{\rho}\frac{\partial \tau_{ij}}{\partial x_i} \ , \tag{2.4}$$

where $\tau_{ij} = \overline{u_i' u_j'}$ is the *Reynolds Stress Tensor*, which cannot formally be expressed in terms of mean flow variables; instead, some level of turbulence modelling has to be applied. The usual way to proceed is to form an analogy between molecular diffusion and turbulent mixing, and thus approximate the Reynolds stress in terms of the mean flow gradient together with a spatially-varying turbulent viscosity based on local turbulent time/velocity and length scales. These scales are obtained by solving two further equations, e.g., for the turbulent kinetic energy per unit mass (k) and the turbulent dissipation (ϵ) for the well-known $k - \epsilon$ model. In this study, the more sophisticated two-equation *Shear-Stress Transport* (SST) $k - \omega$ model is utilised, which calculates the turbulent scales using the turbulence kinetic energy per unit (k), and the specific dissipation rate (ω). The transport equations for k and ω are presented in Eqn. 2.5 and Eqn. 2.6 respectively:

$$\frac{\partial}{\partial t}(\rho k) + \frac{\partial}{\partial x_i}(\rho k u_i) = \frac{\partial}{\partial x_j}(\Gamma_k \frac{\partial k}{\partial x_j}) + \widetilde{G_k} - Y_k + S_k \ , \tag{2.5}$$

$$\frac{\partial}{\partial t}(\rho \omega) + \frac{\partial}{\partial x_j}(\rho \omega u_j) = \frac{\partial}{\partial x_j}(\Gamma_\omega \frac{\partial \omega}{\partial x_j}) + G_\omega - Y_\omega + D_\omega + S_\omega \ . \tag{2.6}$$

The SST $k-\omega$ model is integrated in the *ANSYS FLUENT* solver, and detailed formulations of each term are presented in the *ANSYS Fluent Theory Guide* (Fluent 2009). The *Shear-Stress Transport* (SST) $k - \omega$ model blends the classical $k - \omega$ and $k - \epsilon$ models, noting $k-\omega$ is considered a superior and better behaved model in the near-wall boundary-layer regions, and $k - \epsilon$ is more appropriate in the outer flow. The model also adjusts the approach near separation/reattachment zones, with the aim of better modelling of flows with undefined separation points, such as exist on the smooth surfaces of a high-speed train. Of course, URANS models can only capture large-scale flow features and longer time-scale periodicities, such as the shedding from bluff bodies like circular cylinders, noting that only the very large-scale vortical wake features caused by an absolute instability are likely to be resolved to some level of accuracy.

2.2.2 Large Eddy Simulation

The analytical solution of the Navier-Stokes equations is generally not possible except in very restricted cases. Directly solving the Navier-Stokes equations through numerical methods without any turbulence modelling is known as *Direct Numerical Simulation* (DNS). However, DNS requires resolving the spatial and temporal scales from the largest scales (such as the train) down to the dissipative scale (the Kolmogorov scale), below which the flow energy dissipates through the action of viscosity as thermal energy. Resolving down to the Kolmogorov scale can be extremely computational expensive, and the computational cost increases rapidly at approximately the rate Re^3. In practice, to achieve a satisfactory prediction of the larger length scales of the flow field, where most of the flow energy resides, the range of scales of the turbulence spectrum has to be resolved to a reasonable extent.

Scale Resolving Simulation (SRS) is one approach. The underlying idea is to apply a low-pass filter to the flow variables of the original Navier-Stokes equations. Length and time scales below the cut-off are resolved directly. Those scales above the cutoff cannot generally be represented on the chosen mesh and instead need to be modelled. Effectively, the energy cascading from larger scales has to be removed from the system at the correct rate so that the turbulent energy spectrum maintains the same form below the cutoff. In practice this often involves adding a turbulent diffusion term similar in form to that used in RANS modelling. In this case the eddy viscosity is based on the cutoff length scale and the symmetric past of the rate of strain tensor. This gives the Smagorinsky model, originally developed for climate modelling. The approach is known as (pure) *Large Eddy Simulation* (LES). Specifically, instead of resolving all turbulence structures like DNS or modelling all turbulence scales like RANS, LES functions like a hybrid method that can resolve larger-scale time-dependent turbulence structures according to a pre-defined LES sub-grid-scale cut-off filter. As the filter directly influences the turbulence scales that can be resolved, the determination of the cut-off scale is critical for LES simulations. In practice, the cutoff scale is intimately connected with the computational-mesh cell size, so the construction of the computational mesh determines the range of scales actually captured in the simulation.

Following on from the discussion above, the logic of the cut-off filter selection is visualised by the schematic depicting the energy cascade in Fig. 2.7. Fig. 2.7 shows that the turbulence spectrum can be divided into three regimes: the energy containing range, the inertial range and the dissipation range, each with its own range of turbulent scales. The energy containing range accounts for the formation of turbulent structures, and the inertial subrange accounts for progressive energy cascade from intermediate to still smaller length scales. The energy containing range and lower wavenumber part of the inertial subrange are geometry and boundary condition dependent, and have to be resolved by the LES model. The energetics of smaller eddies at higher wavenumbers is assumed to be isotropic and geometry independent, thus, this process does not need to be resolved but can be modelled, with minimal effect on the energy containing scales, to be a good physical model of a turbulent flow. As described, in

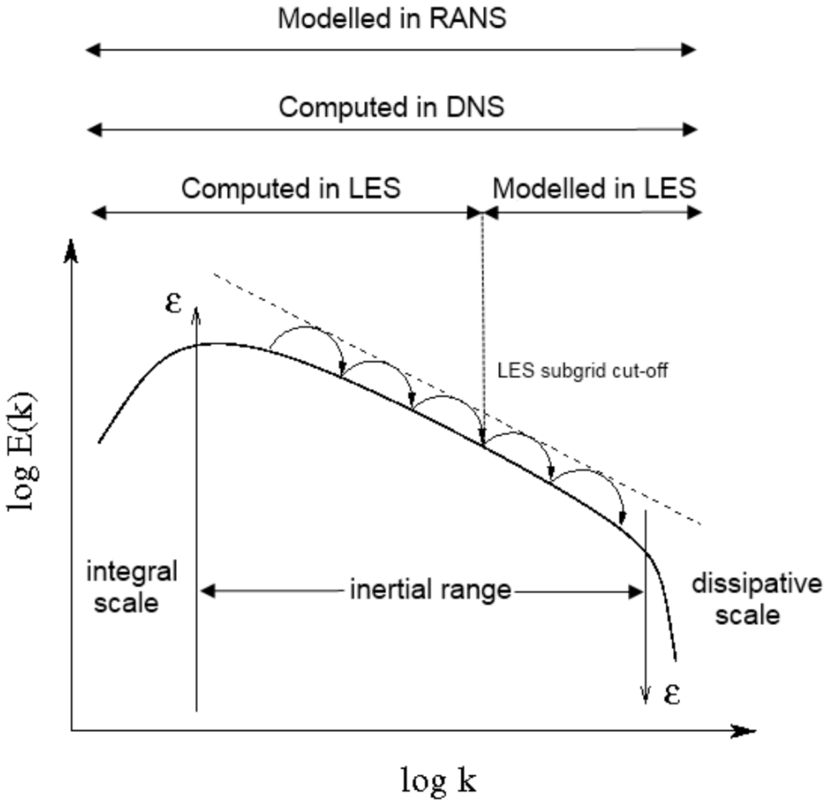

FIGURE 2.7: Schematic of turbulence energy cascade showing the differences between RANS, DNS and LES approaches. Image taken from Parkin (2014).

a numerical simulation, the cut-off scale is generally implicitly chosen by the spatial discretisation (i.e., the grid resolution), therefore, a grid independence study is essential for SRS simulations. Mathematically, the filtered value (denoted as $\widetilde{\phi}$) of a variable ϕ is calculated by applying a compact filter function (G) over the entire domain (D), as described in Eqn. 2.7:

$$\widetilde{\phi}(x) = \int_D \phi(x')G(x,x')dx' \ . \tag{2.7}$$

ANSYS FLUENT adopts a finite-volume discretisation method, which inherently provides a filtering operation, hence Eqn. 2.7 can be rewritten as Eqn. 2.8:

$$\widetilde{\phi}(x) = \frac{1}{\mathcal{V}} \int \phi(x')dx', \tag{2.8}$$

where $\mathcal{V}$ is the volume of a computational cell, and then the cut-off filter (G) is formulated as a step-function.

The filtered governing equations can be written as Eqn. 2.9 and 2.10:

$$\frac{\partial \widetilde{u_i}}{\partial x_i} = 0, \tag{2.9}$$

$$\frac{\partial \widetilde{u_i}}{\partial t} + \widetilde{u_j}\frac{\partial \widetilde{u_i}}{\partial x_j} = -\frac{1}{\rho}\frac{\partial \widetilde{p}}{\partial x_i} + \nu \frac{\partial^2 \widetilde{u_i}}{\partial x_j \partial x_j} - \frac{\partial \tau_{ij}}{\partial x_j}, \tag{2.10}$$

where, $\tau_{ij} = \widetilde{u_i u_j} - \widetilde{u_i}\widetilde{u_j}$ is the sub-grid stress tensor.

ANSYS FLUENT employs the Boussinesq hypothesis for modelling τ_{ij}, and the equations are closed by the Smagorinsky-Lilly Model. The original Smagorinsky-Lilly model was constructed based on the idea initially proposed by Smagorinsky (1963), and it has witnessed a continuous improvements over the past decades. One improvement is in near-wall modelling characteristics, as the classic Smagorinsky-Lilly model requires an excessively high resolution to capture the small eddies within a boundary layer. In fact, the standard model does not give the correct physical behaviour as the wall is approached. The Wall-Modelled LES (WMLES) approach is one of the modified models, which utilises a RANS approach within the inner part of a logarithmic layer while the outer part of the boundary layer is resolved by LES. The modifications involve using a mixing length model with wall-damping to resolve the larger scale variation near the wall. Detailed formulations are presented in Fluent (2009).

2.2.3 Detached Eddy Simulation

Detached Eddy Simulation (DES) is a blend of RANS and LES, utilising RANS to predict the ensemble-mean boundary-layer development and applying LES to capture the time-dependent flow away from boundaries. DES is compatible with different RANS wall models, and the SST $k - \omega$ model is utilised in this project for near-wall modelling. By avoiding trying to solve the fine time-dependent turbulence structures of wall boundary layers under LES, which are unlikely to strongly influence the outer flow, DES significantly reduces the computational cost of applying an LES approach to solve high Reynolds number engineering problems. To achieve this hybrid behaviour, it is necessary to switch between the RANS and LES at a variable point away from the wall—this is the key producing a correct outer flow prediction using DES.

The concept of DES was initially proposed by Spalart *et al.* (1997). The core concept is to use a modified length scale (d_{DES}) as an indicator for switching between RANS and LES:

$$d_{DES} = min(d, C_{DES}\Delta_{max}) \ , \tag{2.11}$$

where, d is the distance to the closest wall, which is a key factor for determining the production and destruction level of turbulent viscosity; Δ_{max} is the max local cell dimension in x, y, z directions; and C_{DES} is an empirical constant of 0.65. To reiterate, the accuracy and validity of DES directly depends on the performance of correctly switching the turbulence model between the attached boundary-layer region (RANS) and free shear-flow region (LES). An underlying assumption of the classic DES model is that, a typical RANS grid employs highly elongated cells within the boundary layer region, i.e., the wall-parallel grid spacing exceeds the boundary thickness, to avoid triggering LES mode within the boundary layer region. However, for an ambiguous mesh for which the wall-parallel grid spacing is less than the wall boundary thickness, LES can be triggered inside the boundary layer where the grid is not fine enough to sustain resolved turbulence. This unintended activation of LES within the boundary layer can produce misleading results, for example, *Modelled-Stress Depletion* and *Grid-Induced Separation* are the two most common issues of the classic DES model. These issues have been gradually addressed through continuous improvements to the model, specifically, much effort has been channelled into developing a more sophisticated switching function. Spalart *et al.* (2006) modified the formulation of the original DES length scale (d_{DES}) by introducing a shield function (f_d), which can preserve the RANS mode within the boundary layer, to produce the Delayed DES (DDES) model. The improved formulation of length scale d_{DDES} is presented in Eqn. 2.12:

$$d_{DDES} = d - f_d \; max(0, d - C_{DES}\Delta_{max}) \; . \tag{2.12}$$

According to Eqn. 2.12, DDES takes the distance to the wall into account for activating each mode compared with d_{DES}. For example, f_d is kept to be 1 within the LES region and 0 inside the boundary layer region, and this mechanism shields the LES mode from being activated inside the boundary-layer region.

The present study employs a more recently developed *Improved-Delayed-DES* (IDDES) model, an optimised hybrid RANS-LES model with DDES and WMLES capabilities, which was initially proposed by Shur *et al.* (2008). IDDES is tuned to accurately switch between DDES and WMLES according to the inflow conditions. By default, IDDES remains in DDES mode; and the WMLES mode is activated only when the inflow conditions are turbulent and the grid resolution is sufficient for resolving boundary layer dominant eddies. IDDES broadens the application range of the RANS/LES hybrid model by permitting the activation of each mode in designated regions. A fuller description is given in Shur *et al.* (2008). SST $k - \omega$ is used for the RANS model for all RANS/LES hybrid simulations used in this project.

2.2.4 Scale Adaptive Simulation

Scale Adaptive Simulation (SAS) is developed from the classical URANS model, noting that the way that turbulence is incorporated is mathematically equivalent between the RANS approach and the subgrid-scale model used for *Large Eddy Simulation.* The innovation of SAS is that the von Karman length scale is introduced to capture the scale-adaptive temporal and spatial scales. This idea was initially proposed by Rotta (1972), and has been gradually improved through the years and recently integrated into the commercial CFD solver ANSYS. Unlike the URANS approach which can only capture large-scale vortex shedding, SAS is capable of resolving part of the turbulence spectrum for unstable flows depending on the spatial and temporal scales, i.e., in this case, effectively the cell size and timestep. The von Karman length scale (L_{vK}) used to construct the turbulent viscosity is given by

$$L_{vK} = \kappa \left| \frac{\bar{U}'}{\bar{U}''} \right|, \tag{2.13}$$

with

$$\bar{U}' = \sqrt{2 S_{ij} S_{ij}} \quad and \quad \bar{U}'' = \sqrt{\frac{\partial^2 \bar{u}_i}{\partial x_j \partial x_j} \frac{\partial^2 \bar{u}_i}{\partial x_k \partial x_k}}, \tag{2.14}$$

where

$$S_{ij} = \frac{1}{2} \left(\frac{\partial \bar{u}_i}{\partial x_j} + \frac{\partial \bar{u}_j}{\partial x_i} \right). \tag{2.15}$$

The second velocity derivative term (Eqn. 2.14) in the L_{vK} formulation allows the model to adjust the local length scale to the turbulence structures that are already resolved in the flow. A full description of the SAS model is given in Menter & Egorov (2010) and Egorov *et al.* (2010). As a *scale-adaptive* method, it shows a gradual transition from URANS-type to LES-type behaviour as the temporal and spatial resolution are increased. For example, SAS remains in RANS mode for wall-bounded flows, i.e. within the boundary layer region, while for unsteady flow regions, i.e. a separated flow region, the SRS mode is activated. Unlike problems with LES or DES caused by insufficient grid or time resolution, SAS utilises URANS as a back-up. A known limitation of SAS is that the scale-resolving mode is not activated unless the flow is sufficiently unstable. For this study the wake is highly turbulent, fed by flow past complex underbody structures and larger-scale shedding in the wake. However, the wake is not a strongly globally unstable flow because the surfaces are relatively streamlined. Hence, how well this approach will work for HST wake flow is not clear a priori.

2.3 Grid Description

2.3.1 Overall Meshing Strategy

This research applies a consistent meshing strategy, even though some geometric variations exist between individual studies. Here, the M2WR mesh is used as an example to demonstrate the meshing strategy. Using a cut-cell mesh with refinement around the train and in the wake region is a common meshing strategy for numerical simulations (Muld *et al.* 2012a) (Hemida *et al.* 2014). In this project, the general meshing strategy is based on the predominately-Cartesian *cut-cell* approach, allowing substantially increased mesh concentration around the train and in the wake, together with a relatively smooth transition to lower resolution away from the train.

This mesh concentration is accomplished by applying virtual refinement zones at the target regions. For example, in this study three different levels of refinement zones are utilised to achieve higher accuracy around the train and within the wake, as illustrated in Fig. 2.8. To ensure all important flow features are captured, the dimensions of the refinement regions were determined based on a preliminary simulation. This method achieves a high uniform resolution in the slipstream measurement regions, and aids in accurately capturing the boundary layers and induced flow separation from smaller-scale geometrical features. *Inflation layers* are applied to all wall boundaries to capture the boundary layer development. A relatively smooth transition is established between the adjacent cells including between the outer inflation layer and the hexahedral grid, and at the interface of two refinement zones, as illustrated in Fig. 2.9.

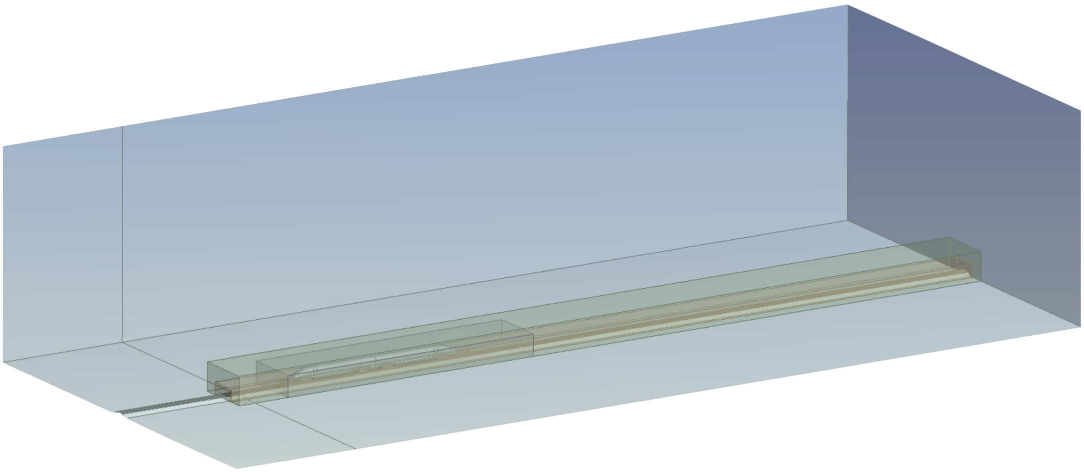

FIGURE 2.8: The layout of virtual mesh refinement zones.

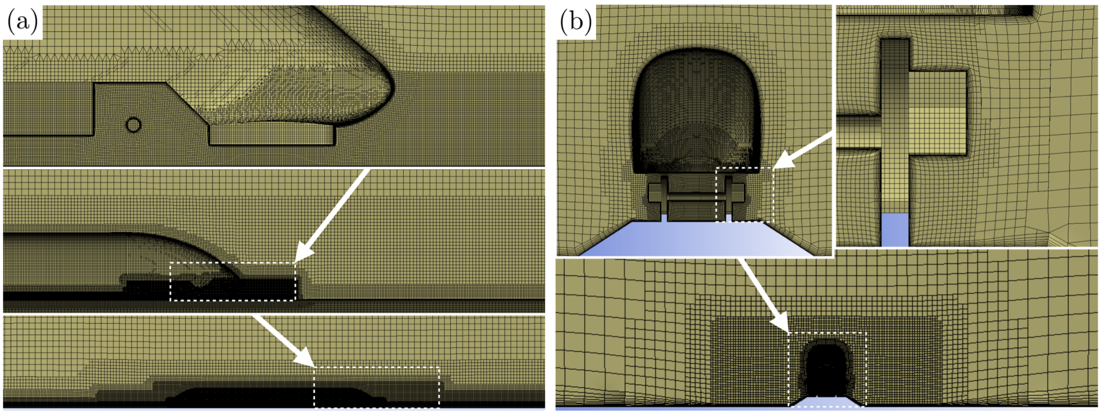

Figure 2.9: The visualisation of grid refinement around the train based on the M2WR configuration: (a): centre-plane; (b): cross-section.

Table 2.3: Cases for mesh independence testing.

	URANS ($0.05T_{ref}$)	SAS ($0.025T_{ref}$)	IDDES ($0.0025T_{ref}$)
Grid resolution	Coarse Medium Fine	Coarse Medium Fine	Coarse Medium Fine

2.3.2 Mesh Independence Test

A mesh independence test was undertaken to ensure the all important flow features are resolved and (reasonable) mesh independence is achieved. The mesh independence testing was conducted based on the M2WR model with the SGSW ground configuration, as it is the most geometrically complex model but also because wind-tunnel experimental results are available for validation.

A useful time scale can be constructed from the train height and freestream velocity, defining a *Reference Time Scale* ($T_{ref} = H/U_\infty$). To study the effect of grid spatial resolution, in order to maintain the consistency of the comparison, the timestep for each model remains fixed with $\Delta t_{URANS} = 0.05T_{ref}$, $\Delta t_{SAS} = 0.025T_{ref}$ and $\Delta t_{IDDES} = 0.0025T_{ref}$, reflecting the sophistication of the models and noting that the successive models progressively try to capture finer spatial and temporal scales. An underlying assumption is that only capturing the larger-scale flow features can still provide reasonable predictions of slipstream and drag. The cases examined for the mesh independence testing are listed in Table 2.3.

The reference timestep is broadly based on common practice; more details regarding timestep selection are presented in § 2.4.3. Three grids with the same meshing strategy but different densities were constructed for this comparison. As described above, the

Table 2.4: Meshing parameters.

Mesh		**Coarse**
Cell size	Train surface mesh	$0.015H \sim 0.12H$
	Under-body refinements	$0.015H \sim 0.06H$
	Wake refinements	$0.06H \sim 0.12H$
	Far-field refinements	$0.24H \sim 0.96H$
No. of inflation layers		4
Train surface wall y^+		$20 \sim 150$
No. of cells (millions)		3.3
Mesh		**Medium**
Cell size	Train surface mesh	$0.0075H \sim 0.06H$
	Under-body refinements	$0.0075H \sim 0.015H$
	Wake refinements	$0.015H \sim 0.06H$
	Far-field refinements	$0.12H \sim 0.48H$
No. of inflation layers		8
Train surface wall y^+		$10 \sim 50$
No. of cells (millions)		17.4
Mesh		**Fine**
Cell size	Train surface mesh	$0.00625H \sim 0.05H$
	Under-body refinements	$0.00625H \sim 0.0125H$
	Wake refinements	$0.0125H \sim 0.05H$
	Far-field refinements	$0.1H \sim 0.4H$
No. of inflation layers		10
Train surface wall y^+		$5 \sim 30$
No. of cells (millions)		26.6

overall meshing strategy is based on the Cartesian *cut-cell* meshing approach with refinements around the train and in the wake region, as introduced in § 2.3.1. The number of cells for the coarse, medium and fine grids are approximately 3.3, 17.4 and 26.6 million, respectively. (The fluid solver (FLUENT) used for the flow predictions employs cell-centred variables, hence these numbers relate to the degrees-of-freedom, i.e., u, v, w, p, to resolve the flow). As the mesh is made progressively finer, the train surface cell size and the cell size of the refinement zones are gradually decreased, and the corresponding number of inflation layers on the wall boundaries is increased. The critical meshing parameters are listed in Table 2.4.

The mesh independence test is conducted based on two parameters: slipstream measurements ($\overline{U}_{slipstream}$ & $\sigma_{slipstream}$) and the train drag coefficient (C_D), to determine how well the predictions are converging. C_D is calculated based on the freestream velocity and train frontal area. The effects of varying grid resolution, in terms of the $\overline{U}_{slipstream}$ and $\sigma_{slipstream}$, are illustrated in Fig. 2.10.

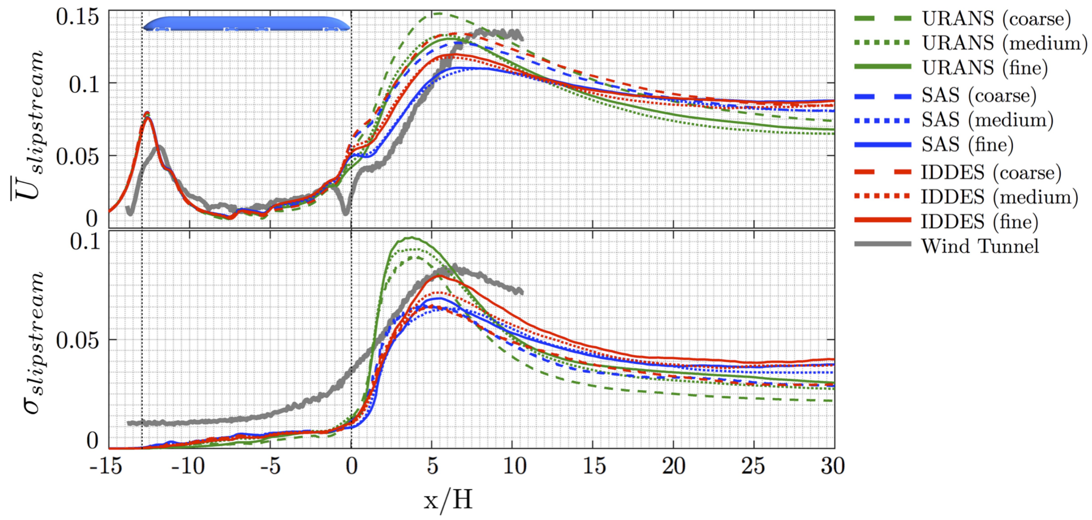

FIGURE 2.10: A comparison of $\overline{U}_{slipstream}$ and $\sigma_{slipstream}$ at the trackside heights for the three different turbulence models with results from experiments, showing the effect of grid resolution.

According to Fig. 2.10, all cases show a qualitatively good agreement with the wind-tunnel experimental data, which was obtained from a parallel experimental study at Monash University. Note that there are some slight differences between the experimental setup and the numerical model that may cause the observed differences, especially from the tail of the train downstream. Further comparisons will be made at the end of this chapter and in later chapters. In addition, it is clear that the upstream turbulence level is higher in the experiments, even though the inflow turbulence level for the numerical models is set to match that of the background wind-tunnel level. This is a known problem with predicting time-dependent turbulent flows. Recent implementations that include time-dependent inflow turbulence, e.g., the point vortex generator and spectrally based generators built into the newer versions of ANSYS, provide a way forward for future similar studies.

A local peak occurs near the train nose due to the head pulse, while the maximum $\overline{U}_{slipstream}$ happens at approximately $x = 5 \sim 8H$. The $\sigma_{slipstream}$ profile witnesses a gradual increase approaching the tail of the train, and after the tail the gradient becomes significantly steeper, and achieves its maximum at approximately $x = 4 \sim 6H$. According to the slipstream profiles of each model, as presented in Fig. 2.10, the difference between the medium and fine grids with respect to $\overline{U}_{slipstream}$ is minor, while shifting to the coarse grid has a much stronger impact on $\overline{U}_{slipstream}$. Compared with SAS, $\sigma_{slipstream}$ shows a stronger dependence on grid size for both URANS and

Table 2.5: The critical values from mesh-independence testing.

	$\overline{U}_{slipstream}$		$\sigma_{slipstream}$		C_D
	Maximum	Location	Maximum	Location	
URANS (coarse)	0.148 (+8.0%)	5.50H	0.088 (+4.8%)	4.08H	0.267
URANS (medium)	0.133 (-2.9%)	5.87H	0.092 (+9.5%)	3.82H	0.268
URANS (fine)	0.130 (-5.1%)	6.24H	0.097 (+15.5%)	3.77H	0.271
SAS (coarse)	0.128 (-6.6%)	6.82H	0.066 (-21.4%)	4.56H	0.269
SAS (medium)	0.110 (-19.7%)	8.13H	0.064 (-23.8%)	6.40H	0.269
SAS (fine)	0.111 (-19.0%)	6.61H	0.069 (-17.9%)	5.61H	0.274
IDDES (coarse)	0.134 (-2.2%)	6.82H	0.066 (-21.4%)	5.03H	0.273
IDDES (medium)	0.118 (-13.9%)	5.98H	0.072 (-14.3%)	5.50H	0.276
IDDES (fine)	0.120 (-12.4%)	6.56H	0.079 (-6.0%)	5.61H	0.274
Wind Tunnel	**0.137**	**8.03H**	**0.084**	**6.46H**	**N/A**

IDDES. The lower influence of the grid size for SAS on $\sigma_{slipstream}$ may be due to its scale-adaptive nature, although it is unclear why. It could be that the SAS model may not be properly switching to LES mode as the grid is refined, which may be due to the fact that the wake is not strongly globally unstable. The maximum magnitude of $\overline{U}_{slipstream}$ and $\sigma_{slipstream}$, and their percentage deviation relative to the wind tunnel measurement, are presented in Table 2.5. Additionally, the corresponding locations of peak values are listed in the same table. According to Table 2.5, even though a variation can be identified for slipstream properties, C_D is very consistent across all cases (e.g., the deviation remains within 4%). One explanation is that due to the unique shape of HSTs, the skin friction is the main source of C_D for typical full-scale trains. In this study, despite the reduction of the train length-to-height ratio, skin friction still contributes to a large proportion of the aerodynamic drag. Numerically, the skin friction prediction depends on the train-surface boundary-layer modelling, while the three models utilise the same RANS approach for wall modelling.

Overall, the optimal mesh parameters are derived from the testing, to provide fine-mesh equivalent set-up, and then applied to all studies. Some key meshing parameters are listed in Table 2.6. Again, the discrepancies between the wind tunnel and numerical results is explicitly discussed in § 2.5; for example, the existence of a local minimum near the tail in experimental data is not reproduced in any of the numerical simulations.

Table 2.6: Optimal mesh parameters applied in Study 2, 3 and 4.

Cell size	Train surface mesh	$0.00625H \sim 0.025H$
	Under-body refinements	$0.00625H \sim 0.0125H$
	Wake refinements	$0.0125H \sim 0.05H$
	Far-field refinements	$0.1H \sim 0.4H$
No. of inflation layers		10
Train surface wall y^+		$1 \sim 20$
No. of cells (millions)		$25 \sim 30$, depending on the geometry

2.4 Solver Description

2.4.1 Solver Selection and Computational Resource

The numerical solver utilised in this research is the commercial CFD code *FLUENT* that is part of the ANSYS 16.2 software suite. One reason for this choice is that *ANSYS FLUENT* is a widely-used CFD engine, with its performance and validity well-documented through many previous related studies. As important, *ANSYS FLUENT* has the capabilities required for this study, for example, it provides the range of turbulence models required. Additionally, the Department has access to many ANSYS HPC licences on the National Computational Infrastructure (NCI), and parallel computing is essential for the proposed project.

2.4.2 Discretisation Scheme and Solver Settings

Due to the turbulent nature of slipstream, a pressure-based transient solver is used for all simulations. Interestingly, high-speed trains travel at a non-negligible fraction of the sound speed. However, since compressibility effects depend on the Mach number squared, the incompressibility assumption would still seem appropriate. The *Pressure-Velocity Coupling Scheme* for the RANS and SAS simulations is *SIMPLEC*, while the *Fractional-Step Scheme* with *Non-Iterative Time Advancement* is used for DES, as long as the Courant number is less than unity. For the spatial discretisation, the *second-order upwind scheme* is applied for all flow equations, except for SAS and DES, which utilise *bounded central differencing* for the momentum equation. The *bounded second-order implicit* formulation is applied for transient simulations. Note that since the maximum cell Courant number is less than unity, at least for the fine-mesh IDDES simulations, the effect of *bounding* of the central-difference scheme should be minimal, given that it is used to prevent the development of *central-difference wiggles* caused by the cell

Courant number taking values greater than 2.

2.4.3 Sensitivity Study of Solver Timestep

The solver timestep is an important parameter that can significantly affect the accuracy of results and the computational cost. Therefore, the selection of the solver timestep is finalised according to a sensitivity study in which its effect on slipstream measurement and drag prediction are examined. Similar to the *Mesh Independence Testing*, this sensitivity study is based on the same geometrical configuration (i.e. M2WR) with SGSW boundary conditions for consistency. Additionally, the sensitivity study is based on the optimal mesh configuration as presented in § 2.3.2, maintaining all other solver settings and only varying the timestep. This study examines three different timesteps: $\Delta t = 0.05T_{ref}$, $0.025T_{ref}$ and $0.0025T_{ref}$. The timestep sensitivity for all three turbulence models utilised in this study is examined, and the list of simulations is presented in Table 2.7.

Table 2.7: Cases for timestep sensitivity test.

$0.05T_{ref}$	$0.025T_{ref}$	$0.0025T_{ref}$
URANS	URANS	
	SAS	SAS
	IDDES	IDDES

The smallest timestep of $0.0025T_{ref}$ is chosen because this restricts the Courant number ≤ 1 for the typical smallest cells of the fine grid, which is one of the suggested criteria for conducting DES simulations. The largest timestep of $0.05T_{ref}$ is approximately 1/30 of the period of the dominant wake frequency, which is ideal for the URANS simulations, as only the dynamics of dominant flow features are (hoped to be) resolved.

The effect of timestep on the slipstream measurement is illustrated in Fig. 2.11, and the magnitudes and locations of the maximum $\overline{U}_{slipstream}$ and $\sigma_{slipstream}$ are presented in Table 2.8. Percentage differences in $\overline{U}_{slipstream}$ for the URANS, SAS and IDDES models are 5, 15 and 12%, respectively, relative to the wind tunnel result. For the $\overline{U}_{slipstream}$ prediction, there is a good match before the flow approaches the tail, while further downstream, the differences from the observed experimental variation are higher. This is likely to be connected with the predicted $\sigma_{slipstream}$ variation, as the turbulence level in the wake is much higher than that along the train. For the range

TABLE 2.8: The critical values for the timestep sensitivity study.

	$\overline{U}_{slipstream}$		$\sigma_{slipstream}$		C_D
	Maximum	Location	Maximum	Location	
URANS ($0.05T_{ref}$)	0.130 (-5.1%)	6.24H	0.097 (+15.5%)	3.77H	0.267
URANS ($0.025T_{ref}$)	0.130 (-5.1%)	5.82H	0.094 (+11.9%)	4.56H	0.265
SAS ($0.025T_{ref}$)	0.111 (-19.0%)	6.61H	0.069 (-17.9%)	5.61H	0.269
SAS ($0.0025T_{ref}$)	0.117 (-14.6%)	6.82H	0.071 (-15.5%)	5.61H	0.268
IDDES ($0.025T_{ref}$)	0.119 (-13.1%)	6.61H	0.078 (-7.1%)	5.61H	0.274
IDDES ($0.0025T_{ref}$)	0.120 (-12.4%)	6.56H	0.079 (-6.0%)	5.61H	0.273
Wind Tunnel	**0.137**	**8.03H**	**0.084**	**6.46H**	**N/A**

of timesteps considered, the accuracy of predicting highly turbulent flow is only weakly dependent on the timestep, except for the URANS model. The results from Fig. 2.11 show that the difference between SAS and IDDES is small in terms of $\overline{U}_{slipstream}$, while IDDES has a slightly better prediction of $\sigma_{slipstream}$.

Compared with SAS and IDDES, URANS over-predicts both $\overline{U}_{slipstream}$ and $\sigma_{slipstream}$. Regarding the force prediction, C_D is insensitive to the timestep regardless of the turbulence model. According to this comparison, the optimal solver timesteps for URANS, SAS and IDDES is chosen as $0.05T_{ref}$, $0.025T_{ref}$, $0.0025T_{ref}$, respectively.

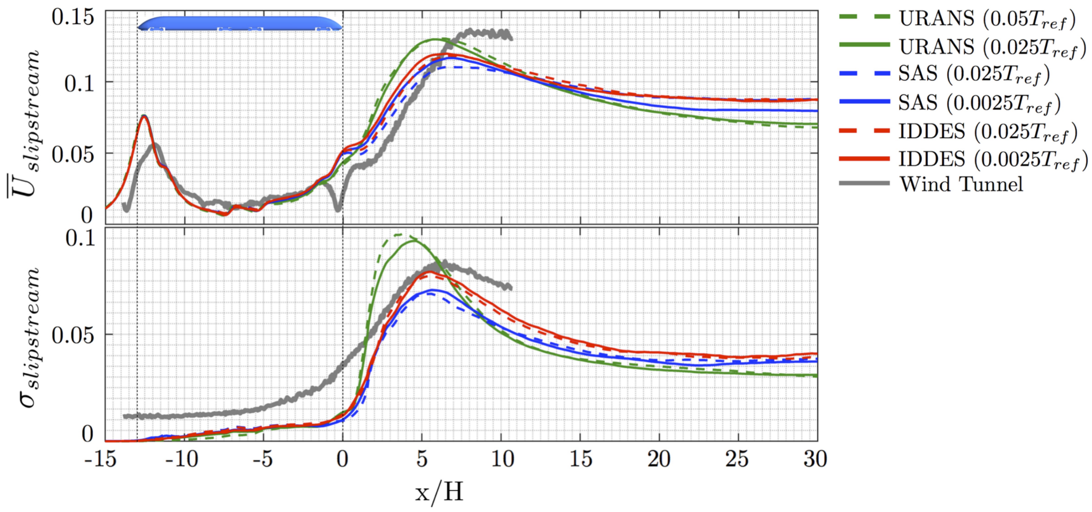

FIGURE 2.11: The comparison of $\overline{U}_{slipstream}$ and $\sigma_{slipstream}$ at the trackside heights for the timestep sensitivity test.

2.4.4 Data Sampling

For all simulations in this study, the flow field is initialised with a second-order accurate steady-state RANS simulation based on the Shear-Stress Transport (SST) RANS model.

Unsteady statistics are obtained by averaging the flow after it is first checked to have reached its asymptotic state. This is checked through comparisons with predictions from smaller averaging periods. Unsteady statistics are gathered over $195T_{ref}$, which is equivalent to three times the time taken for the freestream flow to advect through the entire domain from inlet to outlet, or approximately 15 times the time taken for the flow to advect the length of the train.

2.5 Validation and Uncertainty Analysis

The numerical model is validated against wind tunnel experiments that were conducted at Monash University based on the same ICE3 train geometry, and the key numerical modelling parameters: solver timestep, grid resolution and turbulence model, are deduced from this comparison. The layout of the wind-tunnel experiment and the schematic of the set-up are presented in Fig. 2.12 (a) and (b), respectively. In terms of the slipstream assessment, time-averaged wake structure and wake dynamics in general, good agreement is seen between the different turbulence model predictions and physical experiments. In addition to the relatively small influences of the grid resolution and timestep, potential causes of discrepancies between the numerical and experimental results in each region are discussed below.

2.5.1 Nose Region

First of all, the discrepancy in the peak slipstream velocity magnitude might be caused by slightly different floor configurations. Even though the cross-sectional dimensions of the ballast for the CFD and wind-tunnel modelling are identical, for the numerical simulations the ballast starts at the domain inlet, whereas the ballast for wind tunnel experiment only starts just upstream of the head of the train with a ramp (Bell *et al.* 2016b) (due to restrictions imposed by the working section of the wind tunnel), as shown in Fig. 2.12. Additionally, the slight shift of the location of the peak $\overline{U}_{slipstream}$ location might be caused by a slightly different length of the HST models: the wind tunnel model has an exact length of 5 m, while the numerical model has a slightly longer length of 5.165 m based on the model provided by the DIN Standards Railway Committee (CAD 2014). Note that the streamwise origin for both models is at the tail of the HST.

2.5.2 Train Side Boundary Layers

The higher slipstream standard deviation seen along the length of the train is due to the upstream turbulence present in the tunnel. In comparison, the numerical simulations show negligible standard deviation along the train, despite the turbulence level at the inlet nominally being approximately set to the tunnel background turbulence level. This suggests that it is necessary to better duplicate upstream background turbulence, including relevant time and length scales of turbulent structures. As reported previously, FLUENT has two different ways to generate synthetic turbulence at the domain inlet. Although not included for the current set of simulations, this is clearly worth exploring for future modelling efforts.

2.5.3 Near-wake Region

The main discrepancy in the near-wake region (around the tail) is that the wind-tunnel experiment shows a local slipstream minimum, which is not seen in any of the numerical simulations. Possible causes include the following. First of all, slight simplification of the numerical HST model, especially the underbody structures, may alter the underbody flow which interacts with the downwash over the upper surface in the near-wake region. Secondly, as this local minimum is not recorded in other moving model experiments and full-scale testing for the same train model, this may imply that the near-wake flow is sensitive to the wind-tunnel measurement techniques (Bell *et al.* 2014b). The slipstream velocity is calculated based on U_{GF} and V_{GF} (Eqn. 1.1 and 1.2). While in most of the wake region U_{GF} is significantly higher than V_{GF}, near the tail the magnitude of U_{GF} drops to zero, and then gradually increases on moving further downstream. Therefore, in the region, $U_{slipstream}$ is dominated by V_{GF}. The experiments use 4-hole cobra probes to determine U_{TF} and V_{TF}. In terms of the raw measuring data, the V_{TF} is much smaller than U_{TF} by an order of magnitude, and this might amplify errors in this region.

2.5.4 Intermediate-wake Region

The discrepancy in the intermediate wake ($x = 5 \sim 8H$) may be caused by amplification of upstream deficiencies or local effects. The difference in background turbulence levels between the simulations and experiments may be one possible cause. In addition, the peak slipstream velocity is recorded about $8H$ behind the tail, which is moving beyond the optimal working section of the tunnel. Imposed pressure gradients in this region may have a small effect on the results.

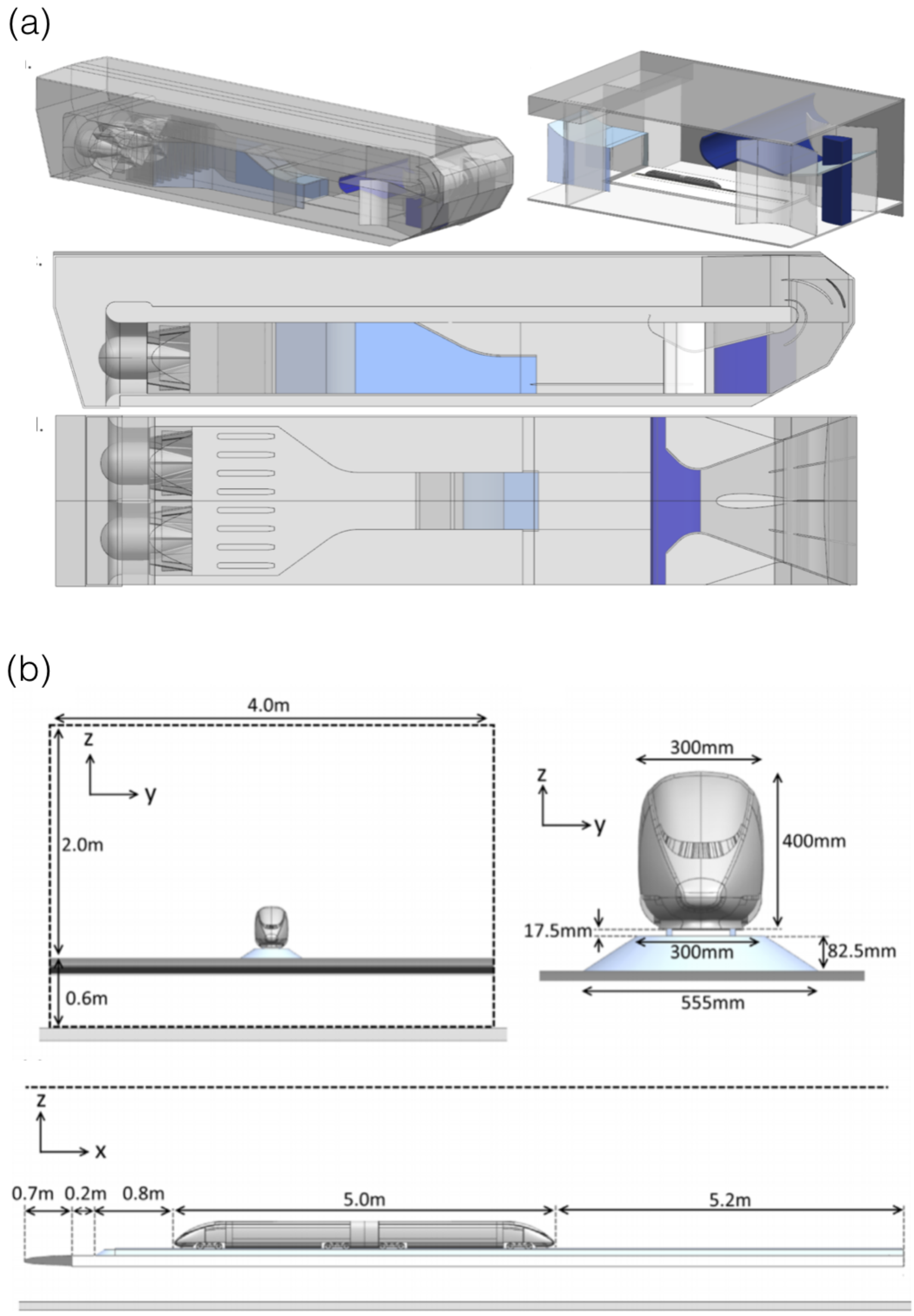

FIGURE 2.12: Illustration of the wind-tunnel experiment used for validation: (a) layout of the wind tunnel; (b) schematic of the wind tunnel test section. Image obtained from Bell (2015).

Chapter 3

Post-Processing Techniques

This chapter aims to provide a comprehensive description of the three extensively applied post-processing techniques in this research program: gust analysis (§ 3.1), conditional phase-averaging and cross-correlation (§ 3.2), and proper orthogonal decomposition (§ 3.3). The function of each technique followed by a description of the implementation procedure is presented in the corresponding sections.

3.1 Gust Analysis

According to the description of the *TSI value* calculation procedure as presented in Appendix A, the measurement in performed based on a ground-fixed reference frame, where the measurement is taken at a fixed position on the ground with a train passing through still air. However, numerical simulations are based on a train-fixed reference frame, where the train model is fixed with air moving past it. To artificially replicate the field-testing approach for numerical simulations, gust analysis is implemented using the *Moving Probe Technique*. This technique was initially introduced by Muld *et al.* (2012b), and a step-by-step procedure is described below, and an example of applying the moving probe technique to calculate the *TSI value* is given in § 4.2.1.

Step 1:

The first step is to place an artificial probe at the starting point of a slipstream measurement line (according to the TSI specified location), and then allow this probe to move downstream at the freestream speed (U_∞). The longitudinal span of the slipstream measurement line is checked to cover the entire flow disturbance region, where the slipstream effect is significant. The streamwise and spanwise velocity (U_{GF} and V_{GF}) are recorded over the time taken for the probe to travel from the start to the end point, and $U_{slipstream}$ is calculated based on Eqn. 1.1 and 1.2 at the same time. To provide independence between individual measurements from two adjacent probes, the TSI (2014) requires a minimum spacing of 20 meters between two probes at field testings. To replicate this requirement in the numerical simulation, the artificial moving probes are released every 5 T_{ref} to give the equivalent spatial separation. Within the total simulation time of 195 T_{ref}, 58 independent measurements can be achieved (29 at each side), which satisfies the requirement of a minimum of 20 independent measurements, as specified in TSI (2014).

Step 2:

The equivalent of a 1 s MA (moving-average) filter (according to the TSI requirements), with the calculation is shown below, is applied to individual measurements. The typical HST operation speed is assumed to be 250 km/h, and a 1 s MA represents a moving average over 70 meters in space at full-scale. This is equivalent to 7 meters for the numerical simulations, given the reduced model scale to match the wind-tunnel model. Next, the spatial filter length can be converted back to an equivalent temporal scale of $17.5T_{ref}$, and then applied to the measurements obtained from *Step 1*.

Step 3:

The maximum reading of individual filtered measurement is then recorded as U_{peak} The time-average and standard deviation of the scattered distribution of U_{peak} are then calculated and denoted as $\overline{U}_{peak}$ and σ_{peak}.

Step 4:

The final maximum slipstream velocity U_{max} (also known as the *TSI value*) can be obtained by substituting $\overline{U}_{peak}$ and σ_{peak} into

$$U_{max}(\mathit{TSI\ value}) = \overline{U}_{peak} + 2\sigma_{peak}. \tag{3.1}$$

In this study, the duration of the equivalent sampling time of per artificial probe is $52T_{ref}$, with the starting and ending time for the train passage corresponding to $2.5T_{ref}$ and $15.4T_{ref}$, respectively.

3.2 Conditional Phase-averaging and Cross-correlation

Unlike traditional time-averaging, phase-averaging is useful to identify the periodic flow behaviour. Additionally, a band-pass filter is integrated with the phase-averaging to extract the periodic motion from small-scale chaotic flow features. In this project, conditional phase-averaging is intensively used for studying the periodic wake characteristics; for example, the spanwise oscillation of the wake structures. For this reason, cross-correlation is always coupled with the phase-averaging to interpret the spanwise motion by determining the phase-correlation (i.e. time-delay) of the spanwise velocity (V_{GF}) between two centre-plane symmetric points. The detailed procedure is presented as follows.

Step 1:

The first step is to select a reference point in the flow field that the phase-average is based on. The underlying strategy of the reference point selection is that the point should be placed where a specific flow structure is known to occur. For the purposes of the analysis here, this can be determined through examination of the frequency content at a point. For example, to visualise the spanwise motion of the train wake structure, inserting the reference point inside the wake region where the oscillation is significant is better than locating the a probe in the far field.

Step 2:

The frequency content at the reference point is calculated through a *Fast Fourier Transform* (FFT), and subsequently filtered by the bandwidth filter around its dominant frequency, which is typically around $St_w = 0.19 \sim 0.21$.

Step 3:

The filtered sinusoidal reference signal is then split into cycles, and the average period is calculated. The cycles with a percentage error greater than 10% are considered as invalid and discarded. After obtaining all valid cycles, the starting and ending indices for the valid cycles are recorded.

Step 4:

All the points in the domain are then filtered and split into cycles based on the cycle indices of valid cycles of the reference signal. The cycles are then interpolated to have an identical length, and the ensemble average of the cycles is calculated. After that, the averaged cycle is divided into a certain number of bands or bins (i.e. phase ranges). In this project, the full cycle of a dynamic flow feature is deposited into 40 phase bins. A number of 40 phase bins is utilised to describe the wake motion. Thus, from the left- or right-most position to the mid-position can be described by 10 bins, by assuming a sinusoid oscillation. This is sufficient to provide an accurate representation of the wake behaviour across a cycle.

Step 5:

Finally, the periodicity of a flow feature can be determined by plotting the flow field at consecutive phase instances, and the coherence of the periodic motion is often further verified by cross-correlation.

3.3 Proper Orthogonal Decomposition

Proper Orthogonal Decomposition (POD) is a powerful technique that can be used to extract coherent transient features from a turbulent flow field, by calculating the optimal orthogonal bases of fluctuations. POD decomposes the chaotic flow field data, and extracts the POD modes (orthogonal bases) ordering them from the most to the least total energy. This makes POD very useful for identifying coherent flow structures, filtering highly turbulent data, and for data compression. POD has been extensively utilised in aerodynamics, especially the field of bluff-body aerodynamics, with applications generally having a highly turbulent wake region. In more recent years, POD has been applied to study train aerodynamics, as train wakes are very chaotic and consist of a wide range of turbulence scales. In this project, POD is used to study the turbulent train slipstream by extracting the coherent flow structures based on ordering by energy proportion. The coherent flow modes obtained by POD, are also known as POD modes or POD bases. By this manner, a complex turbulent flow field can be disassembled into a certain number of POD modes with simpler dynamical behaviour. Thus, instead of looking at the complex time-dependent turbulent flow field as a whole, one can acquire an insightful understanding of the flow field by interpreting the physical causes and features of individual modes contributing to the overall flow.

3.3.1 Introduction of Snapshot POD Method

This project utilises the *Snapshot POD* method, which was originally proposed by Sirovich (1987). This method has been widely used to analyse the turbulent flow structures of many aspects of flows, and it has been well developed as a robust and powerful post-processing tool for extracting coherent flow structures from the snapshots of flow field. Even though the method is compatible with uneven distributed snapshots, i.e., unequal time increments between samples, using a weighting function; this project does not incorporate this aspect as all snapshots are automatically exported at a constant sampling frequency during data acquisition. The following description and algorithm are based on the snapshot POD method for equal timesteps. The concept of the Snapshot POD method is briefly introduced here, and then the corresponding implementation procedure within the *MATLAB* framework and applications of POD are presented.

The Snapshot POD is based on the time-series flow data at a fixed spatial location, and the flow data at each time instance is referred as a snapshot. For example, the time-series data of slipstream velocity on a vertical plane within the wake region is a typical input for Snapshot POD analysis. The input matrix ($\Phi(x,t)$) is constructed by a series of snapshots of the raw flow data, and each snapshot is reshaped as a column vector. The arrangement of $\Phi(x,t)$ is illustrated in the Eqn. 3.2. For a data set consisting of m grid points sampled over n timesteps, it has a size of $[m \times n]$.

$$\begin{aligned}\Phi(x,t) &= [\phi_1 \quad \phi_2 \quad \phi_3 \quad ... \quad \phi_n] \\ &= \begin{bmatrix} \phi(x_1,t_1) & \phi(x_1,t_2) & \phi(x_1,t_3) & ... & \phi(x_1,t_n) \\ \phi(x_2,t_1) & \phi(x_2,t_2) & \phi(x_2,t_3) & ... & \phi(x_2,t_n) \\ \phi(x_3,t_1) & \phi(x_3,t_2) & \phi(x_3,t_3) & ... & \phi(x_3,t_n) \\ \vdots & \vdots & \vdots & \ddots & \vdots \\ \phi(x_m,t_1) & \phi(x_m,t_2) & \phi(x_m,t_3) & ... & \phi(x_m,t_n) \end{bmatrix} (size : [m \times n]).\end{aligned} \tag{3.2}$$

The ultimate aim of POD is to determine the optimal orthogonal pairs which give:

$$\Phi(x,t) \approx \sum_{i=1}^{N_M} (a_i(t)\sigma_i(x))^T = (A \times S)^T, \tag{3.3}$$

where

$$A = \begin{bmatrix} a_1(t_1) & a_2(t_1) & ... & a_{N_M}(t_1) \\ a_1(t_2) & a_2(t_2) & ... & a_{N_M}(t_2) \\ \vdots & \vdots & \ddots & \vdots \\ a_1(t_n) & a_2(t_n) & ... & a_{N_M}(t_n) \end{bmatrix} (size : [n \times n]), \tag{3.4}$$

$$S = \begin{bmatrix} \sigma_1(x_1) & \sigma_1(x_2) & ... & \sigma_1(x_m) \\ \sigma_2(x_1) & \sigma_2(x_2) & ... & \sigma_2(x_m) \\ \vdots & \vdots & \ddots & \vdots \\ \sigma_{N_m}(x_1) & \sigma_{N_m}(x_2) & ... & \sigma_{N_m}(x_m) \end{bmatrix} (size : [n \times m]). \tag{3.5}$$

The matrices A and S are known as the mode coefficient matrix and POD basis, respectively. The number of modes (N_m) equals to the number of time-steps of the raw data (n). The mode coefficient describes the temporal dependence of each mode, while the POD basis identifies the spatial structure of each mode. The arrangements of A and S are illustrated by

$$A = \begin{bmatrix} Mode(1) & Mode(2) & ... & Mode(n) \\ \uparrow & \uparrow & \uparrow & \uparrow \\ \vdots & Time & Series & \vdots \\ \downarrow & \downarrow & \downarrow & \downarrow \\ Mode(1) & Mode(2) & ... & Mode(n) \end{bmatrix} (size : [n \times n]), \tag{3.6}$$

$$S = \begin{bmatrix} Mode(1) & \leftarrow & ... & \rightarrow & Mode(1) \\ Mode(2) & \leftarrow & Spatial & \rightarrow & Mode(2) \\ \vdots & \leftarrow & Grids & \rightarrow & \vdots \\ Mode(N_m) & \leftarrow & ... & \rightarrow & Mode(N_m) \end{bmatrix} (size : [n \times m]). \tag{3.7}$$

In regard to the aim of determining the orthogonal pairs (Eqn. 3.3), the mathematical formulation is to solve for the minimum of I, with I given by

$$I = \frac{1}{T} \int_T \int \int_\Omega \left(U(x,t) - \sum_{i=1}^{N_M} a_i(t)\sigma_i(x) \right)^2 d\Omega dt, \tag{3.8}$$

where Ω represents the two-dimensional spatial mode distribution (for a planar data set), and T represents the temporal domain.

3.3.2 Implementation Procedure

Based on the concept of Snapshot POD as introduced in Section 3.3.1, the procedure of the POD calculation is presented here. The algorithm is written based on the Snapshot POD method proposed by Sirovich (1987), and has been applied to study HST wake structures based on both numerical (Muld *et al.* 2012a) and experimental data (Bell *et al.* 2016a). The present code is developed and implemented under a MATLAB framework, but the underlying concept is of course general.

Step 1:

The first step is to calculate the temporal auto-correlation matrix (C) of the raw data ($\Phi(x,t)$), and normalise it by the number of time-steps (n):

$$C = \frac{\Phi^T \times \Phi}{n}. \tag{3.9}$$

Step 2:

The eigenvalue (Λ) and eigenvector (A) matrices of the auto-correlation matrix C are computed by *Singular Value Decomposition* (SVD), which decomposes C into three components as shown in Eqn. 3.10:

$$C = A \times \Lambda \times \mathcal{R}^T, \tag{3.10}$$

where:

- A is the left singular matrix, also known as the mode coefficient matrix in Eqn. 3.3;
- Λ is the diagonal matrix which contains energy information of each mode;
- $\mathcal{R}^T$ is the transpose of the right singular matrix, which is not used in further calculations.

The decomposition given in Eqn. 3.10 is obtained using the Matlab in-built function *svd.* For a full description of the svd algorithm see Golub & Van Loan (2012).

Step 3:

The spatial POD basis matrix is obtained by projecting the raw data onto the mode coefficient matrix, as illustrated in the Eqn. 3.11

$$S = (\Phi * A)^T, \tag{3.11}$$

where S is the POD basis matrix containing the spatial distribution of each mode ($\sigma_i(x)$), as illustrated in Eqn. 3.3. To normalise per POD basis, each mode basis vector (i represents the mode index) is divided by its second-norm ($\|\sigma_i(x)\|$), as presented in Eqn. 3.12

$$M_i(x) = \frac{\sigma_i(x)}{\|\sigma_i(x)\|}. \tag{3.12}$$

This makes the norm of each mode basis ($\|M_i\|$) unity, and integrating the scalar product over the spatial domain for each mode equal to 1.

$$\langle M_i \cdot M_i \rangle_\Omega = 1, \tag{3.13}$$

where $\langle \cdots \rangle_\Omega$ is a shorthand notation for $\int_\Omega \cdots d\Omega$.

3.3.3 POD Mode Convergence

It is important to verify that the sampling time is sufficient to achieve converged POD modes, i.e., those actually representative of the long-term flow evolution. In this project, convergence is checked by the orthogonality (ε_{orth}) between *identical* modes that are determined by two different sampling times (denoted as $M_{i,a}$ and $M_{i,b}$). Note that ε_{orth} can be considered to be an indicator of the angle between two modes, through the expression for ε_{orth} presented below. Theoretically, a fully converged POD mode should achieve a ε_{orth} close to unity. To start with, the *angle* between $M_{i,a}$ and $M_{i,b}$ can be obtained from

$$\cos\theta = \frac{\langle M_{i,a} \cdot M_{i,b} \rangle_\Omega}{\|M_{i,a}\| \cdot \|M_{i,b}\|}. \tag{3.14}$$

Additionally, since Eqn. 3.13 shows that all mode arrays (M_i) are normalised, i.e., $\|M_{i,a}\| \cdot \|M_{i,b}\|$ equals to unity. Therefore, the angle between $M_{i,a}$ and $M_{i,b}$ can be described by $\langle M_{i,a} \cdot M_{i,b} \rangle_\Omega$, which is defined as ε_{orth} in this study:

$$\varepsilon_{orth} = \langle M_{i,a} \cdot M_{i,b} \rangle_\Omega . \tag{3.15}$$

3.3.4 Application of POD

In this project, the POD is utilised for the following two purposes: to extract dominant flow features and to allow reduced-order flow-field reconstruction.

The dominant flow features (spatial mode distribution) is visualised by projecting the specific mode vector (M_i) onto the corresponding spatial grid. Additionally, the energy of each mode can be determined by the diagonal elements of the eigenvalue (Λ) matrix, denoted as $E(i)$. Therefore the percentage of the total fluctuating energy of an arbitrary mode (e.g., mode c: E_c) can be obtained from

$$E_c = \frac{E(c)}{\sum_{i=1}^{n} E(i)}. \tag{3.16}$$

The energy percentage (E_c) can be used to determine the energy percentage of a specific mode, and also importantly, how many modes are required to recover a certain amount of the total energy.

Additionally, the transient flow field can be approximated by a reduced-order reconstruction based on the first few mode coefficients of A and the matching POD bases of S according to Eqn. 3.3. An example of reconstruction based on the first three mode is demonstrated in Eqn. 3.17:

$$\begin{aligned}\Phi_{mode1,2,3}(x,t) &= \sum_{i=1}^{3}(a_i(t)\sigma_i(x))^T \\ &= (a_1(t)\sigma_1(x))^T + (a_2(t)\sigma_2(x))^T + (a_3(t)\sigma_3(x))^T \\ &= (A[n,3] \times S[3,m])^T.\end{aligned} \tag{3.17}$$

Note that the reduced-order reconstruction can also be considered as a filtered representation of the flow, and naturally allows a method of compressing the dataset.

Chapter 4

Performance of Different Turbulence Models

4.1 Problem Description

This study investigates and evaluates the performance of three widely-used turbulence models: URANS, SAS and DES, to predict slipstream of a full-featured generic train model, and the results are compared with wind-tunnel experimental data to determine the fidelity of the models. Specifically, this study aims to determine the suitability of different turbulence modelling approaches, involving significantly different computational resources, for modelling different aspects of slipstream. Generally, a model that captures more of the full range of flow structures is more computationally demanding. Therefore, a trade-off exists between accuracy and computing cost. However, a systematic comparison of the strengths and weaknesses of different turbulence models for predicting different aspects of HST slipstream is yet to be undertaken, and this has motivated this current study. Specifically, this study aims to investigate and evaluate the accuracy of three widely used turbulence models, URANS, SAS and DES, for predicting the flow field around a typical HST model: *ICE3*, and the detailed description of each turbulence model is presented in § 2.2.

For URANS, the case with timestep $= 0.05T_{ref}$ and the coarse mesh was utilised, as the mesh independence test in § 2.3.2 shows that URANS predictions are not sensitive to the grid size, at least beyond a minimum level. Whilst there is some timestep dependence, the underlying philosophy for selection here is that the URANS model should be considerably cheaper than the other more complex models, especially as the turbulent time and length scales are not a function of temporal or spatial modelling scales.

The medium mesh with the timestep of $0.025T_{ref}$ was selected for SAS, to optimise the balance between the cost and accuracy. As an adaptive method, its accuracy is based on the solver settings, switching between URANS and LES-like modelling capability as spatial and temporal resolution are increased.

For IDDES, the fine mesh with a timestep of $0.0025T_{ref}$ was employed, as good practice for DES simulations requires a local Courant number of unity or less. Overall, IDDES is typically used to study transient flow behaviour, with a range of spatial (and temporal) scales extending into the inertial subrange.

4.2 Results and Analysis

The performance of different turbulence models are evaluated from three perspectives: gust analysis, mean flow structure and wake dynamics, and the numerical results are compared with wind tunnel experimental data to determine the fidelity of the models.

4.2.1 Gust Analysis

The gust analysis utilises the *Moving Probe technique*, which was previously applied by Muld *et al.* (2012b) to study slipstream under TSI specifications. To begin with, a brief introduction of the gust analysis technique is presented below, and more details can be found in § 3.1.

The first step is to place an artificial probe at the starting point of a slipstream measurement line, and then allow this probe to move downstream at the speed of U_∞. Over the time taken for this probe to travel from the start to the end point, U_{GF} and V_{GF} are recorded, and then $U_{slipstream}$ is calculated based on Eqn. 1.1, and plotted as grey solid curves in Fig. 4.1. To replicate the 20 meters distance between two individual measurements in a field testing environment, the artificial moving probes are released every $5T_{ref}$. Thus, within the total simulation sampling time of $195T_{ref}$, 58 independent measurements can be made (29 at each side), which satisfies the requirement of minimum 20 independent measurements of the TSI regulations (TSI 2014). The peak values of individual measurements are plotted as black dot points, and the mean and standard deviation of the peak values are calculated and presented in Table 4.1. Next, the equivalent of a 1s MA filter is applied to each data set, and presented as light blue curves in Fig. 4.1, with the peak values indicated by the blue dot points. The final maximum slipstream velocity $U_p + 2\sigma_{uv}$ under a 1s MA filter is calculated and presented in Table 4.1. In practice, the maximum value would be compared with the maximum allowable slipstream velocity specified by TSI as a part of an acceptance procedure. In this study, the duration of the equivalent sampling time of per artificial probe is $52T_{ref}$, with the starting and ending time for the train passage corresponding to $2.5T_{ref}$ and $15.4T_{ref}$, respectively.

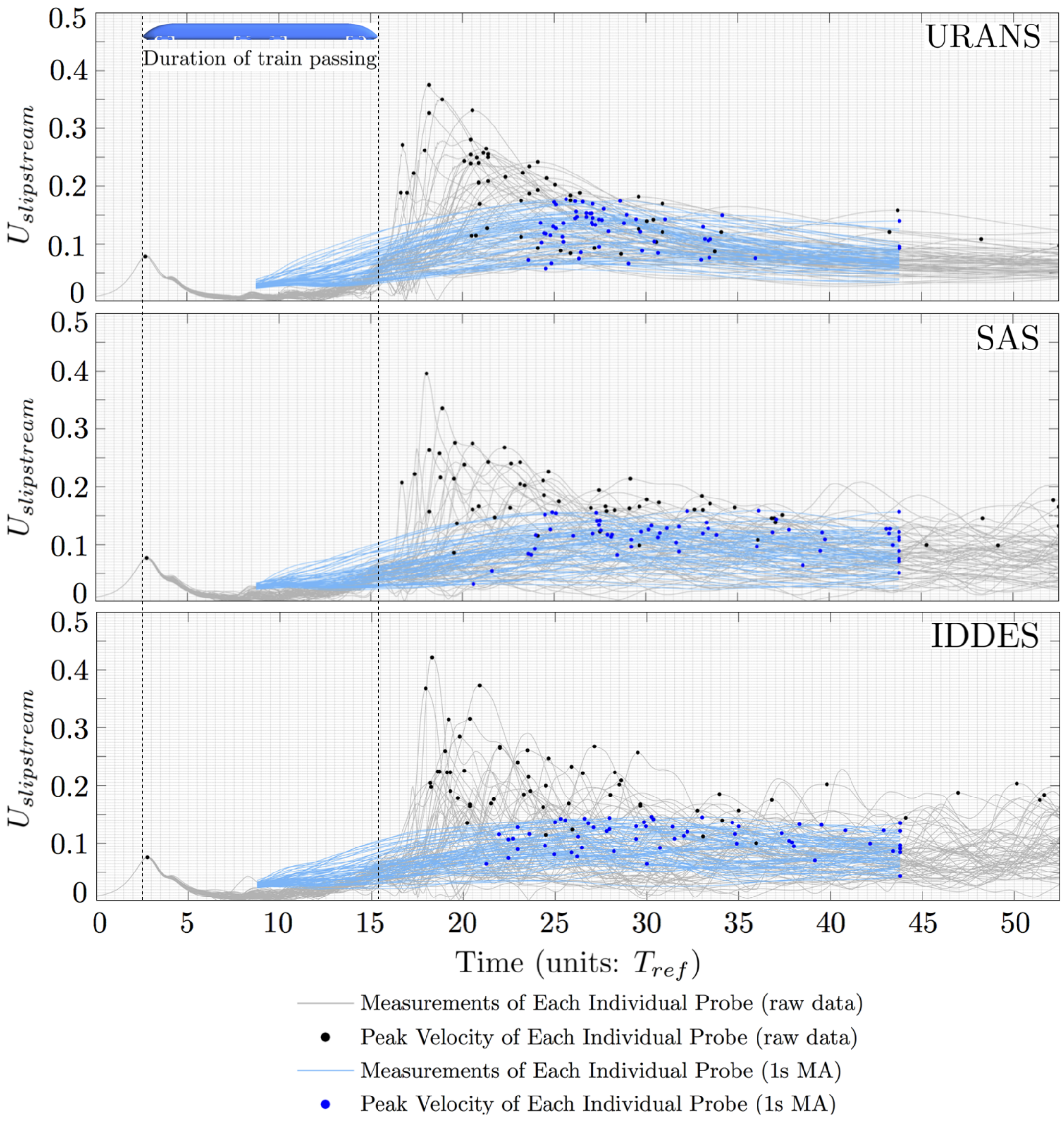

FIGURE 4.1: The gust analysis based on the measurements from the artificial *moving probe technique* under TSI regulation.

From Fig. 4.1, the models predict that the maximum $U_{slipstream}$ occurs in the wake about $2 \sim 25$ T_{ref} after the tail. Although all the turbulence models depict a statistically similar distribution, a significant run-to-run variance is observed between model data sets, especially for IDDES. This large variation is also reported in full-scale and

Table 4.1: The unsteady statistics of gust measurement with and without applying a 1 second moving average.

	Without 1s MA			With 1s MA		
	$\overline{U}_p$	σ_{uv}	$\overline{U}_p + 2\sigma_{uv}$	$\overline{U}_p$	σ_{uv}	$\overline{U}_p + 2\sigma_{uv}$
URANS	0.189	0.073	0.335	0.125	0.033	0.189
SAS	0.183	0.060	0.302	0.114	0.028	0.170
IDDES	0.207	0.065	0.338	0.111	0.024	0.159
Wind Tunnel	**0.322**	**0.138**	**0.597**	**0.118**	**0.021**	**0.159**

scaled experiments, and this is indeed one of the practical difficulties in quantifying slipstream (Bell *et al.* 2015)(Baker 2010). The underlying cause can be seen through examining time-averaged and transient wake properties in § 4.2.2 and § 4.2.3, respectively.

Perhaps of interest is that the maximum peak gust velocity observed in individual runs can be more than a factor of two higher than the filtered $U_p + 2\sigma$ level, and since the pressure disturbance varies with the square of the velocity, this equates to more than a factor of four in the force experienced by a commuter.

4.2.2 Time-averaged Wake Structure

Based on results from previous studies, the dominant wake flow structure of a HST is a pair of counter-rotating vortices (Bell *et al.* 2016a). For this study, the time-averaged wake structure is visualised by x-vorticity (streamwise), in-surface projected velocity vectors and the boundaries of the vorticity-dominated regions, on six vertical planes in the wake, as presented in Fig. 4.2. As the time-averaged flow structure is symmetric about the mid-plane, only the left half of the flow field is presented. The vorticity is calculated based on the normalised spanwise and transverse velocities (v,w). The boundary of the trailing vortex structure corresponds to the iso-line of $\Gamma_2 = 2/\pi$, which is a common vortex identification method often chosen by experimentalists (Graftieaux *et al.* 2001). The two green asterisks represent the locations of trackside and platform slipstream measurement height based on the TSI specifications.

Through Fig. 4.2, the downstream evolution of the time-mean trailing vortices can be visualised as the plane shifts from $x = 0.5H$ to $x = 6H$. Qualitatively, all three methods show a similar flow structure to that from the wind tunnel measurements. As the vortices move downstream, they roll over the rails and move apart from each other in the spanwise direction. Despite vorticity diffusion and cross-annihilation, the

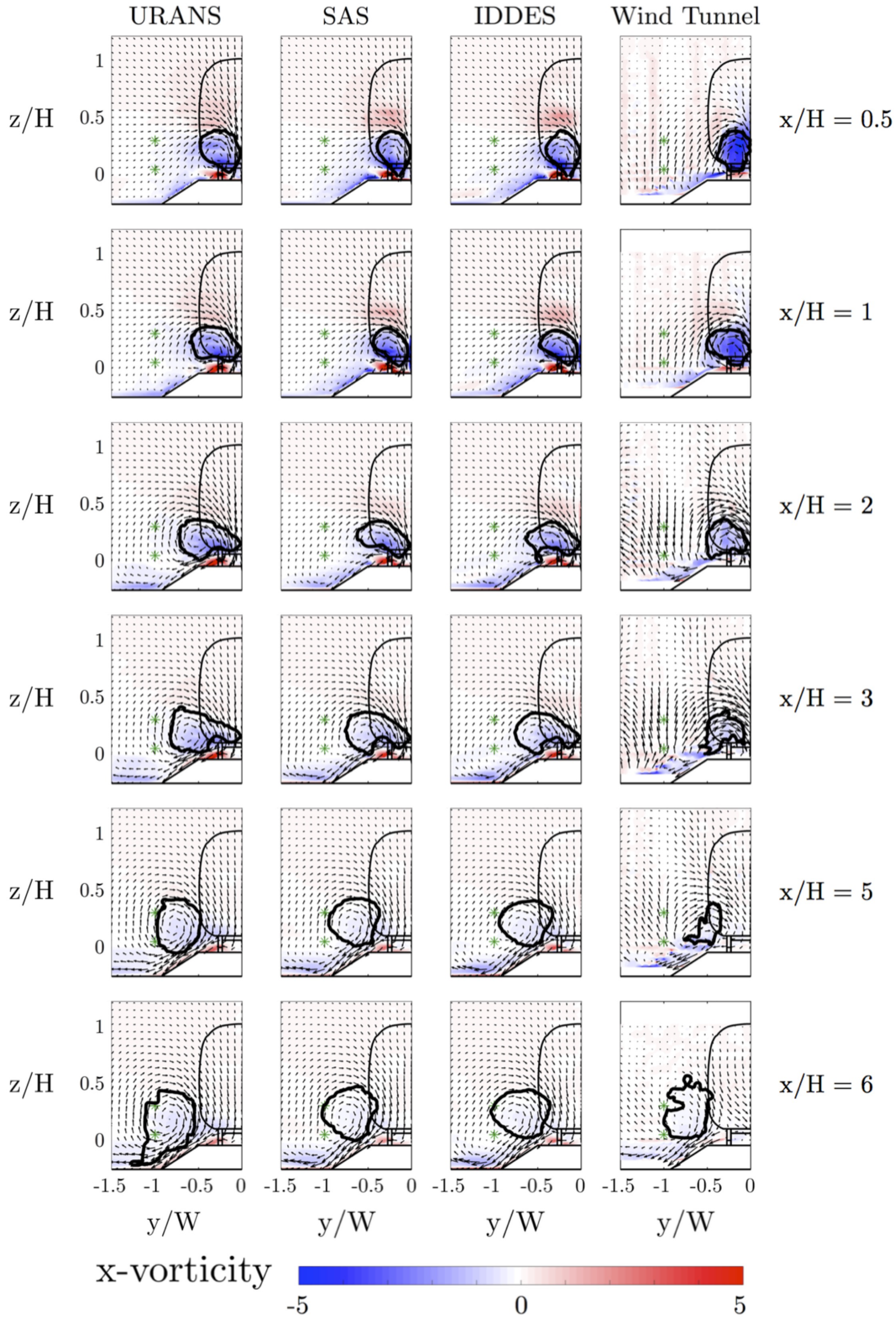

FIGURE 4.2: The comparison of the time-averaged wake structure resolved by different turbulence models. The vortex boundaries, shown by the black lines, are identified by the Γ_2 criterion.

boundary size increases as the vortical structures advect downstream.

Quantitatively, compared with SAS, IDDES and experimental measurements, the vortex boundary predicted by URANS crosses the slipstream measurement lines at an earlier downstream point. As the vortex core contains lower momentum fluid, this induces a higher local slipstream velocity. From the contribution of large-scale streamwise vortical structures to the overall wake structure, it can be seen that the slipstream velocity is not only sensitive to the strength of the trailing vortex arms, but also their location. Therefore, accurately predicting the location and size of these vortices is critical for accurate slipstream assessment. As the wake structure is highly turbulent and shows strong variation between runs, representative prediction of the vortex location, size and cross-stream movement is challenging both numerically and experimentally. Experimentally, the location of the vortices may be affected by the environment conditions, for example the ambient wind conditions, and invasive measurement techniques. Numerically, to achieve good accuracy of the predicted $U_{slipstream}$ requires adequate resolution of the region for up to at least $5 \sim 10H$ downstream, since this is where the maximum slipstream velocity occurs. This requires a large mesh refinement region in the wake and a sufficiently small timestep, satisfying both requirements can be computationally demanding.

4.2.3 Wake Dynamics

According to the wind tunnel experiments, the wake witnesses a strong spanwise oscillation at a Strouhal number (St_W) of $0.19 \sim 0.21$, based on train width (W) (Bell *et al.* 2016b). In this study, the spanwise oscillation is visualised by phase-averaging the pressure coefficient C_P in a horizontal plane at $z = 0.15H$. This study adopts the same formula of calculating C_P as used for the wind tunnel experiments (Bell *et al.* 2016a), which is defined as:

$$C_P = \frac{P_i - P_s}{P_t - P_s}, \tag{4.1}$$

where P_i is the local static pressure that C_P is based on, and P_t is the total pressure, noting that due to the limitation of the measuring technique, it only takes the streamwise component of velocity into account. P_s is the reference static pressure from an upstream reference pitot-static tube. As for the numerical simulations the reference pressure is defined as zero static pressure at outlet, for the numerical comparison a value of $P_s = -0.025$ is used to account for the increased downstream losses in the wind tunnel relative to the open-domain numerical model. The phase-averaging is conducted based on the signal at a reference point with coordinates $(0.84H, -0.5W, 0.15H)$, visualised by the white circles in Fig. 4.3.

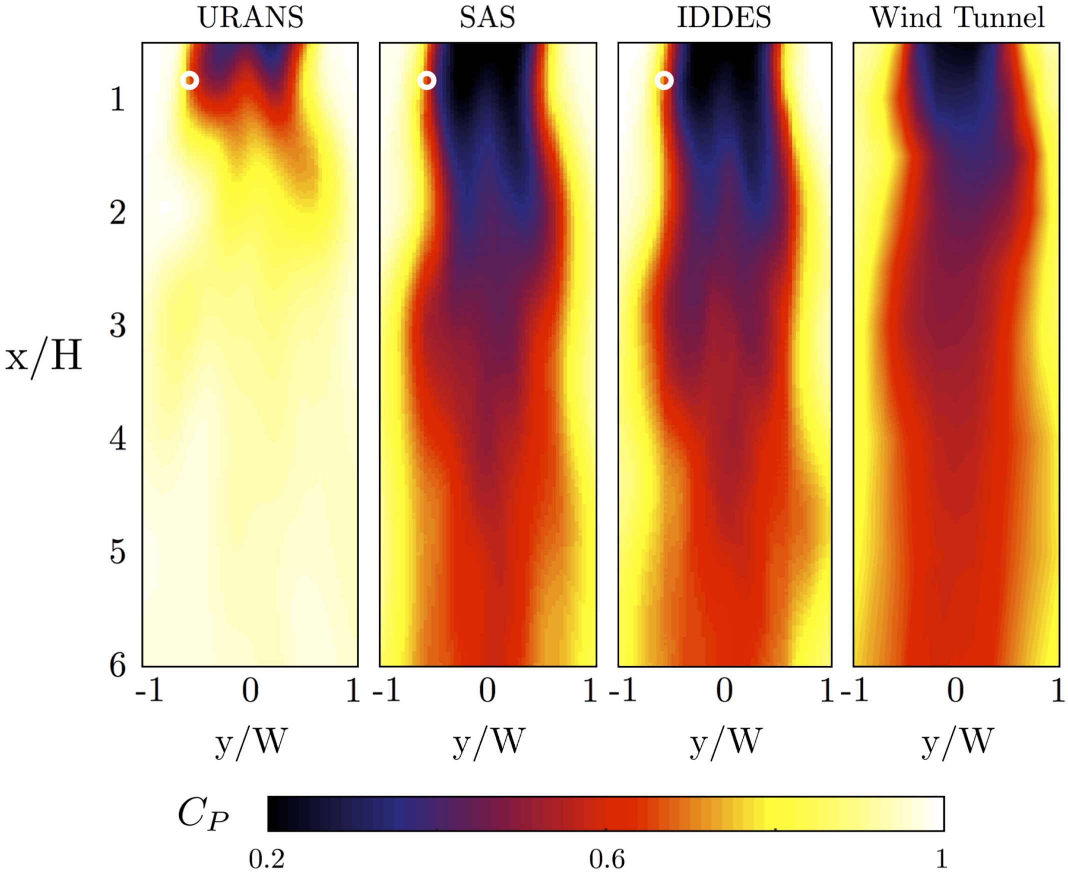

FIGURE 4.3: The comparison of transient wake structures predicted by different turbulence models based on the phase-averaged C_P in a horizontal plane at $z = 0.15H$.

As shown in Fig. 4.3, the spanwise oscillation observed in the experiments is clearly captured by all three models. Despite the different time and mesh resolutions, SAS and IDDES predict wake structures consistent with the wind tunnel experiments, with the prediction of the URANS model less good. The predicted longitudinal wavelength of the spanwise motion is close to $3H$ in each case.

Proper Orthogonal Decomposition (POD) is also used to examine the performance of each turbulence model to resolve the detailed makeup of transient wake structures. POD is a widely used technique to extract the coherent flow structures from a turbulent flow field, by calculating the optimal orthogonal bases (modes) of fluctuations. This study employs the snapshot POD method, which was initially proposed by Sirovich (Sirovich 1987), and has been applied to study HST wake structures based on both numerical (Muld *et al.* 2012b) and experimental data (Bell *et al.* 2016b). In this study, the POD is conducted based on the total pressure (in line with the experiments) on a vertical plane at the location of $x = 0.5H$, and the first four energetic modes are presented in Fig. 4.4.

Qualitatively, the first four most energetic modes resolved by different turbulence models are consistent with the wind tunnel measurements (Bell *et al.* 2016a). The structures of the first two modes show approximately the same sizes of time-averaged longitudinal vortices as depicted in § 4.2.2. The first mode indicates that the most energetic component is an out-of-phase increase/decrease, which associates with a left/right oscillation in the strength of the trailing vortices, is inline with the phase-averaged results. The second mode shows a simultaneous energy increase/decrease centred on the vortices, corresponding to a longitudinal pulsing of the trailing vortices. The third and fourth modes illustrate smaller energy oscillations above the ballast shoulder. Mode 3 indicates an symmetrical in-phase horizontal/diagonal energy oscillation, while Mode 4 shows an out-of-phase vertical energy oscillation. Modes 1 and 3 acting together can account for the spanwise oscillation of the trailing vortices as they advect downstream. Quantitatively, the mode structures predicted by SAS and DES remain closer to the centreplane, relative to those predicted by URANS. Presumably the loss of centreplane symmetry for modes 3 and 4 is an indication that the length of the dataset used to extract POD modes is insufficient; however, given the computation expense incurred for these simulations, it was difficult to justify increased integration times to better resolve these modes.

In addition to the mode contours illustrated in Fig. 4.4, the energy percentage of each mode is presented in Table 4.2 and the cumulative energy percentage distribution of the first 50 modes is shown in Fig. 4.5. According to Table 4.2 and Fig. 4.5, the energy is more concentrated in a few energetic modes for the URANS simulations, whereas IDDES and SAS indicate a wider energy distribution across the modes. For example, the total energy proportion of the first four modes for SAS and IDDES are 0.44 and 0.425 respectively, while for URANS it is 0.726. Additionally, to recover 80% of the total fluctuating energy, URANS, SAS and IDDES requires 6, 24 and 32 modes respectively. This is inline with the nature of each turbulence model that URANS only predicts the dominant structures, while IDDES and SAS resolve smaller flow structures and obtain a wider turbulence spectrum, as is discussed further below.

Additionally, the frequency content of each modelled wake is compared based on the power spectral density of U_{TF} at the point $(1H, -0.4W, 0.2H)$. The experimental

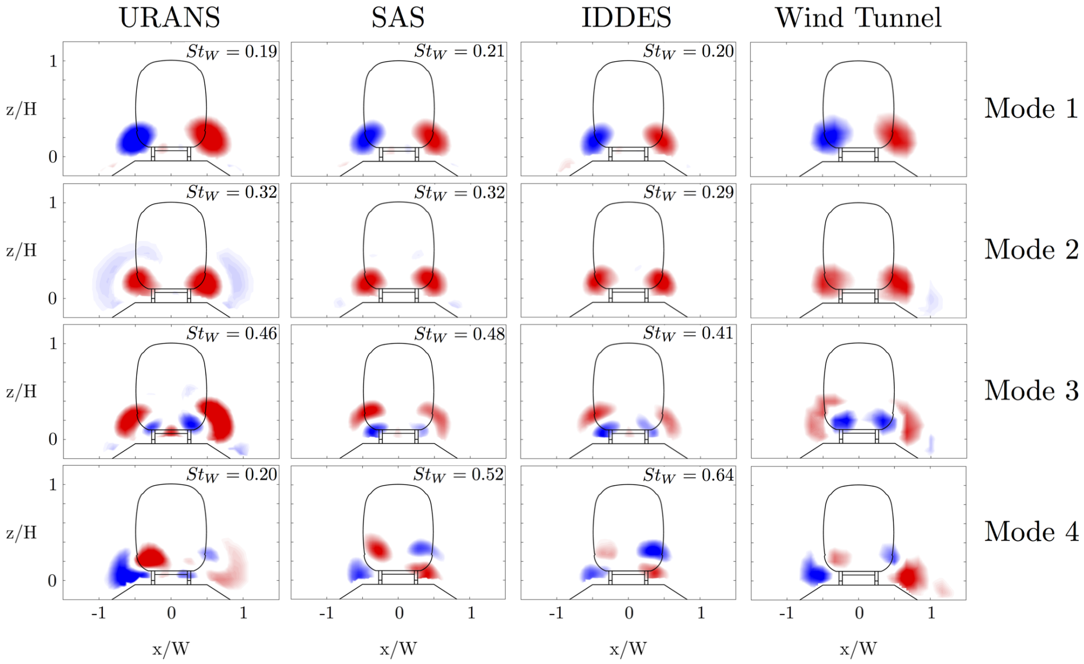

FIGURE 4.4: The comparison of first four POD mode structures at $x = 1H$.

TABLE 4.2: Energy percentage of the four most energetic POD modes

	URANS	SAS	IDDES	**Wind Tunnel**
Mode 1	0.499	0.240	0.246	**0.235**
Mode 2	0.120	0.079	0.077	**0.069**
Mode 3	0.072	0.066	0.054	**0.038**
Mode 4	0.047	0.055	0.048	**0.036**
Total	0.726	0.440	0.425	**0.387**

data shows a wide band at a dominant frequency of $St = 0.21$ (Bell *et al.* 2016b). Spectral analysis of the velocity signals from numerical simulations at the same point are presented in Fig. 4.6.

In terms of the dominant shedding frequency, all three methods achieve good agreement with the experimental data of $St = 0.19 \sim 0.21$, suggesting a Karman-like vortex shedding from the side surfaces of the train, consistent with the left-right oscillation observed in the phase-averaged wake. With respect to the broadness of the frequency spectrum, as expected, URANS has only two narrow peaks, consistent with its failure to capture finer-scale wake structures. Both SAS and IDDES show a slower decay at higher frequencies, implying that a greater range of smaller flow structures is resolved, and this is verified by the turbulent kinetic energy cascade plot presented in Fig. 4.7.

The turbulent kinetic energy spectra at the same near-wake point $(1H, -0.4W, 0.2H)$ are compared to determine the minimum turbulent length scale that each method can

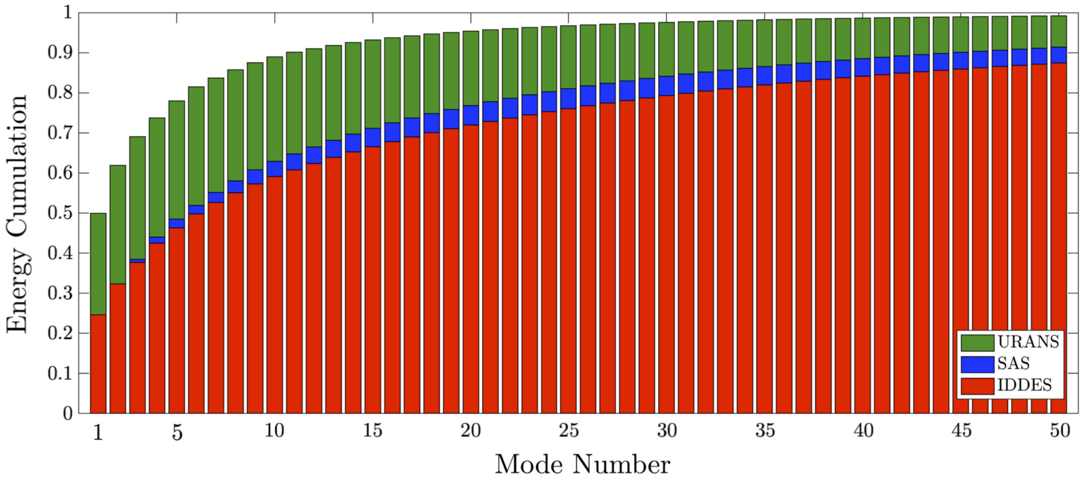

FIGURE 4.5: The cumulative energy percentage with respect to the number of modes.

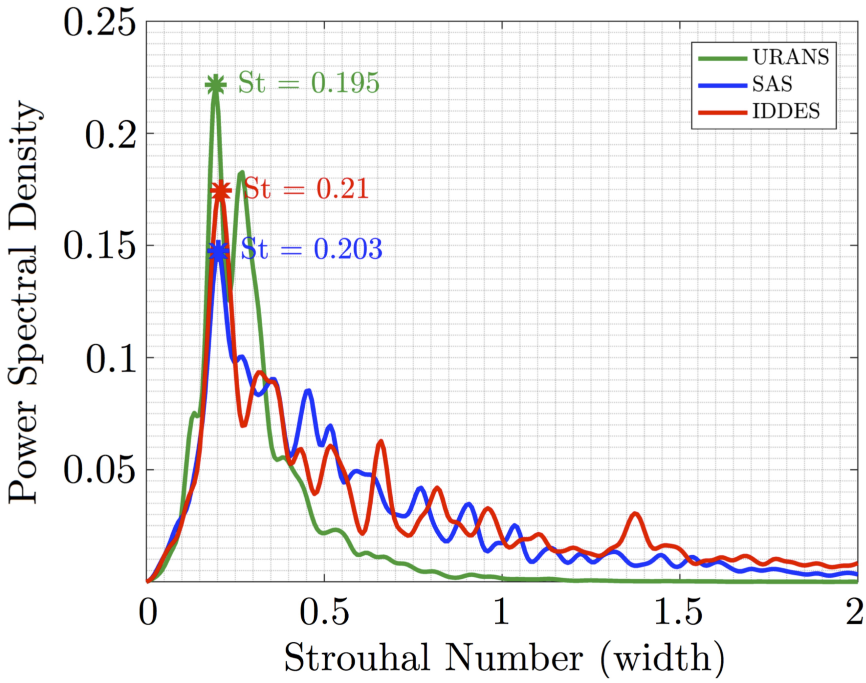

FIGURE 4.6: The comparison of wake shedding frequency based on St_w at the point of $[1H, -0.4W, 0.2H]$.

resolve, and to indicate how energy is transferred from larger to smaller length scales. Fig. 4.7 shows that all three methods achieve a similar prediction to beyond the maximum energy containing scales, which suggests that all the models can reasonably predict the formation of dominant turbulence structures in the near-wake region. In the inertial subrange, both SAS and IDDES show the expected $-5/3$ slope (Pope 2001), even though SAS shows a steeper gradient approaching the dissipation range. In contrast, URANS does not capture the inertial subrange, due to its limitation in predicting the

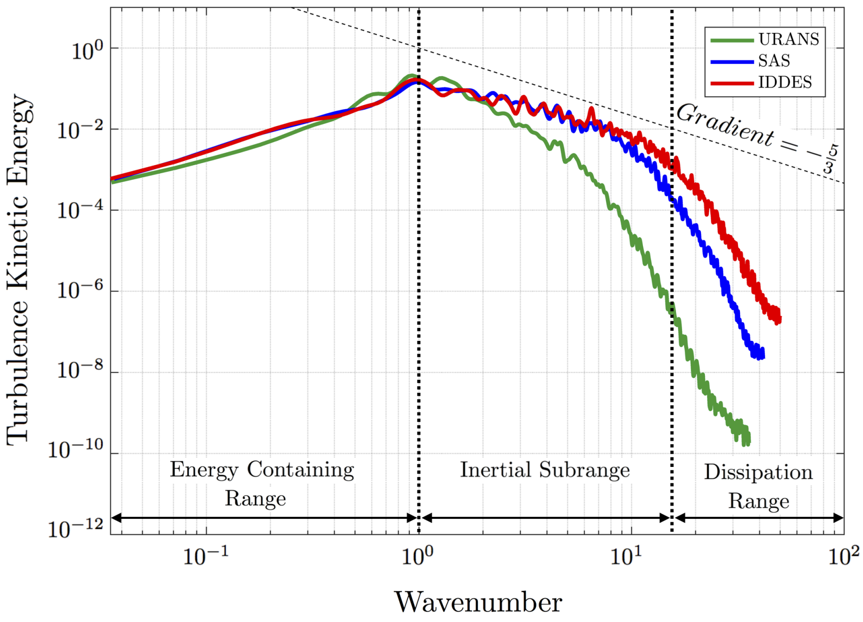

FIGURE 4.7: The Turbulence kinetic energy cascade at the point of $[1H, -0.4W, 0.2H]$.

cascade of energy from larger to smaller scales. Additionally, the prediction of the correct energy transfer to higher wavenumbers implies that smaller turbulence scales are better resolved by IDDES model. However, of course, resolving smaller turbulence scales can be very expensive; for example, the IDDES case is approximately 20 times more expensive than the URANS simulation.

4.3 Conclusion

In this study, the ability of three widely used turbulence models to predict the flow past a high-speed train is investigated. This is achieved through a comparison with wind-tunnel experimental data, based on accuracy in predicting slipstream velocity profiles and correlation with wake structures.

Although simulations based on different turbulence models show qualitatively consistent results with wind tunnel measurements for slipstream assessment, quantitatively the predictions do show a level of dependence on grid resolution and timestep choice. Naturally, HST slipstream assessment depends strongly on flow development around the train and downstream. Qualitatively, the dominant time-averaged and transient flow features, longitudinal vortices and corresponding spanwise oscillation, can be predicted by all three models. Quantitatively, URANS fails to predict the cross-stream development of the trailing vortices and the correlated dynamic response, which makes it unsuitable for quantitative slipstream assessment. IDDES shows superior consistency with the experimental data, perhaps due to its ability to capture a wider range of turbulence scales in the wake. As the first systematic study of using SAS to predict the HST slipstream, the results show that SAS may be a reasonable alternative of IDDES as it achieves a similar level of accuracy at a lower cost.

In practice, trade-offs exist between accuracy and computational cost, and computational cost is one of the important parameters in determining the selection of a turbulence model. The ratio of the estimated computational costs of the three representative cases are 1:10:20 (URANS:SAS:IDDES). The IDDES simulation used approximately 40 KCPU hours on the Australian *National Computing Infrastructure* (NCI) (RAIJIN) high-performance computing cluster, typically running on 128–256 cores. As better accuracy is typically associated with higher cost, a compromise often needs to be made with turbulence model selection. This study has quantified the level accuracy of each turbulence model for predicting different flow aspects, thus provide guidelines in selecting the models that satisfy accuracy requirements at minimum cost.

Chapter 5

Effect of Ground Boundary Condition

5.1 Problem Description

According to the previous research discussed in the *Literature Review* (§ 1), the ground motion has been verified to have a significant effect on the HST aerodynamic loading and surrounding flow field. Even though the effect of the ground motion has been identified and partially investigated, a comprehensive study of the mechanism on how it alters the train slipstream development is yet to be undertaken and this has motivated the present study. The knowledge of how the ground boundary layer alters the flow development around a HST is practically important for understanding the potential limitations of studying the HST aerodynamics by wind tunnel experiment with a stationary floor.

The aim of current study is to investigate the effect of the relative ground motion on the slipstream development around a generic HST model, including identifying the mechanism how it alters the flow structure around the train and within the wake region. Additionally, the effects of ground motion on slipstream assessment and aerodynamic loading are studied. Specifically, for a systematic comparison and determination of the effect introduced by the ground motion and the wheel rotation, three cases with different ground/wheel motions are studied: (i) Stationary Ground with Stationary Wheels (SGSW), (ii) Moving Ground with Stationary Wheels (MGSW) and (iii) Moving Ground with Rotating Wheels (MGRW). The specifications regarding the numerical settings are described in § 2.

5.2 Results and Analysis

The effect of ground motion is studied from the following three perspectives: slipstream assessment (§ 5.2.1), flow structure (§ 5.2.2), and aerodynamic loading (§ 5.2.3). In § 5.2.1, the slipstream assessment is implemented under the TSI specifications (TSI 2014), including the unsteady statistics of the slipstream velocity profiles and gust phenomenon. Additionally, the flow field at the slipstream measurement location is investigated to reveal how ground motion alters the slipstream measurement. In § 5.2.2, further investigations of the ground motion effect on the flow structures are conducted. For explicitly studying the ground motion effect at each stage of train slipstream development, the overall flow field is divided into two regions, the flow development region and wake propagation region. The alteration on the aerodynamic loading is visualised based on the train surface pressure distribution, and the resultant force variation (drag and lift) is presented in § 5.2.3.

5.2.1 Slipstream Assessment

To understand the effects of ground motion on the slipstream velocity measurement and the corresponding mechanism, the analysis is implemented from the following perspectives. To begin with, the unsteady statistics (time-averaging and standard deviation) of $U_{slipstream}$ at TSI specified locations are compared. Next, gust analysis is conducted to understand the ground motion effect on the maximum slipstream velocity defined by TSI specification. The mechanism of how ground motion interferes with the slipstream measurements is then examined by analysing the flow field at the slipstream assessment location.

5.2.1.1 Statistical Slipstream Profiles

In this study, the longitudinal displacements of slipstream velocity measurements for both heights are from $x = -15H$ to $x = 30H$. The time-averaging and standard deviation profile of the slipstream velocity ($U_{slipstream}$) and its streamwise (U_{GF}) and spanwise (V_{GF}) velocity components at the two measurement heights are presented in Fig. 5.1, and the maximum points are listed in Table 5.1.

Fig. 5.1 shows that in general the ground motion has a significant impact on the slipstream measurement ($\overline{U}_{slipstream}$ and $\sigma_{slipstream}$), while the effect of wheel rotation is negligible. Here, $\overline{U}_{slipstream}$ represents a time-averaged slipstream velocity and

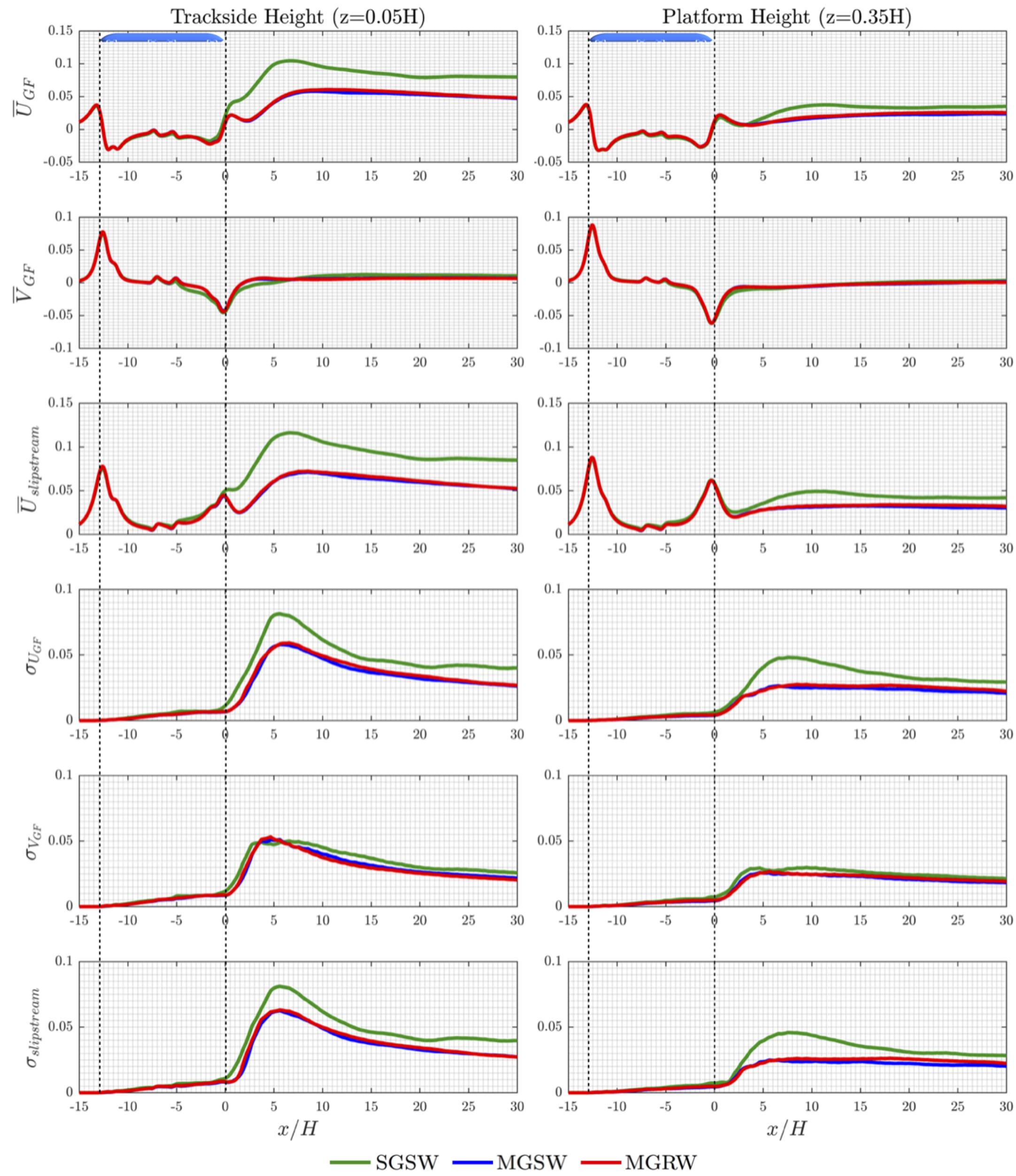

FIGURE 5.1: The comparison of the slipstream profiles between SGSW, MGSW and MGRW at the trackside and platform heights.

$\sigma_{slipstream}$ its standard deviation. Even though the ground motion effect is determined at both heights, its impact is more significant at a lower height. Therefore, the following discussion focuses on the trackside height unless stated otherwise. Qualitatively, identical trends of the $\overline{U}_{slipstream}$ profiles can be seen for all three cases. Local peak values occur near the nose and tail, and $\overline{U}_{slipstream}$ increases to a maximum behind the tail and then decreases gradually. This is a characteristic HST $\overline{U}_{slipstream}$ profile that has been determined across different train models with various techniques (Bell *et al.*

Table 5.1: The critical values in the slipstream profile comparison.

		$\overline{U}_{slipstream}$		$\sigma_{slipstream}$	
		Maximum	Location (x/H)	Maximum	Location (x/H)
Trackside	SGSW	0.116	6.61	0.081	5.61
	MGSW	0.078	-12.63	0.063	5.61
	MGRW	0.078	-12.63	0.063	5.61
Platform	SGSW	0.087	-12.57	0.046	7.55
	MGSW	0.088	-12.57	0.025	5.66
	MGRW	0.088	-12.57	0.026	18.06

2016b)(Huang *et al.* 2016)(Baker 2010)(Bell *et al.* 2015).

The peak value of $\overline{U}_{slipstream}$ in the wake is reduced and delayed due to the ground motion, which is consistent with the trend that was also identified by Xia *et al.* (2016) based on the CRH3 model on a flat ground configuration. Due to the ground motion, the peak $\overline{U}_{slipstream}$ caused by the trailing vortices in the wake is reduced, while the local peak near the nose remains essentially identical. Consequently, the maximum $\overline{U}_{slipstream}$ for MGSW and MGRW occurs at the nose, instead of within the wake. However, high $\sigma_{slipstream}$ still occurs within the wake region, with the maximum located at approximately $x = 5 \sim 6H$. Given this, the wake region is still the most critical region for HST slipstream assessment, and this is also identified by the gust analysis presented in § 5.2.1.2.

Furthermore, by looking at $\overline{U}_{GF}$ and $\overline{V}_{GF}$, the results show that the discrepancy in $\overline{U}_{slipstream}$ is predominantly caused by the alteration to $\overline{U}_{GF}$. Because the ground motion is in the streamwise direction, a moving ground removes the ground boundary layer growth, which causes a high $\overline{U}_{GF}$ near the ground, and further affects the slipstream velocity. The mechanism of how the ground boundary layer development influences the slipstream measurement is presented in § 5.2.1.3.

5.2.1.2 Gust Analysis

The TSI (2014) defines how the slipstream velocity should be measured under field testing, and the procedure of calculating the maximum slipstream velocity (also known as the *TSI value*) is briefly introduced here. The slipstream should be measured at two fixed positions: trackside height and platform height, as introduced before. The entire flow disturbance, including the train passing and the wake, needs to be recorded. Additionally, a 1-second moving-average (1s MA) filter is required to be applied to the raw data, and the peak slipstream velocity of the filtered data is recorded as one measurement. The distance between two independent measurements has to be more than 20 meters, and a minimum of 20 independent measurements are required for calculating the maximum slipstream velocity (*TSI value*). The *TSI value* is calculated as the mean of the peak velocities plus two standard deviations. The *TSI value* indicates the maximum slipstream velocity of the HST within 95% confidence, and this assessment is integrated into the HST acceptance procedure. The peak values of individual measurements are plotted as black dot points, and the mean and standard deviation of the peak values are calculated and presented in Table 5.2. Next, the equivalent of a 1s MA filter is applied to each data set, and presented as light blue curves in Fig. 5.2, with the peak values indicated by the blue dot points. The final maximum slipstream velocity $\overline{U}_p + 2\sigma_{uv}$ under a 1s MA filter is calculated and presented in Table 5.2. In practice, the maximum value would be compared with the maximum allowable slipstream velocity specified by TSI as a part of the acceptance procedure. For this study, the duration of the equivalent sampling time per artificial probe is $52T_{ref}$, with the starting and ending time for the train passage corresponding to $2.5T_{ref}$ and $15.4T_{ref}$, respectively.

Similar to full-scale testing (Baker *et al.* 2014b) and moving-model experiments (Bell *et al.* 2015), the gust analysis shows a large run-to-run variance for all cases. Comparing the measurements at the trackside height and platform height, the measurements at the trackside height in general show a more identifiable peak at the near wake. The reason is that the high energy containing longitudinal vortices in the wake are closer to the trackside position. More details about how the wake structures influence the slipstream measurement are presented in § 5.2.2.

Additionally, for the SGSW probes at the trackside height a few measurements show a maximum $U_{slipstream}$ a long time after the passage of the tail, while this phenomenon is not identified in MGSW and MGRW measurements. The high $U_{slipstream}$ in the far wake for SGSW is expected to be caused by the ground boundary layer growth of which the mechanism is revealed in § 5.2.1.3. The unrealistic high peaks in the far wake can affect the accuracy of gust analysis, not only in terms of the magnitudes of the maximum slipstream velocities (*TSI values*), but also their locations.

5.2.1.3 Flow Field at the Slipstream Assessment Location

According to the comparison in § 5.2.1.1 and 5.2.1.2, the ground motion has an effect on both the unsteady statistical profiles and maximum slipstream velocity determination

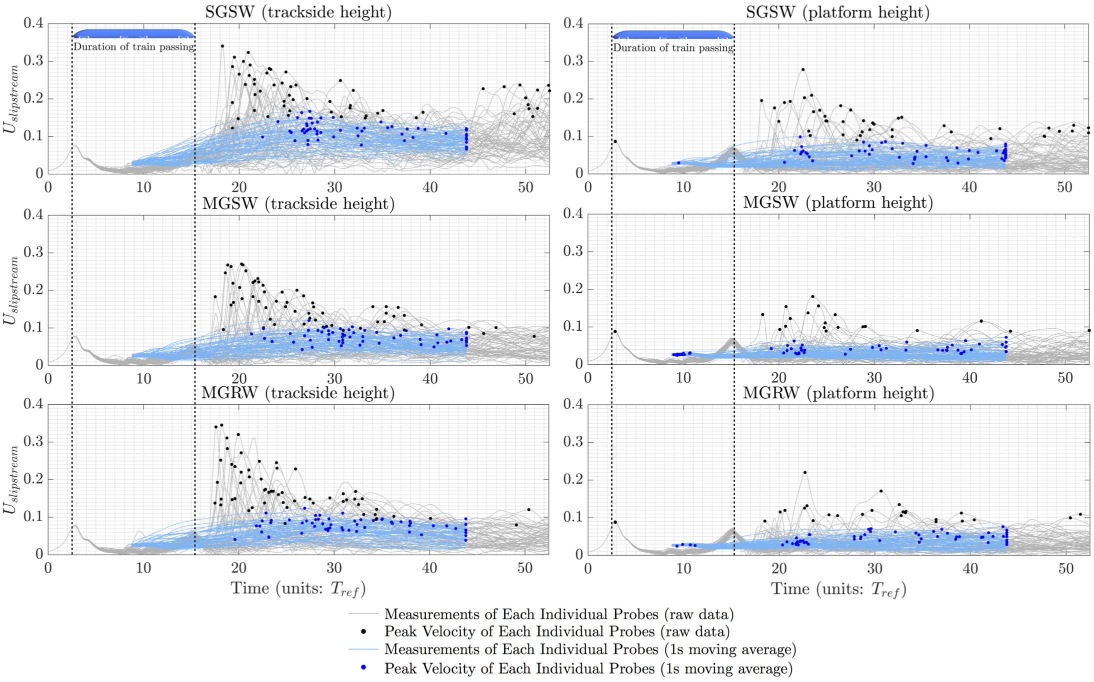

FIGURE 5.2: The gust analysis based on the *Moving Probe technique* under TSI specifications.

TABLE 5.2: The unsteady statistics of gust analysis (the values in brackets are the raw data without 1s MA)

		Mean Peak ($\overline{U}_p$)	σ_{uv}	$\overline{U}_p + 2\sigma_{uv}$
Trackside	SGSW	0.115 (0.214)	0.022 (0.051)	0.159 (0.316)
	MGSW	0.076 (0.160)	0.016 (0.053)	0.108 (0.267)
	MGRW	0.079 (0.175)	0.018 (0.065)	0.114 (0.303)
Platform	SGSW	0.055 (0.126)	0.016 (0.041)	0.088 (0.208)
	MGSW	0.039 (0.098)	0.011 (0.020)	0.061 (0.138)
	MGRW	0.045 (0.100)	0.013 (0.023)	0.072 (0.145)

(*TSI values*). In this section, the mechanism of how the ground motion alters the slipstream measurements is explained by examining the flow field at the slipstream measurement location (3 m away from the centreplane at full-scale).

The stationary ground introduces a streamwise shear between the ground and incoming air. This shear effect introduces y-vorticity (ω_y) into the flow field, and this can significantly alter the flow field near the ground and further affect the slipstream measurement, as illustrated in Fig. 5.3. SGSW shows a constant growth of positive $\overline{\omega}_y$ above the ground. The moving ground removes the relative motion, and an alteration of $\overline{\omega}_y$ can be seen within the wake, which is covered by the ground boundary layer in SGSW. This alteration of $\overline{\omega}_y$ is purely introduced by the velocity difference between the wake propagation and ground motion. SGSW shows a high unsteadiness of ω_y near the ground due to the ground boundary layer, while MGSW and MGRW indicate that the high unsteadiness should predominately be caused by the wake, especially the region with an altered $\overline{\omega}_y$.

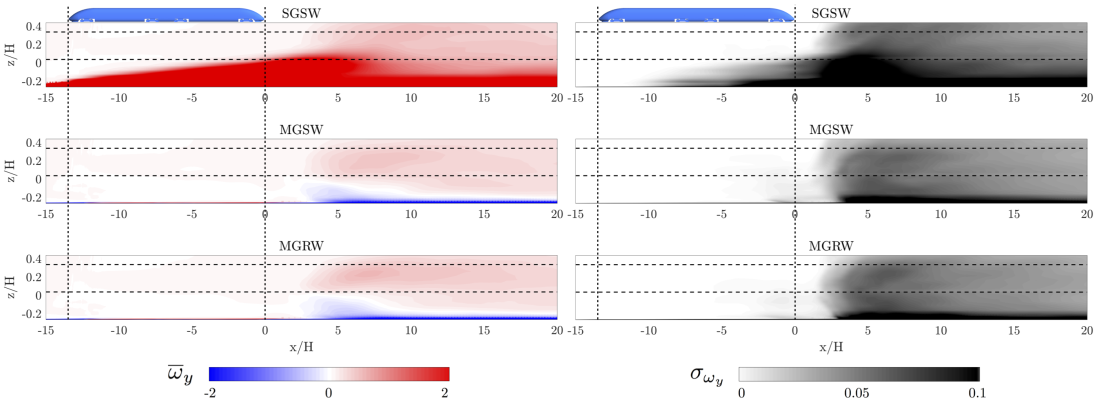

FIGURE 5.3: $\overline{\omega}_y$ and σ_{ω_y} at the slipstream measurement location (not to scale).

The influence on the slipstream measurement from the introduction of ω_y caused by the ground motion is illustrated in Fig. 5.4. MGSW and MGRW predict an identical $U_{slipstream}$ distribution, while SGSW superposes a gradually increase of $\overline{U}_{slipstream}$ and $\sigma_{slipstream}$ near the ground associated with the ground boundary layer. Fig. 5.4 shows that the ground boundary layer initially touches the trackside measurement line at approximately $x = 0H$, which is consistent with location of the differences between the slipstream profiles plotted in Fig. 5.1. Additionally, Fig. 5.4 also explains why the ground motion effect is more significant at trackside height than at platform height, because the stationary ground imposes a local effect that is closer to the lower measurement line. Also the ground boundary layer can alter the wake propagation and then affect the slipstream measurement. This mechanism is revealed by analysing the flow structures in § 5.2.2.

5.2.2 Flow Structures

In this section, the train-induced slipstream flow is split into two regions: flow development region and wake propagation region, as illustrated in Fig. 5.5. The flow development region is where the flow disturbance develops, while the wake propagation region covers where the developed flow structures propagate downstream. The classification is visualised in terms of $\overline{U}_{slipstream}$ at trackside height, as illustrated in Fig. 5.5, and the dashed lines indicate the positions of slipstream measurement specified by TSI guidelines (TSI 2014). It can be seen in Fig. 5.5 that the difference within the flow de-

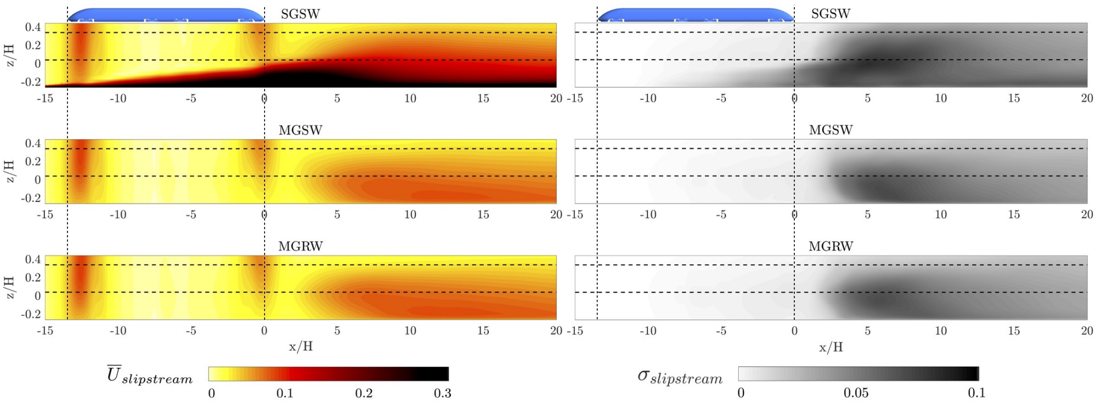

FIGURE 5.4: $\overline{U}_{slipstream}$ and $\sigma_{slipstream}$ at the slipstream measurement location (not to scale).

velopment region is negligible, while SGSW shows a wider wake in the wake propagation region. The effect of the ground motion in each region is analysed in the following two subsections, and this approach aims to identify the effects of ground motion at each stage of slipstream development.

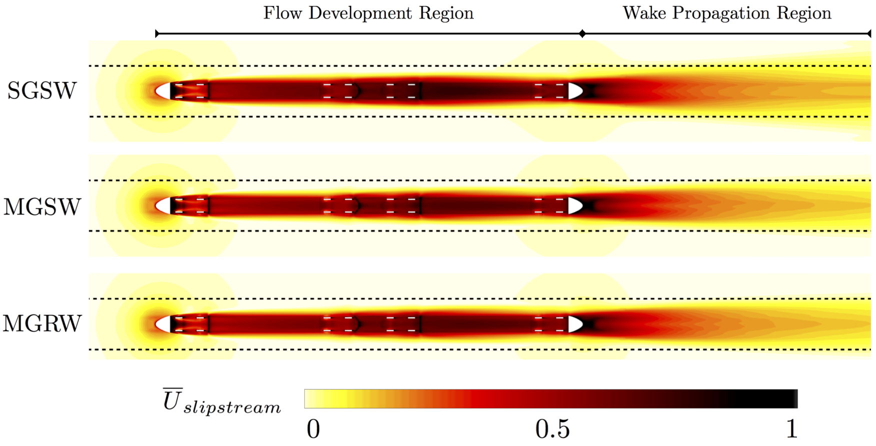

FIGURE 5.5: The flow region classification visualised by $\overline{U}_{slipstream}$ at $z = 0.05H$.

5.2.2.1 Flow Development Region

The flow development region is identified as the region where the flow develops as it passes over the HST model, which covers approximately from the nose to tail. The ground motion effect within this region is visualised by the time-averaged y-vorticity ($\overline{\omega}_y$) in the vertical spanwise centreplane ($y = 0W$), as shown in Fig. 5.6.

An identical boundary layer development over the train top surface is indicated by the continuous growth of the positive $\overline{\omega}_y$ region. Compared with MGSW and MGRW, SGSW shows a persistent thin positive $\overline{\omega}_y$ region above the ground surface due to the ground boundary layer. Even though MGSW and MGRW have different wheel motion, the underbody flow fields are consistent with only minor differences observed around the axles.

A main flow alteration caused by the ground motion occurs between the tail tip and the ground, as highlighted in Fig. 5.6. According to the $\overline{\omega}_y$ and in-surface projected velocity streamlines, two coherent recirculation regions (vortex A and B) are formed when the downwash from the top surface meets the underbody flow. From the density of the streamlines, the velocity of the underbody flow in SGSW is significantly lower than that in MGSW and MGRW. Compared with MGSW and MGRW, when the underbody flow meets the downwash from the tail, SGSW does not have a high kinetic energy that can be used to convert into a large vortex (vortex A). Additionally, although the size of vortex A alters significantly, the position of the outside boundary of the vortex B shows little variation.

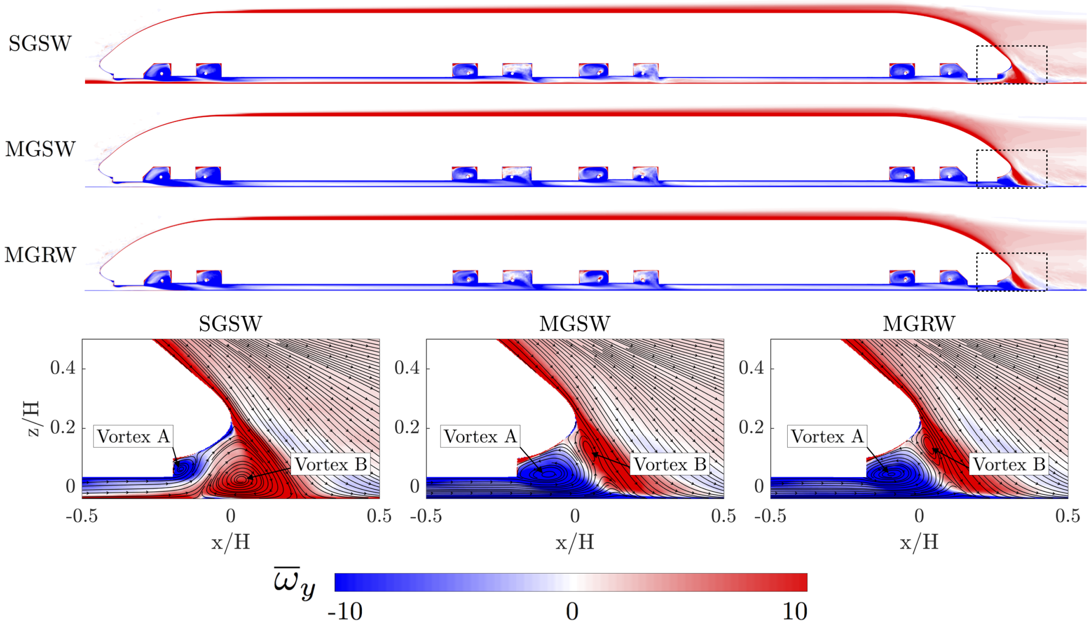

FIGURE 5.6: The flow development region visualised by $\overline{\omega}_y$ and in-surface projected velocity streamlines at $y = 0W$.

5.2.2.2 Wake Propagation Region

The wake propagation region is defined as the region behind the tail, where the vortical flow structures separate from the train surface and move downstream. According to the slipstream profiles presented in § 5.2.1, the ground motion has a significant impact on the slipstream assessment within the wake propagation region. To investigate the interaction between the ground motion and wake propagation, both the time-averaged and transient flow structures are analysed.

Similar to the flow structures that have been identified from previous studies (Bell *et al.* 2016b) (Bell *et al.* 2016a), the dominant wake feature of a HST is a pair of counter-rotating streamwise vortices. In this study, the time-averaged wake is visualised by x-vorticity (ω_x) contours overlaid with in-surface projected velocity streamlines on five sequential vertical planes, as illustrated in Fig. 5.7.

As the time-averaged flow structure is symmetric about the mid-plane, only the left half of the flow field is presented. The black crosses and circles in Fig. 5.7 represent the locations of trackside ($z = 0.05H$) and platform ($z = 0.35H$) slipstream measurement positions. Through Fig. 5.7, the downstream evolution of the time-mean trailing vortices can be visualised as the plane shifts from $x = 0.5H$ to $x = 6H$. Qualitatively, three cases present an identical flow feature: as the vortices move downstream, they roll over the rails and move apart from each other in the spanwise direction. Quantitatively, due to the presence of ground boundary layer, SGSW shows a negative x-vorticity region above the ground that deforms the shape of trailing vortex. Comparing with MGSW and MGRW, the trailing vortex merges into the ground boundary layer region, resulting in the lower end of the vortex shifting closer to the trackside slipstream measurement location. As the vortex core contains lower momentum fluid, it induces a higher local slipstream velocity. Therefore, the slipstream velocity is sensitive to both the strength of the trailing vortex arms and their cross-stream location. As the vortex is deformed towards the trackside slipstream measurement line, SGSW implies a higher slipstream measurement compared with MGSW and MGRW, which is another reason why SGSW shows a higher prediction of $\overline{U}_{slipstream}$.

The transient wake structure is illustrated by phase-averaging $U_{slipstream}$ over a horizontal plane at the trackside height, and the shedding frequency is quantified by the Strouhal number (St_W) based on the train width (W) and streamwise velocity component (U_{TF}) at the point $(1H, -0.4W, 0.2H)$. The power spectra are presented in Fig. 5.8. Note the wind tunnel experiment of the same train model with stationary ground and wheel shows a shedding of $St_W = 0.19 \sim 0.21$ at the same point (Bell *et al.* 2016b). The signal is split into 26 segments filtered with Hanning windows with 25% overlap for each fast Fourier transform to construct the overall spectra and highlight

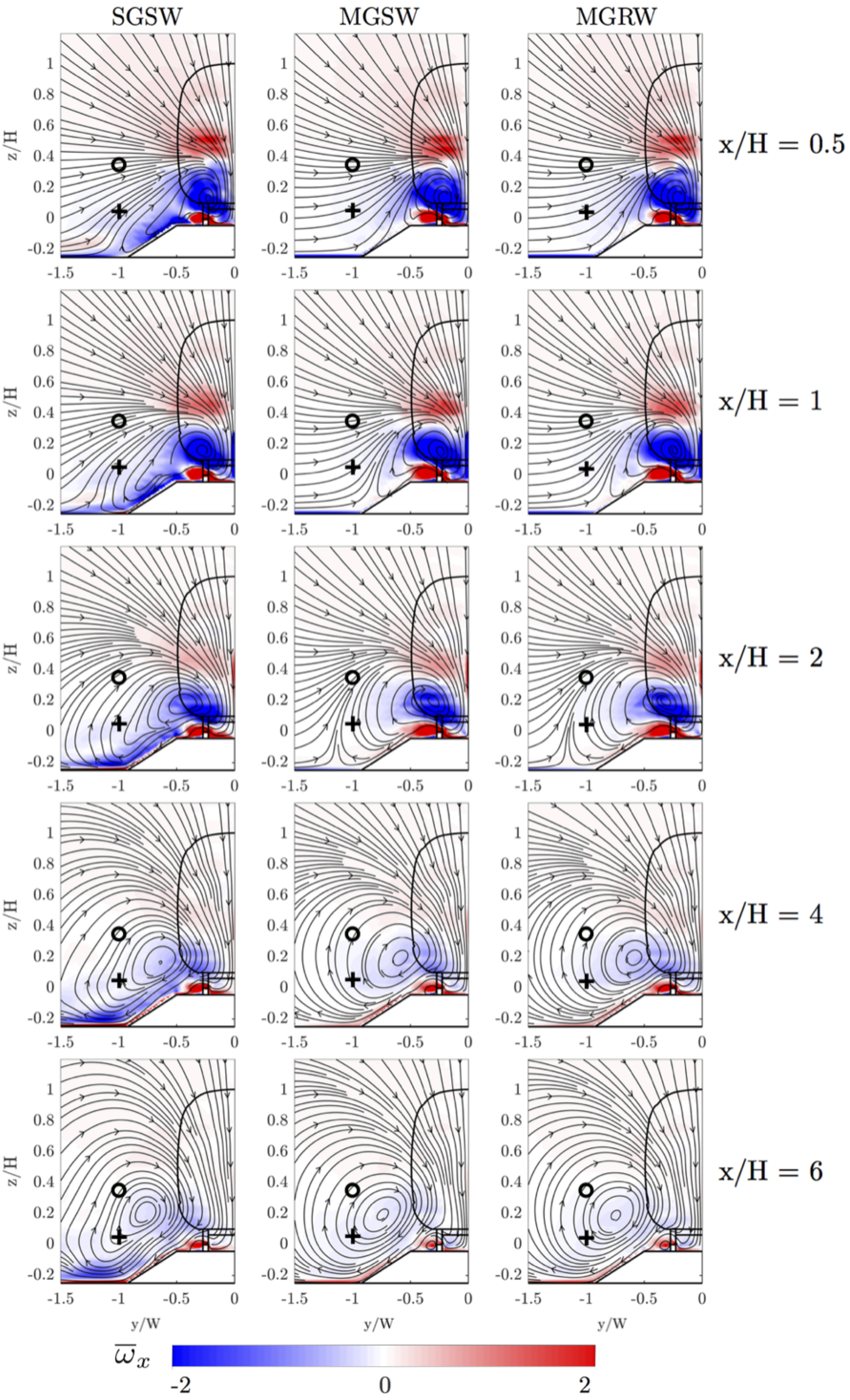

FIGURE 5.7: The time-averaged wake structure visualised by ($\overline{\omega}_x$) contour and in-surface projected velocity streamlines ("+": trackside measurement location; "o": platform measurement location).

the dominant frequencies.

According to Fig. 5.8, the dominant near wake St_W is approximately 0.22, 0.4-0.6

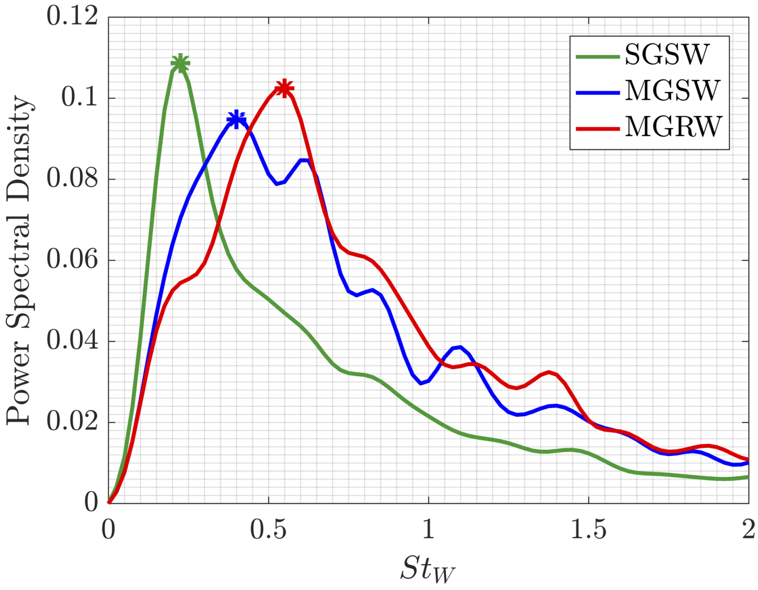

FIGURE 5.8: The comparison of wake shedding frequency based on St_W at the point of $[1H, -0.4W, 0.2H]$.

and 0.55 for SGSW, MGSW and MGRW, respectively. This indicates that the wake oscillates more rapidly with a moving ground. The ground boundary layer reduces the longitudinal velocity in the wake region above the ground, as is clear in Fig. 5.1. This also explains why SGSW demonstrates a cleaner peak, while MGSW and MGRW show a wider bandwidth towards the higher St_W.

The spanwise wake oscillation that has been identified in the wind tunnel experiment (Bell *et al.* 2016a), is visualised by phase-averaging $U_{slipstream}$ in a horizontal plane at the trackside height ($z = 0.05H$), as presented in Fig. 5.9.

In Fig. 5.9, the black dashed lines indicate the location of slipstream assessment according to TSI standards (TSI 2014), and the phase-averaging is conducted based on the signal at the reference point with coordinates ($[2H, -0.5W, 0.05H]$), visualised by the blue circles in Fig. 5.9. The first and second row demonstrate the wake motion that is half a period apart, and the third row illustrates snapshots of the instantaneous wake structure for the three cases. Comparing with MGSW and MGRW, both the phase-averaged and instantaneous wake profiles demonstrate that a stationary ground enhances the amplitude of the spanwise wake oscillation. Additionally, Fig. 5.9 also implies that due to the ground boundary layer development, the side-to-side oscillation is enhanced with distance downstream. Longitudinally, all the cases predict the same longitudinal wavelength of $2.5 \sim 3H$, showing no significant dependency on the ground

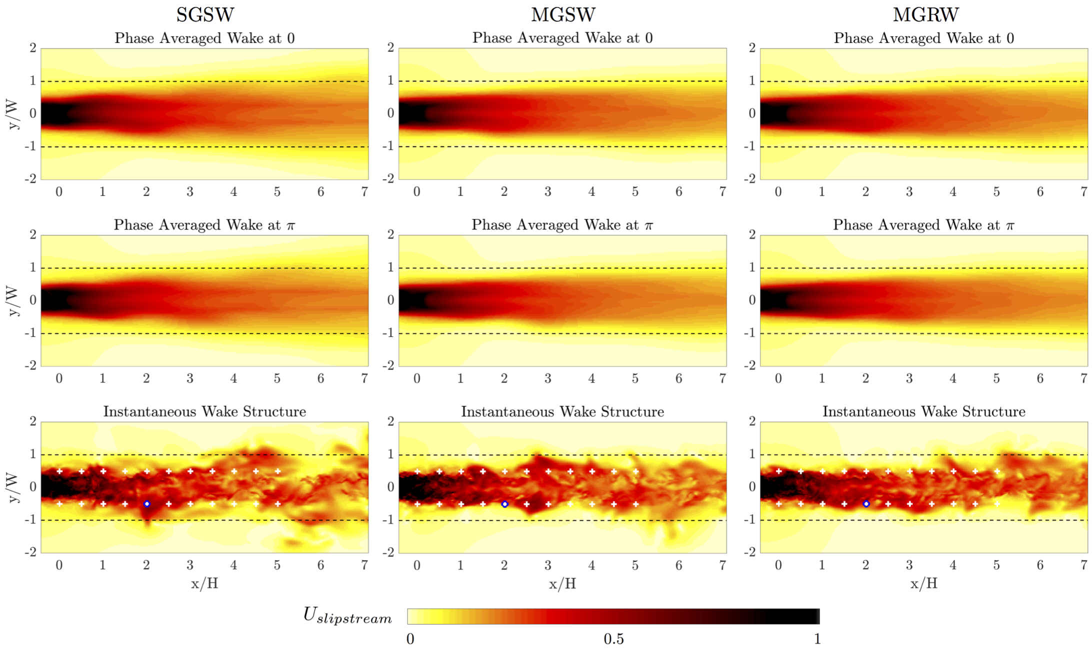

FIGURE 5.9: The wake dynamics visualised by the phase-averaged and instantaneous $U_{slipstream}$ at $z = 0.05H$ ("o": phase-averaging reference points; "+": cross-correlation points).

motion.

The spanwise motion is also quantified by the cross-correlation of a pair of point arrays within the near wake, as visualised by the white crosses in Fig. 5.9. The points are distributed between $x = 0 \sim 5H$ in $0.5H$ increments, and each pair is $0.5W$ from the centreplane. The cross-correlation coefficient of V_{GF} for each pair is calculated, and the average profile of 11 pairs for each case is plotted in Fig. 5.10.

The cross-correlation coefficient of unity represents an in-phase motion, while -1 means an out-of-phase motion, and the time lag is normalised by T_{ref}. Thus, an ideal in-phase spanwise motion should have a cross-correlation coefficient for V_{GF} equal to 1. Fig. 5.10 shows the coefficients of SGSW at 0 time lag is approximately 0.205, doubling the values for MGSW and MGRW that are about 0.1. This is in line with the phase-averaging analysis, which shows a more identifiable spanwise wake oscillation for SGSW. Additionally, the temporal period of the half spanwise motion, determined by the time lag between the positive and negative peak values, is approximately $2T_{ref}$, independent of the ground motion.

The amplification of the spanwise motion is caused by the deformation of the vortex boundary when it interacts with the ground boundary layer. As presented in Fig. 5.7, this deformation causes a wider wake, especially towards the lower part. In contrast, the

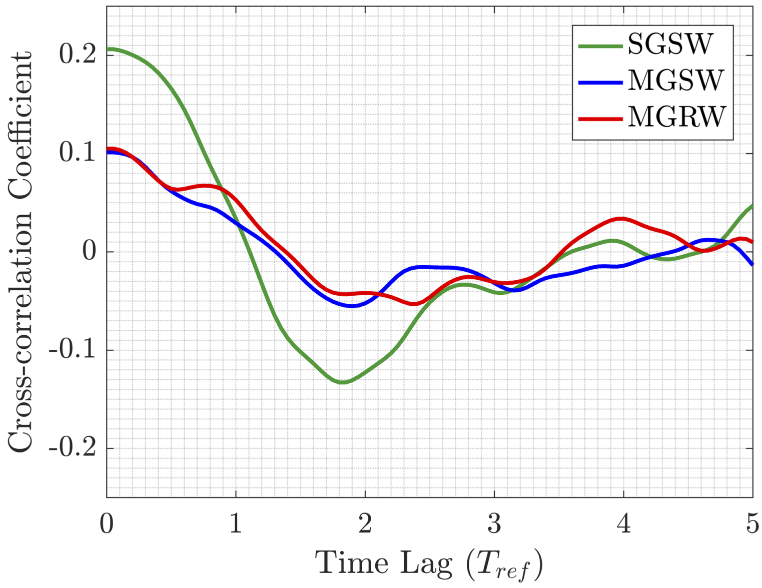

FIGURE 5.10: The cross-correlation coefficient comparison of the spanwise wake oscillation.

vortices stay closer to the centreplane for the moving ground cases with the absence of the ground boundary layer influence. Additionally, the spanwise oscillation is orthogonal to the longitudinal ground boundary layer development, and it seems that the longitudinal ground motion does not alter the spanwise wake oscillation frequency to any significant effect. In conclusion, from the phase-averaging and cross-correlation results, the ground boundary layer enhances the amplitude of the spanwise motion, while the spatial wavelength and temporal period of the spanwise oscillation are effectively independent of ground motion.

5.2.3 Aerodynamic Loading

The aerodynamic (pressure) loading on the train surface is visualised through the Pressure Coefficient (C_P) as presented in Fig. 5.11, where C_P is defined by

$$C_P = \frac{P - P_\infty}{\frac{1}{2}\rho_\infty V_\infty^2}. \tag{5.1}$$

Here, P is the surface pressure, and reference values for the pressure, density and velocity are P_∞, ρ_∞ and V_∞, respectively. Qualitatively, the differences between the C_P distributions are almost negligible, especially on the top surface. The main differences occur along the bottom surface, especially around the bogie regions. Even though almost qualitatively identical pressure distributions are established; quantitatively the moving ground generates a higher pressure deviation on the underbody structures, and wheel rotation causes extra higher pressure deviation on the wheels and axles.

The C_P variation on the bottom surface is clearly caused by different underbody flow conditions. The boundary layer on the stationary ground reduces the underbody flow velocity; therefore, the impact of the incoming flow on the underbody structures is reduced. Compared with the ground motion effect that is exerted over the entire bottom surface, the wheel rotation only increases the pressure magnitude around the wheel sets, due to further acceleration of the local flow field introduced by the wheel rotation. This difference can also be identified from the pressure profiles on the train centreplane, as shown in Fig. 5.12.

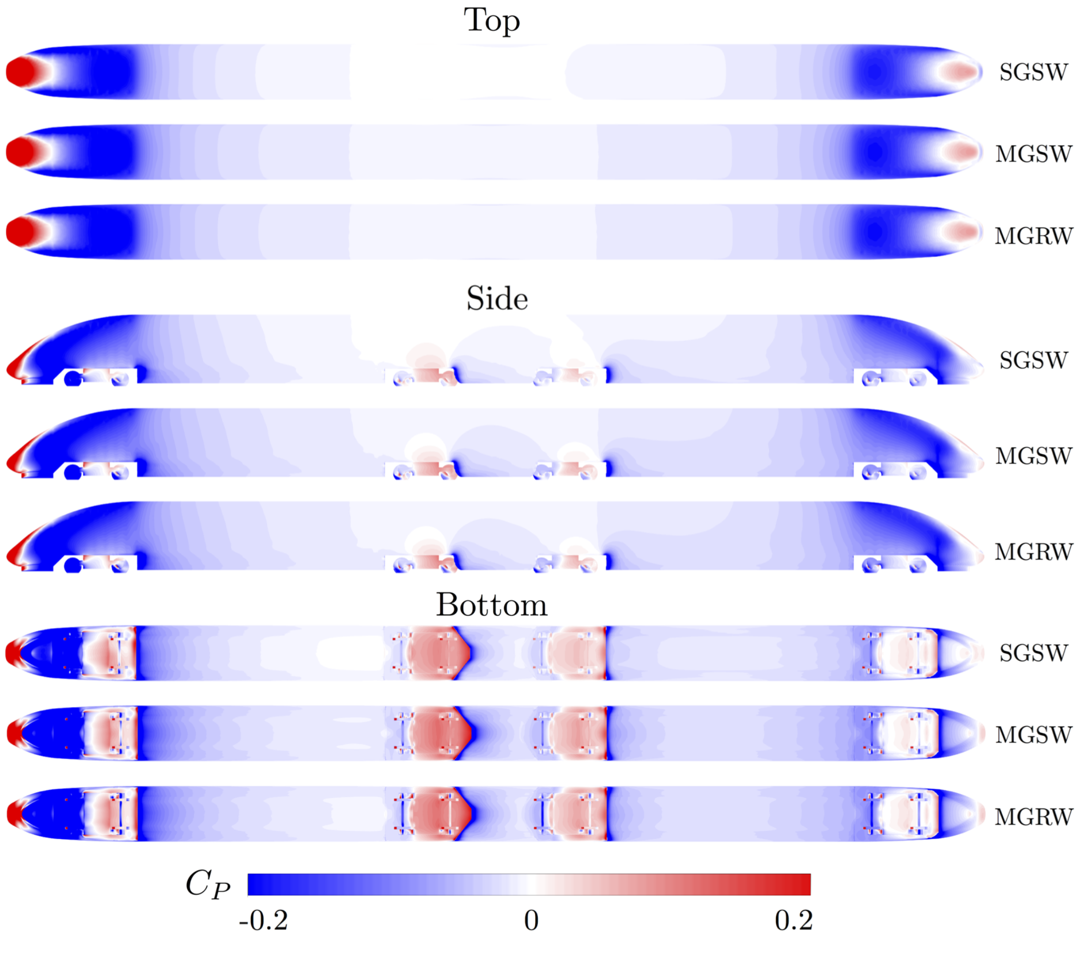

FIGURE 5.11: The comparison of train surface pressure coefficient.

From the C_P distribution over the train surface, both the drag (C_D) and lift (C_L) coefficients are calculated and listed in Table 5.3. The ground motion alone increases C_D from 0.267 to 0.281 (5.1%), while wheel rotation produces another 0.7% increase. The ground motion causes a more significant impact in the vertical direction, resulting in an up to 50% reduction of C_L. The higher C_D for the moving ground cases is a result of the greater impact between the incoming flow and underbody structures.

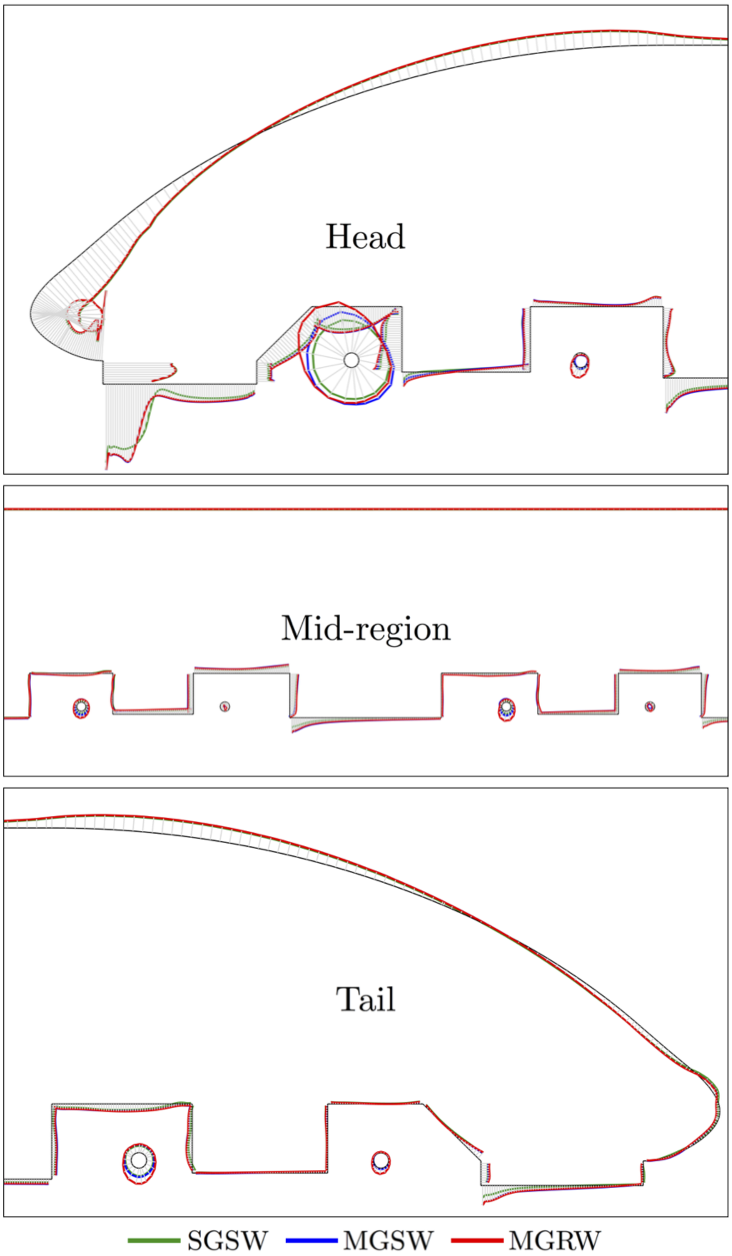

FIGURE 5.12: The comparison of surface pressure coefficient profile at the train centreline.

Additionally, the underbody flow acceleration reduces the velocity difference between the flow over the top and bottom surface, resulting in a smaller pressure difference in the vertical direction, hence the reduction of C_L. A slight higher standard deviation is determined for both C_D and C_L with the stationary ground, which is introduced by the unsteadiness of the ground boundary layer. Additionally, wheel rotation can be another minor source of unsteadiness.

Table 5.3: The comparison of force estimation on the train.

		SGSW	MGSW	MGRW
C_D	Mean	0.267	0.281	0.283
	Standard deviation	0.010	0.008	0.009
C_L	Mean	0.083	0.049	0.051
	Standard deviation	0.017	0.015	0.016

5.3 Conclusion

In this study, based on three different wheel and ground configurations (SGSW, MGSW and MGRW), the effects of the ground motion on a HST slipstream are investigated from the perspectives of slipstream assessment, wake structure and aerodynamic loading. This study not only determines the alteration to slipstream due to ground motion, but also explores the mechanism of how ground motion affects slipstream by analysing the time-averaged wake structure and wake dynamics. In terms of slipstream assessment, a stationary ground increases both $\overline{U}_{slipstream}$ and $\sigma_{U_{slipstream}}$, especially in the wake region at a lower height above the ground. This is in line with the gust analysis that shows that the presence of a ground boundary layer can result in an over-prediction of maximum slipstream velocity (*TSI value*). The ground motion affects slipstream both directly and indirectly. Directly, a stationary ground increases the slipstream velocity $U_{slipstream}$ in the wake due to the difference in the ground and air velocities causing lower wake velocities relative to the train. Indirectly, the spreading of the longitudinal trailing vortices due to the interaction between the wake and ground boundary layer results in a wider wake structure. Additionally, the side-to-side deformation of the longitudinal trailing vortices due to the interaction between the wake and ground boundary layer results in trailing vortices meandering further from the train vertical centreplane, causing increased gusts; and the amplitude of spanwise oscillation increases as the wake propagates downstream. Dynamically, both the streamwise wavelength and temporal period of the spanwise motion are not affected by the ground boundary layer, while the wake shedding frequency is increased with a moving ground. The major ground motion effect within the flow development region is the alteration of the sizes of two coherent vortices between the tail tip and ground, caused by the different underflow conditions. For the aerodynamic loading, a stationary ground predicts a lower C_D and a higher C_L, mainly caused by the train bottom surface pressure alteration due to the variation to the underflow conditions caused by the ground boundary. Additionally, the wheel rotation only alters the local flow field and pressure distribution within the bogie region; its effects on the slipstream assessment and wake structures are insignificant.

Chapter 6

Effect of Bogies

6.1 Problem Description

This study investigates the flow alteration can be introduced by the inclusion of the bogies on HST slipstream characteristics. To isolate the bogie effects, this study systematically studies and compares the slipstream characteristics of two otherwise identical generic train models, i.e., *flat-underbody train model* (M1) and *full-featured train model* (M2), with the only difference being whether the bogies are fully featured. This study utilises generic bogie configurations; in other words, the differences between the articulated and non-articulated bogies are not considered here. The detailed numerical set-ups including the geometric specifications, boundary conditions and boundary conditions can be found in § 2.

As discussed in the *Literature Review* (§ 1), the previous research on the effect of bogies were undertaken from one of the two perspectives: (1) drag reduction and (2) ballast flight. Unlike the previous studies, which mainly focused on ballast flight or drag reduction, the current study investigates bogie effects from a slipstream perspective, which also has a significant practical significance. For example, by reviewing the methodologies for studying HST slipstream through computational analysis indicates that numerical set-ups, both with bogies (Muld *et al.* 2012a)(Yao *et al.* 2013) and without bogies (Östh *et al.* 2015)(Pereira & André 2013), have been adopted. However, the effects of bogies on HST slipstream characteristics are not yet fully understood making it difficult to bridge the gap between the two approaches. Specifically, the wake impact that can be caused by the presence of the bogies have not been fully discovered and characterised, and this is the rationale for undertaking the present study. Additionally, spanwise oscillation of a HST wake has been identified as a typical HST slipstream characteristic, but the correlation between its initiation and the presence of bogies is still ambiguous. Therefore, effort is needed to understand and quantify the effects of bogies on HST slipstream characteristics, for example, the causes of spanwise oscillation of the wake.

For a comprehensive investigation, the flow field is naturally divided into two regions: the flow development region and the wake region, and the bogie effects on each region are studied separately. Beyond this, the influences on slipstream velocity assessment and aerodynamic loading are also investigated.

6.2 Results and Analysis

This study investigates the effects of bogies from three perspectives: *wake flow structure* (§ 6.2.1), *slipstream assessment* (§ 6.2.2) and *aerodynamic loading* (§ 6.2.3). To begin with, the influence of the bogies on each stage of the slipstream development is investigated, including the statistical flow features and wake dynamics. Next, how the altered wake flow further interferes with slipstream measurements is studied in accordance to the TSI specifications. Lastly, the impact of the bogies on aerodynamic loadings is presented by comparing the train surface pressure between two models.

6.2.1 Flow Structures

To explicitly study the effects of bogies as the slipstream develops, the flow field is divided into two regions: the flow development region and the wake region. A schematic of the two regions is illustrated in Fig. 6.1, based on the time-averaged slipstream velocity ($\overline{U}_{slipstream}$) at the trackside height, and the black dotted-lines represent the slipstream assessment location under TSI specifications.

The *flow development region* extends from the train head to the tail, and the wake region starts from where the wake structures separate from the tail to where the slipstream effect is negligible. The flow development region covers where there is direct local disturbance caused by the presence of bogies, and the wake region focuses on how the alteration of upstream conditions further influences the formation and propagation of the wake structures. However, note that as the slipstream development along the train is a continuous process, there is no definite boundary between the two regions. This is especially true around the tail, where the wake structures are formed and separate from the train surface. Fig. 6.1 shows that the bogies increase the underbody slipstream velocity, and widen the wake behind the train. A detailed analysis of the

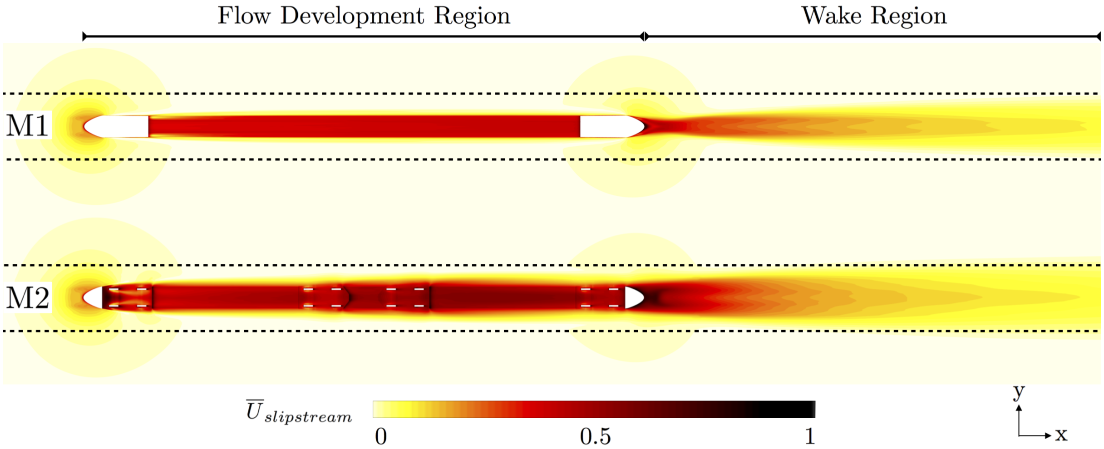

FIGURE 6.1: Classification of the two flow regions visualised by $\overline{U}_{slipstream}$ at $z = 0.05H$, and the slipstream assessment location is represented by the dotted lines.

bogie effect in each region is presented in § 6.2.1.1 and § 6.2.1.2.

6.2.1.1 Flow Development Region

Unsurprisingly, the flow development region is identified as the region where the flow develops as it passes over the HST, arbitrarily taken from the nose to the tail. The bogie influence within this region is visualised in Fig. 6.2 by the turbulent kinetic energy (TKE), and the time-averaged y-vorticity ($\overline{\omega}_y$), in the vertical spanwise centre-plane.

As can be seen in Fig. 6.2, the bogies within this region only locally alter the underbody flow, while the flow over the upper train surface remains almost unaffected. The mechanism of the bogies interfering with slipstream development is to alter the underbody flow by restricting it through blockage, and to increase the TKE level through flow separation from the bogies. According to the TKE contours in Fig. 6.2, the bogies not only locally increase the turbulence level around the bogies, but also the effect advects into the wake.

For the time-averaged flow features, an identical boundary layer growth is seen by the positive $\overline{\omega}_y$ layer over the train top surface. In contrast, a significant alteration of the underbody flow is apparent. A thin boundary layer develops on the flat bottom surface in M1, while the bogies introduce high local $\overline{\omega}_y$ magnitude regions in M2. The main alteration to the flow caused by the bogies is identified between the train tail tip and ballast, which is highlighted by $\overline{\omega}_y$ and time-averaged in-surface projected velocity streamlines in the lower images of Fig. 6.2. This figure illustrates that a pair of coherent time-averaged recirculation regions are formed in M2, while these do not occur in the

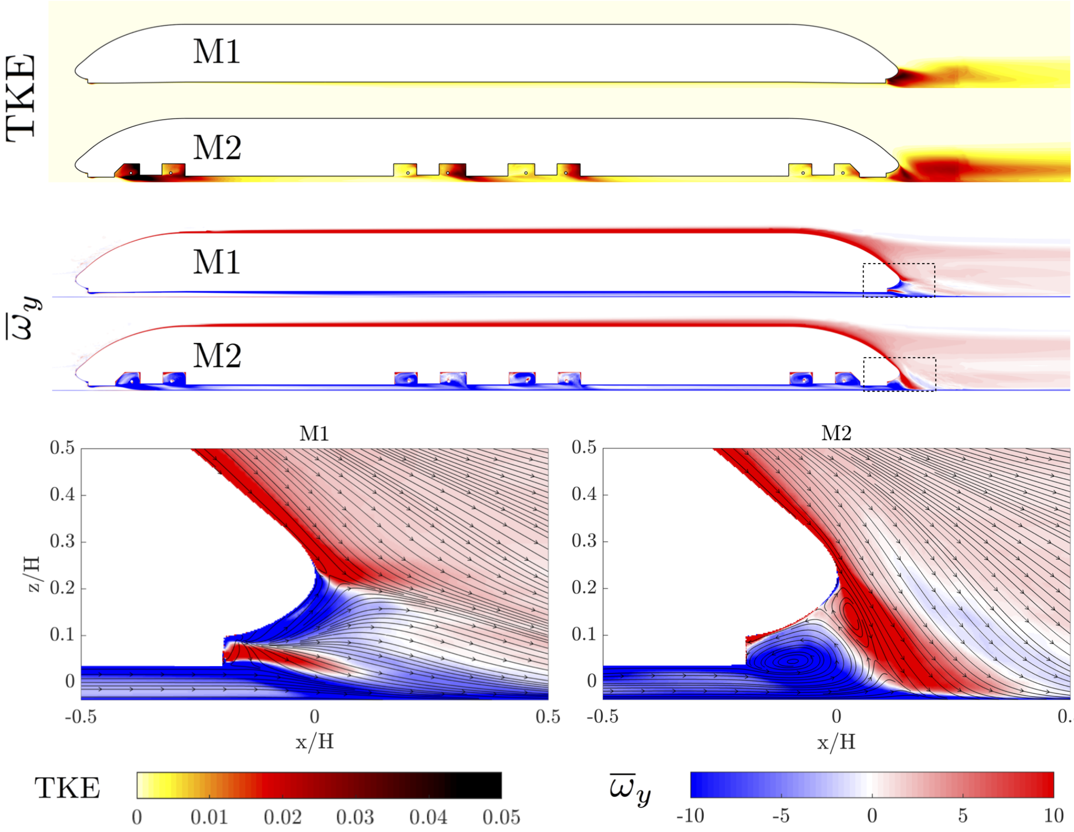

FIGURE 6.2: The bogies effects within the flow development region illustrated by TKE and $\overline{\omega}_y$ with in-surface projected velocity streamlines at $y = 0W$.

M1 near wake. A possible explanation for this is that the twin vortices are formed due to the significant kinetic energy difference between the strong downwash from the train top surface and low-speed underbody flow. Specifically, the lower energy fluid passing under the train is not sufficient to prevent the high-energy fluid passing over the train separating at the trailing nose. Combined with separation of the underbody flow at the snowplough, this leads to the two local counter-rotating recirculation regions. In comparison, the high momentum underbody stream in M1 is sufficient to cause the flow to remain attached to the point of the trailing nose.

6.2.1.2 Wake Region

The *wake region* is defined as the region downstream of the tail, where the vortical flow structures that separate from the train surface propagate downstream. Consistent with wind-tunnel experimental results (Bell *et al.* 2016a) (Bell *et al.* 2016b), the dominant time-mean wake structure is a pair of longitudinal counter-rotating vortices.

In this study, it makes sense to further divide the development and evolution of the wake structure into two regimes: the *wake formation regime* and the *wake propagation regime*, in accordance with the formation and evolution of the time-mean coherent longitudinal vortical structures as illustrated in Fig. 6.3.

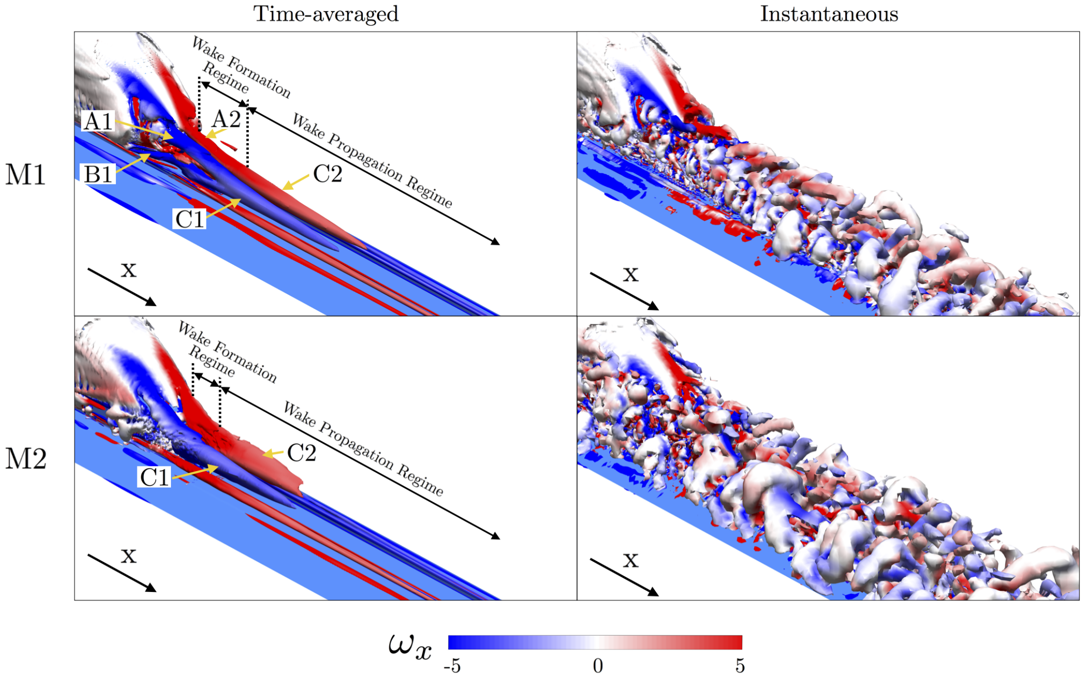

FIGURE 6.3: The comparison of the bogie effects on the development of the wake structure at the tail, visualised by an iso-surface of Q-criterion coloured by ω_x.

The development of the time-mean and instantaneous wake structure behind the tail is depicted through an iso-surface of the *Q-Criterion* ($Q = 2$) in Fig. 6.3, where positive Q highlights rotation-dominated flow structures. Additionally, to indicate the origin of the longitudinal vorticity in the trailing vortices, the Q-criterion iso-surface is coloured by x-vorticity (ω_x). The streamwise vorticity is calculated based on the normalised spanwise and transverse velocities. The instantaneous flow structures in the right-hand column of Fig. 6.3 illustrate that the turbulent wake structures are more concentrated towards the centreplane when they are separated from the tail of M1, while the bogies introduce multi-scale flow structures at a higher turbulence level. According to the comparison between the time-averaged flow structures in Fig. 6.3, the alteration to the underbody flow significantly affects the near-wake formation of the time-mean wake vortices. In M2, the downwash from the tail dominates the underbody stream, and generates a pair of longitudinal trailing vortices (denoted as vortex pair C) behind the tail. This pair is a coherent, persistent wake structure, and initiates from the curved edge between the top and side surfaces of the tail, in a similar way to the

C-pillar vortices identified in vehicle aerodynamics. Additionally, from the $\overline{\omega}_x$ contours, it can be seen that the longitudinal vorticity of the trailing vortices originates from the twisting effect at the C-pillar, which is caused by the pressure difference between the tail side and top surface. This is further illustrated in § 6.2.3. In comparison, with the flat underbody configuration (M1), apart from the primary pillar vortices (denoted as vortex pair A), a pair of secondary vortices (denoted as vortex pair B) is formed at the snow-plough due to the the higher momentum streamlined underbody flow. Note that vortex B2 is not visible in Fig. 6.3 as it is behind vortex A2. As the wake propagates downstream, the two vortex pairs, A and B, meet at approximately $x = 1H$, and then merge into one vortical structure (denoted as vortex pair C), which is analogous to the coherent trailing vortices in M2. Beyond this point, the wake structures of M1 and M2 are qualitatively identical.

The formation and propagation of the time-averaged wake structures are quantitatively depicted by $\overline{\omega}_x$, in-surface projected velocity vectors and the vortex boundaries, on six consecutive vertical planes between $x = 0.5H$ and $5H$, as presented in Fig. 6.4. As the time-averaged flow structure is symmetric about the mid-plane, only the left half of the flow field is presented. The boundary of the trailing-vortex structure is depicted through an iso-line of $\Gamma_2 = 2/\pi$, based on the Γ_2 criterion, a method often chosen by experimentalists to mark the extent of a vortex dominated region (Graftieaux *et al.* 2001). In addition, the core of a vortex is indicated by a green asterisk, which is determined by the maximum local value of Γ_1 (again see (Graftieaux *et al.* 2001)). The crosses ("+") and circles ("o") in Fig. 6.4 represent the trackside ($z = 0.05H$) and platform ($z = 0.35H$) slipstream measurement location respectively, based on the TSI specifications (TSI 2014).

According to Fig. 6.4, when the bogies are included, a pair of trailing vortices (C) is formed immediately behind the tail ($x = 0.5H$), and as it propagates downstream, it rolls over the rails and moves away from the spanwise centre-plane. In comparison, two discrete pairs of vortices (A and B) are identified at $x = 0.5H$ in M1, and they start to merge to form a single vortical structure (C) at $x = 1H$. This description is consistent with the wake structure evolution illustrated in Fig. 6.3. In comparison with M2, M1 shows that vortex pair C stays closer at the centre-plane. Additionally, as the underbody stream pushes against the downwash vortex A, and the cores of C in M1 are slightly shifted upwards.

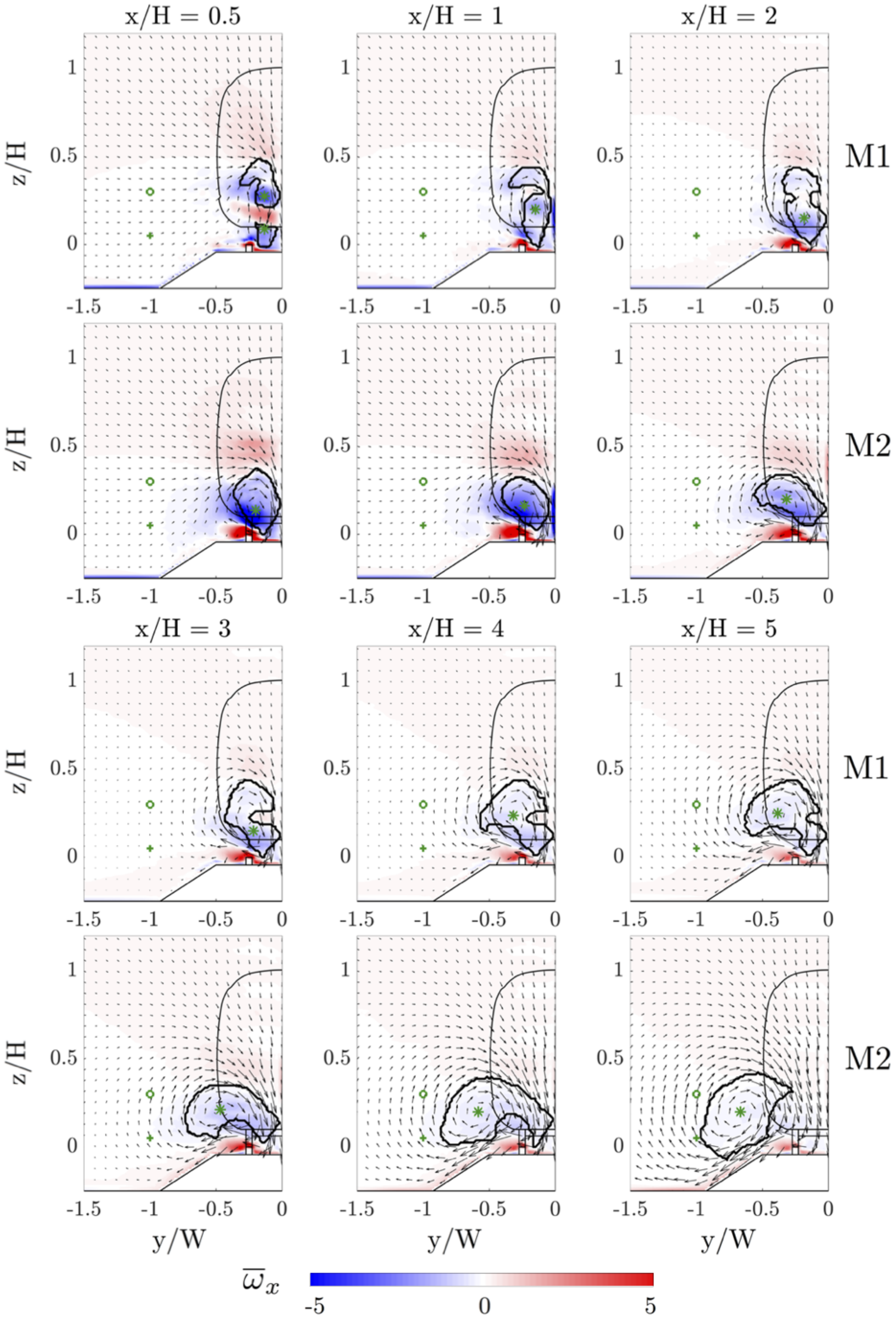

FIGURE 6.4: The comparison of the wake development downstream based on six consecutive vertical planes between $x = 0.5$ and $5H$. Here, "$\circ$": platform slipstream assessment location; "+": trackside slipstream assessment location. The vortex boundaries, shown by the black lines, are identified by the Γ_2 criterion. The vortex centres ("$*$") are identified using local maximum values of Γ_1 (see (Graftieaux *et al.* 2001)).

In this study, the strengths of vortices are quantified through the circulation, which is calculated by the surface integral of $\overline{\omega}_x$ within the vortex boundaries using *Stokes' Theorem*. The strengths of vortex A and B in M1 are $1.41 \times 10^{-3} U_\infty H$ and $1.02 \times 10^{-3} U_\infty H$, respectively. This indicates that the downwash vortices formed from the top surface are approximately 32.1% stronger than the vortices generated from underneath. For completeness, the strength of coherent counter-rotating vortex pair C is described by the mean vortex circulation at $x = 2H$, which is $2.24 \times 10^{-3} U_\infty H$ for M1 and $3.41 \times 10^{-3} U_\infty H$ for M2. This shows that the bogies can alter the strength of trailing vortices by about 30%.

The decay of the wake structure is quantified by the change of $\overline{\omega}_x$ at the vortex core, and the results are plotted in Fig. 6.5. Fig. 6.5 shows that M2 has a significantly higher decay rate within the near-wake compared to that further downstream. This is expected due to the higher turbulence level caused by the perturbations from the bogies. Note that the core vorticity $\overline{\omega}_x$ for M1 model between $x = 1$ and $3H$ cannot well represent the vortex strength as the coherent single vortex pair C is not yet fully formed.

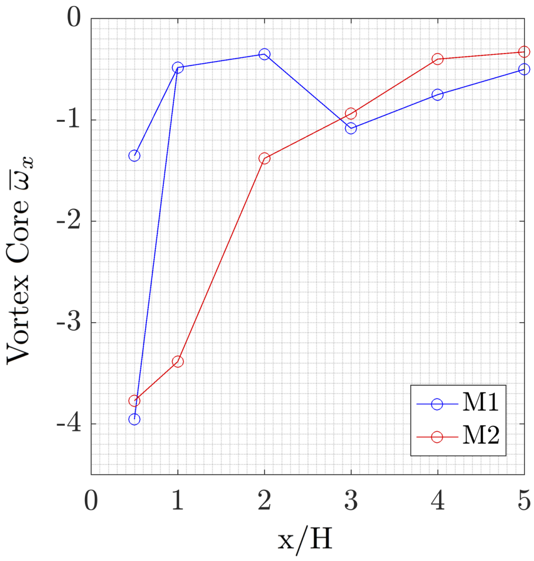

FIGURE 6.5: The comparison of the wake decay rate based on the change of vortex core $\overline{\omega}_x$

In the following, the dynamics of the near-wake flow structures, i.e. vortex pairs A, B in M1, and the vortex pair C in M2, are investigated based on the static pressure in the vortex cores at $x/H = 0.5$. The core coordinates ([y-coordinate, z-coordinate]) for vortex A, B and C at $x/H = 0.5$ are ([±0.133W, 0.275H]), ([±0.133W, 0.0875H]) and ([±0.2W, 0.1375H]), respectively. The frequency spectra and cross-correlation coefficients between adjacent structures are illustrated in Fig. 6.6, where the frequency is quantified by the non-dimensional Strouhal number (St_W) based on the train width (W).

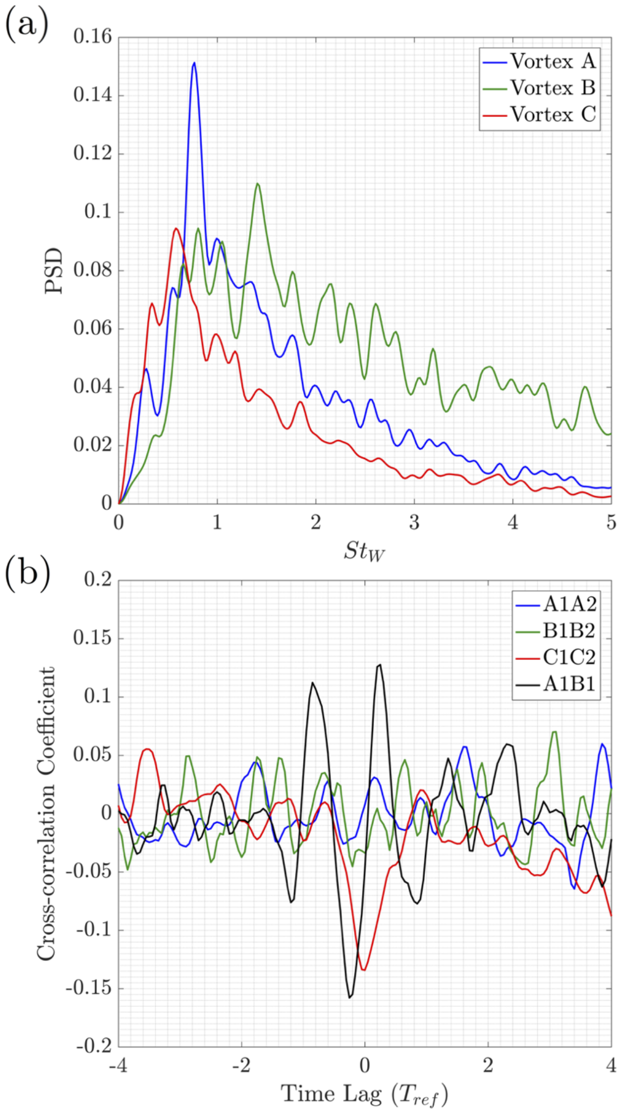

FIGURE 6.6: The comparison of dynamic response of the near-wake structures: (a): the frequency content within the vortex cores; (b): the correlation between the vortex structures.

According to the power spectral density (PSD) profiles in Fig. 6.6 (a), the pillar vortices, i.e. vortex pair A in M1 and vortex pair C in M2, demonstrate identifiable dominant frequencies of 0.75 and 0.58, respectively. In comparison, the lower vortex pair B in M1 shows a broad frequency response without a clear peak frequency. In addition to the frequency responses of individual structures, the interactions between two adjacent structures are studied by the cross-correlation between the core pressure, and the results are presented in Fig. 6.6 (b). The cross-correlation coefficient of 1 represents an in-phase motion, while -1 indicates an out-of-phase motion. The time-lag is normalised by T_{ref}. This figure indicates that for each vortex pair, no significant correlation exists for vortex pairs A and B of M1; however, the trailing vortex pair C of M2 shows a strong out-of-phase correlation. This implies that the spanwise wake oscillation is initiated immediately behind the tail in M2, while it is not established in either vortex pairs in M1, even for the equivalent-origin downwash pillar vortex A. On the other hand, a strong correlation with a $\pi/2$ phase difference is identified between the legs of the pillar vortex pair A and secondary vortex B beneath. This implies that the higher and lower vortices of M1 on the same side demonstrate a stronger vertical dependency, even though there is no spanwise dependency.

Additionally, the dynamic wake features can be understood through Proper Orthogonal Decomposition (POD), especially the detailed makeup of transient wake structures. This study utilises the Snapshot POD method, initially proposed by Sirovich (1987), due to its strength in extracting coherent flow features (denoted as modes), from a turbulent flow field, and ranking them according to their energy proportion. A detailed description of the POD method can be found in § 3.3. In this study, the components of the dominant transient flow features at the near- and intermediate-wake region are illustrated by the two most energetic POD modes resolved at $x/H = 1$ and 5. The POD analysis in the current study is based on the total pressure.

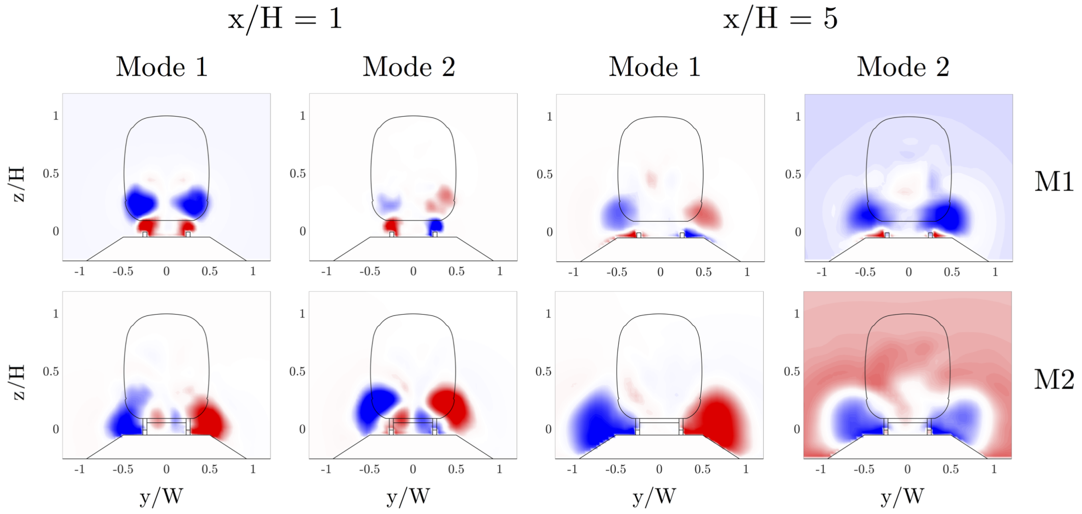

FIGURE 6.7: The comparison of dominant transient wake features resolved by POD for the near- and intermediate-wake region.

Fig. 6.7 shows that the dominant transient feature within the M1 wake formation region is a simultaneous energy increase/decrease centred on the vortices, corresponding to a longitudinal pulsing of the vortices. Additionally, the impulses of the vortex A and B are out-of-phase, which represents a vertical energy fluctuation. The second energetic mode depicts an out-of-phase oscillation within each vortex pair, which associates with the left-to-right oscillation. In comparison, both modes in M2 within the near-wake region are associated with the spanwise energy fluctuation. In the intermediate-wake region ($x = 5H$), the first two most energetic modes between M1 and M2 become qualitatively identical, which are an out-of-phase spanwise oscillation and an in-phase wake pulsing. Quantitatively, M2 shows a larger energy fluctuation region due to the wider unsteady wake.

Additionally, the effect of the bogies on the downstream wake development, especially on the spanwise wake oscillation, is studied based on a horizontal plane at a height at $z = 0.15H$, as shown in Fig. 6.8. The instantaneous flow structures are visualised by contours of $U_{slipstream}$ at an arbitrary time instant.

Firstly, the coherence of the spanwise oscillation is quantitatively described by the cross-correlation of the lateral velocity component (V_{GF}) based on an array of points from $x = 0 \sim 10H$ that are plotted as white circles in Fig. 6.8. The cross-correlation is calculated between each pair of points that are symmetric across the centreplane at $0.33W$ apart, and the downstream distance between two adjacent pairs is $0.25H$. Hence, a total of 50 pairs between $x = 0$ and $10H$ are utilised to capture the development of the wake's spanwise motion with downstream distance, and the cross-correlation profiles for each pair along the longitudinal direction are illustrated in Fig. 6.9 (a).

As the profiles of cross-correlation coefficient against time lag are symmetric at zero time lag, only the positive time lag portion is presented. According to Fig. 6.9 (a), a peak cross-correlation coefficient is determined at zero time lag (except for the pairs within the wake formation region of M1), and its positive value implies the spanwise oscillation. Therefore, the cross-correlation coefficients at zero time-lag for the pairs ranging from $x = 0$ to $10H$ are plotted in Fig. 6.9 (b) for a quantitative description of the coherence of spanwise motion for the wake. Fig. 6.9 (b) shows that without the bogies, the spanwise oscillation cannot be identified until approximately $x = 4H$. This is consistent with the wake dynamics, as illustrated in Fig. 6.6 and Fig. 6.7, in which the dominant transient feature within the M1 wake formation regime is the vertical interaction between primary pillar vortices (vortex pair A) and secondary vortices

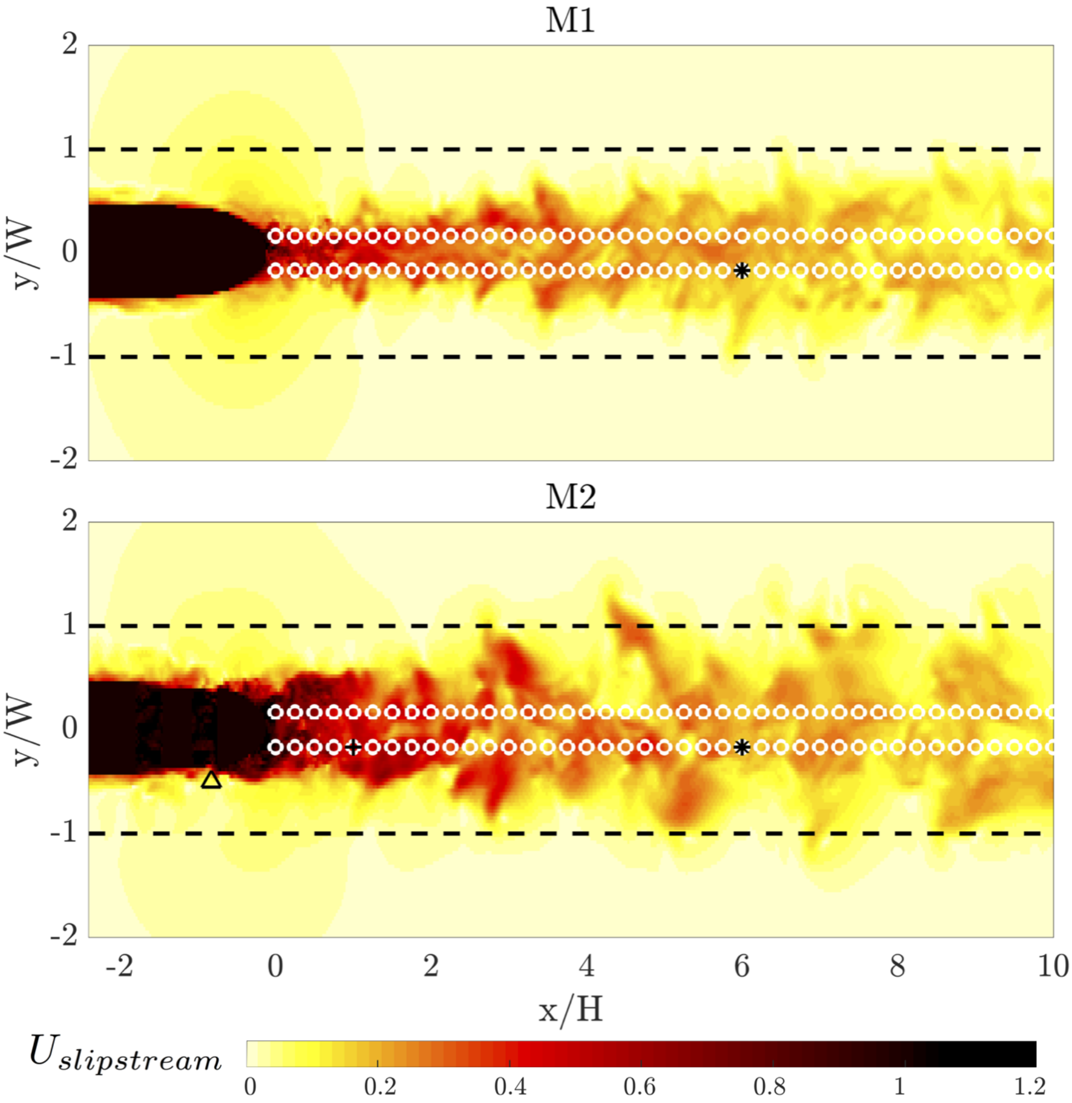

FIGURE 6.8: The wake propagation visualised by the instantaneous $U_{slipstream}$ ("○": an array of point pairs for spanwise motion identification; "△": the probe for measuring the shedding from the bogie; "+": the probe for measuring near-wake dynamics; "∗": the probe for measuring intermediate-wake dynamics).

(vortex pair B) beneath, instead of a spanwise oscillation. As the wake propagates downstream after the formation of vortex pair C, the spanwise correlation between the trailing legs then gradually develops. In comparison, the spanwise wake oscillation is immediately established behind the tail for M2, which is coincident with the formation of twin vortices immediately in the near wake. This indicates that spanwise motion can be identified in both cases once the vortex pair C is properly formed, regardless the presence of the bogies. Together with the similar spanwise oscillation frequency in both cases, this suggests that the bogies are not the ultimate cause of the spanwise oscilla-

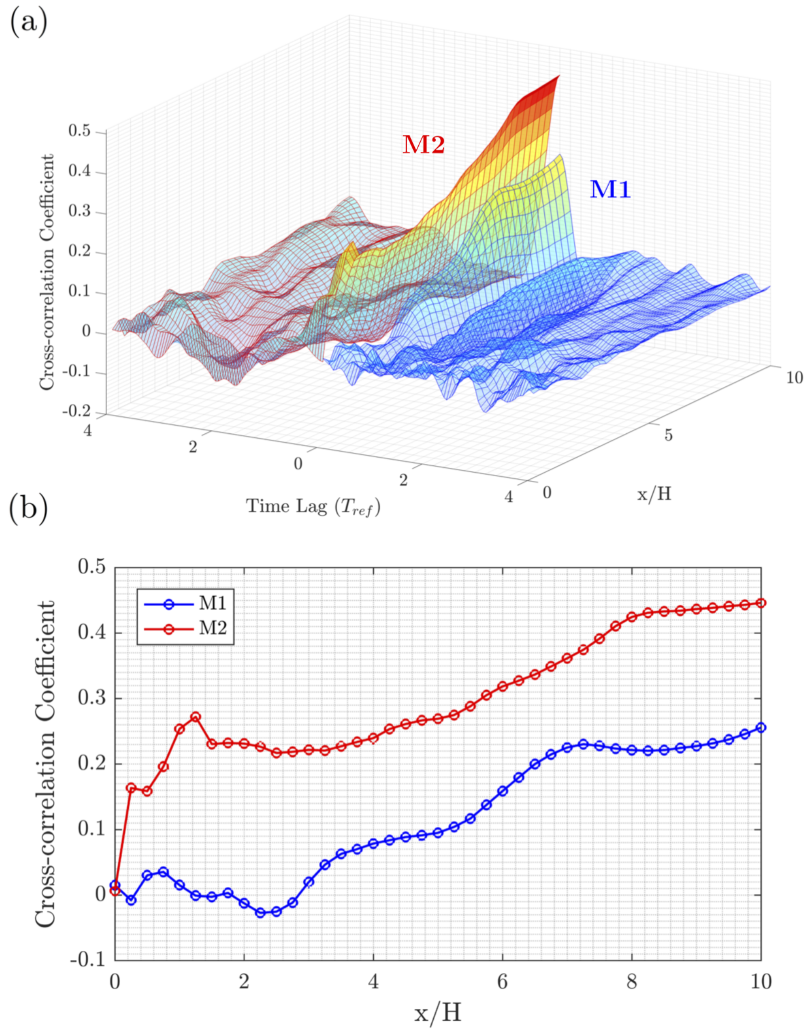

FIGURE 6.9: The cross-correlation of V_{GF} at point pairs (presented as "∘" in Fig. 6.8) for investigating the wake's spanwise oscillation: (a): the cross-correlation profiles per pair; (b): a comparison of the cross-correlation coefficient at zero time lag.

tion, instead, the wake oscillation is an intrinsic convective instability of the trailing vortices.

This hypothesis is further studied by analysing the characteristics of the shedding from the bogies in the near and intermediate wake, and investigating the correlation in between. The characteristics of the spanwise shedding at the bogies, near and intermediate wake are represented by the V_{GF} at three typical points whose the locations ([x-coordinate, y-coordinate]) are highlighted by the triangle ("△"), cross ("+") and asterisk ("∗"), with the coordinates ([-0.825H,-0.5W]), ([1H,-0.1667W]) and ([6H,-0.1667W]) respectively, as shown in Fig. 6.8. Firstly, the frequency response at each point is presented in Fig. 6.10 (a).

Fig. 6.10 (a) illustrates that no dominant shedding frequency can be identified from

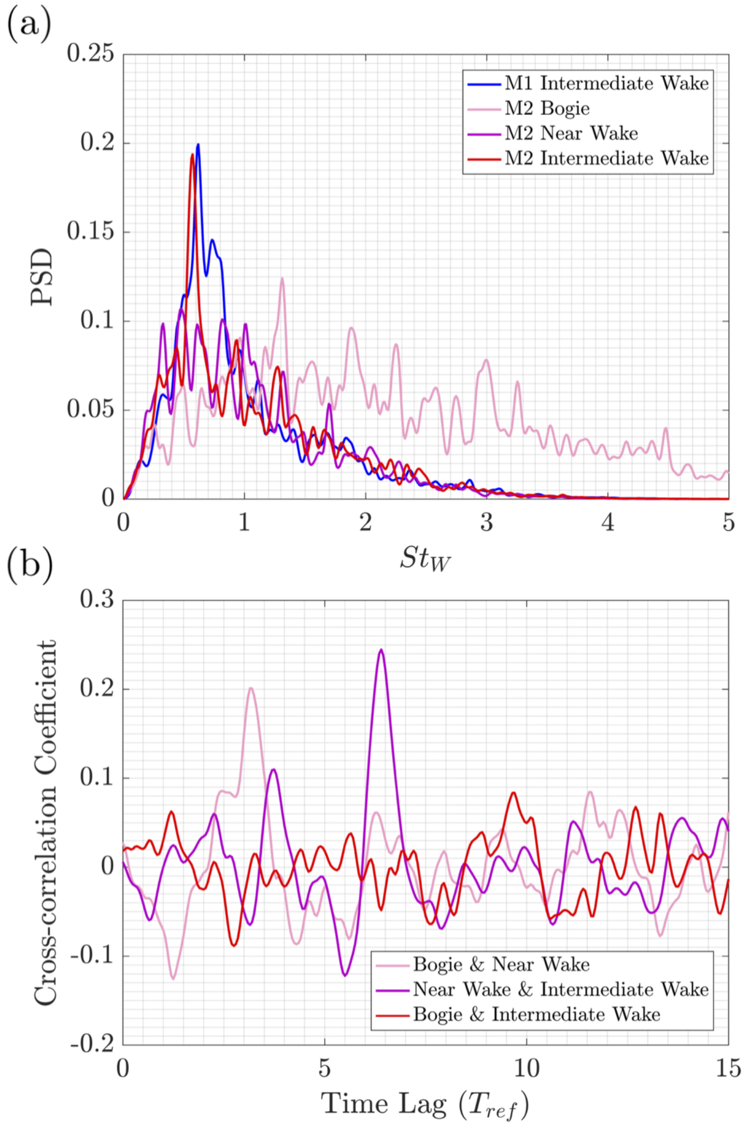

FIGURE 6.10: The characteristics of the shedding from the bogies and spanwise wake oscillation, and the correlation between per two flow features based on V_{GF}: (a) the frequency response; (b) the cross-correlation between flow features.

the bogies. Instead a broad spectral response between $St_W = 0.2 \sim 2$ is identified within the near-wake region, which is likely due to the various length scales introduced by the bogies generating a range of different frequencies. In the intermediate-wake region, where the short length-scale turbulence structures are dissipated and the coherent counter-rotating vortices are fully established, a clear peak frequency at $St_W = 0.6$ results. Additionally, this dominant frequency is identical to the one in M1, again which suggests that the frequency of the spanwise motion is a characteristic of the pair of counter-rotating vortices due to an inherent instability, regardless of the presence of the bogies. Furthermore, the correlations between the points located near the bogie, and the near and intermediate wake are plotted in Fig. 6.10 (b). The strong correlation between the near and intermediate wake points with a time-lag, which approximately equals to the wake advection time between the two points, implies that it is an identical flow feature that convects downstream. Even though the shedding from the bogies is correlated to the near wake over a wide time-lag, it is not correlated with the intermediate wake. Therefore, instead of directly introducing the coherent spanwise oscillation at a particular frequency, the bogies demonstrate a global influence on the near-wake flow field through perturbing the flow over a wide frequency range.

6.2.2 Slipstream Assessment

In this section, the slipstream velocity is studied from two perspectives: based on (1) statistical slipstream profiles and (2) gust analysis. The statistical slipstream profiles illustrate the time-averaged and standard derivation of the slipstream velocity at the TSI specified assessment locations, and hereby, derive the maximum slipstream velocity ($U_{slipstream,max}$) based on a 95% confidence interval assuming Normally distributed statistics. Gust analysis tries to artificially replicate the field measurements of full-scale testing to obtain an ensemble average of the temporal slipstream data under TSI specifications (TSI 2014).

6.2.2.1 Statistical Slipstream Profiles

In this study, the statistical slipstream assessment is taken at the TSI specified trackside height ($z = 0.05H$) and platform height ($z = 0.35H$), over the streamwise range $x = -15H \sim 30H$. The time-averaged and standard deviation profiles of the slipstream velocity ($U_{slipstream}$), and their streamwise (U_{GF}) and spanwise (V_{GF}) velocity components at the two measurement heights are plotted in Fig. 6.11, and critical points are listed in Table 6.1. The maximum expected slipstream velocity ($U_{slipstream,max}$), which is defined as $\overline{U}_{slipstream} + 2\sigma_{slipstream}$, predicts the upper limit of slipstream velocity under 95% confidence interval assuming Normally distributed samples. As illustrated in Fig. 6.11, the bogies alter the slipstream profiles in the same manner, but their influence is more significant at the trackside height; thus, the discussion of the bogie effects on slipstream profiles focuses on the influence at the trackside height.

Over the train and in the near wake, it can be seen that M1 and M2 have qualitatively near identical $\overline{U}_{slipstream}$ profiles, which include the head pulse and a local peak around the tail. After the air passes over the tail, it accelerates and to achieve

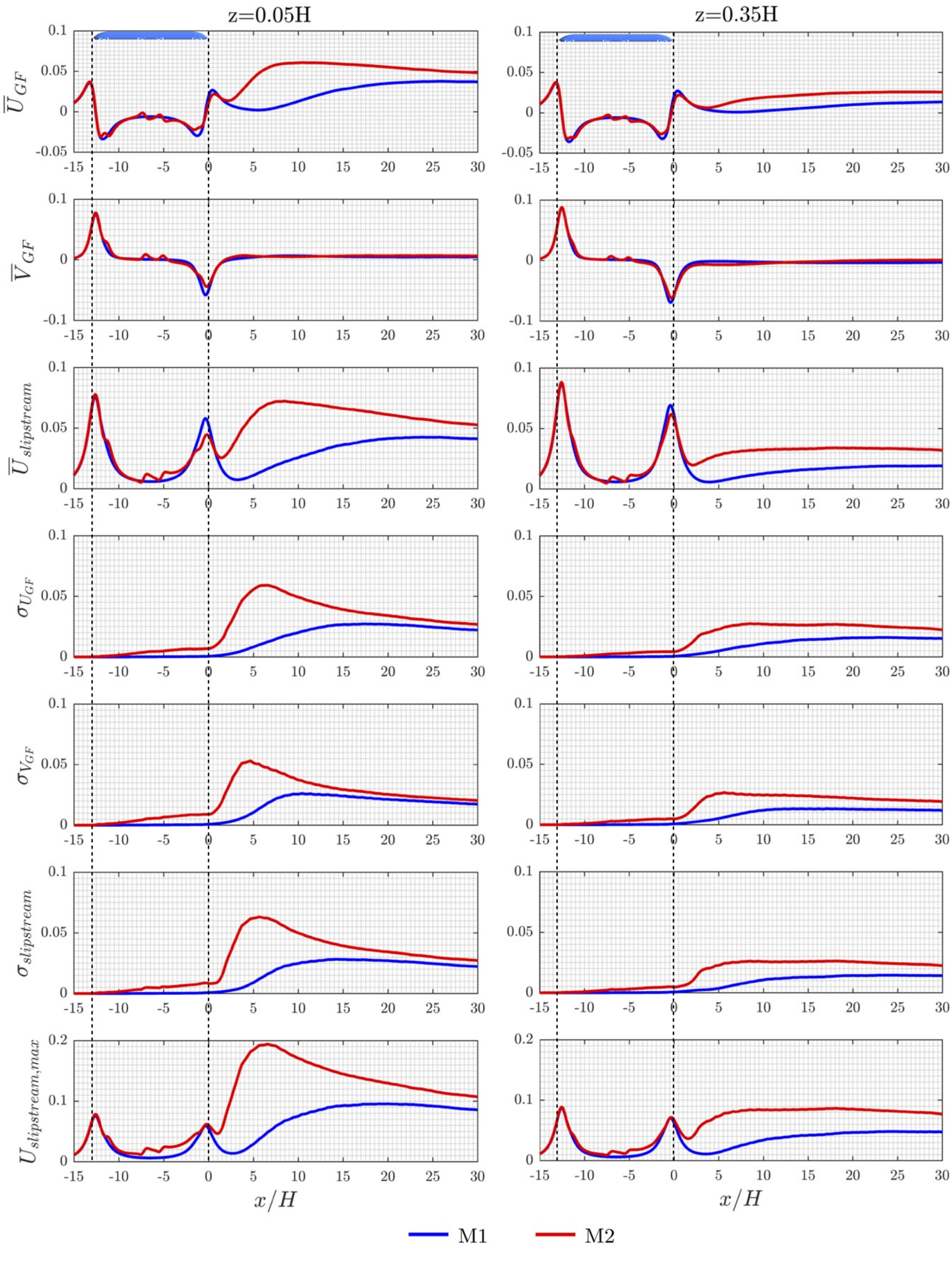

FIGURE 6.11: The comparison of statistical slipstream profiles between M1 and M2 at the trackside ($z = 0.05H$) and platform ($z = 0.35H$) heights.

a maximum velocity before gradually decreasing. This is a typical HST slipstream profile, which has been identified for different train geometries with various techniques (Bell *et al.* 2016b)(Huang *et al.* 2016)(Baker 2010)(Bell *et al.* 2015). Quantitatively, the time-averaged velocity ($\overline{U}_{GF}$, $\overline{V}_{GF}$) profiles prior to the tail region are identical,

Table 6.1: The critical values in the statistical slipstream profile analysis.

	M1		M2	
	Maximum	**Location (x/H)**	**Maximum**	**Location (x/H)**
	Trackside height (z=0.05H)			
$\overline{U}_{slipstream}$	0.076	-12.63	0.078	-12.63
$\sigma_{slipstream}$	0.028	14.28	0.063	5.61
$U_{slipstream,max}$	0.096	20.01	0.190	6.61
	Platform height (z=0.35H)			
$\overline{U}_{slipstream}$	0.087	-12.57	0.089	-12.57
$\sigma_{slipstream}$	0.015	24.79	0.0263	18.06
$U_{slipstream,max}$	0.087	-12.57	0.089	-12.57

except for local fluctuations caused by the bogies captured for M2.

Within region around the tail ($x = -1H \sim 1H$), both models show peaks in $\overline{U}_{GF}$ and $\overline{V}_{GF}$, with the flat underbody amplifying the magnitude of this disturbance. Hence, M1 demonstrates a higher local peak of $\overline{U}_{slipstream}$ around the tail. The reason for this difference is that with a smoother train surface, the flow over the tail is more streamlined and results in a higher magnitude effect at the measurement locations.

Fig. 6.11 also shows that $\overline{U}_{slipstream}$ initially drops in wake region before recovering further downstream. For M1, after the flow passes the tail, $\overline{U}_{slipstream}$ drops to approximately 0.005 at $x = 3H$, and then slowly increases to reach a maximum of 0.04 at $x = 25H$. In contrast, M2 shows a much steeper increase of $\overline{U}_{slipstream}$ starting from $x = 2H$, and achieves its maximum of 0.07 at $x = 7H$. According to $\overline{U}_{GF}$ and $\overline{V}_{GF}$, it can be seen that, the difference in $\overline{U}_{slipstream}$ between M1 and M2 is caused by the change to $\overline{U}_{GF}$. The underlying mechanism is that a sideways shift of the vortical wake structures, which contain lower momentum fluid, can significantly affect the local slipstream velocity. Details of time-mean wake structure were presented in *Section* 6.2.1.

In M2, both $\sigma_{U_{GF}}$ and $\sigma_{V_{GF}}$ show a gradually increase along the train due to the unsteadiness introduced by the bogies, while for M1 the standard deviations are negligible. Additionally, the perturbation caused by the bogies significantly intensifies $\sigma_{slipstream}$ within the wake region, which results in an increase of maximum $\sigma_{slipstream}$ from 0.028 to 0.063. According to the combined effects of $\overline{U}_{slipstream}$ and $\sigma_{slipstream}$, $U_{slipstream,max}$ is predicted to occur at $20H$ and $7H$ with the magnitude of 0.1 and 0.19, respectively, for M1 and M2. Therefore, although the head pulse causes a maximum $\overline{U}_{slipstream}$, the wake region is more critical in terms of maximum potential slipstream velocity due to the high turbulence level within the wake region, leading to considerable excursion from the mean behaviour.

6.2.2.2 Gust Analysis

The TSI regulations (TSI 2014) define how the slipstream velocity should be measured under field testing, and the procedure of calculating the maximum slipstream velocity (also known as the *TSI value*) is briefly described here. The slipstream should be measured at two fixed positions: the trackside ($z = 0.05H$) and platform ($z = 0.35H$) height, as introduced before. The entire flow disturbance, including the train passing and the wake, needs to be recorded. Additionally, a *1-second Moving Average (1s MA) filter* is required to be applied to the raw data, and the peak slipstream velocity of the filtered data is taken as one measurement. The distance between two independent measurements has to be more than 20 meters, and a minimum of 20 independent measurements is required for calculating the maximum slipstream velocity (the *TSI value*). The *TSI value* is calculated as the mean of the peak velocities plus two standard deviations, which indicates the statistical maximum slipstream velocity of the HST within a 95% confidence level, and this assessment is integrated into the HST acceptance procedure. The details regarding the HST slipstream regulations adopted in this project can be found in *Appendix A*.

Numerically, *Gust Analysis* tries to artificially replicate the field measurements of full-scale testing to obtain an ensemble average of the temporal slipstream data based on the above procedure. This study utilises the *Moving Probe Technique* to conduct the gust analysis, and the results are presented in Fig. 6.2.2.2. A full description of the *Moving Probe technique* can be found in § 3.1.

The $U_{slipstream}$ disturbance recorded by each probe is plotted as a function of time as a light grey line, and the peak value of each measurement is highlighted by a black dot. The results with a 1s MA filter are plotted as blue lines, for which the peak values are highlighted by blue points. Similar to the full-scale testing (Baker *et al.* 2014b) and moving-model experiments (Bell *et al.* 2015), gust analysis shows a large run-to-run variance. Consistent with the statistical results presented in *Section* 6.2.2.1, the difference is more significant at the lower height ($z = 0.05H$). In M2, a shape increase of $U_{slipstream}$ after the tail passage is identified, and the peak slipstream velocities (U_{peak}) within the wake region demonstrate a strong left-skewness. In contrast, M1 shows that

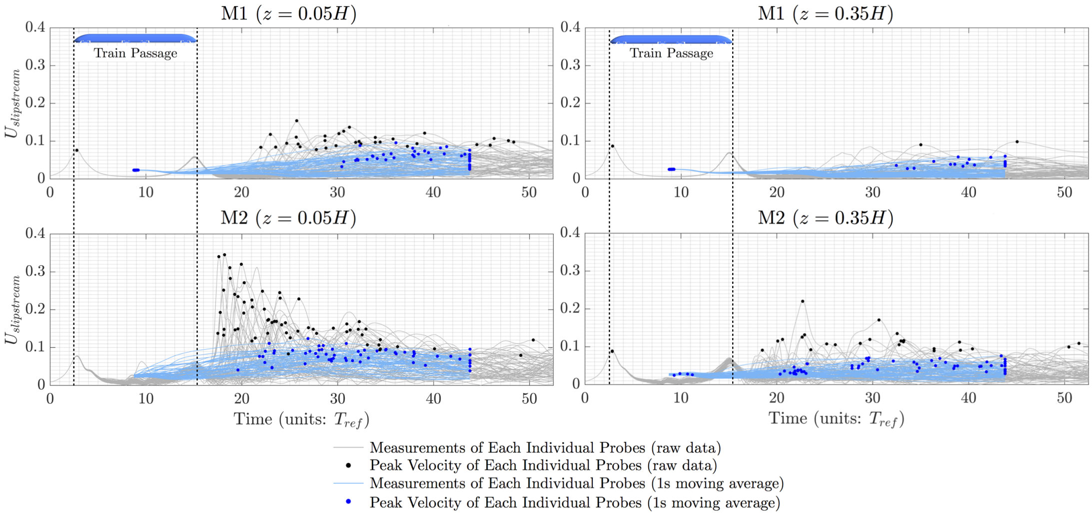

FIGURE 6.12: The results of gust analysis based on the *Moving Probe Technique* under TSI specifications.

TABLE 6.2: The critical values from the gust analysis. The numbers in the brackets are the raw data without applying a 1s moving average.

		Trackside	**Platform**
M1	$\overline{U}_{peak}$	0.050 (0.090)	0.031 (0.088)
	$\sigma_{U_{peak}}$	0.021 (0.018)	0.009 (0.002)
	$U_{TSI,max}$	0.092 (0.126)	0.049 (0.091)
M2	$\overline{U}_{peak}$	0.079 (0.175)	0.045 (0.100)
	$\sigma_{U_{peak}}$	0.018 (0.065)	0.013 (0.023)
	$U_{TSI,max}$	0.114 (0.303)	0.072 (0.145)

peak slipstream velocities have a lower magnitude and their occurrence is significantly delayed downstream. This difference is due to the wider and more turbulent wake structure caused by the bogies, which is discussed and presented in *Section* 6.2.1. As presented in Table 6.2, the *TSI value* assessment is sensitive to the presence of the bogies, especially at a lower height. Table 6.2 determines that the effect of bogies on the wake structures can significantly vary the slipstream assessment, i.e. the presence of bogies can alter the *TSI value* up to 20% at the trackside height.

6.2.3 Aerodynamic Loading

In the final section, the bogie effect on the aerodynamic loading is presented according to the changes induced on the train surface pressure and force integral. The surface pressure is visualised by the pressure coefficient (C_P) as presented in Fig. 6.13, where

C_P is defined by

$$C_P = \frac{P - P_\infty}{\frac{1}{2}\rho_\infty V_\infty^2}. \tag{6.1}$$

Here, P is the surface static pressure, and reference values for the pressure, density and velocity are P_∞, ρ_∞ and V_∞, respectively. Fig. 6.13 shows that the top and side surface pressure distributions are qualitatively identical, and a more quantitatively comparison is obtained by the pressure profiles on the train centreplane surfaces in Fig. 6.14.

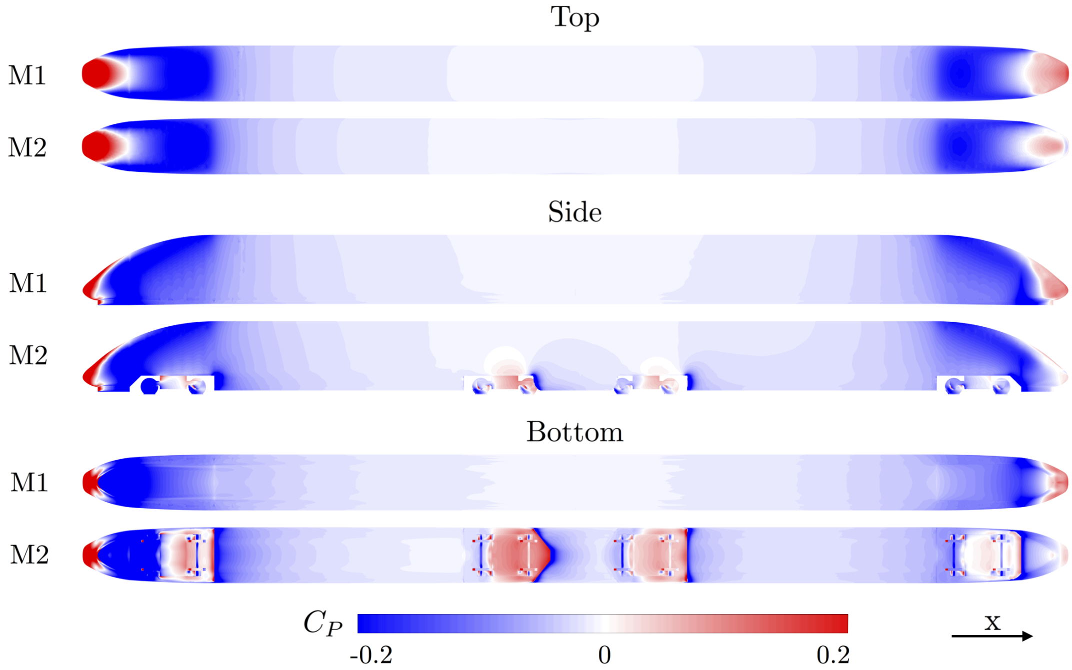

FIGURE 6.13: The comparison of the aerodynamic loading on the train surface based on the pressure coefficient (C_P).

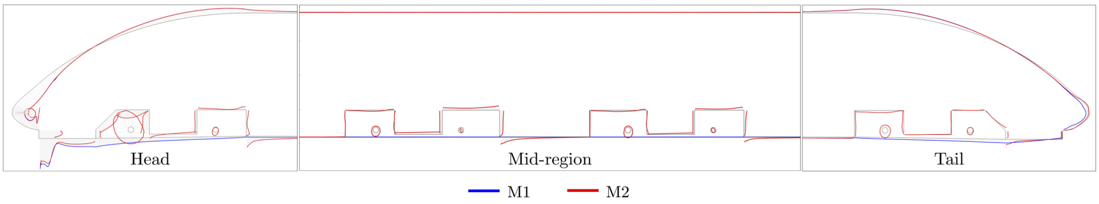

FIGURE 6.14: The centreplane pressure profiles at each train section for a quantitative comparison of the bogie effects on the aerodynamic loading.

A high pressure region due to the impact of the oncoming flow is captured at the head, and the negative pressure region along the curved surface is caused by local flow acceleration. Additionally, a positive pressure region can be identified for both models at the tail due to the reversed flow, while the area of this region for M2 is reduced

Table 6.3: The comparison of the drag (C_D) and lift (C_L) estimation between M1 and M2.

		M1	**M2**
C_D	Mean	0.157	0.283
	Standard deviation	9.11×10^{-4}	9×10^{-3}
C_L	Mean	-0.078	0.051
	Standard deviation	0.0039	0.016

towards the lower height due to the alteration to the flow caused by the bogies. Clearly, the major differences occur over the bottom surface. Comparing the streamlined M1 bottom surface, the bogies not only increase drag through the introduction of blockage, the cavity flow within the bogie cut-outs also produce a positive pressure on the bottom surface, which affects the lift force. From the C_P distribution over the train surface, both the drag (C_D) and lift (C_L) coefficients are calculated and listed in Table 6.3. Not surprisingly, due to the altered surface pressure, the presence of the bogies can alter C_D by almost a factor of 2 (from $C_D = 0.157$ to 0.283). This is consistent with the results of a previous study concluding that bogies are a major aerodynamic drag source, even though the train length-to-height ratio in this study is reduced (Raghunathan *et al.* 2002). The formation of positive pressure regions on the bottom surface alters C_L from a negative value of -0.078 to a positive value of 0.051. Additionally, the local flow shedding introduced by the bogies amplifies the unsteadiness of the aerodynamic loading on the train and results in a significant increases of the standard deviations of C_D and C_L, as shown in Table 6.3.

6.2.4 Summary of Key Findings

In this study, the effects of bogies on HST slipstream characteristics are investigated based on two generic train models: a *Simplified Train Model* (M1) without the bogies, and *Full-featured Train Model* (M2) with the simplified bogies. Through a direct comparison of the time-mean and instantaneous flow structures between M1 and M2, the mechanism of how the bogies alter the slipstream characteristics around the train is elucidated. The origin of the altered flow is that the bogies partially block the underbody flow stream and increase its unsteadiness due to the significant introduced flow perturbations. Without the bogies, a high momentum flow stream from underneath forms a time-mean secondary vortex pair (vortex pair B) around the snowplough, which is not identified in the M2 model. This vortex pair is about 32.1% weaker than the primary downwash pillar vortices (vortex pair A). Additionally, no significant correlation is determined between oscillations of the vortices from each side; instead, a strong correlation between trailing vortices from the two vortex pairs on the same side is identified indicating a near-wake vertical energy oscillation. Without the presence of vortex pair B, the downwash flow from the top of the tail in M1 forms a pair of counter-rotating vortices (vortex pair C), immediately behind the tail, and establishes a spanwise oscillation. The pillar vortices in the near wake ($x/H = 0.5$) for both M1 and M2 show similar identifiable peak frequencies of $St_W = 0.75$ and 0.6 based on the pressure signal, while vortex pair B for M1 shows a wider spectrum with no clearly identifiable dominant frequency. As the flow advects downstream, the vortex pairs A and B of M1 merge into a single coherent vortex pair (vortex pair C), similar to the case for M2. The strength of each vortex of C for M2 is 30% greater than that for M1, while the bogies cause a higher wake decay rate due to the unsteadiness introduced into the wake.

The appearance of a spanwise wake oscillation is found to be correlated with the presence of counter-rotating vortices of vortex pair C, instead of the presence of bogies, according to the following observations. Firstly, the spanwise oscillation has an similar frequency of approximately $St_W \simeq 0.6$ based on spanwise velocity, regardless of the presence or absence of bogies. Secondly, the delay in the establishment of the spanwise wake oscillation is consistent with the longer wake formation region of M1, until vortex C forms. Furthermore, the shedding/turbulent flow from the bogies shows a wide frequency spectrum, which feeds into the near-wake. Therefore, this study proposes that the spanwise motion is not directly triggered by shedding from the bogies; instead, the wide spectrum turbulence generated perturbs the forming counter-rotating vortex pair (vortex pair C) which responds at a preferred convective instability frequency as a spanwise oscillation. Even though the bogies do not directly generate the spanwise motion, they may affect the spanwise oscillation by altering the near wake turbulence level, which deposits energy into the intrinsic instability mode, and also the altering strength of the counter-rotating vortices.

As the wake convects downstream, the pair of counter-rotating vortices moves apart from each other in the spanwise direction. In M2, the strength of the trailing vortices is stronger and they are closer to the slipstream assessment location. Because of this, $\overline{U}_{slipstream}$ is increased due to the increment of $\overline{U}_{GF}$, especially within the wake region. Additionally, the unsteadiness introduced by the bogies increases the standard deviation of velocity components, and result in a significantly greater prediction of $U_{slipstream,max}$. Even though this effect occurs at both slipstream assessment heights, the impact is more significant at the trackside height of $x = 0.05H$ than the platform height of $x = 0.35H$. Similar influences are determined based on the gust analysis, which shows that the *TSI value* at the trackside height is increased from 0.092 to the 0.114 due to the presence of bogies. The bogies also alter the train surface pressure distribution especially on the bottom surface, which results in a significant increase in C_D from 0.157 to 0.283, and an alteration to C_L from -0.078 to 0.051. The unsteadiness caused by the bogies is also reflected in increases of the standard deviations of the aerodynamic loadings.

6.3 Conclusion

In conclusion, the mechanism of how bogies alter the slipstream characteristics is uncovered by analysing the effects on the wake structures including the time-averaged flow features, and their dynamic responses at each stage of the flow development. This study shows that by altering the underbody flow condition, the bogies predominantly change the wake formation topology by generating a pair of recirculation zones under the train tail region. Dynamically, the bogies significantly increase both the underbody flow and wake's turbulence level due to the unsteadiness from induced flow perturbations. This study determines the inter-relationship between the bogies and spanwise wake oscillation. Specifically, by showing that the spanwise motion of the wake occurs without the presence of the bogies at the same oscillation frequency, this study argues that the the bogies do not directly cause this oscillation; instead, the present study proposes that the spanwise motion is due to a natural convective instability of the trailing vortex pair. The presence of the bogies merely generates the turbulence that leads to the early detection of the oscillation as it is amplified downstream. Both statistical and gust analyses show that the alteration of wake flow structures due to the bogies can further increase slipstream, especially at a lower reference height. Additionally, the variation of the train surface pressure due to the bogies can significantly alter the prediction of aerodynamic loading. Above all, this study has provided an insightful understanding of bogie effects on HST slipstream characteristics by systematically comparing the flow features between M1 and M2.

Chapter 7

Effect of Rails

7.1 Problem Description

This study investigates the effect of rails on the HST slipstream characteristics by systematically comparing the flow features of two geometric configurations: *No Rail* (NR) and *With Rail* (WR) models. The train model (i.e., the M2 train model as presented in § 2.1) is identical in both configurations, with the only difference between the two configurations being whether the rails are included in the computational model or not. Detailed specifications regarding the geometry, and other features of the numerical set-up can be found in § 2. The aim of this study is to understand the effects of the rails on HST slipstream characteristics, and discover the underlying mechanism of how the rails interfere with the wake flow structures. Furthermore, how the altered flow affects slipstream assessment is also a major interest of this study.

As well as providing insight into the flow physics, this study also has practical significance. Firstly, reviewing actual methodologies for studying HST slipstream through computational analyses indicates that numerical set-ups, both with rails and without rails, have been adopted. However, there seems to be no study that investigates the potential effects of introducing rails to bridge the gap between the modelling camps. Secondly, the European standard on the inclusion of the rails for HST numerical simulation has changed in the last few years (CEN 2009) (CEN 2011) (CEN 2013). Prior to 2011, the European Committee for Standardisation (CEN) specified that the computational domain for studying the train aerodynamics on an open track should include a ballast bed with rails extruding through the entire domain (CEN 2009) (CEN 2011). In 2013 the standards changed, with the rails being removed from the ballast configurations (CEN 2013); however, the reasons for this modification were not specified. Therefore, this change provide a further rationale for undertaking this study.

7.2 Results and Analysis

To begin with, the effects of rails on the slipstream characteristics are studied by comparing the time-averaged flow structures between the NR and WR configurations in § 7.2.1, and the mechanism of how the rails interfere with the slipstream development is revealed. The effects on the transient wake features are then studied in § 7.2.2. After that, how the alterations to the time-averaged and transient flow structures further affect the slipstream assessment is investigated, according to statistical slipstream profiles and gust analysis in § 7.2.3.

7.2.1 Time-averaged Flow Structure

To understand the effects of rails on each stage of the slipstream development, the entire flow field is divided into a flow development region and a wake region, as shown in Fig. 7.1, and the effects on each region are investigated.

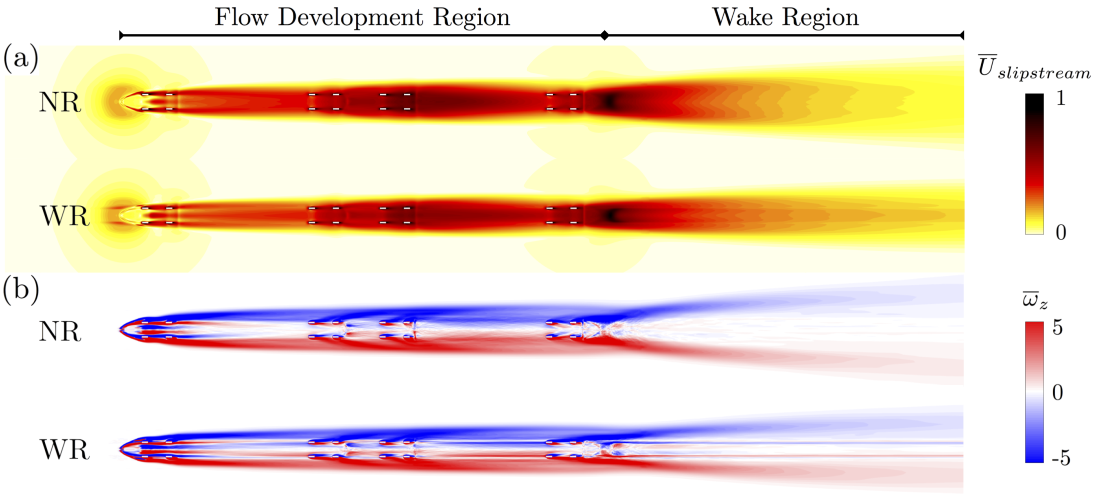

FIGURE 7.1: The overall comparison of rail effects within the flow development and wake regions visualised by (a): $\overline{U}_{slipstream}$ and (b): $\overline{\omega}_z$ at a horizontal plane in the middle of the underbody and TOR.

The flow development region extends approximately from the head to the tail of the train, and the wake region starts from the tail to where the slipstream becomes negligible. Fig. 7.1 shows that the effects of rails within the flow development region are limited within the region in close proximity to the rails. In comparison, a significant difference is observed within the wake region, and both $\overline{U}_{slipstream}$ and $\overline{\omega}_z$ contours demonstrate that the presence of rails widens the wake.

As determined in the previous chapters, the dominant mean wake structure behind a HST is a pair of longitudinal counter-rotating vortices. The impacts of rails on the formation of this coherent flow structure are visualised by the motion of tracer particles, which are realised around the tail tip, as shown in Fig. 7.2. The particles are released at $x = -0.5H$, and 75 mm (in full-scale) offset from the train surface. The wake development is visualised by tracking the movement of these particles in a time-mean flow field, with the tracers coloured by $\overline{U}_{slipstream}$.

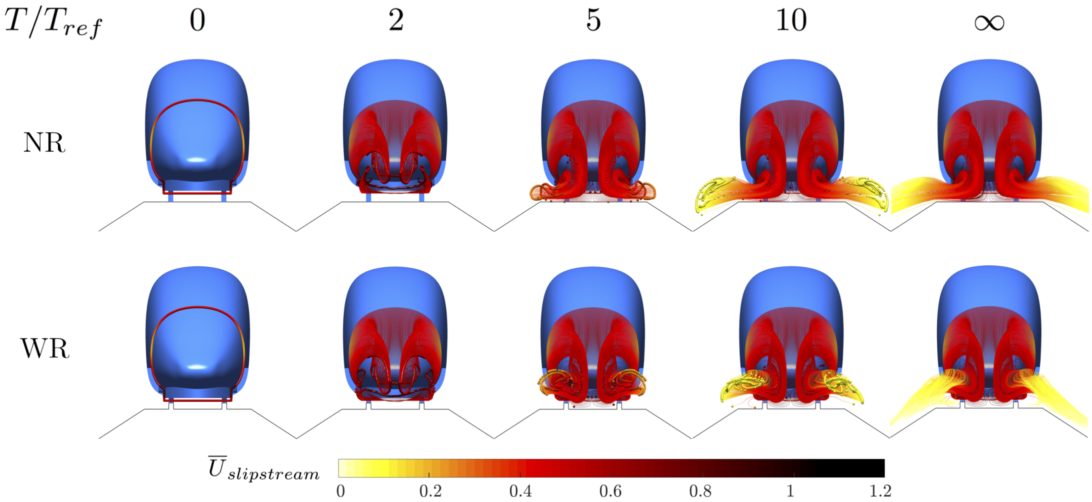

FIGURE 7.2: The interaction between the rails and the tracer particles released from near the tail as time elapses.

Fig. 7.2 shows identical patterns for the two models before the fluid impinges on the ground The trailing vortex pair is generated from the curved edge between the top and side surface of the tail. The alteration of the wake initiates when the downwash from the tail approaches the ballast. Without the rails, the wake can freely drift outwards in the transverse direction. In comparison, the presence of the rails obstructs the fluid's transverse movement; thus, the wake structure has to shift upwards and roll over the rails. Therefore, the rails possess a "lock-in" effect on the trailing vortices, by attempting to keep the trailing vortex pair between the rails. This is the fundamental mechanism of how the rails alter the downstream wake propagation and cross-stream evolution. Apparently, the obstruction of the wake's transverse motion causes a strong side force on the rails, which can significantly alter the aerodynamic loadings on the ballast, as shown in Fig. 7.3 and 7.4.

The "lock-in" effect of the rails can be clearly determined by the time-mean transverse wall-shear stress ($\overrightarrow{\tau_y}$) on the ballast, as plotted in Fig. 7.3. Without the rails, the relative motion between the wake and ballast in the spanwise direction causes a

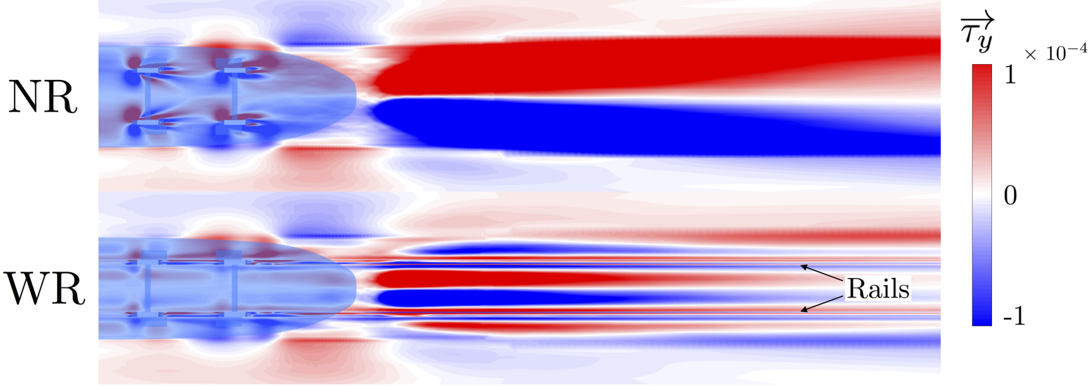

FIGURE 7.3: The “lock-in” effect visualised by the time-mean transverse wall-shear stress at the ballast.

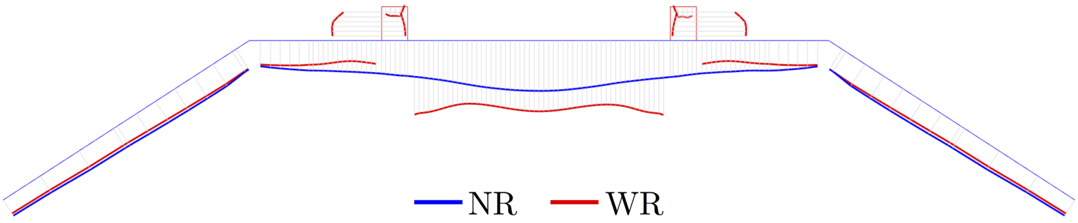

FIGURE 7.4: The comparison of C_P profiles at the ballast surface at $x = 0.5H$.

widespread high $\overrightarrow{\tau_y}$ magnitude region on the top surface of the ballast. In contrast, the presence of rails locks this region between the rails, showing a concentrated $\overrightarrow{\tau_y}$ alteration. To mostly lock the wake between the rails, a strong side aerodynamic loading is exerted on the rails, which can be quantitatively illustrated by the C_P profiles at the ballast cross-section at $x = 0.5H$, as shown in Fig. 7.4.

Fig. 7.4 illustrates that a strong positive pressure exerted on the inner surfaces of the rails, attempting to push the rails outwards. In comparison, a small pressure exerted on the outer sides of the rails that pushes the rails inwards is caused due to the corner recirculation region formed during the rolling-over of the trailing vortices as they advect outwards. Additionally, a significant pressure drop is determined between the inner and outer sides of the rails. The high pressure region between the rails is generated due to the impingement of the downwash, and the “lock-in” effect causes a pressure drop across the rails. Despite these effects, the difference of aerodynamic loading on the ballast slopes between NR and WR is negligible.

The propagation of the trailing vortices are quantitatively depicted by $\overline{\omega}_x$, in-surface projected velocity vectors and the vortex cross-sectional boundaries on six consecutive vertical planes between $x = 0.5H$ and $5H$, as presented in Fig. 7.5. As the time-

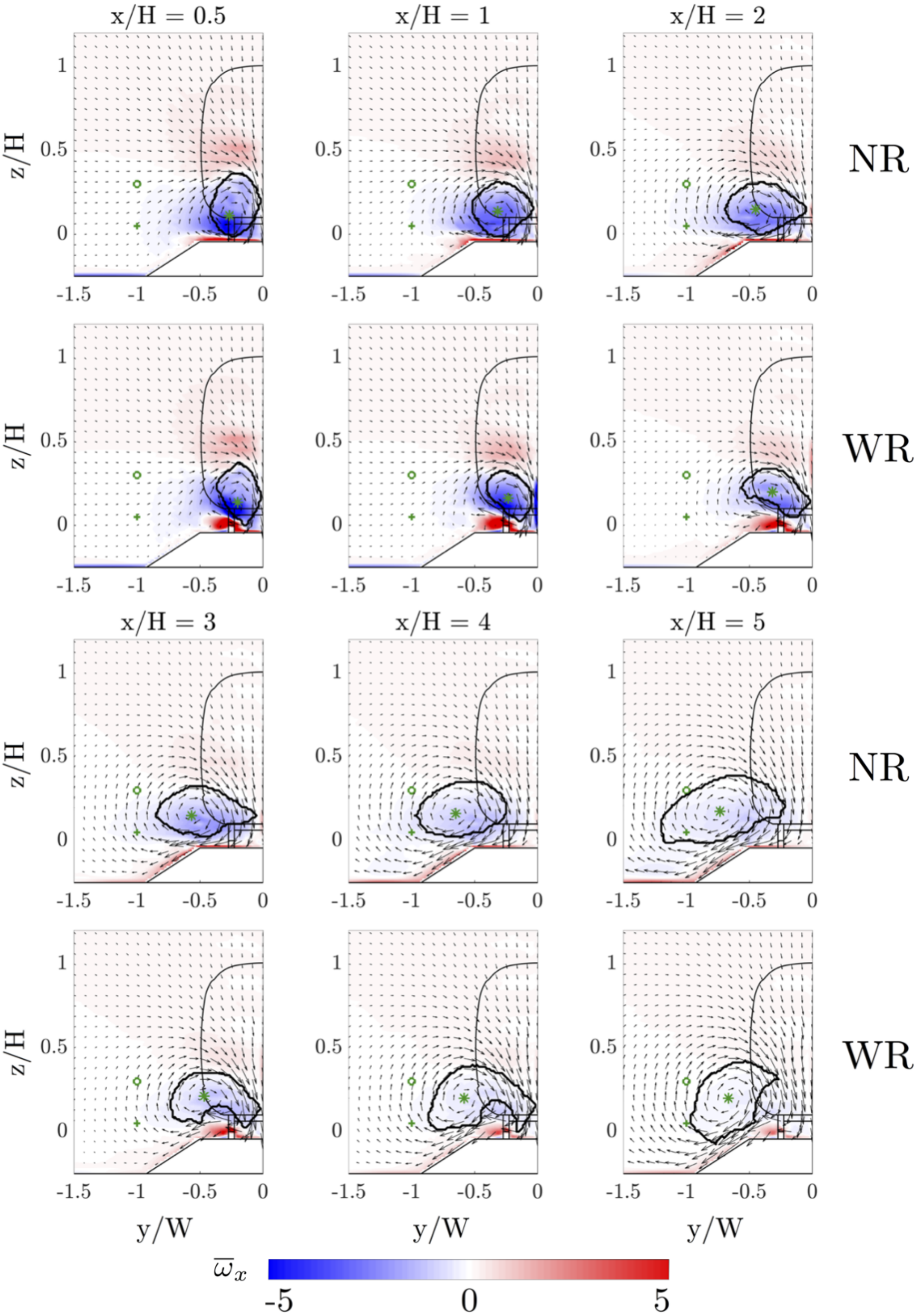

FIGURE 7.5: The wake propagation visualised by ($\overline{\omega}_x$) contour and in-surface projected velocity streamlines at 6 consecutive vertical planes from $x = 0.5 \sim 5H$ ("+": trackside slipstream measurement location; "o": platform slipstream measurement location; "$*$": vortex core).

averaged flow structure is symmetric about the mid-plane, only the left half of the flow field is presented. The boundary of the trailing vortex structure corresponds to the iso-line of $\Gamma_2 = 2/\pi$, which is a common vortex identification method often chosen by experimentalists (Graftieaux *et al.* 2001). Additionally, the core of a vortex is indicated by a green asterisk, which is determined by the maximum local Γ_1 coefficient (again see (Graftieaux *et al.* 2001)). The crosses ("+") and circles ("o") in Fig. 7.5 represent the trackside ($z = 0.05H$) and platform ($z = 0.35H$) slipstream measurement location respectively, based on the TSI specifications (TSI 2014). Fig. 7.5 illustrates that the wake structure in proximity to the rails is identical, but a difference accumulates when the vortices propagates further downstream. Consistent with the results shown by the tracing particles in Fig. 7.2, the rails obstruct the wake's spanwise motion, and the trailing vortices have to roll over the rails and then propagate further downstream. The positive $\overline{\omega}_x$ regions generated at the corner of the rails are indications of the rails' obstruction, which is more obvious during the roll-over process within the near-wake. Additionally, the rails deform the shape of the trailing vortices during roll-over, as illustrated in Fig. 7.5.

Furthermore, the decay in the strength of the trailing vortices is quantified by the change of vortex core streamwise vorticity $\overline{\omega}_x$ in the longitudinal direction, as presented in Fig. 7.6. From $x = 0.5H$ to $5H$, the magnitude of vortex core $\overline{\omega}_x$ drops from 2.97 to 0.66 at an average rate of 0.51 and 3.77 to 0.33 at an average rate of 0.76 for the NR and WR configuration respectively. Overcoming the obstruction of the rails causes a rapid loss of vortex strength, and results in a greater downstream decay rate of $\overline{\omega}_x$. For example, the fastest decay occurs between $x/H = 0.5$ and 2, where the vortex core is approximately right above the rails during the roll-over. Except for the high decay region of $x/H = 0.5 \sim 2$ for WR due to the interference of rails, the overall decay rate in other regions is quantitatively similar between NR and WR configurations.

7.2.2 Wake Dynamics

In this study, the effects of rails on the wake dynamics are illustrated by phase-averaging $U_{slipstream}$ on a horizontal plane at the trackside height ($z = 0.05H$), as presented in Fig. 7.7. The phase-averaging is conducted based on the V_{GF} signal at the point with coordinates ($[2H, -0.5W, 0.05H]$), visualised by the blue crosses in Fig. 7.7. The detailed procedure of phase-averaging is presented in § 3.2. The two black dashed lines

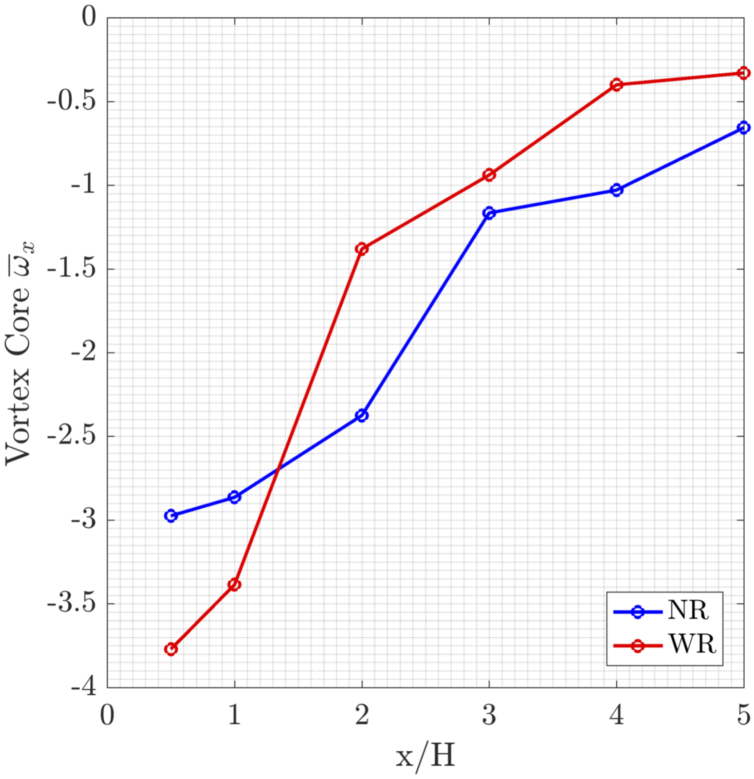

FIGURE 7.6: The change of $\overline{\omega}_x$ at the vortex cores in the longitudinal downstream direction.

represent the locations for slipstream assessments according to the TSI specifications (TSI 2014). The first and second rows in Fig. 7.7 illustrate the wake profile that is half a period apart, and the third column presents the instantaneous wake structure at an arbitrary time instance. Fig. 7.7 shows that without the presence of rails, the wake structure oscillates with a greater amplitude in the spanwise direction. On the other hand, both the NR and MR models determine an identical longitudinal wavelength of approximately $2H$, showing no significant dependency between the spanwise oscillating frequency and the presence or absence of rails.

The frequency response of the dynamic wake structure is studied by power spectrum analysis of the velocity components at the phase-average reference point, and the results are presented in Fig. 7.8. The frequency in this study is non-dimensionalised by the Strouhal number (St_W), which is calculated based on the train width (W), and the power spectral density (PSD) over $St_W = 0 \sim 4$ is presented in Fig. 7.8 for each velocity component. Fig. 7.8 (a) shows that both models have an identical peak frequency of around 0.3 in U_{GF}, which implies that the effect of rails on the longitudinal pulsing is limited. In comparison, NR model indicates a clear peak frequency of 0.21 in the V_{GF}

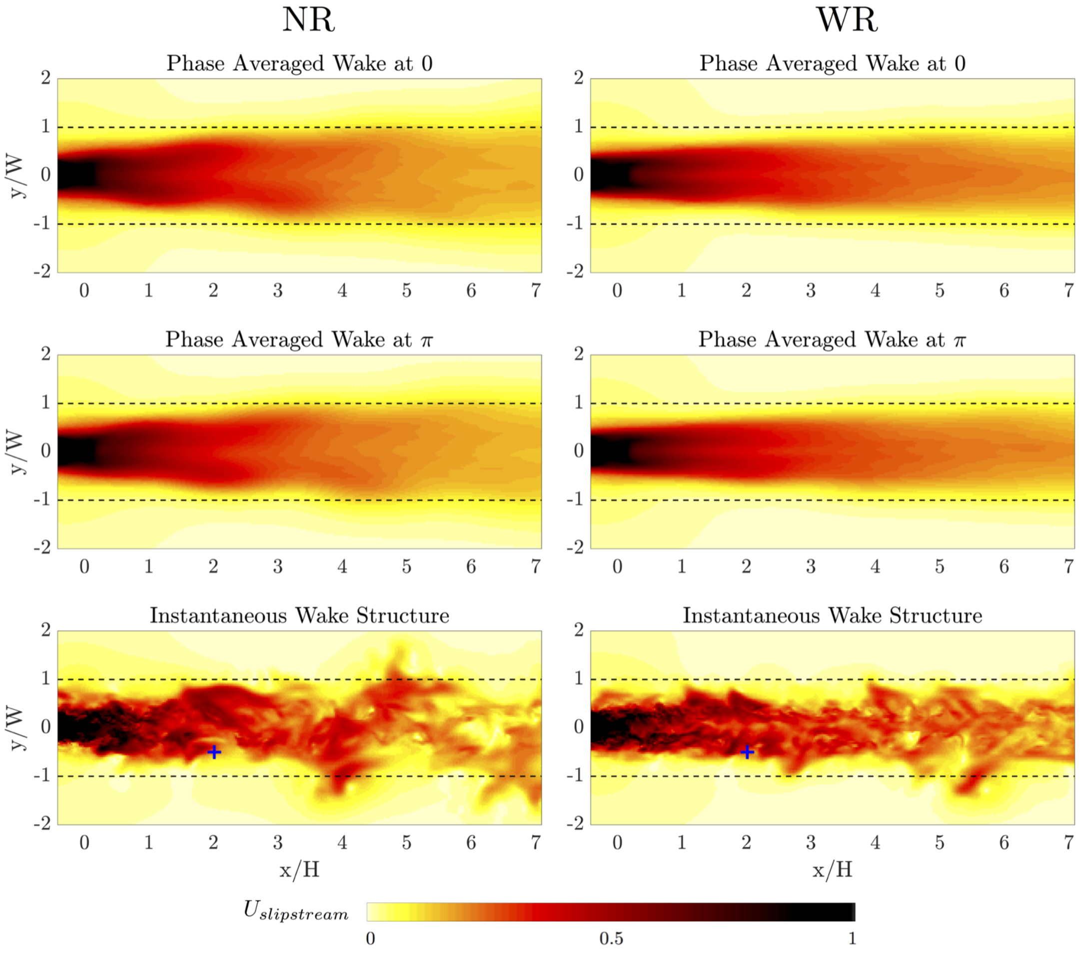

FIGURE 7.7: The wake dynamics visualised by the phase-averaged and instantaneous $U_{slipstream}$ at $z = 0.05H$ ("+": phase-averaging reference point).

signal, while the WR model shows a wider spectrum at a higher frequency, as shown in Fig. 7.8 (b). This implies that a more identifiable spanwise oscillation is established without the presence of the rails, while smaller turbulence scales are introduced by the transverse interaction between the rails and wake. According to Fig. 7.8 (c), an identifiable peak frequency of $St = 1.05$ is determined for the WR model in the W_{GF} signal, while this peak is not captured for the NR model. A possible explanation is that this peak frequency is caused by the vertical fluctuation of the trailing vortices introduced by rails during the roll-over process, as illustrated in Fig. 7.5.

7.2.3 Slipstream Assessment

As in previous chapters, the slipstream velocity is studied from two perspectives: statistical slipstream profiles and gust analysis. The statistical slipstream profiles illustrate the time-average and standard derivation of the velocity measurements at the TSI

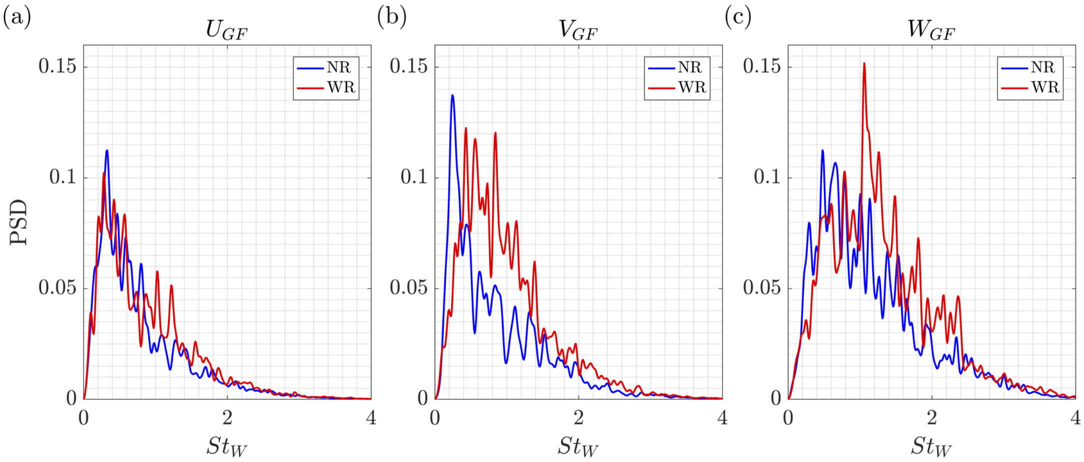

FIGURE 7.8: The spectra contents of the velocity components at the phase-averaging reference point ($[2H, -0.5W, 0.05H]$).

specified assessment locations, and thereby, derive a predicted maximum slipstream velocity ($U_{slipstream,max}$) by adding twice the standard deviation to the slipstream velocity signal. Gust analysis attempts to artificially replicate the field measurements of full-scale testing to obtain an ensemble of the temporal slipstream data under the TSI specifications (TSI 2014), which can then be used to estimate the maximum slipstream induced.

7.2.3.1 Statistical Slipstream Profiles

In this study, the statistical slipstream assessment is taken at both the TSI specified trackside height ($z = 0.05H$) and platform height ($z = 0.35H$), over the longitudinal displacement of $-15H \leq x \leq 30H$. The time-average and standard deviation profiles of the slipstream velocity ($U_{slipstream}$) and their streamwise (U_{GF}) and spanwise (V_{GF}) velocity components at the two measurement heights are plotted in Fig. 7.9, with the critical points listed in Table 7.1. The maximum expected slipstream velocity ($U_{slipstream,max}$), which is defined as $\overline{U}_{slipstream} + 2\sigma_{slipstream}$, predicts the upper limit of the slipstream velocity based on a 95% confidence interval, assuming normally distributed samples.

According to Fig. 7.9, although the rails alter the measurements at both heights, the alteration is more significant at a lower height. As illustrated in Fig. 7.5, the energy-containing vortex core shifts closer to the slipstream measurement location in the NR model causing a significant increase in $\overline{U}_{GF}$, and further altering $\overline{U}_{slipstream}$. In comparison, the impact on $\overline{V}_{GF}$ is insignificant. By keeping the trailing vortices

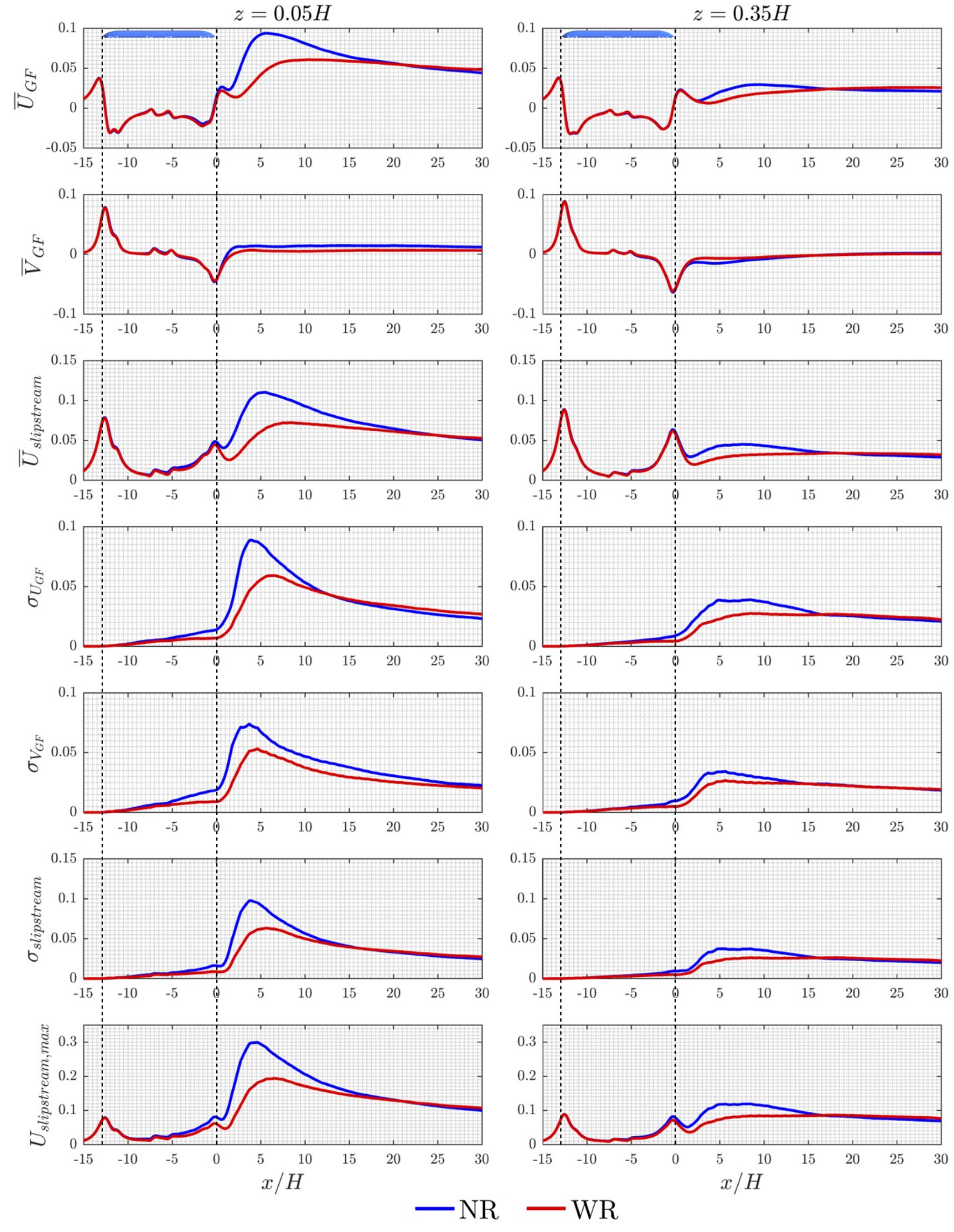

FIGURE 7.9: The comparison of statistical slipstream profiles between NR and WR measured at the trackside ($z = 0.05H$) and platform ($z = 0.35H$) heights.

closer to the spanwise centre-plane in the WR model, both $\sigma_{U_{GF}}$ and $\sigma_{V_{GF}}$ within the wake at measurement locations are reduced. As a result, the NR and MR models share an identical $U_{slipstream,max}$ prior to the tail. Due to the flow alterations caused by the rails, especially within the near-wake region, the difference in $U_{slipstream,max}$ starts

Table 7.1: The critical values in the statistical slipstream profile analysis.

	NR		WR	
	Maximum	Location (x/H)	Maximum	Location (x/H)
		Trackside height (z=0.05H)		
$\overline{U}_{slipstream}$	0.110	5.50	0.078	-12.63
$\sigma_{slipstream}$	0.098	3.82	0.063	5.61
$U_{slipstream,max}$	0.300	4.66	0.194	6.61
		Platform height (z=0.35H)		
$\overline{U}_{slipstream}$	0.089	-12.57	0.088	-12.57
$\sigma_{slipstream}$	0.037	5.03	0.026	18.06
$U_{slipstream,max}$	0.119	8.50	0.089	-12.57

approximately from $x = 0H$ and ends at $x = 15H$. In general, the presence of rails alters the prediction of the $U_{slipstream,max}$ profile in such a manner: (i) a decrease in the peak velocity and (ii) a delay in its occurrence.

7.2.3.2 Gust Analysis

The gust analysis in this study is performed with the *Moving Probe Technique* consistent with the TSI regulations, with the detailed procedure presented previously in § 3.1.

The results of probe measurements are illustrated in Fig. 7.10, and the corresponding critical values and calculation of the *TSI value* are listed in Table 7.2.

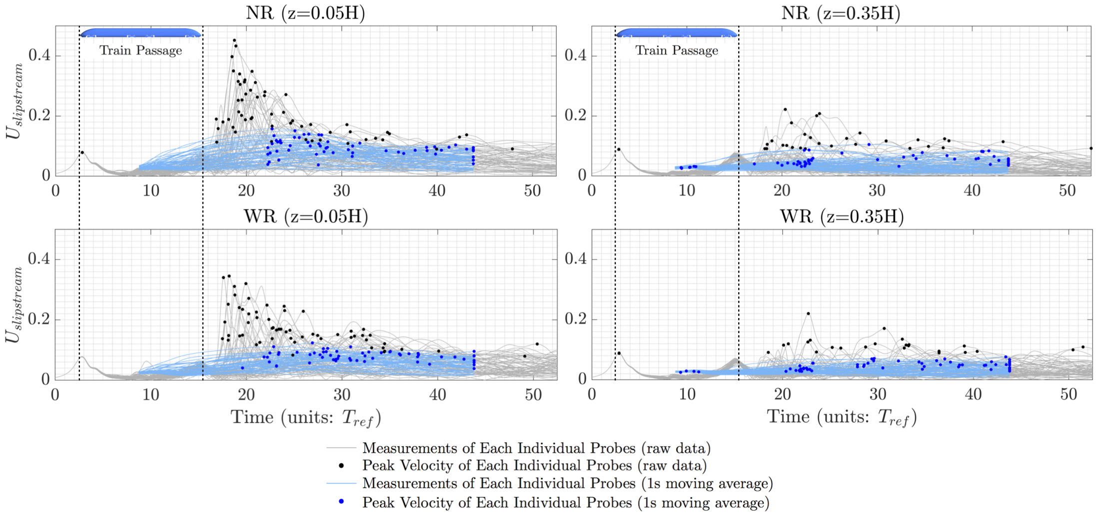

Figure 7.10: The results of Gust Analysis based on the *Moving Probe Technique* under TSI specifications.

Compared with measurements at the platform height ($z = 0.35H$), the impact of rails is more significant at the trackside height ($z = 0.05H$). According to the scattered distribution of the peak recorded velocities (plotted as black dots in Fig. 7.10)

Table 7.2: The critical values in the gust analysis. The numbers in the brackets are the raw data without 1s moving average.

		Trackside ($z = 0.05H$)	Platform ($z = 0.35H$)
NR	$\overline{U}_{peak}$	0.095 (0.204)	0.050 (0.105)
	$\sigma_{U_{peak}}$	0.027 (0.092)	0.018 (0.030)
	$U_{TSI,max}$	0.150 (0.389)	0.086 (0.166)
WR	$\overline{U}_{peak}$	0.079 (0.175)	0.045 (0.100)
	$\sigma_{U_{peak}}$	0.018 (0.065)	0.013 (0.023)
	$U_{TSI,max}$	0.114 (0.303)	0.072 (0.145)

at the trackside height, the NR model shows a higher probability of recording a greater slipstream velocity immediately after the train passage. Both the NR and WR models demonstrate a right-skewed distribution, while a "sharper" peak is identified in the NR model. Ultimately, the absence of the rails can significantly increase the maximum predicted slipstream velocity ($U_{TSI,max}$) by 27% from 0.114 to 0.15. Therefore, the evaluation of the *TSI value* shows a strong dependence on the presence or absence of rails. The TSI specifications refer to the EN standards for method assessment, aiming to provide the requirements on expected slipstream performance (e.g., the maximum allowable slipstream velocity). Thus, it is interesting that the TSI guidelines have dropped the requirement to include rails from the 2013 regulations. Although the current TSI and EN regulations have not specified an appropriate numerical set-up for slipstream prediction, the modelling of rails should require more consideration for future TSI and EN regulation formulation.

7.3 Conclusion

In conclusion, the effect of rails on the slipstream characteristics is fully investigated by studying the alteration to the wake flow structures and the impact on the slipstream assessment. Compared with the minimal alteration to the underbody flow within the flow development region, the rails mainly alter the HST wake structures, especially within the near-wake region when the downwash from the tail impinges on the ballast. The rails alter the downstream wake evolution by obstructing the fluid's transverse motion, and this affects both time-averaged and transient wake features. Without the rails, the trailing vortices move further away from each other in the spanwise direction as they propagate downstream. In contrast, the presence of rails obstruct this transverse motion, thus the trailing vortices have to roll over the rails during propagation. The interaction between the wake and rails causes a strong side loading on the rails and is associated with a greater decay rate of the vortex strength, presumably due to cross-annihilation with secondary vorticity generated at the rail surfaces. Additionally, the rails reduce the amplitude and coherence of the spanwise oscillation of the wake structure, while the alteration to the longitudinal wavelength is negligible. The above alterations to time-averaged and transient flow features further interfere with the slipstream development. Both statistical and gust analyses determine that the peak slipstream velocity in the wake is reduced and its occurrence is delayed in the presence of rails. Furthermore, this study indicates that the maximum predicted slipstream velocity (*TSI value*) has a strong dependence on the presence or absence of rails.

This is a preliminary study focusing on the rail effects, and the investigation is implemented under a simplified and ideal condition. In order to isolate the effect of the rails on the slipstream and aerodynamic loading, detailed features such as the presence of sleepers and ballast roughness, which are likely to have a non-negligible effect on the predicted flow features, are not included in the current study. As such, the results presented in this chapter should be viewed with some caution, since the influence of these other ground feature may significantly affect the wake flow of real HSTs. Clearly, these geometric effects are worth considering in future studies.

Chapter 8

Conclusions

The objective of utilising numerical simulations to investigate HST slipstream characteristics with different geometric variations has been achieved based on four individual but inter-related studies presented in § 4∼7. *Study 1* reviews and evaluates the performance of three state-of-the-art turbulence models for predicting the HST slipstream characteristics, and then the validated numerical model derived from *Study 1* is applied to investigate the aerodynamic effects caused by three different geometric features: ground boundary conditions (*Study 2*), bogies (*Study 3*) and rails (*Study 4*). The key findings of individual studies have been summarised at the end of each chapters. In this chapter, the practical significance and contribution of this project is discussed, with brief recommendations for future studies.

8.1 Contributions of the Project

Compared with the conventional road vehicles, the study of train aerodynamics, especially high-speed train aerodynamics, has a much shorter research history. Recently, HST aerodynamics has attracted considerable attention due to the dramatic speed rise achieved since initial HST development. This makes the aerodynamic performance an important HST design factor. However, due to the distinct geometric features of HSTs, neither the existing knowledge of conventional ground vehicles nor the aircraft aerodynamics can be directly applied to understand HST aerodynamics. Thus, much research is now being channelled into the study of HST aerodynamic performance.

Slipstream, as an important component of HST aerodynamic assessment, has been partially investigated and the up-to-date progress summary is presented in § *1 Literature Review.* Even though coherent structures within the wake and their dynamic response have been identified and analysed, many aspects concerning slipstream characteristics have not been fully understood.

This research program enhances the current understanding of HST slipstream by studying the aerodynamic effects of some important geometric features, and answers important questions related to the flow physics. Additionally, the present project not only focuses on a theoretical analysis, but also aims to deliver important practical knowledge for the relevant industries, communities, and agencies responsible for regulation. The contribution associated with each study is summarised below.

Study 1 reviews three turbulence models (URANS, SAS and IDDES) on their performance for resolving the flow structures and predicting slipstream velocities. According to the comparison of the three representative cases, a trade-off is determined between accuracy and the computational cost. Practically, the strengths and limitations of each turbulence model to resolve different aspects of slipstream are identified, and this study provides guidelines for industries in selecting the appropriate model for different applications. As there is no official agreement on assessing the train slipstream by numerical simulations based on European standards (CEN 2013), the capability of each model as revealed in this study may be helpful as a reference for regulation formulation.

In *Study 2*, by studying the flow alterations caused by different ground boundary conditions, the potential effects are identified and the underlying mechanisms revealed. Practically, this study provides valuable knowledge for bridging the gap between two different experimental approaches: ground-fixed experiment (e.g., full-scale and moving model tests), and train-frame-fixed experiments (e.g., wind-tunnel tests with stationary floor).

Study 3 thoroughly investigates the effects of bogies on HST slipstream by explicitly comparing the overall flow structure between a full-featured train and a flat-underbody train. Unlike other literature studies on bogie effects that focus more on drag reduction and ballast flight, this study focuses on the effects of the bogies on slipstream characteristics, especially on the wake structure. Importantly, by studying the inter-relation between the bogies and wake structure, this study identifies the correlation between the perturbation from the bogies and the spanwise oscillation of the wake structure. In addition, an understanding of the effects introduced by bogies is also valuable for the research community, as both numerical set-ups, namely train geometries with and without bogies, tend to be used in simulations.

Study 4 presents for the first time studies on the impacts of rails on HST wake structures. Rails used to be considered as a trivial geometric feature from the aerodynamic perspective, and have generally been neglected in both physical experiments and numerical simulations. Even the regulations on the inclusion of rails for HST aerodynamic performance assessment were changed in the past few years (CEN 2011) (CEN 2013). This study shows that the rails can strongly alter the time-averaged and transient wake flow features, thus significantly affecting slipstream assessment and *TSI value* evaluation.

8.2 Recommendations for Future Studies

Three recommendations are made for future studies. These are to develop an improved understanding of the effects of (i) cross-wind, (ii) train length on HST slipstream and (iii) transfer function for the slipstream assessment at different heights. Computational simulation provides a means of studying train performance in a crosswind environment. In particular, CFD can simulate a specific turbulent atmospheric boundary layer inflow profile, which can be very difficult to implement experimentally. Cross-wind stability is very important for safety concerns, and it significantly increases the slipstream velocity on the leeward side of the train according to previous research. Additionally, the effect of train length is an important geometric feature that needs more investigation, although much effort has been channelled to push the length-to-height ratio of the train geometry to a higher range. The correlation between the thick boundary layer developed over the train surface and the unsteadiness of the wake structure remains largely unexplored. For example, it is not clear know that how the train boundary layer thickness alters the shear-layer development after separation, and what effect this will have on large-scale wake development downstream. Thirdly, a transfer function for the slipstream measurements at different heights (i.e., trackside and platform height) can be developed from a numerical approach. This study has a strong practical significance as in full-scale testings, it is very expensive to find appropriate sites with the relevant platform height and to perform the dedicated tests according to the TSI regulations. Therefore, it would be very helpful to develop a sophisticated transfer function which can predict the slipstream from a point to another, and consideration of many different cases (e.g., different nose/tail geometries) might be required to make the function general.

Appendix A

Slipstream Regulations

This chapter provides more details regarding the relevant slipstream regulations employed in this project. The European Committee for Standardisation (CEN) specifies the limitations for the slipstream which the train manufacturers have to comply for operating in the European Union, and the Technical Specifications for Interoperability (TSI) interprets the regulations by providing specified annotations and requirements. The requirements for slipstream measurement specified in the TSI guidelines are introduced first, and then the procedure of calculating the maximum allowable slipstream velocity is presented. Please note that all the specifications presented in this chapter all based are on the field testing, as no agreement on predicting slipstream through numerical simulation has been achieved.

Slipstream Measurement

The assessment of train slipstream between 2008 and 2014 was based on the 2008 version of the TSI (TSI 2008), while in late 2014, the European Railway Agency announced a new version, which simplified the assessment procedures (TSI 2014).

Technical specification for interoperability relating to the rolling stock sub-system of the trans-European high-speed rail system, 2008/232/EC (2008 version)

General

- The measurement should be taken during the passage of the whole train, including the wake.

- The maximum permissible slipstream velocity is calculated based on summation of the mean value of at least 20 measurements and two standard deviations.

- The sampling rate of the sensor shall be at least 10 Hz, and the signal shall be filtered using a 1 second window moving average filter.

- The ambient wind speed shall be less than or equal to 2 m/s.

- The uncertainty in the air speed and train measurements shall not exceed ±3% and ±1%, respectively.

Aerodynamic loads on track workers at the lineside (Clause 4.2.6.2.1)

- The tests shall be undertaken on ballasted and straight track, with no obstacles, such as bridges or tunnels, nearer than 500 m ahead and 100 m after the sensors in the longitudinal direction.

- The measurement slipstream intensity should be taken at a height of 0.2 m above the top of trail and at a distance of 3 m from the track centre.

- The whole train-passing event shall consist of the time period starting 1 second before the passing the train head and finishing 10 seconds after the tail passes.

- For the maximum train speed from 190 to 249 km/h, the trackside maximum permissible air speed is 20 m/s; while for the maximum train speed from 250 to 300 km/h, the trackside maximum permissible air speed is 22 m/s.

Aerodynamic loads on passengers on a platform (Clause 4.2.6.2.2)

- The platform height used in the assessment shall be recorded in the rolling stock register, and shall have no obstacles ahead of and after the sensors in the longitudinal direction.

- The permissible maximum slipstream velocity for a full length train at 200 km/h (or at its maximum operating speed if it is lower than 200 km/h) is 15.5 m/s.

- The measurement is taken at a height of 1.2 m above the platform and at a distance of 3.0 m from the track centre, during the whole train passage (including the wake).

In 2009, European Railway Agency proposed TrioTRAIN project to improve the TSI regulation dealing with train slipstream assessment. TrioTRAIN consisted of three sub-projects: AeroTRAIN, DynoTRAIN and PantoTRAIN, which focused on the area of aerodynamics, running dynamics and pantograph-catenary interaction. The Work Package 5 of the AeroTRAIN project focused on the improvement of slipstream measurement methodology. As specified in the TSI (2008/232/EC), the slipstream measurement should be taken at two positions: at trackside and above a platform, and a minimum of 20 train passes are required to obtain an average value. This process was thought to be inefficient by the TrioTRAIN Advisory Council. By analysing a large number of field data in Spain and Germany, a transfer function was developed which enables measurements at one location to be related to those at a different location. The current TSI regulation (1302/2014/EU) is presented below.

Technical specification for interoperability relating to the rolling stock locomotives and passenger rolling stock subsystem of the rail system in the European Union, 1302/2014/EU (2014 version)

Slipstream effects on passengers on platform and on workers trackside (Clause 4.2.6.2.1)

- The measurement should be taken at a height of 0.2 m and 1.4 m above the top of rail at a distance of 3 m from the track centre, during the passage of the unit.
- For a train with a maximum speed between 160 and 250 km/h, the maximum permissible air speed at a height of 0.2 and 1.4 m is 20 m/s and 15.5 m/s respectively.
- For a train with a maximum speed greater than 250 km/h, the maximum permissible air speed at a height of 0.2 and 1.4 m is 22 m/s and 15.5 m/s respectively.
- The maximum permissible slipstream velocity is calculated based on summation of the mean value of at least 20 measurements and two standard deviations.
- The ambient wind speed shall be less than or equal to 2 m/s.
- The measurements shall consist of the time period starting 4 seconds before the passing of the first axle and continue until 10 seconds after the last axle has passed.

Calculation of the *TSI Value*

Based on the velocity measured according to the procedure outlines in the previous section, the TSI further specifies the calculation of the maximum allowable slipstream velocity, which is commonly known as the *TSI Value*. The calculation of the *TSI Value* is identical in both versions, 2008/232/EC and 1302/2014/EU. The first step is to apply a 1 second moving average on the raw velocity data, and then determine the peak velocity recorded for each measurement. The *TSI value* is calculated by the mean of the peak velocities adding two standard deviation, by assuming a normally distributed scattered dataset.

Appendix B

Publications

Journal of Wind Engineering & Industrial Aerodynamics 165 (2017) 46–57

Contents lists available at ScienceDirect

Journal of Wind Engineering and Industrial Aerodynamics

journal homepage: www.elsevier.com/locate/jweia

The performance of different turbulence models (URANS, SAS and DES) for predicting high-speed train slipstream

Shibo Wang[a,*], James R. Bell[a], David Burton[a], Astrid H. Herbst[b], John Sheridan[a], Mark C. Thompson[a]

[a] Fluids Laboratory for Aeronautical and Industrial Research (FLAIR), Department of Mechanical Engineering, Monash University, Australia
[b] Centre of Competence for Aero- and Thermodynamics, Bombardier Transportation, Västeras, Sweden

ARTICLE INFO

Keywords:
High-speed trains
Train aerodynamics
Slipstream
Computational Fluid Dynamics (CFD)
Unsteady Reynolds-Averaged Navier–Stokes equations (URANS)
Scale-Adaptive Simulation (SAS)
Detached Eddy Simulation (DES)

ABSTRACT

The air movement induced by a high-speed train (HST) as it passes, the slipstream, is a safety hazard to commuters and trackside workers, and can cause damage to infrastructure along track lines. Because of its importance, many numerical studies have been undertaken to investigate this phenomenon. However, to the authors' knowledge, a systematic comparison of the accuracy of different turbulence models applied to the prediction of slipstream has not yet been conducted. This study investigates and evaluates the performance of three widely used turbulence models: URANS, SAS and DES, to predict the slipstream of a full-featured generic train model, and the results are compared with wind-tunnel experimental data to determine the fidelity of the models. Specifically, this research aims to determine the suitability of different turbulence modelling approaches, involving significantly different computational resources, for modelling different aspects of slipstream.

1. Introduction

Slipstream depends on the air movement induced by a high-speed train (HST) as it passes. It is defined through the resultant induced horizontal velocity at a specific point from the train vertical centre-plane, measured in the stationary reference frame. Train slipstream can be a safety hazard to commuters and trackside workers, and can also cause damage to infrastructure along track lines. Because of these dangers, many countries have enforced regulations to limit the maximum permissible slipstream velocity, for example, countries in Europe through the European Standards (European Union Agency for Railways, 2014; Railway Applications, 2013). Therefore, minimising slipstream is one of the preliminary goals for HST development, as it poses a constraint on the design, especially if the HST is to operate at high speed. As the induced slipstream velocity depends on the flow development around a HST, an accurate prediction of the flow structure is essential to understanding the slipstream velocity.

Compared with conventional road vehicles, HSTs have a more streamlined shape with no fixed flow separation points, a much larger length-to-width ratio, and they travel significantly faster. Therefore, the flow around a HST is unique, and existing knowledge of neither conventional road vehicles aerodynamics nor aircraft aerodynamics can be directly utilised to understand HST aerodynamics. Consequently, much effort has been channelled towards studying HST slipstream numerically.

For high Reynolds number flows, as the range for time and length scales that describe the flow depends on the Reynolds number, some level of turbulence modelling is required. Much effort has been directed towards improving the accuracy and efficiency of the numerical modelling for complex turbulent flows, e.g., through more adaptable meshing strategies and the development of increasingly complex turbulence models. As a HST wake is highly turbulent, three-dimensional and time-dependent, appropriate turbulence modelling is essential for accurate prediction. Currently, the most widely used time-dependent turbulence models are unsteady-RANS (Reynolds-Averaged Navier–Stokes) (URANS), SAS (Scale-Adaptive Simulation), DES (Detached Eddy Simulation) and LES (Large Eddy Simulation). Due to the high computational cost of (pure) LES at high Reynolds numbers, at this stage utilising LES to study HST aerodynamics is still prohibitive (Hemida et al., 2014; Östh et al., 2015). Therefore, this study focuses on three less expensive numerical approaches that appear more applicable to high-speed train aerodynamics research: URANS, SAS and DES.

RANS decomposes the Navier–Stokes equations by splitting the flow velocity into mean and fluctuating components, focusing on solving for the time- or ensemble-mean flow. RANS has been optimised

---

[*] Corresponding author.
E-mail address: shibo.wang@monash.edu (S. Wang).

http://dx.doi.org/10.1016/j.jweia.2017.03.001
Received 9 December 2016; Received in revised form 10 February 2017
Available online 06 March 2017

for time- or ensemble mean predictions. By retaining the time-dependent terms, (U)RANS can be used to predict the large-scale dynamics for absolutely unstable flows. For example, Schulte-Werning et al. (2003) utilised URANS to predict the spanwise vortex shedding from the tail of a train. Paradot et al. (2002) showed that RANS can achieve a good agreement with the wind tunnel experiments on time-averaged flow topology prediction and drag estimation, while in order to achieve a quantitatively accurate prediction in the complex areas, unsteady calculations are essential. SAS modifies the classic URANS approach by incorporating the von Karman length scale. Interestingly, the modified model can capture the large temporal and spatial scales of the plain URANS approach, but by automatically adjusting the turbulent length and time scales according to the spatial and temporal resolution, it can capture increasingly finer scales (Menter and Egorov, 2010; Egorov et al., 2010). It has been used as an alternative method to study complex industrial flows due to its good balance between accuracy and cost. The fidelity of the SAS model has been verified on various engineering cases, such as bluff body aerodynamics (Egorov et al., 2010), aero-acoustics (Yang et al., 2014) and turbine machinery (Fossi et al., 2015). However, to the authors' knowledge, SAS has not yet been applied to train aerodynamics. DES blends the LES and RANS approaches, utilising RANS to approximate the mean boundary layer behaviour and applying LES to capture the time-dependent flow away from wall boundaries. Therefore, the turbulence spectrum away from boundaries can be adequately resolved. DES has been widely used to study different aspects of train aerodynamics, such as slipstream assessment (Huang et al., 2016) and underbody flows (Zhang et al., 2016). Morden et al. (2015) compared RANS and DES approaches with wind tunnel data on predicting the surface pressures upon a Class 43 High-Speed Train, and concluded that DES is superior in replicating the experimental results. Generally, a model that captures more of the full range of flow structures is more computationally demanding.

However, to the authors' knowledge, a systematic comparison of the strengths and weaknesses of different turbulence models for predicting different aspects of HST slipstream is yet to be undertaken, and this has motivated this current study.

Specifically, this study aims to investigate and evaluate the accuracy of three widely used turbulence models, URANS, SAS and DES, for predicting the flow field around a typical HST: the *ICE3* (described below). The comparison covers five aspects of HST aerodynamics: slipstream assessment, aerodynamic drag coefficient prediction, gust analysis, mean flow structure and wake dynamics. Additionally, the predictive capability of each turbulence model under two control variables, timestep and grid resolution, is investigated, as these are the two key parameters which significantly affect both the accuracy and the computational cost. Moreover, the numerical results are compared with wind tunnel experimental data to determine the fidelity of the models (Bell et al., 2014).

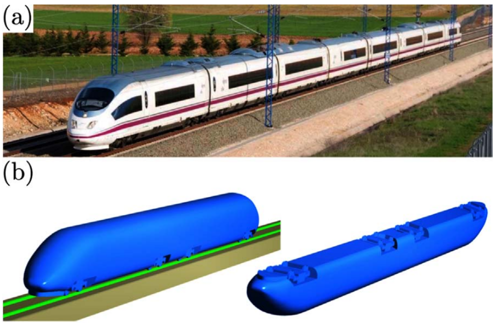

Fig. 1. Comparison between the full-scale ICE train and numerical model: (a) full-scale operational ICE3 train; (b) simplified numerical model. (Photo provided courtesy of Bombardier Transportation).

This paper is structured as follows. Initially, the numerical set-up, including defining the train geometry, the computational domain and corresponding boundary conditions, the meshing strategy, discretisation schemes, and turbulence models are introduced in the *Methodology* section. The *Results and Analysis* section consists of two sub-sections. In the first, all simulation cases are initially compared based on the slipstream velocity and the aerodynamic drag coefficient. In the second section, based on the previous comparison and typical utilisation of each turbulence model, typical cases with representative grid resolutions and timesteps are selected for a more detailed analysis. In this section, gust phenomena, time-averaged flow structure and wake dynamics are studied, and their interrelationship with the slipstream prediction is assessed. To conclude, the strengths and weaknesses of each turbulence model for predicting HST slipstream are summarised.

2. Methodology

2.1. Geometry

This study is based on a *Deutsche Bahn Inter-City-Express 3* (ICE3) high-speed train, a widely operated train in European and Asian countries, as shown in Fig. 1a. *ICE3* has a representative HST external shape, and its Computer-Aided Design (CAD) model is freely available from the DIN Standards Railway Committee (FSF) (FSF, 2014). The numerical analysis is based on a slightly geometrically simplified model, which has a length–width–height ratio of approximately 50:3:4, as illustrated in Fig. 1b. Although the train model is simplified, omitting details such as the gaps between carriages and the air-conditioning units, it still includes key geometry features that have a strong influence on the wake, in particular, the bogies and snowplows. The train is located on a *Single Track Ballast and Rail* (STBR) ground configuration, with the dimensions specified in CEN guidelines (Railway Applications, 2013). The thickness of the rails is extended from 50 mm to the wheel width of 135 mm (in full-scale) in order to represent a realistic contact between the rails and wheels.

2.2. Domain and boundary conditions

The train is positioned in a computational domain consisting of hexahedral elements, as illustrated in Fig. 2. For the discussion, dimensions are generally normalised by the train width (W) in the spanwise direction (y-direction), or by the length (L) of the train in the streamwise direction (x-direction). The origin of the coordinate system is positioned in the spanwise mid-plane, at the height of the top surface of the rails, with x=0 corresponding to the tail tip.

A uniform velocity boundary condition with a turbulence intensity of 1% is applied at the inlet to simulate the low-turbulence horizontal-flow freestream condition in the wind tunnel. The Reynolds number (based on W) is 7.2×10^5. These values are chosen for consistency for a comparison with wind-tunnel experiments, noting that they are not representative of full-scale train operation. A zero static pressure condition is applied at the outlet boundary. A no-slip wall boundary condition is applied to all train surfaces. In order to replicate the splitter plate introduced to remove the floor boundary layer in the wind tunnel experiments (Bell et al., 2014), the floor is split into two parts, named floor 1 and floor 2. Floor 1 is 0.7L long and it employs a zero-shear wall condition. Floor 2 is 4.3L long with a no-slip wall condition. Symmetry boundary conditions are applied at the top and sides of the computational domain. Note that for a clearer visualisation of the computational setup and domain dimensions, Fig. 2 is not drawn to scale.

2.3. Meshing strategy

The general meshing strategy is based on the predominately

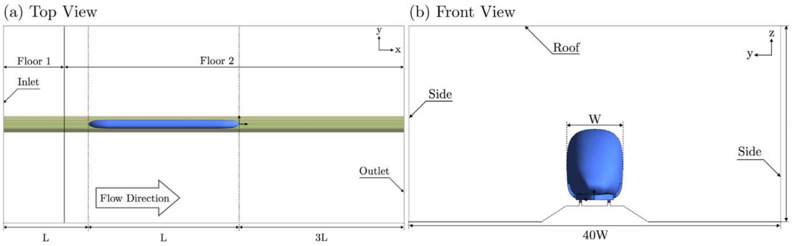

Fig. 2. Schematic of computational domain: (a) top-view; (b) front-view. (Not to scale.)

Cartesian *cut-cell* approach, allowing substantially increased mesh concentration around the train and in the wake, together with a relatively smooth transition to lower resolution away from the train. In particular, it achieves a high uniform resolution in the slipstream measurement regions, and aids in accurately capturing the boundary layers and induced flow separation from smaller-scale geometrical features. In this study, three sequentially refined grids (coarse, medium and fine grids) are constructed based on the identical meshing strategy and generally maintaining the same compression factors between meshes. Three different levels of refinement zones are utilised to achieve higher accuracy in critical regions, as illustrated in Fig. 3. *Inflation layers* are applied to all wall boundaries to capture the boundary layer development, as illustrated in Fig. 4. To ensure that all important flow features are captured, the dimensions of the refinement regions were determined based on a preliminary simulation. A smooth transition is established between the adjacent cells including between the outer inflation layer and the hexahedral grid, and at the interface of two refinement zones, as shown in Fig. 4. More details regarding the individual grid description are presented in Section 3.1.1.

2.4. Brief description of the solver

The numerical solver utilised in this research is the commercial CFD code *FLUENT*, which is part of the ANSYS 16.2 software suite. Due to the turbulent nature of slipstream, a pressure-based transient solver is used for all simulations. The *Pressure–Velocity Coupling Scheme* for RANS and SAS simulation is SIMPLEC, while the *Fractional-Step Scheme* with *Non-Iterative Time Advancement* is applied for DES, as long as the Courant number is less than unity. For spatial discretisation, the *second-order upwind scheme* is applied for all flow equations, except for SAS and DES, which utilise *bounded central differencing* for the momentum equation. The *bounded second-order implicit* formulation is applied for transient simulations for all cases. Also, for all simulations, the flow field is initialised with a second-order accuracy steady-state RANS simulation based on the Shear-Stress Transport (SST) RANS model.

Unsteady statistics are obtained by averaging the flow after it is first checked to have reached its asymptotic state. This is checked through comparisons with predictions from smaller averaging periods. A useful time scale can be constructed from the train height and freestream velocity, defining a *Reference Time Scale* ($T_{ref} = H/U_\infty$). Unsteady statistics are gathered over $195T_{ref}$, which is equivalent to three times the time taken for the freestream flow to advect through the entire domain from inlet to outlet, or approximately 15 times the time taken for the flow to advect the length of the train.

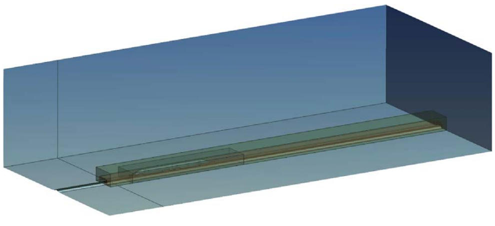

Fig. 3. The schematic of mesh refinement zones.

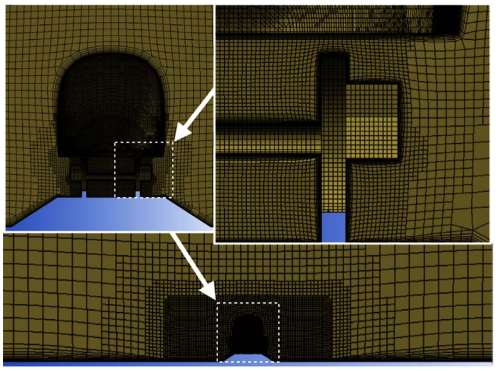

Fig. 4. A cross-section view of the mesh refinements around the train (based on the fine grid).

The turbulence models are described briefly below.

2.4.1. URANS

Reynolds-averaging proceeds by first splitting the flow variables into mean and fluctuating components. Putting this decomposition into the Navier–Stokes equations and averaging gives the *Reynolds-Averaged Navier–Stokes* (RANS) equations. Keeping the time derivative of the mean velocity, which implies that the averaging procedure can be thought of as averaging over an ensemble of turbulent flow states, gives the *Unsteady* RANS (i.e., URANS) model.

The equations for the mean velocity components $\overline{u}_i$ and pressure ($\overline{p}$) are summarised as

$$\frac{\partial \overline{u}_i}{\partial x_i} = 0, \tag{1}$$

$$\frac{\partial \overline{u}_i}{\partial t} + \overline{u}_j \frac{\partial \overline{u}_i}{\partial x_j} = -\frac{1}{\rho}\frac{\partial \overline{p}}{\partial x_i} + \frac{\partial}{\partial x_j}\left(\nu \frac{\partial \overline{u}_i}{\partial x_j}\right) + \frac{1}{\rho}\frac{\partial \tau_{ij}}{\partial x_i}, \tag{2}$$

where $\tau_{ij} = \overline{u'_i u'_j}$ is the *Reynolds Stress Tensor*, which cannot formally be expressed in terms of mean flow variables; instead some level of turbulence modelling has to be applied. The usual way to proceed is to form an analogy between molecular diffusion and turbulent mixing, and thus approximate the Reynolds stress in terms of the mean flow gradient together with a spatially varying turbulent viscosity based on local turbulent time/velocity and length scales. These scales are obtained by solving two further equations, e.g., for the turbulent kinetic energy per unit mass (k) and the turbulent dissipation (ϵ) for the well-known k–ϵ model. In this study, the more sophisticated two-equation *Shear-Stress Transport* (SST) k–ω model is utilised. *Shear-Stress Transport* (SST) k–ω model is also determined as the optimal RANS model by studying a range of RANS models based on their performances of predicting the surface pressure on a High-Speed Train (Morden et al., 2015). This blends the classical k–ω and k–ε models, noting k–ω is considered a superior and better behaved model in the near-wall boundary-layer regions, and k–ε is more appropriate in the outer flow. The aim is to better model flows with undefined separation points, such as exist on the smooth surfaces of a high-speed train. Of course, URANS models can only capture large-scale flow features and periodicities, such as the shedding from bluff bodies such as circular cylinders, noting that only the very large-scale vortical wake features caused by absolute instability are likely to be resolved to some level of accuracy. For a smooth geometry like a high-speed train, it is unclear how well the wake flow is likely to be captured by such a model.

2.4.2. SAS

SAS is developed from the classical URANS model, noting that the way that turbulence is incorporated is mathematically equivalent between the RANS approach and the subgrid-scale model used for *Large Eddy Simulation*. The innovation of SAS is that the von Karman length scale is introduced to capture the scale-adaptive temporal and spatial scales. This idea was initially proposed by Rotta (1972), and has been gradually improved through the years and recently integrated into the commercial CFD solver ANSYS (Menter, 2012). Unlike the URANS approach which can only capture large-scale vortex shedding, SAS is capable of resolving part of the turbulence spectrum for unstable flows depending on the spatial and temporal scales, i.e., in this case, effectively the cell size and timestep. The length scale used to construct the turbulent viscosity is given by

$$L_{vK} = \kappa\left|\frac{\overline{U}'}{\overline{U}''}\right|, \tag{3}$$

with

$$\overline{U}' = \sqrt{2S_{ij}S_{ij}} \quad \text{and} \quad \overline{U}'' = \sqrt{\frac{\partial^2\overline{u}_i}{\partial x_j\partial x_j}\frac{\partial^2\overline{u}_i}{\partial x_k\partial x_k}}, \tag{4}$$

where

$$S_{ij} = \frac{1}{2}\left(\frac{\partial\overline{u}_i}{\partial x_j} + \frac{\partial\overline{u}_j}{\partial x_i}\right). \tag{5}$$

A full description of the SAS model is given in Menter and Egorov (2010) and Egorov et al. (2010).

As a scale-adaptive method, it shows a gradual transition from URANS-type to LES-type behaviour as the temporal and spatial resolution are increased. Unlike problems with LES or DES caused by insufficient grid or time resolution, SAS utilises URANS as a back-up (Menter and Egorov, 2010). A known limitation of SAS is that the scale-resolving mode is not activated unless the flow is sufficiently unstable. For this study the wake is highly turbulent, fed by flow past complex underbody structures and large-scale shedding in the wake.

2.4.3. DES

DES is a blend of RANS and LES models, utilising RANS to approximate the boundary layer and applying LES to capture the time-dependent flow away from boundaries. This study uses SST as the RANS turbulence model within the wall region. By trying not to solve the fine-scale time-dependent turbulence structures of wall boundary layers under LES, which are unlikely to strongly influence the outer flow, DES significantly reduces the computational cost of applying an LES approach to solve high Reynolds number engineering problems. To achieve this hybrid behaviour, a switch function based on the grid size is utilised to trigger the corresponding model for the respective region. The accuracy and validity of DES directly depend on accurately switching the turbulence model between the attached boundary-layer region (RANS) and free shear-flow region (LES). *Modelled-Stress Depletion* and *Grid-Induced Separation* are the two most common issues of the classical DES model (Spalart, 2009). These issues have been gradually addressed through the continuous improvements to the model. This study utilises the *Improved-Delayed-DES* (IDDES) model, which applies an improved delayed shielding function to achieve a higher accuracy within the RANS–LES blending region, which also improves the wall-modelling capability. A fuller description is given in Spalart (2009).

2.5. Wind tunnel validation case

This study has been validated against results from a wind-tunnel study based on the same simplified scale model of a high-speed train. The Reynolds number is also matched. The experiment was conducted in the Monash University 1.4 MW closed-circuit wind tunnel. A full description of the experimental set-up and results are reported in Bell et al. (2016a,b).

3. Results and analysis

To achieve the aim of systematically comparing the capability of different turbulence models for modelling HST aerodynamics, the results are presented from two perspectives. In Section 3.1, the predicted slipstream velocity profile and the aerodynamic drag coefficient of all cases are compared as a function of grid resolution and timestep. The cases run are listed in Table 1. In Section 3.2, representative cases of each model are chosen for further investigation, noting that a key selection criterion is that a URANS simulation should be significantly cheaper than SAS, which in turn should be cheaper than DES. For that study, three representative cases are studied through comparison to the wind tunnel data according to slipstream prediction, time-averaged wake structure and large-scale wake dynamics.

3.1. Overall result analysis

In this section, all cases are studied and compared based on the predictions of slipstream and aerodynamic drag. The slipstream profile is recorded 3 m (in full scale) away from the centreline of the train and at two different heights i.e., trackside height and platform height, according to the TSI specifications (European Union Agency for Railways, 2014). In this section, the comparison focuses on measurements at the trackside height (z=0.05H). Slipstream is defined as the air movement induced by a moving train, which is measured in a ground-fixed (GF) stationary reference frame, while CFD simulations are based on the train-fixed (TF) reference frame, hence a change of frame is required. The *slipstream velocity* ($U_{slipstream}$) is defined by

$$U_{slipstream} = \sqrt{(U_{GF}^2 + V_{GF}^2)}, \tag{6}$$

where

$$U_{GF} = U_\infty - U_{TF}, \quad V_{GF} = V_{TF}. \tag{7}$$

In Eqs. (6) and (7), the subscripts *GF* and *TF* indicate *ground-fixed* and *train-fixed* reference frames, respectively. Velocities, including slipstream velocities, quoted in this study are typically normalised by

Table 1
The list of all simulation cases.

Grid resolution	$0.05T_{ref}$	$0.025T_{ref}$	$0.0025T_{ref}$
Fine	URANS	URANS SAS IDDES	SAS IDDES
Medium	URANS	SAS	IDDES
Coarse	URANS	SAS	IDDES

the freestream velocity (U_∞). Also note that slipstream is only based on the downstream (U) and transverse (V) components of the velocity. The vertical velocity component is ignored.

The comparison in this section is based on the time-averaged slipstream velocity ($\overline{U}_{slipstream}$), and its standard deviation ($\sigma_{slipstream}$). The discrepancy between the wind tunnel measurements and numerical simulations is discussed in Section 4, and potential sources of these differences are identified.

3.1.1. The influence of grid resolution

To study the effect of grid spatial resolution, in order to maintain the consistency of the comparison, the timestep for each model remains fixed with $\Delta t_{\text{URANS}} = 0.05T_{ref}$, $\Delta t_{\text{SAS}} = 0.025T_{ref}$ and $\Delta t_{\text{IDDES}} = 0.0025T_{ref}$, reflecting the sophistication of the models and noting that the successive models progressively try to capture finer spatial and temporal scales. An underlying assumption is that only capturing the large-scale flow features can still provide reasonable predictions of slipstream and drag. This will be tested in the following sections. The reference timestep is broadly based on common practice; more details regarding timestep selection are presented in the following section on timestep selection.

Three grids with the same meshing strategy but different densities were constructed for this comparison. The overall meshing strategy is based on the Cartesian *cut-cell* meshing approach with refinements around the train and in the wake region, as introduced in the *Methodology* section. The number of cells for the coarse, medium and fine grids are approximately 3.3, 17.4, 26.6 million respectively. As the mesh gets finer, the train surface cell size and the cell size of the refinement zones are gradually decreased, and the corresponding number of inflation layers on the wall boundaries is increased. The critical meshing parameters are listed in Table 2.

The effects of grid resolution, in terms of the $\overline{U}_{slipstream}$ and $\sigma_{slipstream}$, are illustrated in Fig. 5. According to this figure, all cases show a qualitatively good agreement with the wind tunnel data. A local peak occurs near the train nose due to the head pulse, while the maximum $\overline{U}_{slipstream}$ happens at approximately x=5–8H. The $\sigma_{slipstream}$ profile witnesses a gradual increase approaching the tail of the train, and after the tail the gradient becomes significantly steeper, and achieves its maximum at approximately x=4–6H.

According to the slipstream profiles of each model, as presented in Fig. 5, the difference between medium and fine grids with respect to $\overline{U}_{slipstream}$ is minor, while shifting to the coarse grid has a much stronger impact on $\overline{U}_{slipstream}$. Compared with SAS, $\sigma_{slipstream}$ shows a stronger dependence on grid size for both URANS and IDDES. The lower influence of SAS grid size on $\sigma_{slipstream}$ may be due to its scale-adaptive nature, although it is unclear why. The maximum magnitude of $\overline{U}_{slipstream}$ and $\sigma_{slipstream}$, and their corresponding locations, are presented in Table 3. The discrepancy between the wind tunnel and numerical results is explicitly discussed in Section 4; for example, the existence of a local minimum near the tail in experimental data is not captured in any of the numerical simulations.

Table 2
Meshing parameters.

Mesh		Coarse	Medium	Fine
Cell size	Train surface mesh	0.015H–0.12H	0.0075H–0.06H	0.00625H–0.05H
	Under-body refinements	0.015H–0.06H	0.0075H–0.015H	0.00625H–0.0125H
	Wake refinements	0.06H–0.12H	0.015H–0.06H	0.0125H–0.05H
	Far-field refinements	0.24H–0.96H	0.12H–0.48H	0.1H–0.4H
No. of inflation layers		4	8	10
Train surface wall y^+		20–150	10–50	5–30
No. of cells (millions)		3.3	17.4	26.6

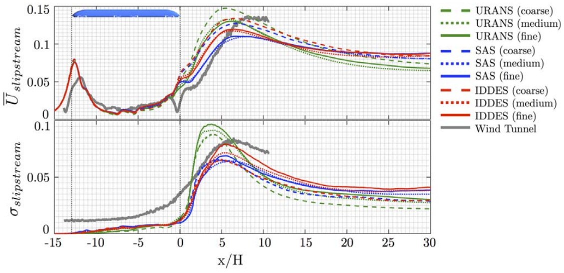

Fig. 5. A comparison of $\overline{U}_{slipstream}$ and $\sigma_{slipstream}$ for the three different turbulence models with results from experiments, showing the effect of grid resolution.

Table 3
The critical values in grid resolution comparison.

Grid resolution	$\overline{U}_{slipstream}$		$\sigma_{slipstream}$	
	Maximum	Location (x/H)	Maximum	Location (x/H)
URANS (coarse)	0.148	5.50	0.088	4.08
URANS (medium)	0.133	5.87	0.092	3.82
URANS (fine)	0.130	6.24	0.097	3.77
SAS (coarse)	0.128	6.82	0.066	4.56
SAS (medium)	0.110	8.13	0.064	6.40
SAS (fine)	0.111	6.61	0.069	5.61
IDDES (coarse)	0.134	6.82	0.066	5.03
IDDES (medium)	0.118	5.98	0.072	5.50
IDDES (fine)	0.120	6.56	0.079	5.61
Wind tunnel	**0.137**	**8.03**	**0.084**	**6.46**

3.1.2. The influence of timestep

The timestep study is based on the fine mesh, maintaining all other solver settings and only varying the timestep. This study examines 3 different timesteps: $\Delta t = 0.05T_{ref}$, $0.025T_{ref}$ and $0.0025T_{ref}$. The smallest timestep of $0.0025T_{ref}$ is chosen because this restricts the Courant number ≤1 for the typical smallest cells of the fine grid, which is one of the suggested criteria for conducting DES simulations. The largest timestep of $0.05T_{ref}$ is approximately 1/30 of the period of the dominant wake frequency, which is ideal for URANS simulations, as only the dynamics of dominant flow features are resolved. Additionally, all turbulence models are compared at the timestep of $0.025T_{ref}$ to evaluate the performance of the turbulence models based on an identical medium timestep.

The effect of timestep is illustrated in Fig. 6, and the magnitudes and locations of the maximum $\overline{U}_{slipstream}$ and $\sigma_{slipstream}$ are presented in Table 4. Percentage differences in $\overline{U}_{slipstream}$ for the URANS, SAS and IDDES models are 5%, 15% and 12%, respectively, relative to the wind

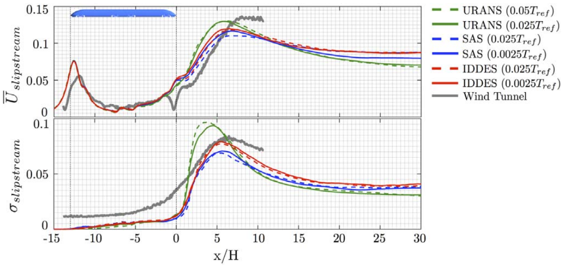

Fig. 6. The comparison of $\overline{U}_{slipstream}$ and $\sigma_{slipstream}$ under timestep effect.

Table 4
The critical values in timestep comparison.

Grid resolution	$\overline{U}_{slipstream}$		$\sigma_{slipstream}$	
	Maximum	Location (x/H)	Maximum	Location (x/H)
URANS ($0.05T_{ref}$)	0.130	6.24	0.097	3.77
URANS ($0.025T_{ref}$)	0.130	5.82	0.094	4.56
SAS ($0.025T_{ref}$)	0.111	6.61	0.069	5.61
SAS ($0.0025T_{ref}$)	0.117	6.82	0.071	5.61
IDDES ($0.025T_{ref}$)	0.119	6.61	0.078	5.61
IDDES ($0.0025T_{ref}$)	0.120	6.56	0.079	5.61
Wind tunnel	**0.137**	**8.03**	**0.084**	**6.46**

tunnel result. For the $\overline{U}_{slipstream}$ prediction, there is a good match before the flow approaches the tail, while further downstream, the differences from the observed experimental variation are higher. This is likely to be connected with the predicted $\sigma_{slipstream}$ variation, as the turbulence level in the wake is much higher than that along the train. For the range of timesteps considered, the accuracy of predicting highly turbulent flow is only weakly dependent on the timestep, except for the URANS model. Additionally, the three cases, URANS ($0.025T_{ref}$), SAS ($0.025T_{ref}$) and IDDES ($0.025T_{ref}$), have the same timestep and are based on the same mesh, allowing a direct comparison between the performance of the turbulence models. The results from Fig. 6 show that the difference between SAS and IDDES is small in terms of $\overline{U}_{slipstream}$, while IDDES has a slightly better prediction of $\sigma_{slipstream}$. URANS over-predicts both $\overline{U}_{slipstream}$ and $\sigma_{slipstream}$, and this is consistent with the difference in mean and transient flow structures presented in Section 3.2.

3.1.3. Aerodynamic drag coefficient

The train aerodynamic drag coefficient (C_D) for each case is listed in Table 5. Overall, this shows that the differences between the C_D predictions are very small for the different cases. For example, the largest difference between the two cases, IDDES-medium-$0.0025T_{ref}$ and URANS-fine-$0.025T_{ref}$, is approximately 4%. One explanation is that due to the unique shape of HSTs, the skin friction is the main source of C_D for typical full-scale trains (Baker, 2010). In this study, despite the reduction of the train length-to-height ratio, skin friction still contributes to a large proportion of the aerodynamic drag. Numerically, the skin friction prediction depends on the train surface boundary layer modelling, while the three models utilise the same RANS approach for wall modelling. These results indicate that compared with slipstream assessment, the prediction of C_D is less dependent on the sophistication of the turbulence modelling, mesh quality and timestep. This suggests that for future studies where C_D is the main interest, a more expensive model would not seem justified.

3.2. Typical case analysis

Based on the preliminary analysis in Section 3.1, a representative case for each model was selected for more detailed analysis, focusing on gust analysis, the time-averaged wake structure and the wake dynamics.

For URANS, the case with timestep=$0.05T_{ref}$ and the coarse mesh was utilised, because Section 3.1 shows that URANS predictions are not sensitive to grid size, at least beyond a minimum level. Whilst there is some timestep dependence, the underlying philosophy for selection here is that the URANS model should be considerably cheaper than the other more complex models, especially as the turbulent time and length scales are not a function of temporal or spatial modelling scales.

The medium mesh with the timestep of $0.025T_{ref}$ was selected for SAS, to optimise the balance between the cost and accuracy. As an adaptive method, its accuracy is based on the solver settings, switching between URANS and LES-like modelling capability as spatial and temporal resolution are increased.

Table 5
The comparison of C_D for all simulation cases.

Grid resolution	$0.05T_{ref}$	$0.025T_{ref}$	$0.0025T_{ref}$
Fine	0.267 (URANS)	0.265 (URANS) 0.269 (SAS) 0.274 (IDDES)	0.268 (SAS) 0.273 (IDDES)
Medium	0.268 (URANS)	0.269 (SAS)	0.276 (IDDES)
Coarse	0.271 (URANS)	0.274 (SAS)	0.274 (IDDES)

For IDDES, the fine mesh with a timestep of $0.0025T_{ref}$ was employed, as good practice for DES simulations requires a local Courant number of unity or less. Overall, IDDES is typically used to study transient flow behaviour, with a range of spatial (and temporal) scales extending into the inertial subrange.

In practice, computational cost is one of the important parameters in determining the selection of a turbulence model. The ratio of the estimated computational costs of the three representative cases are 1:10:20 (URANS:SAS:IDDES). The IDDES simulation used approximately 40 KCPU hours on the Australian *National Computing Infrastructure* (NCI) (RAIJIN) high-performance computing cluster, typically running on 128–256 cores. As better accuracy is typically associated with higher cost, a compromise often needs to be made with turbulence model selection. One of the aims is to quantify the level of accuracy of each turbulence model for predicting different flow aspects, and provide guidelines in selecting the models that satisfy accuracy requirements at minimum cost.

3.2.1. Gust analysis

Based on the TSI guidelines (European Union Agency for Railways, 2014) that define how slipstream should be measured, the time variation of the velocity should be recorded at 3 m distance from the vertical centreplane of the train, recorded with two adjacent probes placed at least 20 m apart. The recording time needs to be sufficiently long to capture the entire flow disturbance including the wake. Furthermore, a 1 second moving average (1s MA) filter is applied to the raw data, and the maximum slipstream value is calculated based on the mean of the filtered peak value plus two standard deviations.

Gust analysis artificially replicates the field measurements of full-scale testing to obtain an ensemble average of the temporal slipstream data as introduced above. This study utilises the *Moving Probe technique*, which was previously applied by Muld et al. (2012b) to study slipstream under TSI regulations.

To begin with, a brief introduction of the gust analysis technique is presented. The first step is to place an artificial probe at the starting point of a slipstream measurement line, and then allow this probe to move downstream at the speed of U_∞. Over the time taken for this probe to travel from the start to the end point, U_{GF} and V_{GF} are recorded, and then $U_{slipstream}$ is calculated based on Eq. (7), and plotted as grey solid curves in Fig. 7. To replicate the 20 m distance between two individual measurements in a field testing environment, the artificial moving probes are released every $5T_{ref}$. Thus, within the total simulation sampling time of $195T_{ref}$, 58 independent measurements can be made (29 at each side), which satisfies the requirement of minimum 20 independent measurements of the TSI regulations (European Union Agency for Railways, 2014). The peak values of individual measurements are plotted as black dot points, and the mean and standard deviation of the peak values are calculated and presented in Table 6. Next, the equivalent of a 1s MA filter is applied to each data set, and presented as light blue curves in Fig. 7, with the peak values indicated by the blue dot points. The final maximum slipstream velocity $\overline{U}_p + 2\sigma_{uv}$ under a 1s MA filter is calculated and presented in Table 6. In practice, the maximum value would be compared with the

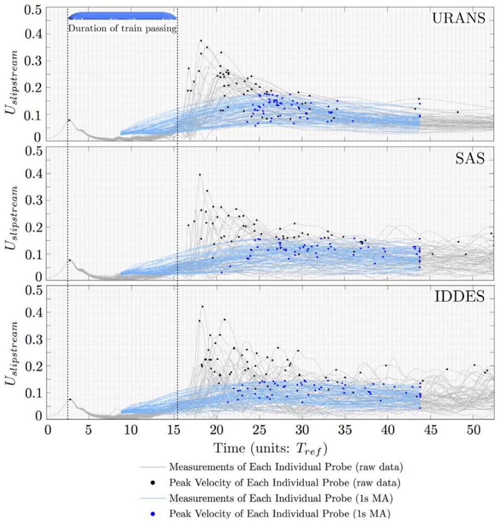

Fig. 7. The gust analysis based on the measurements from the artificial moving probe technique under TSI regulation. (For interpretation of the references to colour in this figure caption, the reader is referred to the web version of this paper.)

Table 6
The unsteady statistics of gust measurement with and without applying a 1 second moving average.

Grid resolution	Without 1s MA			With 1s MA		
	Mean peak ($\overline{U}_p$)	σ_{uv}	$\overline{U}_p + 2\sigma_{uv}$	Mean peak ($\overline{U}_p$)	σ_{uv}	$\overline{U}_p + 2\sigma_{uv}$
URANS	0.189	0.073	0.335	0.125	0.033	0.189
SAS	0.183	0.060	0.302	0.114	0.028	0.170
IDDES	0.207	0.065	0.338	0.111	0.024	0.159
Wind tunnel	**0.322**	**0.138**	**0.597**	**0.118**	**0.021**	**0.159**

maximum allowable slipstream velocity specified by TSI as a part of an acceptance procedure. In this study, the duration of the equivalent sampling time of per artificial probe is $52T_{ref}$, with the starting and ending time for the train passage corresponding to $2.5T_{ref}$ and $15.4T_{ref}$, respectively.

From Fig. 7, the models predict that the maximum $U_{slipstream}$ occurs in the wake about $2–25T_{ref}$ after the tail. Although all the turbulence models depict a statistically similar distribution, a significant run-to-run variance is observed between model data sets, especially for IDDES. The skewness of the time for the raw peak velocities (black dot points) within the wake for URANS, SAS and IDDES is 1.85, 1.15, 1.39 respectively. The percentage differences of the filtered $\overline{U}_p + 2\sigma_{uv}$ values for URANS, SAS and IDDES are +18.9%, +6.9% and +0.0%, respectively, relative to the experimental measurements. This large variation is also reported in full-scale and scaled experiments, and this is indeed one of the practical difficulties in quantifying slipstream (Bell et al., 2015; Baker, 2010). The underlying cause can be seen through examining time-averaged and transient wake properties in Sections 3.2.2 and 3.2.3.

Perhaps of interest is that the maximum peak gust velocity observed in individual runs can be more than a factor of two higher than the filtered $\overline{U}_p + 2\sigma_{uv}$ level, since the pressure disturbance varies with the square of the velocity, this equates to more than a factor of four in the force experienced by a commuter.

3.2.2. Time-averaged wake structure

Based on the results from previous studies, the dominant wake flow structure of a HST is a pair of counter-rotating vortices (Bell et al., 2016a). For this study, the time-averaged wake structure is visualised by x-vorticity (streamwise), in-surface projected velocity vectors and the boundaries of the vorticity-dominated regions, on six vertical planes in the wake, as presented in Fig. 8. As the time-averaged flow structure is symmetric about the mid-plane, only the left half of the flow field is presented. The vorticity is calculated based on the normalised spanwise and transverse velocities. The boundary of the trailing vortex structure corresponds to the iso-line of $\Gamma_2 = 2/\pi$, which is a common vortex identification method often chosen by experimentalists (Graftieaux et al., 2001). The two green asterisks represent the locations of trackside (z=0.05H) and platform (z=0.3H) slipstream measurement height based on TSI specifications (European Union Agency for Railways, 2014).

Through Fig. 8, the downstream evolution of the time-mean trailing vortices can be visualised as the plane shifts from x=0.5H to x=6H. Qualitatively, all three methods show a similar flow structure to that from the wind tunnel measurements. As the vortices move downstream, they roll over the rails and move apart from each other in the spanwise direction. Despite vorticity diffusion and cross-annihilation, the boundary size increases as the vortical structures advect downstream.

Quantitatively, compared with SAS, IDDES and experimental measurements, the vortex boundary predicted by URANS crosses the slipstream measurement lines at an earlier downstream point. As the vortex core contains lower momentum fluid, this induces a higher local slipstream velocity, consistent with the predictions in Figs. 5 and 6. This widening of the wake can also be seen in the planar phase-averaged and instantaneous coloured contours of $U_{slipstream}$ in Section 3.2.3.

From the contribution of large-scale streamwise vortical structures to the overall wake structure, it can be seen that the slipstream velocity is not only sensitive to the strength of the trailing vortex arms, but also their location. Therefore, accurately predicting the location and size of these vortices is critical for accurate slipstream assessment. As the wake structure is highly turbulent and shows strong variation between runs, representative prediction of the vortex location, size and cross-stream movement is challenging both numerically and experimentally. Experimentally, the location of the vortices may be affected by the environment conditions, for example the ambient wind conditions, and invasive measurement techniques. Numerically, to achieve good accuracy of the predicted $U_{slipstream}$ requires adequate resolution of the region for up to at least 5–10H downstream, since this is where the maximum slipstream velocity occurs. This requires a large mesh refinement region in the wake and a sufficiently small timestep, satisfying both requirements can be computationally demanding.

3.2.3. Wake dynamics

According to the wind tunnel experiments, the wake witnesses a strong spanwise oscillation at a Strouhal number (St_W) of 0.19–0.21, based on train width (W) (Bell et al., 2016a). In this study, the spanwise oscillation is visualised by phase-averaging the pressure coefficient C_P in a horizontal plane at z=0.15H. This study adopts the same formula of calculating C_P as used for the wind tunnel experiments (Bell et al., 2016b), which is defined as:

$$C_P = \frac{P_i - P_s}{P_t - P_s}, \tag{8}$$

where P_i is the local static pressure that C_P is based on, and P_t is the total pressure, noting that due to the limitation of the measuring technique, it only takes the streamwise component of velocity into account. P_s is the reference static pressure from an upstream reference pitot-static tube. As for the numerical simulations the reference

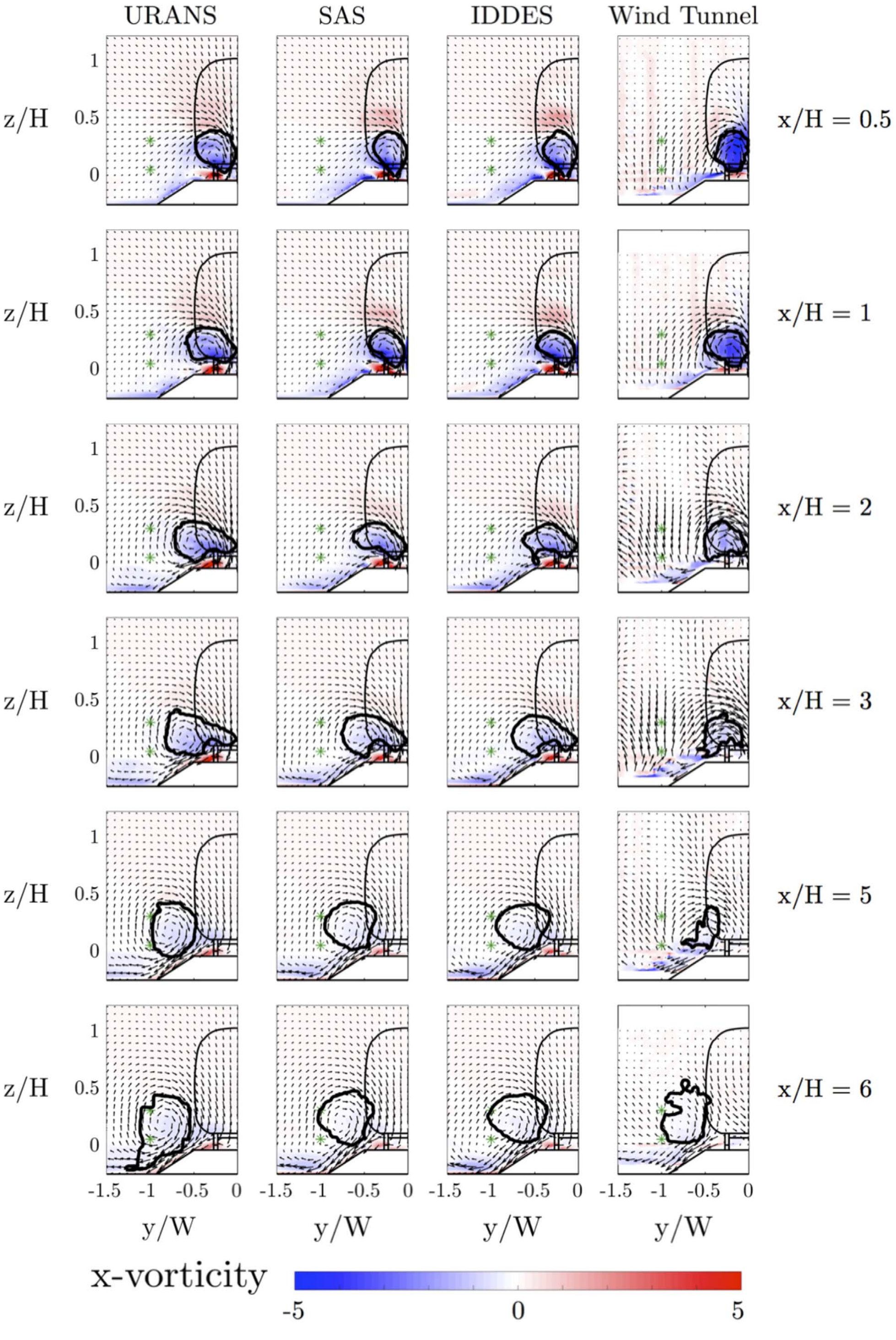

Fig. 8. The comparison of time-averaged wake structure. (For interpretation of the references to color in this figure caption, the reader is referred to the web version of this paper.)

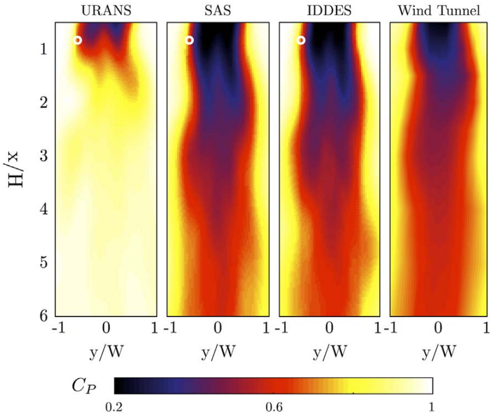

Fig. 9. The comparison of transient wake structures predicted by different turbulence models based on the phase-averaged C_P in a horizontal plane at z=0.15H.

pressure is defined as zero static pressure at outlet, for the numerical comparison a value of $P_s = -0.025$ is used to account for the increased downstream losses in the wind tunnel relative to the open-domain numerical model. The phase-averaging is conducted based on the signal at a reference point with coordinates (0.84H, −0.5W, 0.15H), visualised by the white circles in Fig. 9.

As shown in Fig. 9, the spanwise oscillation observed in the experiments is clearly captured by all three models. Despite the different time and mesh resolutions, SAS and IDDES predict wake structures consistent with the wind tunnel experiments, with the prediction of the URANS model less good. The predicted longitudinal wavelength of the spanwise motion is close to 3H in each case.

Proper Orthogonal Decomposition (POD) is also used to examine the performance of each turbulence model to resolve the detailed makeup of transient wake structures. POD is a widely used technique to extract the coherent flow structures from a turbulent flow field, by calculating the optimal orthogonal bases (modes) of fluctuations. This study employs the snapshot POD method, which was initially proposed by Sirovich (1987), and has been applied to study HST wake structures based on both numerical (Muld et al., 2012a) and experimental data (Bell et al., 2016b). In this study, the POD is conducted based on the total pressure (in line with the experiments) on a vertical plane at the location of x=0.5H. The first four energetic modes are presented in Fig. 10, and the corresponding frequency (St_W) of each mode is determined.

Qualitatively, the first four most energetic modes resolved by different turbulence models are consistent with the wind tunnel measurements (Bell et al., 2016b). The structures of the first two modes show approximately the same sizes of time-averaged longitudinal vortices as depicted in Section 3.2.2. The first mode indicates that the most energetic component is an out-of-phase increase/decrease, which associates with a left/right oscillation in the strength of the trailing vortices, is inline with the phase-averaged results. The spanwise oscillation at $St_W \approx 0.2$ is an indication that the dominant dynamic structure is collaborated with the Karman-like vortex shedding. The second mode shows a simultaneous energy increase/decrease centred on the vortices, corresponding to a longitudinal pulsing of the trailing vortices. The third and fourth modes illustrate smaller energy oscillations above the ballast shoulder. Mode 3 indicates a symmetrical in-phase horizontal/diagonal energy oscillation, while Mode 4 shows an out-of-phase vertical energy oscillation. Modes 1 and 3 acting together can account for the spanwise oscillation of the trailing vortices as they advect downstream. Quantitatively, the mode structures predicted by SAS and DES remain closer to the centreplane, relative to those predicted by URANS. Presumably the loss of centreplane symmetry for modes 3 and 4 is an indication that the length of the dataset used to extract POD modes is insufficient; however, given the computation expense incurred for these simulations, it was difficult to justify increased integration times to better resolve these modes.

In addition to the mode contours illustrated in Fig. 10, the energy percentage of each mode is presented in Table 7 and the cumulative energy percentage distribution of the first 50 modes is shown in Fig. 11. According to Table 7 and Fig. 11, the energy is more concentrated in a few energetic modes for the URANS simulations, whereas IDDES and SAS indicate a wider energy distribution across the modes. For example, the total energy proportion of the first four modes for SAS and IDDES is 0.44 and 0.425 respectively, while for URANS it is 0.726. Additionally, to recover 80% of the total fluctuating energy, URANS, SAS and IDDES require 6, 24 and 32 modes respectively. This is inline with the nature of each turbulence model that URANS only predicts the dominant structures, while IDDES and SAS resolve smaller flow structures and obtain a wider turbulence spectrum, as is discussed further below.

Additionally, the frequency content of each modelled wake is compared based on the power spectral density of U_{TF} at the point (1H, −0.4W, 0.2H). The experimental data shows a wide band at a dominant frequency of St=0.21 (Bell et al., 2016a). Spectral analysis of the velocity signals from numerical simulations at the same point is presented in Fig. 12. In terms of the dominant shedding frequency, all three methods achieve good agreement with the experimental data of St=0.19–0.21, suggesting a Karman-like vortex shedding from the side surfaces of the train, consistent with the left–right oscillation observed in the phase-averaged wake. With respect to the broadness of the frequency spectrum, as expected, URANS has only two narrow peaks, consistent with its failure to capture finer-scale wake structures. Both SAS and IDDES show a slower decay at higher frequencies, implying that a greater range of smaller flow structures is resolved, and this is verified by the turbulent kinetic energy cascade plot presented in Fig. 13.

The turbulent kinetic energy spectra at the same near-wake point (1H, −0.4W, 0.2H) are compared to determine the minimum turbulent length scale that each method can resolve, and to indicate how energy is transferred from larger to smaller length scales. Fig. 13 shows that all three methods achieve a similar prediction to beyond the maximum energy containing scales, which suggests that all the models can reasonably predict the formation of dominant turbulence structures in the near-wake region. In the inertial subrange, both the SAS and IDDES spectra appear consistent than the expected $-5/3$ ($\simeq -1.67$) theoretical slope (Pope, 2000), even though SAS shows a steeper gradient approaching the dissipation range. Specifically, for the linear part within the inertial subrange, using least-squares linear regression, the gradients within a 95% confidence interval (shown in the brackets) of SAS and IDDES are $-2.10(-2.40$ to $-1.81)$ and $-1.78(-2.01$ to $-1.54)$ respectively. Thus, statistically the IDDES model is consistent with the expected energy falloff in the inertial subrange. In contrast, URANS does not capture the inertial subrange, due to its increased damping. The linear inertial subrange is not clearly identifiable for URANS, but for comparison, its gradient within the same range is approximately $-3.53(-3.76$ to $-3.31)$. Additionally, the prediction of the correct energy transfer to higher wavenumbers implies that smaller turbulence scales are better resolved by IDDES model. However, of course, resolving smaller turbulence scales can be very expensive; for example, the IDDES case is approximately 20 times more expensive than the URANS simulation.

4. Validation and uncertainty analysis

In terms of the slipstream assessment, time-averaged wake structure and wake dynamics, in general good agreement is seen between the different turbulence model predictions and physical experiments. In addition to the relatively small influences of the grid resolution and

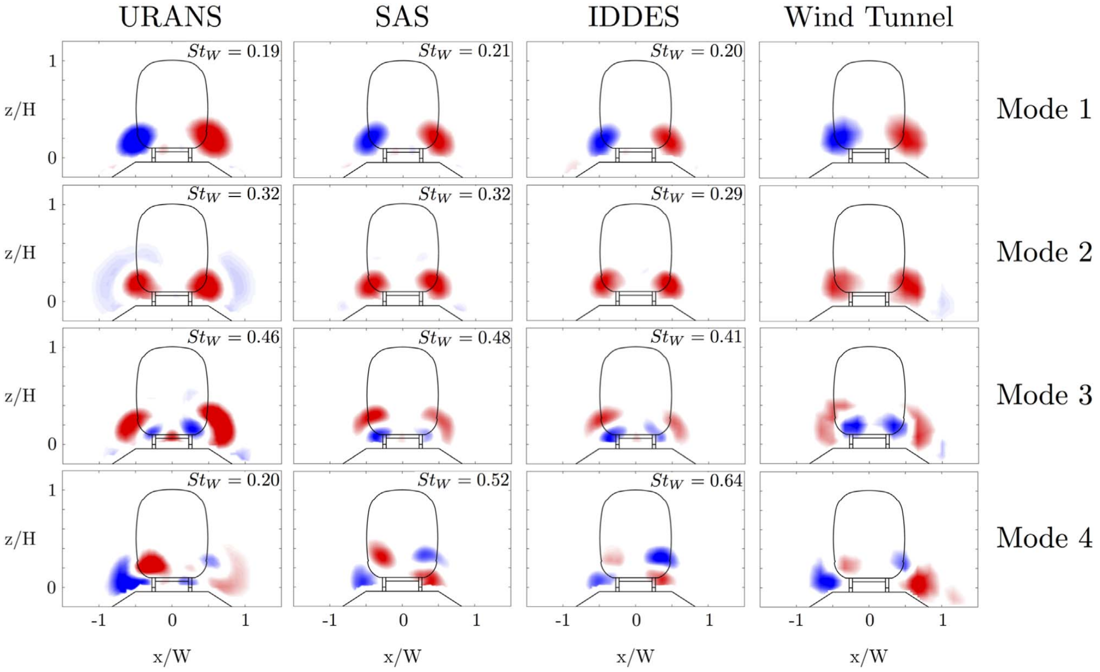

Fig. 10. The comparison of first four POD mode structures at x=1H.

Table 7
Energy percentage of the four most energetic POD modes.

Grid resolution	URANS	SAS	IDDES	**Wind tunnel**
Mode 1	0.499	0.240	0.246	**0.235**
Mode 2	0.120	0.079	0.077	**0.069**
Mode 3	0.072	0.066	0.054	**0.038**
Mode 4	0.047	0.055	0.048	**0.036**
Total	0.726	0.440	0.425	**0.387**

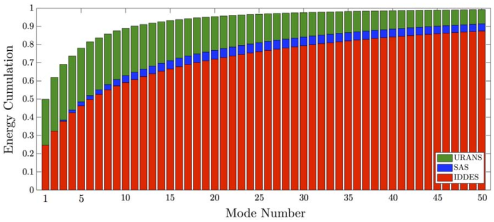

Fig. 11. The cumulative energy percentage with respect to the number of modes.

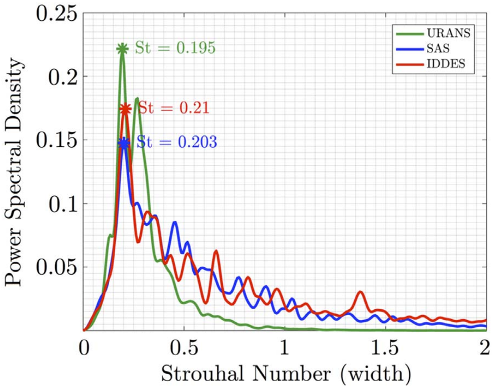

Fig. 12. The comparison of wake shedding frequency based on St_W at the point of [1H, −0.4W, 0.2H].

timesteps, potential causes of discrepancies between the numerical and experimental results in each region are discussed below.

4.1. Nose region

First of all, the discrepancy in the peak slipstream velocity magnitude, as shown in Section 3.1 might be caused by slightly different floor configurations. Even though the cross-sectional dimensions of the ballast for CFD and wind tunnel models are identical, for the numerical simulations the ballast starts at the domain inlet, whereas the ballast for wind tunnel experiment only starts just upstream of the head of the train with a ramp (Bell et al., 2014) (due to restrictions imposed by the working section of the wind tunnel). Additionally, the slight shift of the location of the peak $\overline{U}_{slipstream}$ location might be caused by a slightly different length of the HST models: the wind tunnel model has an exact length of 5 m, while the numerical model has a slightly longer length of 5.165 m based on the model provided by the DIN Standards Railway Committee (FSF, 2014).

4.2. Train side boundary layers

The higher slipstream standard deviation seen along the length of the train is due to upstream turbulence present in the tunnel. In comparison, the numerical simulations show negligible standard deviation along the train, despite the turbulence level at the inlet nominally being approximately set to the tunnel background turbulence level. This suggests that it is necessary to better duplicate upstream background turbulence, including relevant time and length scales of turbulent structures. FLUENT has two different ways to

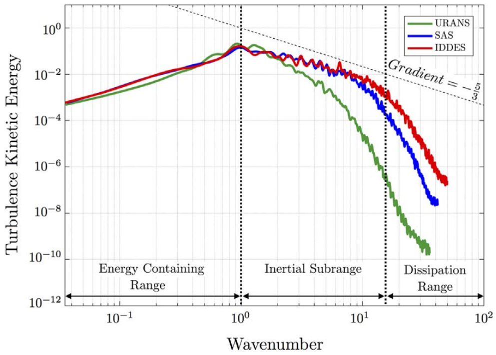

Fig. 13. The turbulence kinetic energy cascade at the point of [1H, −0.4W, 0.2H].

generate synthetic turbulence at the domain inlet. Although not included for the current set of simulations, this is clearly worth exploring for future modelling efforts.

4.3. Near-wake region

The main discrepancy in the near-wake region (around the tail) is that the wind tunnel experiment shows a local slipstream minimum, which is not seen in any of the numerical simulations. Possible causes include the following. First of all, slight simplification of the numerical HST model, especially the underbody structures, may alter the underbody flow which interacts with the downwash over the upper surface in the near-wake region.

Secondly, as this local minimum is not recorded in other moving model experiments and full-scale testing for the same train model, this may imply that the near-wake flow is sensitive to the wind-tunnel measurement techniques (Bell et al., 2014). The slipstream velocity is calculated based on U_{GF} and V_{GF} (Eqs. (6) and (7)). While in most of the wake region U_{GF} is significantly higher than V_{GF}, near the tail the magnitude of U_{GF} drops to zero, and then gradually increases on moving further downstream. Therefore, in the region, $U_{slipstream}$ is dominated by V_{GF}. The experiments use 4-hole cobra probes to determine U_{TF} and V_{TF}. In terms of the raw measuring data, the V_{TF} is much smaller than U_{TF} by an order of magnitude, and this might amplify errors in this region.

4.4. Intermediate-wake region

The discrepancy in the intermediate wake (x=5–8H) may be caused by amplification of upstream deficiencies or local effects. The difference in background turbulence levels between the simulations and experiments may be one possible cause. In addition, the peak slipstream velocity is recorded about 8H behind the tail, which is moving beyond the optimal working section of the tunnel. Imposed pressure gradients in this region may have a small effect on the results.

5. Conclusion

In this study, the ability of three widely used turbulence models to predict the flow past a high-speed train is investigated as a function of grid resolution and timestep. This is achieved through a comparison with wind-tunnel experimental data, based on accuracy in predicting slipstream velocity profiles and correlation with wake structures.

Although simulations based on different turbulence models show qualitatively consistent results with wind tunnel measurements for slipstream assessment, quantitatively the predictions do show a level of dependence on grid resolution and timestep choice. In contrast, all the turbulence models demonstrate a consistency in predicting C_d, which means that if the drag evaluation is the sole purpose, utilisation of IDDES or even SAS is not justified. At least, for the simplified model we have considered.

Naturally, HST slipstream assessment depends strongly on flow development around the train and downstream. Qualitatively, the dominant time-averaged and transient flow features, longitudinal vortices and corresponding spanwise oscillation can be predicted by all three models. Quantitatively, URANS fails to predict the cross-stream development of the trailing vortices and the correlated dynamic response, which makes it unsuitable for quantitative slipstream assessment. IDDES shows superior consistency with the experimental data, perhaps due to its ability to capture a wider range of turbulence scales in the wake. As the first systematic study of using SAS to predict the HST slipstream, the results show that SAS may be a reasonable alternative of IDDES as it achieves a similar level of accuracy at a lower cost.

In practice, trade-offs exist between accuracy and computational cost. This paper has attempted to quantify how well each turbulence-model/mesh/timestep combination reproduces different aspects of the flow past a high-speed train, especially in relation to slipstream characteristics and wake dynamics.

References

Baker, C., 2010. The flow around high speed trains. J. Wind Eng. Ind. Aerodyn. 98 (6), 277–298.

Bell, J.R., Burton, D., Thompson, M.C., Herbst, A.H., Sheridan, J., 2014. Wind tunnel analysis of the slipstream and wake of a high-speed train. J. Wind Eng. Ind. Aerodyn. 134, 122–138.

Bell, J.R., Burton, D., Thompson, M.C., Herbst, A.H., Sheridan, J., 2015. Moving model analysis of the slipstream and wake of a high-speed train. J. Wind Eng. Ind. Aerodyn. 136, 127–137.

Bell, J.R., Burton, D., Thompson, M.C., Herbst, A.H., Sheridan, J., 2016a. Flow topology and unsteady features of the wake of a generic high-speed train. J. Fluids Struct. 61, 168–183.

Bell, J.R., Burton, D., Thompson, M.C., Herbst, A.H., Sheridan, J., 2016b. Dynamics of trailing vortices in the wake of a generic high-speed train. J. Fluids Struct. 65, 238–256.

Egorov, Y., Menter, F., Lechner, R., Cokljat, D., 2010. The scale-adaptive simulation method for unsteady turbulent flow predictions. Part 2: application to complex flows. Flow Turbul. Combust. 85 (1), 139–165.

European Union Agency for Railways, 2014. Commission Regulation (EU) No 1302/2014 concerning a technical specification for interoperability relating to the ‘rolling stock — locomotives and passenger rolling stock’ subsystem of the rail system.

Fossi, A., DeChamplain, A., Akih-Kumgeh, B., 2015. Unsteady rans and scale adaptive simulations of a turbulent spray flame in a swirled-stabilized gas turbine model combustor using tabulated chemistry. Int. J. Numer. Methods Heat. Fluid Flow 25 (5), 1064–1088.

DIN Standards Committee Railway/Normenausschuss Fahrweg und Schienenfahrzeuge (FSF), 2014 ⟨http://www.fsf.din.de⟩.

Graftieaux, L., Michard, M., Grosjean, N., 2001. Combining PIV, POD and vortex identification algorithms for the study of unsteady turbulent swirling flows. Meas. Sci. Technol. 12 (9), 1422.

Hemida, H., Baker, C., Gao, G., 2014. The calculation of train slipstreams using large-eddy simulation. Proc. Inst. Mech. Eng. Part F: J. Rail Rapid Transit 228 (1), 25–36. http://dx.doi.org/10.1177/0954409712460982.

Huang, S., Hemida, H., Yang, M., 2016. Numerical calculation of the slipstream generated by a crh2 high-speed train. Proc. Inst. Mech. Eng. Part F: J. Rail Rapid Transit 230 (1), 103–116.

Menter, F.R., 2012. Best practice: Scale-resolving simulations in ANSYS CFD. ANSYS Germany GmbH, ANSYS Germany, 1–70.

Menter, F., Egorov, Y., 2010. The scale-adaptive simulation method for unsteady turbulent flow predictions. Part 1: theory and model description. Flow Turbul. Combust. 85 (1), 113–138.

Morden, J.A., Hemida, H., Baker, C.J., 2015. Comparison of rans and detached eddy simulation results to wind-tunnel data for the surface pressures upon a class 43 high-speed train. J. Fluids Eng. 137 (4), 041108.

Muld, T.W., Efraimsson, G., Henningson, D.S., 2012a. Flow structures around a high-speed train extracted using proper orthogonal decomposition and dynamic mode decomposition. Comput. Fluids 57, 87–97.

Muld, T.W., Efraimsson, G., Henningson, D.S., 2012b. Mode decomposition and slipstream velocities in the wake of two high-speed trains. Int. J. Railw. Technol.

Östh, J., Kaiser, E., Krajnović, S., Noack, B.R., 2015. Cluster-based reduced-order modelling of the flow in the wake of a high speed train. J. Wind Eng. Ind. Aerodyn. 145, 327–338.

Paradot, N., Talotte, C., Garem, H., Delville, J., Bonnet, J.-P., 2002. A comparison of the numerical simulation and experimental investigation of the flow around a high speed train. In: ASME 2002 Joint US-European Fluids Engineering Division Conference,

19th Australasian Fluid Mechanics Conference
Melbourne, Australia
8-11 December 2014

Characteristics of Flow over a Double Backward-Facing Step

S. Wang[1], D. Burton[1], J. Sheridan[1] and M. C. Thompson[1]

[1]Fluids Laboratory for Aeronautical and Industrial Research (FLAIR)
Department of Mechanical and Aerospace Engineering
P.O. Box 31, Monash University, Clayton, 3800, Australia

Abstract

A *double backward-facing step* (DBFS) is a sequence of two steps with the distance between the steps in the fluid flow direction representing a variable parameter. For this research, the flow characteristics of a DBFS are studied numerically as a function of this distance, with each step height equal and constant. The flow is characterised in terms of the reattachment lengths of the recirculation bubbles behind each step, the overall flow topology and the base pressure on the vertical step surfaces. The predictions are based on two-dimensional (2D) Computational Fluid Dynamics (CFD) simulations using Reynolds-Averaged Navier-Stokes (RANS) turbulence models.

Introduction and Literature Review

The flow over a *single backward-facing step* (SBFS) is a classic problem in fluid dynamics and has been extensively studied. Although it is one of the simplest geometries, it exhibits rich flow physics, including flow separation, flow reattachment, and multiple recirculating bubbles [12].

In 1983, Armaly et al. [2] conducted a systematic study of a SBFS and reported additional regions of flow separation downstream of the step and on both sides of the channel test section, which is not documented in previous studies [10]. Therefore, that study is regarded as a milestone in this area, and much subsequent research has been conducted while referencing that paper. The reattachment length of the recirculation bubble is an important feature, and its behaviour over a range of Reynolds number, step surface roughness, expansion ratio and width-to-height ratio conditions has been studied [3, 9, 12].

A *double backward-facing step* (DBFS) is a sequence of two steps with the distance between the steps in the fluid flow direction representing a variable parameter. In contrast to the SBFS, the DBFS has received little attention from fluid mechanists. A variant of DBFS flow is that associated with a ship-like object of finite span, placed in an open-air environment, where the first step is between the upper and lower deck, and the second step between the lower deck and the water surface. Based on particle image velocimetry (PIV) and qualitative oil-flow visualisations, Tinney and Ukeiley [11] proposed that the flow over a ship-like 3D DBFS object consists of a combination of flow elements, including a horseshoe vortex, horizontal entrainment of air and the presence of two counter-rotating vortices initiated at reattachment. Herry et al. [4] further investigated the stability of this flow and found that the mean flow field can be described by at least two solutions at zero-degree drift angle, with those two solutions mutually symmetric.

In recent years, researchers have started to focus attention onto the DBFS, as it has some practical significance to the automotive and marine industries. For the marine industry, understanding the typical flow field structure around the fight deck, which is normally simplified to a DBFS geometry, has important significance in analysing the interaction between the helicopter rotors and the airwake behind the ship [8]. For the automotive industry, a utility vehicle, also known as a pickup truck, can be approximated as a DBFS over its rear half. Understanding the near-wake flow of a utility vehicle provides valuable information on drag reduction and consequent fuel savings [1].

Based on these and other potential practical applications, it is apparent that understanding the flow over a DBFS has some practical significance. Even though the flow behaviour of a ship airwake and flow over a pickup truck have both been studied, an understanding of the underlying fundamental flow physics is still very limited. Here, we undertake a systematic study to investigate the fundamental flow physics of DBFS flow. Important flow features are quantified including the reattachment length, formation of recirculation bubbles and base pressure variations of the step surfaces.

Numerical Method

Preliminary Simulations

In this study, we focus on the flow over a two-dimensional DBFS. To provide confidence in the CFD simulations for the DBFS, two SBFS flow problems are studied. These phases of the research are referred as stages 1 and 2. In the first stage, the experimental set-up of Armaly et al. [2] is reproduced. The CFD simulations investigate the influence of turbulence model, mesh resolution and blockage. As determined by Armaly et al. [2], the bulk flow structure is primarily two dimensional when the flow is fully turbulent for $Re > 6000$. These 2D simulations are conducted in this fully turbulent flow regime. We compared reattachment length and time-mean flow structure predictions for the k-ε (both the standard and enhanced wall treatment model), SST k-ω, standard k-ω and Spalart-Allmaras (S-A) turbulence models. The results show that SST k-ω turbulence model is the most appropriate turbulence model, providing the best fit to the experimental data on reattachment length as the Reynolds number is varied. This concurs with observations of Menter [6] for similar flow conditions.

An orthogonal block-structured grid is used for this stage to provide better grid point placement control at boundaries and within the domain. Based on grid independence tests, the flow field effectively converges to within 0.23% when each step face consists of 60 to 80 divisions. As this study is based on a high expansion ratio flow (outlet to inlet height ratio equals 1.36), to validate the CFD settings for an open case, for which the top boundary is removed, a second validation stage is carried out. The CFD settings obtained from the stage 1 are then applied to predict the reattachment length results of Kostas et al. [5], which has low expansion ratio of 1.02. Based on the consistency of the experimental and numerical results, it is concluded that the CFD settings (i.e., resolution, turbulence model, etc,) are also valid for this case. Thus, based on these two validation cases, the preferred solver settings and meshing strategy are applied to the subsequent DBFS flow simulations.

Project Description

The flow over a DBFS is studied using 2D steady-state RANS simulations. The Reynolds number is 20,000, calculated based on the freestream velocity and the combined heights of the two steps. The flow is in the turbulent regime, so it is not anticipated that the flow behaviour will be highly sensitive to Reynolds number.

The domain of the CFD simulation is illustrated in figure 1 below. Each step has a height of *h*. The distances in front of the first step and behind the second step are 50*h* and 75*h* respectively, and the heights of the inlet and outlet are 50*h* and 52*h* respectively. This gives an expansion ratio of 52/50 = 1.04. The distance between the steps is characterised by the variable, *d*. The domain has 4 boundaries, and the corresponding boundary conditions for the inlet, outlet, upper boundary and ground (including step faces) are velocity inlet, pressure outlet, symmetry, and no-slip wall. The turbulent intensity level at inlet and outlet is 1%, and the corresponding turbulent length scale is 10% of the step height (*h*). Cases of *d/h* between 0 and 10, with an increment of 1 are studied.

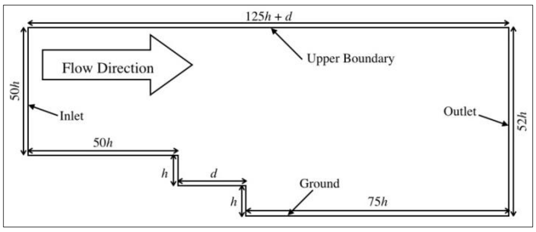

Figure 1: Layout of the computational domain (not to scale).

The solver used in this project is ANSYS FLUENT, 64-bit commercial software, and the simulations are discretised by finite-volume method based on the RANS approach. The turbulence model chosen is SST k-ω. A pressure-based, implicit coupled solver, based on second-order upwind discretisation is used to converge the initial guess to provide an accurate steady-state (time-mean) solution. Convergence is assumed when the residuals of continuity, momentum, turbulent kinetic energy and specific dissipation rate equations reach a level of 10^{-6} or better.

Grid Description and Refinement

An orthogonal block-structured grid with higher resolution over the recirculation regions is the general meshing strategy, with inflation layers applied at all wall boundaries to capture the boundary layers. The adequacy of the near-wall inflation layers is checked by monitoring the converged values of the turbulence-wall Y-plus parameter. In order to fully solve the boundary layer to determine the position of reattachment and separation, the values of Y-plus near the steps are kept near 1. An enhanced wall treatment is used, which allows the solution close to the walls to be computed explicitly.

A finer grid is applied to the region where the flow behaviour is expected to be more complex, such as the recirculation regions. In order to avoid the loss of discretisation accuracy due to a sudden change in the lengths of adjacent cells, the expansion ratio between any two adjacent cells is kept below 1.1.

Additionally, a mesh convergence study based on the geometry for d/h=10 is applied to investigate grid independence. The meshing strategy for each grid is identical, while the number of cells is gradually increased from 0.03 to 2.2 million. The mesh convergence test is based on the primary reattachment length behind the first step, and the results are plotted in figure 2. The results indicate that the mesh achieves grid independence when the number of cells is 1.3 million. This gives 80 divisions for each step base and 50 divisions per step height. This grid density is applied for all other cases.

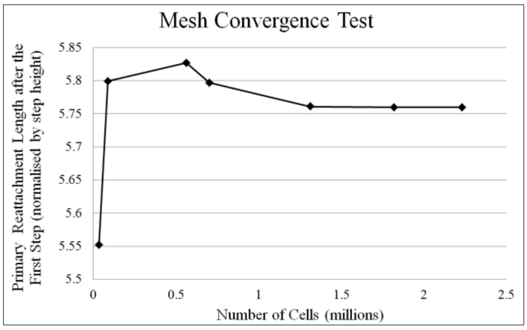

Figure 2: Mesh convergence study.

Result Analysis

The results in this study are presented from two perspectives: overall result analysis and individual case analysis. In the first section, the variations of reattachment length and step base pressure coefficient with *d/h* from 0 to 10 are presented and analysed. In the second section, more detailed flow field results for distinctive individual cases (i.e. *d/h* = 0, 1, 3, 5 and 6) are presented. Note that all lengths, e.g., the reattachment length, are normalised by the step height (*h*). The step base pressure coefficient is calculated based on the freestream velocity and the reference pressure at the outlet (i.e., 0 units). The reattachment length is determined based on the extrapolation of the zero-velocity line along the wall [2]. The intensity of the vortex is quantified by the magnitude of the stream function, which describes the mass flow rate of recirculating fluid within each individual recirculation bubble.

Overall Result Analysis

1. *Reattachment Length Variation with d/h*

As *d/h* varies from 0 to 10, the flow structure can be divided into two regimes, as shown in figure 3. The top sketch shows the typical flow behaviour for *d/h* between 1 and 5, with the flow separating at the first step and reattaching downstream of the second step. For cases of *d/h* from 6 to 10, the recirculation bubbles downstream of the first and second step become independent, as shown in the bottom sketch in figure 3. When *d/h* equals 0, the geometry reverts to a SBFS with the step height of 2*h*. The reattachment length for each recirculation bubble is defined in figure 3, where the d_0 represents the overall reattachment length of the entire DBFS.

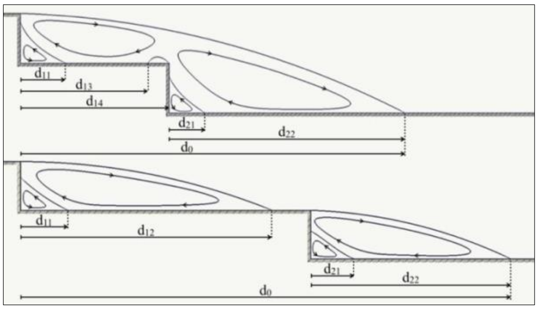

Figure 3: Schematic highlighting the recirculation bubbles and respective reattachment lengths.

The change in the reattachment lengths as *d/h* is varied between 0 and 10 is illustrated in figure 4. In the first regime, as the second step is shifted away from the first step, a small recirculation bubble is formed at d_{13} when *d/h* is 3 and then disappears when *d/h* is greater than 4. In the second regime, as the second step is shifted further downstream, the sizes of the recirculation bubbles behind the two steps become near identical as the differences between d_{11} and d_{21}, and d_{12} and d_{22} are reduced. Additionally, the overall reattachment length (d_0) does not increase until the second step is six step heights from the first.

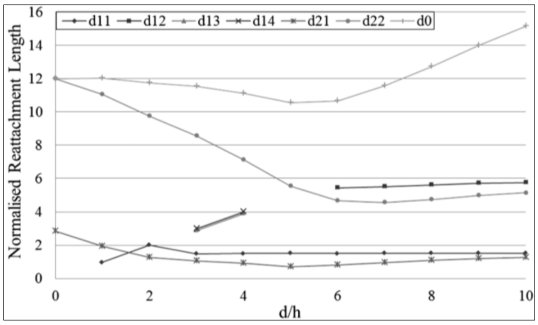

Figure 4: Variation of the reattachment lengths as *d/h* is varied between 0 and 10.

2. *Step Base Pressure Coefficient Variation with d/h*

The base pressure coefficient is calculated based on the average surface pressure at each step base, and its variation with *d/h* is plotted in figure 5. For *d/h* = 0, the first and second step coincide. Thus the average C_p of the two step bases are identical for *d/h* = 0. When the second step is shifted downstream, the difference of the average C_p between the two steps gradually increases, and achieves the maximum at *d/h* = 6. With the second step shifted even further downstream, the difference of step base pressure coefficient between the two steps reduces.

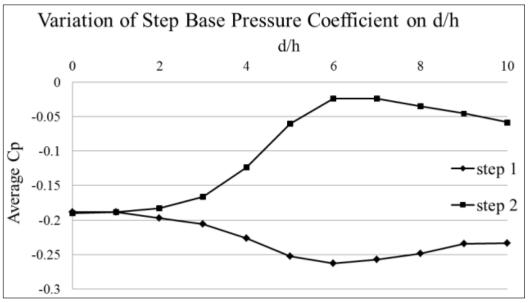

Figure 5: Variation of the step base pressure coefficient as *d/h* is varied between 0 and 10.

Individual Case Analysis

Case 1: *d/h* = 0

At *d/h* = 0, the double backward-facing step is equivalent to a SBFS with a step height of 2h. This is used as a reference case to calculate the vortex intensity. To compare the relative strength of the different recirculation bubbles, the *intensity* of a vortex is represented by the magnitude of stream function difference between the recirculation centre and dividing outer streamline, normalised by the value for vortex A (the primary recirculation bubble of *d/h* = 0). The flow structure is presented by the streamlines as shown in figure 6, and the intensities of vortices are presented in Table 1. The flow structure is identical to the flow structure for a SBFS. This consists of a primary recirculation bubble (i.e., vortex A) and a corner vortex (i.e., vortex B). Due to the high grid resolution in this study, a tiny tertiary eddy is captured at the step corner (this feature also exists occasionally in other cases). This series of vortices is in line with the theory of *Moffatt eddies* in a concave corner [7]. Because the size of this eddy is extremely small and its influence on the main flow structure is negligible, information about this eddy is not reported in the present study.

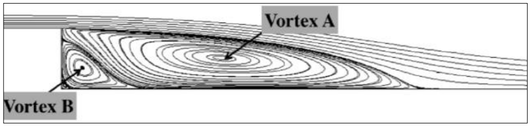

Figure 6: Streamlines showing the recirculation bubbles behind the step (*d/h* = 0).

	Intensity of Vortices (normalised)
d/h	0
Vortex A	1
Vortex B	0.061

Table 1: Intensity of vortices (*d/h* = 0)

Case 2: *d/h* = 1

The flow structures for *d/h* = 1 and 2 are very similar, consequently only the *d/h* =1 case is presented here. When the second step is shifted away from the first step, a corner vortex is formed behind each step (vortices D and E), as shown in figure 7. The corner vortices at *d/h* = 1 and 2 are weaker than the corner vortex in the single step case (i.e., *d/h* = 0). The intensity of each vortex is presented in table 2.

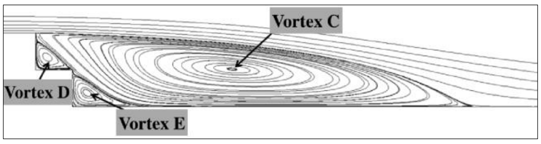

Figure 7: Streamlines showing the recirculation bubbles behind the steps (*d/h* = 1).

	Intensity of Vortices (normalised)	
d/h	1	2
Vortex C	1.013	0.962
Vortex D	0.034	0.027
Vortex E	0.017	0.032

Table 2: Intensity of vortices (*d/h* = 1 and 2)

Case 3: *d/h* = 3

In this case the primary recirculation bubble, as shown in the previous cases, breaks into two vortices (vortices F and G). Due to the similarity of the flow structure of *d/h* = 3 and 4, only the flow structure for *d/h* = 3 is presented in figure 8. Additionally, as the second step is shifted from *d/h* = 3 to 4, the intensity of vortex F remains almost identical, while the intensity of vortex G drops significantly, as shown by the results in table 3. At this stage, apart from the major recirculation bubbles (i.e., vortices F and G) and corner eddies (i.e., vortices H and I), a tiny recirculation bubble (vortex J) is formed at above the edge of the second step, associated with separation of reversed flow.

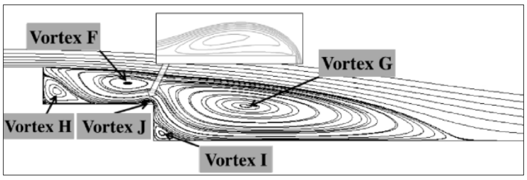

Figure 8: Streamlines showing the recirculation bubbles behind the steps (*d/h* = 3).

	Intensity of Vortices (normalised)	
d/h	3	4
Vortex F	0.441	0.460
Vortex G	0.873	0.647
Vortex H	0.029	0.030
Vortex I	0.022	0.018
Vortex J	0.010	0.004

Table 3: Intensity of vortices (*d/h* = 3 and 4).

Case 4: *d/h* = 5

When the second step is five step heights from the first step, the small recirculation bubble above the edge of the second step disappears, as illustrated in figure 9. This is the last case before the recirculation bubbles behind the two steps effectively become independent. Additionally, the intensity of the primary recirculation bubble behind the first step (i.e., vortex K) surpasses the intensity of the primary recirculation bubble behind the second step (i.e., vortex L), as presented in table 4.

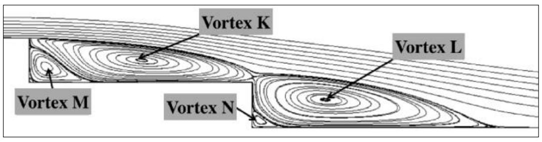

Figure 9: Streamlines showing the recirculation bubbles behind the steps (*d/h* = 5).

	Intensity of Vortices (normalised)
d/h	5
Vortex K	0.461
Vortex L	0.351
Vortex M	0.033
Vortex N	0.010

Table 4: Intensity of vortices (*d/h* = 5)

Case 5: *d/h* = 6

When the distance between the two steps is increased to six step heights, the main recirculation zones behind each step become fully separated, as illustrated in figure 10. From *d/h* =6 on, the flow firstly reattaches behind the first step. Moving further downstream, the boundary layer further develops until it reaches the edge of the second step, and then the flow reattaches behind the second step. Additionally, as the second step is shifted further downstream, the difference between the vortices behind the first and second step reduces (see table 5), as the influence of the upstream vortices (vortices O and Q) on downstream flow field is reduced.

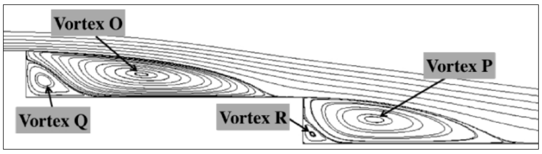

Figure 10: Streamlines showing the recirculation bubbles behind the steps (*d/h* = 6).

	Intensity of Vortices (normalised)				
d/h	6	7	8	9	10
Vortex O	0.462	0.461	0.461	0.449	0.459
Vortex P	0.262	0.276	0.305	0.317	0.345
Vortex Q	0.033	0.033	0.033	0.031	0.032
Vortex R	0.011	0.017	0.022	0.024	0.027

Table 5: Intensity of vortices (*d/h* = 6, 7, 8, 9 and 10)

Conclusions

In conclusion, the characteristics of the time-mean DBFS flow with different configurations (i.e., *d/h* varying between 0 and 10) were investigated by solving for the flow field based on the 2D Reynolds-Averaged Navier–Stokes equations. A number of distinct flow regimes were identified. The flow behaviour had been quantified based on the variation of reattachment lengths, intensities of the associated vortices and step base pressure.

Acknowledgements

This research was supported under Australian Research Council's Linkage Projects funding scheme, project number LP130100953, and computing time support from the National Computational Infrastructure (NCI) (project d71) are gratefully acknowledged.

References

[1] Al-Garni, A.M. and L.P. Bernal, *Experimental study of a pickup truck near wake.* J. Wind Eng. Ind. Aerodyn., 2010. **98**(2): p. 100-112.

[2] Armaly, B.F., et al., *Experimental and theoretical investigation of backward-facing step flow.* J. Fluid Mech., 1983. **127**: p. 473-496.

[3] Biswas, G., M. Breuer, and F. Durst, *Backward-facing step flows for various expansion ratios at low and moderate Reynolds numbers.* J. Fluids Eng.-Trans. ASME, 2004. **126**(3): p. 362-374.

[4] Herry, B.B., et al., *Flow Bistability Downstream of Three-Dimensional Double Backward Facing Steps at Zero-Degree Sideslip.* J. Fluids Eng.-Trans. ASME, 2011. **133**(5).

[5] Kostas, J., J. Soria, and M.S. Chong, *Particle image velocimetry measurements of a backward-facing step flow.* Experiments in Fluids, 2002. **33**(6): p. 838-853.

[6] Menter, F.R., *Two-equation eddy-viscosity turbulence models for engineering applications.* AIAA journal, 1994. **32**(8): p. 1598-1605.

[7] Moffatt, H.K., *Viscous and resistive eddies near a sharp corner.* Journal of Fluid Mechanics, 1964. **18**(01): p. 1-18.

[8] Reddy, K.R., R. Toffoletto, and K.R.W. Jones, *Numerical simulation of ship airwake.* Comput. Fluids, 2000. **29**(4): p. 451-465.

[9] Schafer, F., M. Breuer, and F. Durst, *The dynamics of the transitional flow over a backward-facing step.* J. Fluid Mech., 2009. **623**: p. 85-119.

[10] Taylor, T. and E. Ndefo. *Computation of viscous flow in a channel by the method of splitting*. in *Proceedings of the Second International Conference on Numerical Methods in Fluid Dynamics*. 1971. Springer.

[11] Tinney, C.E. and L.S. Ukeiley, *A study of a 3-D double backward-facing step.* Exp. Fluids, 2009. **47**(3): p. 427-438.

[12] Wu, Y., H. Ren, and H. Tang, *Turbulent flow over a rough backward-facing step.* International Journal of Heat and Fluid Flow, 2013.

The Accuracy of Different Turbulence Models (URANS, SAS and DES) for Predicting High-Speed Train Slipstream

Shibo Wang[a,*], James R. Bell[a], David Burton[a], John Sheridan[a], Astrid Herbst[b], Mark C. Thompson[a]

[a]*Monash University, Australia*
[b]*Bombardier Transportation*

Abstract

Slipstream, i.e., the air movement induced by a high-speed train (HST) as it passes, is a safety hazard to commuters and trackside workers, and can even cause damage to infrastructure along track lines. Because of its importance, many numerical studies have been undertaken into this phenomenon. However, to the authors' knowledge, a systematic comparison of predictions from different turbulence models used to simulate slipstream has not yet been conducted. This study aims to investigate and evaluate the capability of three widely used turbulence models: URANS, SAS and DES; to predict slipstream from a full featured train model, comparing results with experimental data to determine the fidelity of the models.

Keywords: High-speed trains, Train aerodynamics, Slipstream, Computational Fluid Dynamics (CFD), Unsteady Reynolds-Averaged Navier-Stokes equations (URANS), Scale-Adaptive Simulation (SAS), Detached Eddy Simulation (DES)

---

1. Introduction

The slipstream of a high-speed train is highly turbulent, three-dimensional and time-dependent, which poses a significant challenge to predict numerically. Much effort has been channelled into improving the accuracy and efficiency of the numerical simulations of complex turbulent flows, for example, through the development of more complex turbulence models. Generally, a model that captures more of the full range of flow structures is more computationally demanding. Therefore, a trade-off generally exists between accuracy and computing cost. To the authors' knowledge, a systematic comparison of different turbulence models to predict slipstream is yet to be conducted. In this study, three current state-of-the-art methods (i.e., URANS, SAS, DES) are studied, and compared based on their capability to predict both time-averaged and transient flow features.

2. Numerical method

2.1. Geometry

This study is based on a *Deutsche Bahn Inter-City-Express 3* (ICE3) high-speed train, a widely operated train operated in European and Asian countries. The numerical analysis was conducted based on a slightly geometrically simplified ICE3 model. It used a length-width-height ratio of approximately 50:3:4. A comparison of the real operational train and the simplified numerical simulation model is illustrated in Figure 1. Although the train model was significantly simplified, omitting details such as the gaps between carriages and the air-conditioning units, it still included important geometry features that have a strong influence on the wake, in particular, the bogies and snowplows. The train was positioned on a standard single-track ballast rail (coloured in green), the dimensions of which are based on the CEN specification [1].

2.2. Computational domain and grid description

The train was located in a hexahedral computational domain, as illustrated in Figure 2. Its dimensions were normalised by the width (W) in the cross-stream directions, and by the length (L) of the train in the streamwise direction.

---

[*] Corresponding author
Email address: `shibo.wang@monash.edu` (Shibo Wang)

Preprint submitted to Aerovehicles 2 *January 20, 2016*

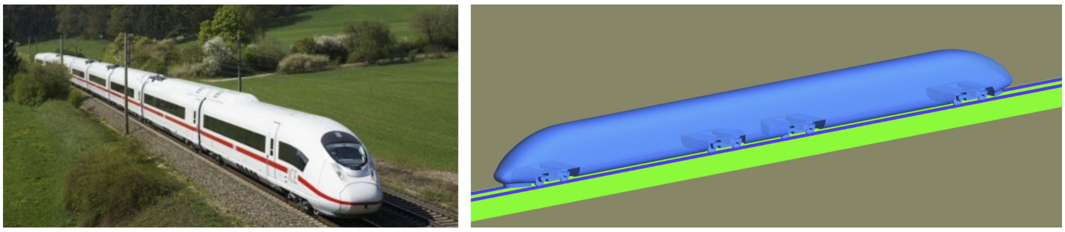

Figure 1: Left: A photograph of the ICE3 train in operation (provided by *Bombardier Transportation*); Right: The simplified version of the train model used for numerical simulations.

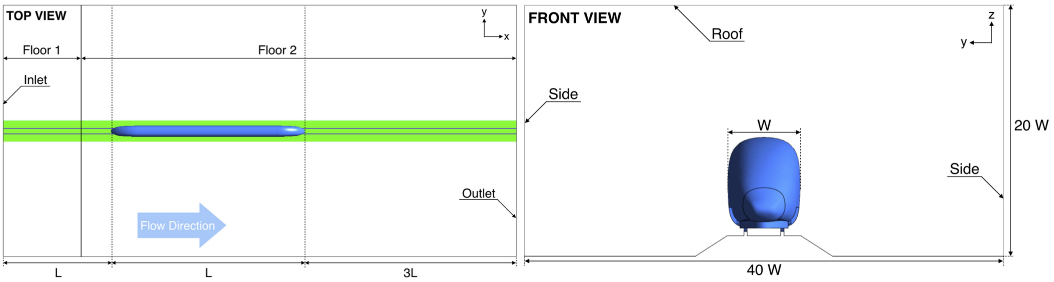

Figure 2: The schematic of computational domain (not to scale), showing the placement of the train and domain dimensions.

The uniform velocity boundary condition was applied at the inlet. The free-stream Reynolds number based on the train width was set to 7.2×10^5. A zero static-pressure boundary condition was applied at the outlet boundary. Symmetry boundary conditions were used at the roof and side boundaries. The floor boundary constitutes the ground, ballast and rails. In order to replicate the splitter plate introduced to remove the floor boundary layer in the wind tunnel experiments, the floor was split into two parts, namely *floor 1* and *floor 2*. Floor 1 was $0.7L$ long, and employed a zero-shear wall condition. Floor 2 was $4.3L$ long with a no-slip wall condition. Additionally, a no-slip wall condition was applied to all train surfaces.

A Cartesian cut-cell grid with substantially increased mesh concentration around the train and in the wake was developed to achieve a higher resolution in the slipstream measurement regions and to accurately capture the boundary layers and induced flow separation from small-scale geometrical features. The grid had approximately 26.6 million cells. The train surface had 10 inflation layers to capture the boundary layer, and the wall y^+ at the first cell was maintained approximately between 1 to 30. As an aim of this study was to compare and contrast the capabilities of different numerical models, the same grid was used for each simulation. The influence of grid resolution on the numerical predictions is not reported in this study; however, it should be noted that considerable care was used to generate a subjectively optimal mesh, through the generation of a sequence on successively improved meshes combined with self-consistency testing and experimental validation.

2.3. Governing equations and solver details

Due to a high degree of variation in slipstream flow observed between experimental runs, it seems likely that the highly unsteady flow can only be simulated accurately by transient simulation. Currently, the most widely used transient solvers are URANS, SAS, DES and Large Eddy Simulation (LES). Due to the high computational cost of (pure) LES at high Reynolds numbers, it is still limited to studying fundamental flows over simple geometries [2]. Therefore, this study focused on three less expensive numerical approaches that appear more applicable to high-speed train aerodynamics research: URANS, SAS and DES.

Even though URANS can provide a time-dependent solution, it does not provide spectral content of the flow. At best, it only predicts the large-scale dynamics of the main flow structures. For example, Schulte-Werning et al. utilised URANS to study the unsteady wake structure and further investigate the last-car-oscillation effect [3]. SAS modifies the classic RANS approach by incorporating the von Karman length scale. Interestingly, the modified model can capture the larger-scale temporal and spatial scales, and captures more of the turbulence spectrum as the spatial and temporal resolution are increased [4]. To the authors' knowledge, SAS has not yet to be applied for studying train aerodynamics. DES is a blend of RANS and LES models, utilising RANS to approximate the boundary layer and applying LES to capture the time-dependent flow away from boundaries. Therefore, the turbulence spectrum can be partially solved, and spectral analysis can then be conducted to analyse the chaotic wake structures [5]. This study used a modified DES model, the *Improved-Delayed-DES* (IDDES) model, which had an improved on wall-modelling capability. All results are obtained using the commercial CFD software package *FLUENT* as part of the ANSYS 16.2 suite.

The RANS turbulence model used as part of all higher-level turbulence models was the k-ω Shear Stress Transport (SST) model. The time-step was normalised by T_{ref}, which was calculated as T_{ref}= $\frac{freestreamvelocity}{trainheight}$, i.e., the time taken for the fluid to advect 1 train height. The time-steps chosen for URANS, SAS and DES were $0.4T_{ref}$, $0.04T_{ref}$ and $0.004T_{ref}$, respectively. The unsteady statistics averaged the flow over $312T_{ref}$ after the flow was checked to be dynamic stable through comparisons with predictions from smaller averaging periods.

3. Result and analysis

3.1. *Time-averaged flow structure*

The dominant flow structure around a high-speed train is a counter-rotating vortex pair in the wake. This structure originates from boundary-layer vorticity fed into the wake as the flow separates at the tail of the train. This vorticity realigns into a streamwise counter-rotating vortex pair as the fluid passes beyond the complex near wake. Further downstream the vortices move downwards and outwards, through the combined effects of self induction and image vortices situated beneath the ground plane. One assessment of the capability of each model to accurately predict the time-averaged flow field was based on the x-vorticity map at a plane $1H$ downstream of the tail, as shown in figure 3(a). In this figure, the y-position was normalised by W, and the z-position by H. The formation of the vortex was also visualised through in-plane velocity vectors (white arrows); with the vortex boundary identified via $\Gamma_2 = 2/\pi$ (black solid line). Based on this figure, all three methods provide a reasonable prediction of the near-wake time-averaged wake structure, accurately predicting the location and extent of the counter-rotating vortices.

3.2. *Transient flow features*

One measure of characterising the unsteady wake behaviour is the Strouhal number. For the present study this was determined at a monitor point $1H$ behind the tail. The URANS, SAS and DES predictions of the Strouhal number were 0.113, 0.243 and 0.206, respectively, compared with a result from wind tunnel testing of $0.20 \sim 0.21$ [6]. Hence, for this measure DES provides a closer prediction, while URANS significantly under predicts the wake frequency and SAS slightly over predicts it. Of course, it needs to be borne in mind that the cost of SAS is approximately 1/10th of DES, and URANS is approximately 1000 times less expensive than DES. Views of the instantaneous wake structure as predicted by the different approaches are also given in figure 3(b). This wake is depicted using isosurfaces of Q-criterion at an arbitrary time instant. Clearly URANS does not capture the chaotic finer-scale flow structures explicitly, although the meandering large-scale counter-rotating vortex pair is visible, even though it oscillates at the wrong frequency. Both SAS and DES predict smaller-scale features of the wake, and there is some evidence that DES predicts features down to a smaller length-scale, as might be expected.

3.3. *Slipstream velocity predictions*

The slipstream velocity was measured at: (1) the trackside height along the length of the train, (2) $1W$ offset from the centre plane0 and, (3) $0.05H$ above the top of rail, as specified by European regulations [7]. The slipstream velocity was calculated through the following equations, with all velocity components normalised by the free-stream velocity:

$$U_{GF}= 1\text{-}\frac{U_{TF}}{U_L}\ ,\ U_{slipstream}=\sqrt{U_{GF}^2+V^2}.$$

Here, U_{GF} is the ground-fixed streamwise velocity; U_{TF} is the train-fixed streamwise velocity; U_L the freestream velocity; V the lateral velocity; and $U_{slipstream}$ the slipstream velocity.

Qualitatively, the slipstream profiles for the three methods have the same trend: a local peak near the head, with the slipstream velocity gradually increasing towards the tail, as presented in Figure 4. After another local peak at the tail, the slipstream velocity reaches its maximum in the near wake. Quantitatively, URANS obtained a maximum slipstream velocity of 0.19, while SAS and DES predicted a magnitude between 0.1 and 0.11. These predictions can be compared with experimental results from tests conducted at Monash University and DLR in Germany: wind-tunnel testing gave 0.13, a moving model rig experiment gave 0.1 and full-scale testing indicated 0.09. Thus, SAS and DES methods show better consistency with experiments.

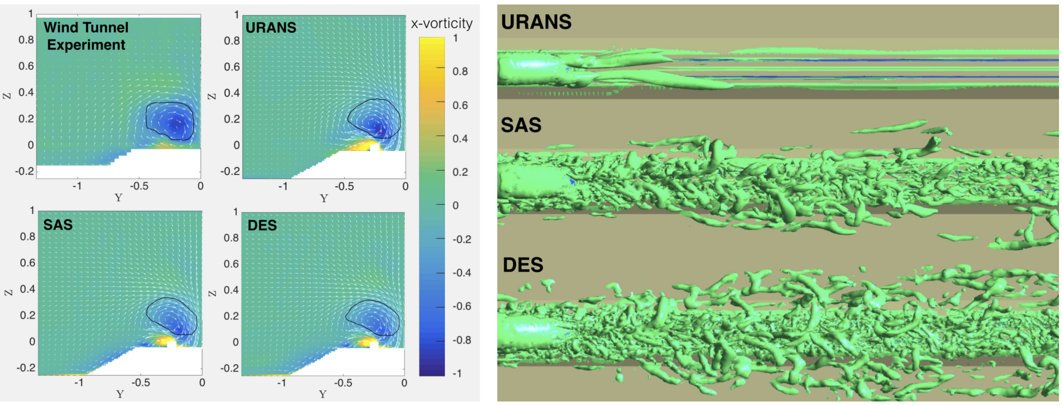

Figure 3: Left: Comparison of the time-averaged flow structure, visualised through vorticity contours in a cross-stream plane at $1H$ behind the tail; Right: Comparison of the transient wake structure, visualised by isosurfaces of constant Q criterion.

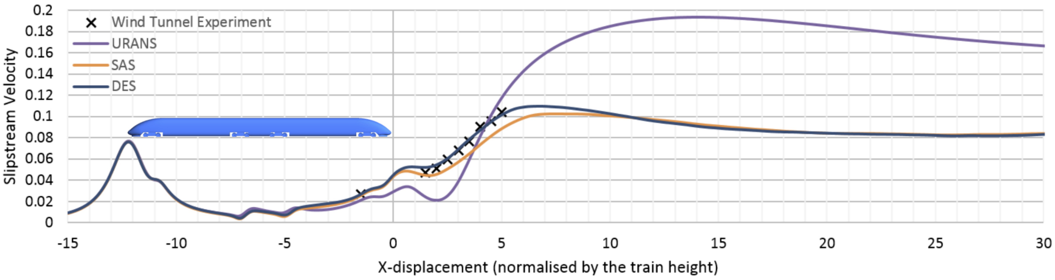

Figure 4: The comparison of slipstream velocity profiles measured at $z = 0.05H$.

4. Conclusion

Three widely used turbulence models, URANS, SAS and DES, have been evaluated based on their capabilities for the prediction of high-speed train slipstream. URANS predicts the dominant wake flow structure qualitatively. However, due to its inability to predict even medium-scale turbulent features, the time-mean wake is not accurately predicted and thus its capability to estimate the slipstream velocity profile is limited. Both the time-averaged and low frequency unsteadiness obtained from SAS and DES are in good agreement, and are reasonably consistent with full-scale and wind-tunnel experimental measurements. Although DES predicts turbulence down to finer scales, its computational cost is approximately one order of magnitude higher than SAS simulation, in large part because of the order of magnitude smaller timestep used for DES.

5. References

[1] European Committee for Standardisation. Cen railway applications - aerodynamics - part 4: Requirements and test procedures for aerodynamics on open track, en 14067-4:2005+a1. 2009.

[2] Hemida H. and Krajnović S. Les study of the influence of the nose shape and yaw angles on flow structures around trains. *Journal of Wind Engineering and Industrial Aerodynamics*, 98(1):34 – 46, 2010.

[3] Schulte-Werning B., Heine C, and Matchke G. Unsteady wake flow characteristics of high-speed trains. *Proc. Appl. Math. Mech.*, 2:332–333, 2003.

[4] Egorov Y., Menter F.R., Lechner R., and Cokljat D. The scale-adaptive simulation method for unsteady turbulent flow predictions. part 2: Application to complex flows. *Flow, Turbulence and Combustion*, 85(1):139–165, 2010.

[5] Muld T.W., Efraimsson G., and Henningson D.S. Flow structures around a high-speed train extracted using proper orthogonal decomposition and dynamic mode decomposition. *Computers and Fluids*, 57:87–97, 2012.

[6] J.R. Bell, D. Burton, M.C. Thompson, A.H. Herbst, and J. Sheridan. Flow topology and unsteady features of the wake of a generic high-speed train. *Journal of Fluids and Structures*, 61:168 – 183, 2016.

[7] Commission regulation (eu) no 1302/2014 of 18 november 2014 concerning a technical specification for interoperability relating to the ‘rolling stock — locomotives and passenger rolling stock’ subsystem of the rail system in the european union. *Official Journal of the European Union*, November 2014.

Submission #8, submitted 22 Jan 2016, 03:25

Mr. Shibo Wang, Ph.D.
`shibo.wang@monash.edu`
Mr.

On the Suitability of Scale-Adaptive Simulation to Predict High-Speed Train Slipstream

Shibo Wang, James R. Bell, David Burton, Astrid Herbst, John Sheridan, Mark C. Thompson

Slipstream is defined as the induced airflow caused by the high-speed train (HST) movement, which can cause safety hazards and damage concerns. Therefore, much effort has been invested to numerically predict the slipstream. As the flow over a HST is highly turbulent, a Scale-Resolving Solver (SRS) is essential to accurately capture the dynamic flow features: for example, Large-Eddy Simulation (LES) and Detached-Eddy Simulation (DES). In comparison to the Reynolds-Averaged Navier-Stokes (RANS) simulations, both LES and DES are computationally demanding, especially LES, which is rarely used for real-life industrial flows. This study aims to evaluate the capability of a relative new turbulence model, Scale-Adaptive Simulation (SAS), to predict HST slipstream, which is less computationally demanding than conventional SRSs. The present research systematically studies the performance of SAS under different time-steps, and the results are compared with DES predictions and experimental data.

Keywords: Aerodynamics, Computational methods, Turbulence

I am **not interested** in publication of my research results in “Archive of Mechanical Engineering” following the conference.

Bibliography

Aita, S., Tabbal, A., Mestreau, E., Montmayeur, N., Masbernat, F., Wolfhugel, Y. & Dumas, J. 1992 Cfd aerodynamics of the french high-speed train. *Tech. Rep.*. SAE Technical Paper.

Ambrósio, J., Pombo, J., Pereira, M., Antunes, P. & Mósca, A. 2012 A computational procedure for the dynamic analysis of the catenary-pantograph interaction in high-speed trains. *Journal of theoretical and applied mechanics* **50** (3), 681–699.

Baker, C. 2010 The flow around high speed trains. *Journal of Wind Engineering and Industrial Aerodynamics* **98** (6), 277–298.

Baker, C., Dalley, S., Johnson, T., Quinn, A. & Wright, N. 2001 The slipstream and wake of a high-speed train. *Proceedings of the Institution of Mechanical Engineers, Part F: Journal of Rail and Rapid Transit* **215** (2), 83–99.

Baker, C. J., Quinn, A., Sima, M., Hoefener, L. & Licciardello, R. 2014a Full-scale measurement and analysis of train slipstreams and wakes. part 1: Ensemble averages. *Proceedings of the Institution of Mechanical Engineers, Part F: Journal of Rail and Rapid Transit* **228** (5), 451–467.

Baker, C. J., Quinn, A., Sima, M., Hoefener, L. & Licciardello, R. 2014b Full-scale measurement and analysis of train slipstreams and wakes. part 2 gust analysis. *Proceedings of the Institution of Mechanical Engineers, Part F: Journal of Rail and Rapid Transit* **228** (5), 468–480.

Bell, J. 2015 The slipstream and wake structure of high-speed trains.

Bell, J., Burton, D., Thompson, M., Herbst, A. & Sheridan, J. 2014a The effect of length to height ratio on the wake structure and surface pressure of a high-speed train. In *19th Australasian Fluid Mechanics Conference (AMFC), Melbourne, Australia*, pp. 8–11.

Bell, J., Burton, D., Thompson, M., Herbst, A. & Sheridan, J. 2014b Wind tunnel analysis of the slipstream and wake of a high-speed train. *Journal of Wind Engineering and Industrial Aerodynamics* **134**, 122–138.

Bell, J., Burton, D., Thompson, M., Herbst, A. & Sheridan, J. 2015 Moving model analysis of the slipstream and wake of a high-speed train. *Journal of Wind Engineering and Industrial Aerodynamics* **136**, 127–137.

Bell, J., Burton, D., Thompson, M., Herbst, A. & Sheridan, J. 2016a Dynamics of trailing vortices in the wake of a generic high-speed train. *Journal of Fluids and Structures* **65**, 238–256.

Bell, J., Burton, D., Thompson, M., Herbst, A. & Sheridan, J. 2016b Flow topology and unsteady features of the wake of a generic high-speed train. *Journal of Fluids and Structures* **61**, 168–183.

Bell, J., Burton, D., Thompson, M., Herbst, A. & Sheridan, J. 2017 The effect of tail geometry on the slipstream and unsteady wake structure of high-speed trains. *Experimental Thermal and Fluid Science* **83**, 215–230.

Burgin, K., Adey, P. & Beatham, J. 1986 Wind tunnel tests on road vehicle models using a moving belt simulation of ground effect. *Journal of Wind Engineering and Industrial Aerodynamics* **22** (2-3), 227–236.

CAD 2014 DIN Standards Committee Railway/Normenausschuss Fahrweg und Schienenfahrzeuge (FSF), http://www.fsf.din.de.

CEN 2009 Railway applications - aerodynamics part 4: Requirements and test procedures for aerodynamics on open track, cen en 14067-4.

CEN 2011 Railway applications - aerodynamics part 4: Requirements and test procedures for aerodynamics on open track, cen en 14067-4.

CEN 2013 Railway applications - aerodynamics part 4: Requirements and test procedures for aerodynamics on open track, cen en 14067-4.

Cheli, F., Corradi, R., Rocchi, D., Tomasini, G. & Maestrini, E. 2010 Wind tunnel tests on train scale models to investigate the effect of infrastructure scenario. *Journal of Wind Engineering and Industrial Aerodynamics* **98** (6), 353–362.

Cogotti, A. 1998 A parametric study on the ground effect of a simplified car model. *Tech. Rep.*. SAE Technical Paper.

Cooper, R. 1981 The effect of cross-winds on trains. *Journal of Fluids Engineering* **103**, 170–178.

Copley, J. 1987 The three-dimensional flow around railway trains. *Journal of Wind Engineering and Industrial Aerodynamics* **26** (1), 21–52.

Délery, J. M. 2001 Robert legendre and henri werlé: Toward the elucidation of three-dimensional separation. *Annual review of fluid mechanics* **33** (1), 129–154.

Egorov, Y., Menter, F., Lechner, R. & Cokljat, D. 2010 The scale-adaptive simulation method for unsteady turbulent flow predictions. part 2: Application to complex flows. *Flow, Turbulence and Combustion* **85** (1), 139–165.

European Commission 2014 Eu transport in figures, statistical pocketbook. Belgium.

Fago, B., Lindner, H. & Mahrenholtz, O. 1991 The effect of ground simulation on the flow around vehicles in wind tunnel testing. *Journal of Wind Engineering and Industrial Aerodynamics* **38** (1), 47–57.

Ferziger, J. H. & Perić, M. 2002 *Computational Methods for Fluid Dynamics*, 3rd edn. Springer.

Fluent 2009 12.0 theory guide.

Fossi, A., DeChamplain, A. & Akih-Kumgeh, B. 2015 Unsteady rans and scale adaptive simulations of a turbulent spray flame in a swirled-stabilized gas turbine model combustor using tabulated chemistry. *International Journal of Numerical Methods for Heat & Fluid Flow* **25** (5), 1064–1088.

García, J., Crespo, A., Berasarte, A. & Goikoetxea, J. 2011 Study of the flow between the train underbody and the ballast track. *Journal of Wind Engineering and Industrial Aerodynamics* **99** (10), 1089–1098.

Gil, N., Baker, C., Roberts, C. & Quinn, A. 2010 Passenger train slipstream characterization using a rotating rail rig. *Journal of Fluids Engineering* **132** (6), 061401.

Golub, G. H. & Van Loan, C. F. 2012 *Matrix computations*, , vol. 3. JHU Press.

Graftieaux, L., Michard, M. & Grosjean, N. 2001 Combining piv, pod and vortex identification algorithms for the study of unsteady turbulent swirling flows. *Measurement Science and technology* **12** (9), 1422.

Hemida, H., Baker, C. & Gao, G. 2014 The calculation of train slipstreams using large-eddy simulation. *Proceedings of the Institution of Mechanical Engineers, Part F: Journal of Rail and Rapid Transit* **228** (1), 25–36.

Hemida, H., Gil, N. & Baker, C. 2010 Les of the slipstream of a rotating train. *Journal of Fluids Engineering* **132** (5), 051103.

Huang, S., Hemida, H. & Yang, M. 2016 Numerical calculation of the slipstream generated by a crh2 high-speed train. *Proceedings of the Institution of Mechanical Engineers, Part F: Journal of Rail and Rapid Transit* **230** (1), 103–116.

Infrastructure Partnerships Australia 2016 East coast high capacity infrastructure corridors. `http://infrastructure.org.au/wp-content/uploads/2016/12/VFT_20101.pdf`.

Japan Railway Company 2017 About the shinkansen. `http://english.jr-central.co.jp/about/index.html`.

Jönsson, M., Wagner, C. & Loose, S. 2014 Particle image velocimetry of the underfloor flow for generic high-speed train models in a water towing tank. *Proceedings of the Institution of Mechanical Engineers, Part F: Journal of Rail and Rapid Transit* **228** (2), 194–209.

Jordan, S., Johnson, T., Sterling, M. & Baker, C. 2008 Evaluating and modelling the response of an individual to a sudden change in wind speed. *Building and Environment* **43** (9), 1521–1534.

Jordan, S., Sterling, M. & Baker, C. 2009 Modelling the response of a standing person to the slipstream generated by a passenger train. *Proceedings of the Institution of Mechanical Engineers, Part F: Journal of Rail and Rapid Transit* **223** (6), 567–579.

Kaltenbach, H.-J., Portillo, I. A. & Schober, M. 2008 A generic train-underfloor experiment for cfd validation. In *BBAA VI International Colloquium on: Bluff bodies aerodynamics and applications*, pp. 20–24. Citeseer.

Krajnović, S. & Davidson, L. 2005 Influence of floor motions in wind tunnels on the aerodynamics of road vehicles. *Journal of wind engineering and industrial aerodynamics* **93** (9), 677–696.

Kwon, H.-b., Park, Y.-W., Lee, D.-h. & Kim, M.-S. 2001 Wind tunnel experiments on korean high-speed trains using various ground simulation techniques. *Journal of Wind Engineering and Industrial Aerodynamics* **89** (13), 1179–1195.

Mancini, G., Malfatti, A., Violi, A. G. & Matschke, G. 2001 Effects of experimental bogie fairings on the aerodynamic drag of the etr 500 high speed train. In *Proceedings of the World Congress of Railway Research WCRR*.

Menter, F. & Egorov, Y. 2010 The scale-adaptive simulation method for unsteady turbulent flow predictions. part 1: theory and model description. *Flow, Turbulence and Combustion* **85** (1), 113–138.

Mizushima, F., Takakura, H., Kurita, T., Kato, C. & Iida, A. 2007 Experimental investigation of aerodynamic noise generated by a train-car gap. *Journal of Fluid Science and Technology* **2** (2), 464–479.

Morden, J. A., Hemida, H. & Baker, C. J. 2015 Comparison of rans and detached eddy simulation results to wind-tunnel data for the surface pressures upon a class 43 high-speed train. *Journal of Fluids Engineering* **137** (4), 041108.

Morgan Stanley 2011 Morgan stanley research global. Morgan Stanley Blue Paper, China High-Speed Rail.

Muld, T. W., Efraimsson, G. & Henningson, D. S. 2012a Flow structures around a high-speed train extracted using proper orthogonal decomposition and dynamic mode decomposition. *Computers & Fluids* **57**, 87–97.

Muld, T. W., Efraimsson, G. & Henningson, D. S. 2012b Mode decomposition and slipstream velocities in the wake of two high-speed trains. *The International Journal of Railway Technology* .

Muld, T. W., Efraimsson, G. & Henningson, D. S. 2014 Wake characteristics of high-speed trains with different lengths. *Proceedings of the Institution of Mechanical Engineers, Part F: Journal of Rail and Rapid Transit* **228** (4), 333–342.

Österlund, J., Kaiser, E., Krajnović, S. & Noack, B. R. 2015 Cluster-based reduced-order modelling of the flow in the wake of a high speed train. *Journal of Wind Engineering and Industrial Aerodynamics* **145**, 327–338.

Paradot, N., Talotte, C., Garem, H., Delville, J. & Bonnet, J.-P. 2002 A comparison of the numerical simulation and experimental investigation of the flow around a high speed train. In *ASME 2002 Joint US-European Fluids Engineering Division Conference*, pp. 1055–1060. American Society of Mechanical Engineers.

Parkin, D. 2014 A numerical investigation of periodic actuation on bluff bodies in ground proximity.

Penwarden, A., Grigg, P. & Rayment, R. 1978 Measurements of wind drag on people standing in a wind tunnel. *Building and environment* **13** (2), 75–84.

Pereira, I. & André, J. M. C. 2013 A semi-analytical model of the 3d boundary layer over the streamlined nose of a train. *Journal of Wind Engineering and Industrial Aerodynamics* **119**, 78–88.

Phase 1 2011 Department of infrastructure and regional development. High Speed Rail Study, Phase 2 Report. *Commonwealth Government of Australia.*

Phase 2 2013 Department of infrastructure and regional development. High Speed Rail Study, Phase 2 Report. *Commonwealth Government of Australia.*

Pii, L., Vanoli, E., Polidoro, F., Gautier, S. & Tabbal, A. 2014 A full scale simulation of a high speed train for slipstream prediction. In *Transport Research Arena (TRA) 5th Conference: Transport Solutions from Research to Deployment*.

Pope, S. B. 2001 Turbulent flows .

Quinn, A., Hayward, M., Baker, C., Schmid, F., Priest, J. & Powrie, W. 2010 A full-scale experimental and modelling study of ballast flight under high-speed trains. *Proceedings of the Institution of Mechanical Engineers, Part F: Journal of Rail and Rapid Transit* **224** (2), 61–74.

Raghunathan, R. S., Kim, H.-D. & Setoguchi, T. 2002 Aerodynamics of high-speed railway train. *Progress in Aerospace sciences* **38** (6), 469–514.

Rotta, J. C. 1972 Turbulente strömungen .

Sardou, M. 1986 Reynolds effect and moving ground effect tested in a quarter scale wind tunnel over a high speed moving belt. *Journal of Wind Engineering and Industrial Aerodynamics* **22** (2-3), 245–270.

Schetz, J. A. 2001 Aerodynamics of high-speed trains. *Annual Review of fluid mechanics* **33** (1), 371–414.

Schulte-Werning, B., Heine, C. & Matschke, G. 2001 Slipstream development and wake flow characteristics of modern high-speed trains. *ZEITSCHRIFT FUR ANGEWANDTE MATHEMATIK UND MECHANIK* **81**, S789–790.

Schulte-Werning, B., Heine, C. & Matschke, G. 2003 Unsteady wake flow characteristics of high-speed trains. *PAMM* **2** (1), 332–333.

Shur, M. L., Spalart, P. R., Strelets, M. K. & Travin, A. K. 2008 A hybrid rans-les approach with delayed-des and wall-modelled les capabilities. *International Journal of Heat and Fluid Flow* **29** (6), 1638–1649.

Sirovich, L. 1987 Turbulence and the dynamics of coherent structures. i. coherent structures. *Quarterly of applied mathematics* **45** (3), 561–571.

Smagorinsky, J. 1963 General circulation experiments with the primitive equations: I. the basic experiment. *Monthly weather review* **91** (3), 99–164.

Spalart, P., Jou, W., Strelets, M., Allmaras, S. *et al.* 1997 Comments on the feasibility of les for wings, and on a hybrid rans/les approach. *Advances in DNS/LES* **1**, 4–8.

Spalart, P. R., Deck, S., Shur, M., Squires, K., Strelets, M. K. & Travin, A. 2006 A new version of detached-eddy simulation, resistant to ambiguous grid densities. *Theoretical and computational fluid dynamics* **20** (3), 181–195.

STERLING, M., BAKER, C., JORDAN, S. & JOHNSON, T. 2008 A study of the slipstreams of high-speed passenger trains and freight trains. *Proceedings of the Institution of Mechanical Engineers, Part F: Journal of Rail and Rapid Transit* **222** (2), 177–193.

TSI 2008 European union agency for railways. Commission Regulation (EU) No 1302/2014 concerning a technical specification for interoperability relating to the 'rolling stock — locomotives and passenger rolling stock' subsystem of the rail system. *Official Journal of the European Union.*

TSI 2014 European union agency for railways. Commission Regulation (EU) No 1302/2014 concerning a technical specification for interoperability relating to the 'rolling stock — locomotives and passenger rolling stock' subsystem of the rail system. *Official Journal of the European Union.*

VINO, G., WATKINS, S., MOUSLEY, P., WATMUFF, J. & PRASAD, S. 2005 Flow structures in the near-wake of the ahmed model. *Journal of fluids and structures* **20** (5), 673–695.

XIA, C., SHAN, X. & YANG, Z. 2016 Influence of ground configurations in wind tunnels on the slipstream of a high-speed train. In *8th International Colloquium on Bluff Body Aerodynamics and Applications*. Northeastern University, Boston.

XIA, C., WANG, H., SHAN, X., YANG, Z. & LI, Q. 2017 Effects of ground configurations on the slipstream and near wake of a high-speed train. *Journal of Wind Engineering and Industrial Aerodynamics* **168**, 177–189.

YANG, Z., GU, Z., TU, J., DONG, G. & WANG, Y. 2014 Numerical analysis and passive control of a car side window buffeting noise based on scale-adaptive simulation. *Applied Acoustics* **79**, 23–34.

YAO, S.-B., SUN, Z.-X., GUO, D.-L., CHEN, D.-W. & YANG, G.-W. 2013 Numerical study on wake characteristics of high-speed trains. *Acta Mechanica Sinica* **29** (6), 811–822.

ZHANG, J., LI, J.-J., TIAN, H.-Q., GAO, G.-J. & SHERIDAN, J. 2016 Impact of ground and wheel boundary conditions on numerical simulation of the high-speed train aerodynamic performance. *Journal of Fluids and Structures* **61**, 249–261.